UNIVERSITAT
POLITÈCNICA
DE VALÈNCIA

DOCTORAL THESIS

COMPUTATIONAL ASSESSMENT OF COMBUSTION NOISE OF AUTOMOTIVE COMPRESSION-IGNITED ENGINES

PRESENTED BY

Josep Gómez Soriano

SUPERVISED BY

Dr. Alberto Broatch Jacobi

October 2018
DEPARTAMENTO DE MÁQUINAS Y MOTORES TÉRMICOS

UNIVERSITAT POLITÈCNICA DE VALÈNCIA

DEPARTAMENTO DE MÁQUINAS Y MOTORES TÉRMICOS

—— DOCTORAL THESIS ——

COMPUTATIONAL ASSESSMENT OF COMBUSTION NOISE OF AUTOMOTIVE COMPRESSION-IGNITED ENGINES

PRESENTED BY

D. Josep Gómez Soriano

SUPERVISED BY

Dr. D. Alberto Broatch Jacobi

FOR THE DEGREE OF

Doctor of Philosophy

OCTOBER 2018

DOCTORAL THESIS

"Computational assessment of combustion noise of automotive compression-ignited engines"

Presented by: D. Josep Gómez Soriano
Supervised by: Dr. D. Alberto Broatch Jacobi

THESIS EXAMINERS

Dr. D. Gianluca Montenegro
Dr. D. Angelo Onorati
Dr. D. Jacobo Porteiro Fresco

DEFENSE COMITEE

Chairman: Dr. D. Antonio José Torregrosa Huguet
Secretary: Dr. D. Jorge Luis Parrondo Gayo
Member: Dr. D. Angelo Onorati

Valencia, October 2018

A Anna

Abstract

The ever-increasing demands of industry are changing the way we understand society and the environment in which we live. In the face of the need for rapid and globalised trade, a number of sustainability issues are emerging which, on the one hand, encourage sectors such as transport to radically increase their activities, but, on the other hand, cause a negative impact on terrestrial ecosystems. In this context, the negative effects of environmental and noise pollution are reaching really worrying limits, these being especially visible in the main urban areas where the authorities are even restricting the circulation of vehicles powered with thermal engines.

In particular, the noise produced by the fuel burning in vehicles powered by reciprocating internal combustion engines, being one of the main acoustic sources ahead of others such as aviation or railways, is being the focus of recent studies to reduce its harmful effects on the population.

The main objective of this thesis focuses on the study and characterization of combustion as a source of noise emissions. Specifically, this research focuses on addressing the physical phenomena associated with noise generation in compression-ignited engines, as well as proposing some guidelines in order to better understand and improve –from the point of view of noise emissions and fuel consumption– the design of current engines.

In a first approach, experimental techniques are used to characterise the source of the acoustic disturbances by recording the instantaneous pressure inside the combustion chamber. Although the information provided by these methods is relevant, there are some limitations to recreate the spatiality of the acoustic field and, therefore, make it difficult to understand the non-stationary phenomena associated with it.

For this reason, in subsequent studies the Computational Fluid Dynamics or CFD approach is utilized, thereby overcoming the limitations of experimental techniques and allowing a complete visualization of the problem. As a

preliminary and indispensable step, we proceed to implement and validate the CFD model to ensure a good accuracy in the results and a reasonable calculation time.

The application of frequency analysis and modal decomposition methods has made it possible to study the pressure field inside the chamber and thus better understand its behaviour. In this way, it has been possible to find relationships between the combustion and the spectral response of the internal acoustic field. The pressure oscillation patterns show that the most energetic structures, and thus contributing the most to the acoustic emission, are centred on macroscopic structures of similar size to the chamber geometry. In addition, the ignition position of the fuel has been shown to have a direct effect on the amplitude of the resonant modes and their spatial distribution.

Finally, regarding the evaluation of different strategies for mitigating noise, different studies are proposed in which the trends in noise emission are analysed by modifying the sound source through the injection configuration and the geometry of the combustion system.

Resumen

Las crecientes exigencias de la industria están cambiando la forma en que entendemos la sociedad y el entorno en el que vivimos. Frente a la necesidad de un comercio rápido y globalizado, están emergiendo varios problemas de sostenibilidad. Por una parte, ciertos sectores resultan favorecidos, como es el caso del transporte y su radical incremento de actividades. Por otra parte, esto causa un impacto negativo considerable en los ecosistemas terrestres. En este marco, los efectos negativos de la contaminación ambiental y sonora están llegando a límites realmente preocupantes, siendo estos especialmente visibles en los principales núcleos urbanos, donde las autoridades están incluso restringiendo la circulación de los vehículos térmicos.

Particularmente, el ruido producido por la quema del combustible en vehículos propulsados por motores de combustión interna alternativos, siendo una de las principales fuente acústicas por delante de otras como la aviación o el ferrocarril, está siendo objeto de recientes estudios para reducir sus efectos perjudiciales en la población.

El objetivo principal de esta tesis se centra en el estudio y caracterización de la combustión como fuente de emisiones acústicas. Concretamente, esta investigación tiene como propósito dar respuesta a cuáles son los fenómenos físicos asociados a la generación del ruido en motores de encendido por compresión, así como proponer algunas directrices que ayuden a entender y mejorar –desde el punto de vista de emisiones acústicas y consumo– el diseño de los motores actuales.

En una primera aproximación, se recurre a técnicas experimentales de medida para, con el registro de la presión instantánea dentro de la cámara de combustión, caracterizar el origen de las perturbaciones acústicas. A pesar de que la información aportada por estos métodos es relevante, existen limitaciones para recrear la espacialidad del campo acústico y, por tanto, dificultan la comprensión de los fenómenos no estacionarios asociados a este.

Por esta razón, en posteriores estudios se recurre al uso de la dinámica de fluidos computacional o CFD, superando así las limitaciones de las técnicas experimentales y permitiendo una visualización completa del problema. Como paso previo e indispensable, se procede a implementar y validar del modelo CFD para asegurar una buena precisión en los resultados y un tiempo de cálculo razonable.

La aplicación de métodos de análisis en frecuencia y descomposición modal han permitido estudiar el campo de presiones en el interior de la cámara y así entender mejor su comportamiento. De este modo, ha sido posible encontrar relaciones entre la combustión y la respuesta espectral del campo acústico interno. Los patrones de oscilación de la presión muestran que las estructuras más energéticas, y que por tanto contribuyen a la emisión acústica en mayor medida, están centradas en estructuras macroscópicas de tamaño similar a la geometría de la cámara. Además, se ha demostrado que la posición de la ignición del combustible tiene un efecto directo sobre la amplitud de los modos resonantes y su distribución espacial.

Por último, en cuanto a la evaluación de estrategias para mitigar el ruido, se proponen distintos estudios en los que se analizan las tendencias en la emisión acústica al modificar la fuente sonora, mediante la configuración de la inyección y la geometría del sistema de combustión.

Resum

Les creixents exigències de la indústria estan canviant la forma en què entenem la societat i l'entorn en què vivim. Davant la necessitat d'un comerç ràpid i globalitzat estan sorgint diversos problemes de sostenibilitat que, per una part afavoreixen que sectors com el del transport incrementen les seues activitats de forma radical, però que per l'altra, causen un impacte negatiu en els ecosistemes terrestres. En aquest context, els efectes negatius de la contaminació ambiental i sonora estan arribant a límits realment preocupants, sent aquests especialment visibles als principals nuclis urbans on les autoritats estan inclús restringit la circulació dels vehicles tèrmics.

Particularment, el soroll causat per la crema de combustible en vehicles propulsats per motors de combustió interna alternatius, sent una de les principals fonts acústiques per davant d'altres com l'aviació o el ferrocarril, està sent objecte de recents estudis per tal de reduir els efectes perjudicials en la població.

L'objectiu principal d'aquesta tesi es centra en l'estudi i caracterització de la combustió com a font d'emissions acústiques. Concretament, aquesta investigació té com a propòsit donar resposta a quins són els fenòmens físics associats a la generació de soroll en motors d'encès per compressió, així com proposar algunes directrius que ajuden a entendre i millorar –des del punt de vista de les emissions acústiques i consum– el disseny dels motors actuals.

En una primera aproximació, es recorre a tècniques experimentals de mesura per a, amb el registre de la pressió instantània en la cambra de combustió, caracteritzar l'origen de les pertorbacions acústiques. Tot i que la informació aportada per aquests mètodes és rellevant, existeixen limitacions per a reconstruir l'espacialitat del camp acústic i, per tant, dificulten la comprensió dels fenòmens no estacionaris associats a aquest.

Per aquesta raó, en posteriors estudis es recorre a l'ús de la dinàmica de fluids computacional o CFD, superant així les limitacions de les tècniques experimentals i permetent una visualització completa del problema. Com a pas previ i indispensable, es procedeix a implementar i validar el model CFD per assegurar una bona precisió en els resultats i un temps de càlcul raonable.

L'aplicació de mètodes d'anàlisi en freqüència i descomposició modal ha permès estudiar el camp de pressions en l'interior de la càmera i així entendre millor el seu comportament. D'aquesta forma, ha sigut possible trobar relacions entre la combustió i la resposta espectral del camp acústic intern. Els patrons d'oscil·lació de la pressió mostren que les estructures més energètiques, i que per tant contribueixen a l'emissió acústica en major mesura, estan centrades en estructures macroscòpiques de grandària similar a la geometria de la càmera. A més, s'ha demostrat que la posició de la ignició del combustible té un efecte directe sobre l'amplitud dels modes ressonants i la seua distribució espacial.

Per últim, pel que fa a l'avaluació de diverses estratègies per a mitigar el soroll, es proposen distints estudis en què s'analitzen les tendències en l'emissió acústica en modificar la font sonora mitjançant la configuració de l'injector i la geometria del sistema de combustió.

List of publications

Following the work performed in the framework of this doctoral thesis and its associated projects, the following journal papers have been published:

[1] A. BROATCH, X. MARGOT, R. NOVELLA, and J. GOMEZ-SORIANO. "Combustion noise analysis of partially premixed combustion concept using gasoline fuel in a 2-stroke engine". *Energy* 107, 2016, pp. 612–624.

[2] A. BROATCH, X. MARGOT, R. NOVELLA, and J. GOMEZ-SORIANO. "Impact of the injector design on the combustion noise of gasoline partially premixed combustion in a 2-stroke engine". *Applied Thermal Engineering* 119, 2017, pp. 530–540.

[3] A. J. TORREGROSA, A. BROATCH, X. MARGOT, and J. GOMEZ-SORIANO. "Towards a Predictive CFD Approach for Assessing Noise in Diesel Compression Ignition Engines. Impact of the Combustion Strategies". *International Conference on Modeling and Diagnostics for Advanced Engine systems: the 9th COMODIA, Okayama (Japan)*, 2017.

[4] A. J. TORREGROSA, A. BROATCH, R. NOVELLA, J. GOMEZ-SORIANO, and L. F. MÓNICO. "Impact of gasoline and Diesel blends on combustion noise and pollutant emissions in Premixed Charge Compression Ignition engines". *Energy* 137, 2017, pp. 58–68.

[5] A. J. TORREGROSA, A. BROATCH, J. GARCÍA-TÍSCAR, and J. GOMEZ-SORIANO. "Modal decomposition of the unsteady flow field in compression-ignited combustion chambers". *Combustion and Flame* 188, 2018, pp. 469–482.

[6] A. J. TORREGROSA, A. BROATCH, A. GIL, and J. GOMEZ-SORIANO. "Numerical approach for assessing combustion noise in compression-ignitied Diesel engines". *Applied Acoustics* 135, 2018, pp. 91–100.

[7] A. BROATCH, R. NOVELLA, J. GARCÍA-TÍSCAR, and J. GOMEZ-SORIANO. "Potential of dual spray injectors for optimising the noise emission of gasoline partially premixed combustion in a 2-stroke HSDI CI engine". *Applied Thermal Engineering*, 2018, pp. 369–378.

[8] A. Broatch, J. J. López, J. García-Tíscar, and J. Gomez-Soriano. "Experimental Analysis of Cyclical Dispersion in Compression-Ignited Versus Spark-Ignited Engines and Its Significance for Combustion Noise Numerical Modeling". *Journal of Engineering for Gas Turbines and Power* 140, 10 2018, pp. 102808–102808–8.

[9] A. Broatch, R. Novella, J. Gomez-Soriano, P. Pal, and S. Som. "Numerical Methodology for Optimization of Compression-Ignited Engines Considering Combustion Noise Control". *SAE International Journal of Engines* 2018-01-0193, 2018.

[10] P. Pal, C. Kolodziej, S. Choi, A. Broatch, et al. "Development of a Virtual CFR Engine Model for Knocking Combustion Analysis". *SAE International Journal of Engines* 2018-01-0187, 2018.

[11] A. J. Torregrosa, A. Broatch, X. Margot, and J. Gomez-Soriano. "Understanding the unsteady pressure field inside combustion chambers of compression ignition engines using a CFD approach". *International J of Engine Research (available on-line)*, 2018.

Additionally, three more manuscripts have been submitted to different journals and are undergoing peer-review:

[12] A. Broatch, R. García-Tíscar, J. Gomez-Soriano, P. Pal, and S. Som. "Large Eddy Simulation for combustion acoustics in compression-ignited engines". *Submited to Combustion and Flame*, 2018.

[13] A. Broatch, R. García-Tíscar, J. Gomez-Soriano, P. Pal, and S. Som. "Advantages of Large Eddy Simulations in the prediction of compression-ignited combustion unsteadiness". *Submited to Applied Energy*, 2018.

[14] A. Broatch, R. Novella, R. García-Tíscar, and Gomez-Soriano. "On the shift of acoustic characteristics of compression-ignited engines when operating with gasoline partially premixed combustion". *Submited to Applied Thermal Engineering*, 2018.

Division of work between authors

The work leading up to this thesis was done in collaboration with other researchers. The respondent is the co-author of all papers on which this thesis is based, with author signatures being in order of seniority in the Institute. The respondent implemented the proposed methodology into the different engine set-ups, performed the calculations, processed the numerical results and extracted the presented conclusions. Discussions were also performed in collaboration with supervisor Prof. Broatch and the rest of the co-authors. Experimental activities were not performed by the respondent, and are thus gratefully acknowledged.

Funding acknowledgements

Acknowledgements

I would like to record my sincere gratitude to my advisor Prof. Alberto Broatch for his guidance and support during the chase of this research. A gratitude that also must be extended to Prof. Payri and Prof. Desantes on behalf of CMT – Motores Térmicos and Universitat Politècnica de València for offering me the chance to become part of this research group during these four years.

I owe my most special thanks to Prof. Ricardo Novella for his advice and invaluable help in the most difficult moments but especially for the good ones we shared during the fruitless lunchtime discussions, sports sessions... I just can say, *moltes gràcies per tot Rick*. Many thanks as well to Dr. José Manuel Pastor for being a never-ending source of knowledge about simulation and also for making lunchtimes really fun.

I also wish to thank all the members of the Noise Control research line, specially Prof. Torregrosa, Dr. Jorge García and Bernardo Planells for providing numerous and priceless suggestions. Also, I want to include in this recognition Prof. Olmeda, my office-mates, and the rest of professors, researchers, technicians, students, the administrative staff, etc., for creating the environment in which I have felt very lucky to work.

I would like to thank Dr. Sibendu Som, Dr. Pinaki Pal and the rest of the staff at the Center for Transportation Research for hosting me as a visiting researcher during my doctoral stay at Argonne National Laboratory and also for their productive collaborations as well.

Last, but not least, I wish to thank my family and friends, specially my parents and sister for their unlimited support. And finally, thank you, Anna, for your unconditional support and for showing me that things are never as difficult as they seem.

Valencia, 2018

"Fes be i no fages mal, i tindràs el que cal."

José Soriano Beltran, *Quartell, 1910-2005*

Contents

List of Figures

List of Tables

List of Symbols

Latin

a	Speed of sound	$\mathrm{m\,s^{-1}}$
B	Cylinder bore	m
C	Model coefficients	—
d	Nozzles diameter	m
$\mathrm{d}p/\mathrm{d}t$	Pressure rise rate	$\mathrm{Pa\,s^{-1}}$
E_{res}	Energy of resonance	$\mathrm{Pa^2\,s}$
f	Frequency	Hz
M	Mach number	—
n	Engine rotational speed	rpm
p	Pressure	Pa
R	Specific gas constant	$\mathrm{J\,kg^{-1}\,K^{-1}}$
R^{norm}	Normalized cylinder radius	—
T	Temperature	K
t	Time	s

Greek

$\Delta f, t$	Frequency or time step	Hz or s
γ	Ratio of specific heats	—
$\alpha_{m,n}$	Modal coefficients	—
η	Efficiency	%
ϕ	Equivalence ratio	—
Φ	DMD mode	—
ρ	Density	$\mathrm{kg\,m^{-3}}$
Θ	FFT mode	—
Ψ	POD mode	—

Sub- and superscripts

comb	Related to combustion
comp	Related to compression
cyl	Related to cylinder
idle	Related to idle condition
ign	Relative to the conditions at the ignition timing
inj	Relative to fuel injection
int	Relative to intake manifold conditions
IVC	Relative to the conditions at IVC timing
main	Referred to the main injection
max	Maximum
norm	Normalized value
pilot	Referred to the pilot injection
post	Referred to the post injection

Acronyms

AMR	Adaptive Mesh Refinement
aTDC	after Top Dead Centre
BDC	Bottom Dead Centre
CA10	Crank Angle for 10% of Fuel Burnt
cad	Crank Angle Degree
CCD	Central Composite Design
CCV	Cycle-to-Cycle Variation
CDC	Conventional Diesel Combustion
CF	Cost Function
CFD	Computational Fluid Dynamics
CFL	Courant-Friedrichs-Levy (number)
CI	Compression-Ignited
CPL	Cylinder Pressure Level
DDM	Discrete Droplet Model
DI	Direct Injection
DMD	Dynamic Mode Decomposition
DNS	Direct Numerical Simulation
DoE	Design of Experiments
EGR	Exhaust Gas Recirculation
EVO	Exhaust Valves Opening
FEM	Finite Element Model
FFT	Fast Fourier Transform
GA	Genetic algorithm
GEP	Gas Exchange Process
HCCI	Homogeneous Charge Compression Ignition
HSDI	High Speed Direct Injection

IA	Included Angle
ICE	Internal Combustion Engine
IMEP	Indicated Mean Effective Pressure
ISFC	Indicated Specific Fuel Consumption
IVC	Intake Valves Closing
KH	Kelvin-Helmholtz
LES	Large Eddy Simulation
LTC	Low Temperature Combustion
MF	Merit Function
MZ	Multi-Zone
NN	Number of Nozzles
NO_x	Nitrous Oxides (NO and NO_2)
NVH	Noise, Vibration, and Harshness
ON	Overall Noise
PCA	Principal Component Analysis
PCCI	Premixed Charge Compression Ignition
PISO	Pressure Implicit with Splitting of Operators
PIV	Particle Image Velocimetry
POD	Proper Orthogonal Decomposition
PPC	Partially Premixed Combustion
PPRR	Peak Pressure Rise Rate
PRF	Primary Reference Fuel
RANS	Reynolds-averaged Navier-Stokes
RI	Ringing Intensity
RNG	Re-Normalized Group
RoHR	Rate of Heat Release
RON	Research Octane Number
RSM	Response Surface Method
RT	Rayleigh-Taylor
SAGE	Detailed Chemistry Solver
SD	Standard Deviation
SGS	Sub-Grid Scale
SI	Spark-Ignited
SoE	Start of Energizing of the Injector
SoI	Start of injection
SoPE	Start of Pressure Excitation ($\approx$ CA10)
SPL	Sound Pressure Level
STFFT	Short-Time Fast Fourier Transform
SVD	Singular Value Decomposition
TDC	Top Dead Centre
TJI	Turbulent Jet Injection
UDF	User Defined Function
URANS	Unsteady Reynolds-averaged Navier-Stokes
VVT	Variable Valve Timing

Introduction

The rapid population growth produced over the last decades is causing a big transformation of life on Earth; while the need of better transportation networks is thoroughly changing the way we understand society, our environments are becoming more and more unhealthy. This issue is particularly evident in urban areas in which the population density is specially high.

Nowadays, the adverse effects of the global warming are being constantly announced in the media, and it has created a raising concern about the greenhouse gases emission and its undesired consequences. Furthermore, news about the air quality degradation due to the vehicles emissions and how the number of respiratory diseases has significantly grown owing to this, also enhanced their popularity.

Although being outside of the centre of the media's attention, links between traffic noise and increased sleep disorders, hypertension, hearing loss, strokes and mortality have been established [15], especially in those environments where engine noise is prevalent over tire noise due to lower speeds and the people living, working and sleeping close to busy roads. This can be easily seen in Fig. 1.1, in which the percentage of people exposed to noise per decibel band is plotted for inside and outside urban areas in Europe.

The health of our ecosystems are also at risk. Actual noise data plotted in the same figure reveal how the space of moderate levels of noise is covering large territories outside the cities and populated regions endangering habitats and species that are particularly susceptible to noise.

Noise coming from road traffic is generated by multiple sources within the vehicle and that introduces an inherent complexity. For instance, while the mechanical parts, combustion or friction noises are such examples of

Percentage of people exposed
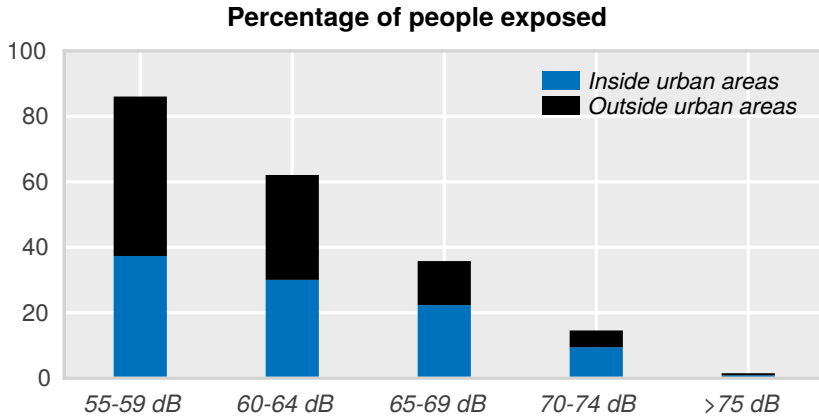
Figure 1.1: *Percentage of people exposed to noise per decibel band in Europe. Data provided by the European Environment Agency.*

emissions purely generated by the vehicle itself, the interaction with the ambient also produces other annoying acoustic emissions –aerodynamic or tire noise.

The management of all emission issues together, including pollutants, greenhouse gases and noise, is an extremely hard and intricate task that still does not have a clear solution today.

1.1. Internal combustion engines

Since Rudolf Diesel and Nicolaus Otto unveiled their own engine prototypes at the end of XIX century, none of them could imagine that both concepts would become the world wide leading powerplants.

Thanks to the extraordinary R&D conducted over the last thirty years, their original designs allowed to fulfil all imposed sociopolitical restrictions while improving their driveability and fuel consumption.

Turbocharging, direct injection systems or exhaust gas recirculation (EGR) are some examples of technological advances that supposed an important boost in their implantation.

Specifically, owing to its flexibility and improved efficiency, Rudolf's concept has been installed as the largest transportation engine for heavy-duty applications while competing at the same level with spark-ignited (SI) engines in the light-duty automotive segment.

Nonetheless, despite the benefits for society –especially in terms of costs and comfort– of using internal combustion engines for transportation purposes, this is not exempt of disadvantages. The transport sector represents

nearly 26% of the total CO_2 emissions and, in particular, the passenger cars segment is the largest source of both greenhouse and pollutant emissions in vehicles.

In consequence, the number of actions for searching an inclusive and sustainable solution has significantly increased in resent years, becoming a topic of current interest in all society collectives[1]. For example, one of the current trends in the automotive industry is to migrate towards the vehicle electrification. However, as oil, gas and coal-fired power plants are still notably featured in the generation mix of several countries, it is conceivable that the effective environmental footprint of electric vehicles could be matched by their thermal counterparts, at least until cleaner and more efficient energy sources become widespread.

The struggle with this "new" competitor is leading to increase the efforts for enhancing Internal Combustion Engines (ICE) performance by promoting cleaner and quieter combustion that radically reduces the impact on our environment. However, since combustion implies, by definition, a sudden energy release which is in turn inherently noisy, this matter becomes extremely intricate and its assessment is not trivial.

1.2. Acoustic emissions

While pollutant and greenhouse emissions are a recurring focus of the regulation organisms and research efforts, Noise, Vibration and Harshness (NVH) is an often-overlooked issue, traditionally removed form the engine design process, mainly due to its inherent complexity and lack of awareness. This fact entails a large investment of resources to mitigate the undesired effects of noise in subsequent development stages –causing severe fuel consumption penalties– or even in expensive infrastructures [16].

The European Environmental Agency reported that over 70 million people in EU cities are subjected to day-evening-night noise levels above 55 dB, while only 7% of the proposed solutions to enhance this societal problem have been addressed to the source itself.

Within the actual paradigm, where population density and human activities increase industry demands, transportation is the main cause of noise. In particular, road traffic is by far the biggest source of noise, ahead of other external sources such as aircraft, industry or railway noise [17]. Moreover, the

---

[1]In this context, the Paris climate conference (COP21), the United Nations Conference on sustainable Development (Rio + 20) or Horizon 2020 are such examples of administrative measures to deal with the actual paradigm.
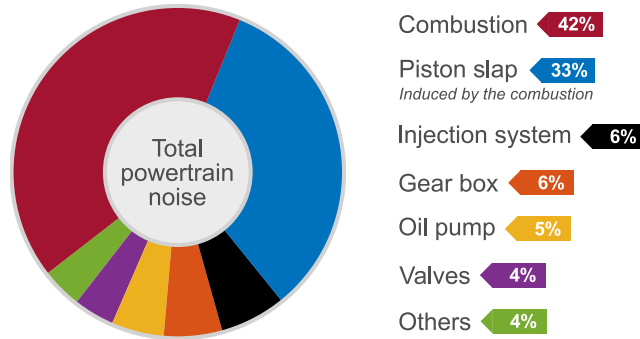
Figure 1.2: *Noise source contribution to the overall noise of a direct injection compression-ignited powertrain [20].*

engine and the exhaust system are the larger sources of acoustic emissions inside the overall vehicle noise [18]. For instance, in compression-ignited (CI) powertrains, in which the combustion is particularly noisy, the powertrain can easily cover 30% of the total noise emission [19].

Similarly, the powertrain noise is a host of several sub-sources linked to the different engine devices and processes. Figure 1.2 illustrates how each device/process contributes to the total powertrain noise. As it can be seen, combustion represents the 42% of the total emission. Data plotted in this graph was obtained from a given direct injection (DI) compression-ignited powertrain and applying the methodology developed by Kanda et al. [20], in which each specific acoustic level is isolated from the total measured powertrain level by multiple experimental techniques and spectral analysis. It is important to note that, although many authors consider the exhaust noise within the powertrain acoustics, it is taken as a detached source in this diagram.

Thereby, although the combustion is not the sole source of noise in passenger cars, since other sources such as turbochargers, exhaust, pumps, wheels or aerodynamics are also relevant, it is certainly the most relevant one, specially in urban environment where some authorities are already considering a permanent ban on thermal vehicles.

Since the human acoustic perception is very sensitive to the level but also to the frequency of the sound [15], similar noise levels can affect differently if they are emitted at distinct frequencies [21, 22]. Another relevant aspect to take into account is therefore that not only the noise level plays a relevant role in the acoustics, also the subjective or psychoacoustic

perception is important. Thus, the sound quality perceived by the customers can condition the purchasing decision [23, 24], increasing the concern of the engine manufacturers about noise-related issues.

1.3. Objectives

The principal objective of this thesis is to develop a numerical methodology for assessing combustion noise in compression-ignited engines, thereby contributing to the combustion-induced acoustics comprehension. Moreover, other specific objectives related to this will be pursued:

- Determining the combustion noise origin and characterizing the source of acoustic emissions due to the combustion. Since the available literature is still scarce, expanding the knowledge on this matter while identifying all involved physical phenomena will improve the comprehension of such complex regard.

- Examining the effects of the combustion acoustic signature on the external-propagated field. The understanding of the connection between source emission and observer perception will enhance the discernment of how the combustion changes the engine acoustics.

- Establishing optimal operating strategies and design paths which promote a new generation of quieter, more efficient and sustainable engines will be a background target that will give a more pragmatic standpoint of this research work.

1.4. Thesis outline

The content of this thesis is organized in the nine chapters. After this introduction that constitutes Chapter 1, an exhaustive literature review on combustion noise analysis in compression-ignited engines will be performed in Chapter 2. This search will present the relevant achievements on combustion noise characterization research through different approaches and measurement techniques, while emphasizing the importance of the numerical simulations to improve the comprehension of such physical mechanisms which lead to the acoustic emission.

As a preliminary study to confirm several statements introduced in the prior chapter, Chapter 3 will show a study to characterize the acoustic source by means of the experiments carried out directly on a real engine. Although

measurement methodologies are considered out of the scope of this thesis, a brief description of the experimental facilities will be given. Moreover, processing methods will be widely explained since they will be used in the subsequent chapters. The limitations of this approach will be clearly identified and the use of numerical methods will be proven.

Chapter 4 will show the implementation of the numerical model, paying special attention on examining the effects of several calculation parameters, hypotheses and models on the acoustic field inside the combustion chamber. General calculation features, such as turbulence modelling, mesh resolution or time discretization, will be evaluated in order to determine a numerical set-up that ensure high accuracy with reasonable computation timings.

Results of the numerical model validation using data available after the experimental campaigns will constitute Chapter 5. Pressure spectra and some acoustic metrics will be utilized for both qualitative and quantitative comparisons in two distinct CI engines and two combustion modes.

The numerical model will be used to provide more insight about the understanding of combustion noise origin in Chapter 6. In particular, the numerical solution is used to further understand the generation phenomena linked to the conventional Diesel combustion. Several flow decomposition techniques will be applied in order to resolve the underlying modal structure of in-cylinder pressure field and also its temporal and frequency behaviour.

In Chapter 7, the knowledge acquired in Chapter 6 will be combined with distinct optimization techniques in order to propose guidelines and potential alternatives to mitigate the undesired effects of noise. Different optimization methods, e.i. based on statistical techniques or genetic algorithms, will be employed to establish cause-effect relationships between the most influencing engine parameters and their response, but also to find the optimum design traits.

The same approach followed for the Diesel combustion will be applied to the partially premixed combustion using gasoline fuel in Chapter 8. The objective here will be to attain the noise problem from a practical point of view, suggesting new technological solutions to improve the concept capabilities.

Lastly, Chapter 9 will outline the main conclusions reached through this research. Some future works will be also suggested to continue this research line and to advance on the comprehension of the combustion noise issue.

CHAPTER 2

Literature review

Since the combustion noise has been identified as relevant for the overall vehicle noise, a review of the literature is a first, essential step in order to frame the problem and to provide a general overview of the involved phenomena.

This chapter is therefore devoted to the literature review of combustion noise in internal combustion engines or, more specifically, in those ignited by compression. The aim here is to provide the reader with a better context of the phenomenological description of the different phases observed in this particular combustion process and their effects on acoustic emissions.

A brief introduction of the state of the art in combustion noise issues produced by CI engines is provided, along with the formulation of different analysis techniques of interest to better understand this particular problem. Special emphasis have been put in numerical methods that describe temporal and spatial features of combustion since they are becoming a reference tool to overcome limitations of experimental techniques, thus achieving an enhanced view and comprehension of in-cylinder physical processes.

2.1. Physics of combustion noise generation

The combustion of a volume element with a reactive blend implies a sudden release of energy; only a minor part of this energy is related to noise generation. In a given combustor device, the sound power emitted is approximately 5 or 6 order of magnitude less than its thermal input. However, combustion noise has been established as a critical issue in industrial environments but also in powertrain sectors such as aeronautical or road transport vehicles.

Although all these combustion systems are completely different and the flame features can be distinct, the fundamentals of the combustion noise origin are common in all systems [25].

From a physical point of view, combustion noise is the result of the turbulence and combustion interaction [26]. Depending on the application, the contribution of each phenomenon may be completely different. Therefore, the knowledge about noise fundamentals is essential to analyse the connection between the combustion and the corresponding acoustics.

Combustion noise can be split –based on the phenomena involved– into direct and indirect components [27, 28]. Direct noise is linked to periodic combustion oscillations or stochastic fluctuations of the heat release in the flame surface [29, 30] whereas indirect noise, or entropy noise, is related to temperature non-uniformities which are connectively transported [30–32].

Combustion systems emit direct and indirect noise [33], being the latter an exclusive feature of continuous-flux combustor devices [34], for instance, due to the entropy spots accelerated downstream the gas-turbine combustion chamber [35].

In positive displacement devices such as reciprocating internal combustion engines however, the interplay between thermal and acoustical phenomena is completely different due to their cyclic, unsteady operation, and to the fact that the process occurs in a closed fluid domain. Thus, even being merely direct, combustion noise can be generated by distinct causes within the same combustion process [36, 37]. Moreover, the acoustic response can be different owing to the interference between the pressure waves and the chamber walls [38].

The magnitude of the pressure waves and the proximity of chamber surfaces could suggest that thermoacoustic instabilities can play a relevant role in these particular combustion chambers. However, the pulsating nature of the combustion itself –the burning is only established during a few milliseconds– causes no significant feedback in the acoustics onto the flame [39, 40]. On the contrary, this acoustic interaction is of great importance for the design of combustion chambers in gas turbines where thermoacoustic instabilities can even extinguish the flame [41, 42].

2.2. Combustion noise in compression-ignited chambers

Although the noise emission of combustion systems has been extensively studied for more than a century [43], research on internal combustion engines is relatively scarce.

The issue of combustion noise in relation to the in-cylinder pressure trace of CI engines has been studied experimentally over the last sixty years, but it is not until the work of Priede and Grove [44, 45] in the decade of 1960 that clear differences are drawn between the raw pressure measured in the chamber along the different engine cycles, that includes the effect of the mechanical compression and the mean combustion pressure rise, and the resonant oscillations inside the combustion chamber specifically caused by the combustion. It is worth considering the following quote from Priede [44]:

> "The rapid pressure rise in a Diesel engine caused by the sudden combustion of an appreciable fraction of the fuel-air mixture [...] initiates also pronounced gas oscillations in the combustion chamber. These oscillations produce a broad peak on the cylinder-pressure spectrum and thus enhance the emitted noise in that frequency range."

Therefore, Priede [38, 44] showed for the first time that chamber resonances, also named as reverberation by other authors, in ICEs exist and they have an impact on engine acoustics [33].

Further studies developed by Strahle [25, 46] in the late 70's revealed different behaviours between the spatially uniform increase of pressure and the unsteady oscillations due to the combustion.

All these classical works meant a big push in the understanding of the in-cylinder acoustics. For example, they give a basis for decomposing the raw pressure signal of each cycle into its components still used today [47, 48].

This decomposition, further expanded by Payri et al. [49] in a more recent work, allows a connection between engine-related parameters and their acoustic response. In that sense, low frequencies are completely dominated by the compression-expansion process, the rate of pressure change due to the combustion gathers the medium range, while the resonant phenomena hogs the higher frequencies. Further details about this method will provided in section 3.2 of Chapter 3.

2.2.1. Combustion chamber resonance

The pressure instabilities caused by combustion are propagated as pressure waves, whose different interactions and reflections at the chamber walls force the gas to oscillate according to particular patterns [50]. This phenomenon,

that may be observed by the presence of high frequency oscillations along the in-cylinder pressure evolution or by the characteristic broad peak in the spectrum also cited by Priede [44], is traditionally referred to as combustion chamber resonance, reverberation or even knocking.

Already since the work of Draper in 1938 [51], knock effects of SI combustion engines were investigated by comparison with the ideal vibration modes of a cylinder. Priede also indicated that *"the frequency of gas oscillations is determined by the geometric shape of the combustion chamber"*, a concept that would be linked to resonance modes in a follow-up paper [45], in which he mentions the simple side-to-side mode already detected by Draper when sudden knocking events occurred in SI engines. However, neither of them had the means to resolve the actual, 3D gas oscillation modes caused by the combustion and the chamber geometry.

Targeting open chambers and assuming several simplifications, Hickling et al. [50] tried to improve upon purely theoretical formulas using a Finite Element Model (FEM). Still, his 16-element, quiescent gas FEM model lacked the capability to resolve actual flow or combustion, or even small-scale gas oscillations and thus, only a slight variation from the theoretical modal coefficients was obtained.

Figure 2.1 shows the terminology used in this document to designate theoretical acoustic modes in the combustion chamber determined by Hickling et al. [50] in an attempt to establish a coherent notation showing the spatial pattern of each cavity mode.

The natural frequency of these oscillation patterns, or resonant modes, is given by the equation

$$f_{\mathrm{R}} = \frac{\sqrt{\gamma R T}}{B} \alpha_{\mathrm{m,n}} \tag{2.2.1}$$

These frequencies (f_{R}) depend on the gas temperature (T) and are inversely proportional to the combustion chamber bore (B). The modal coefficients ($\alpha_{\mathrm{m,n}}$) were also theoretically estimated by Hickling et al. [50].

Considering the particular case of CI engines, all axial (longitudinal) modes are out of the human hearing range owing to the characteristic length of the combustion chambers used in automotive applications. In addition, the transversal azimuthal modes of third order or higher ($m > 3$) are out of the human hearing range, traditionally bounded by 20 Hz and 20 kHz, whereas the transversal modes of first or second order correspond to characteristic frequencies within the highly sensitive human perception span [52]. On the other hand, only the first transversal radial mode is gathered within the hearing range ($n = 1$).
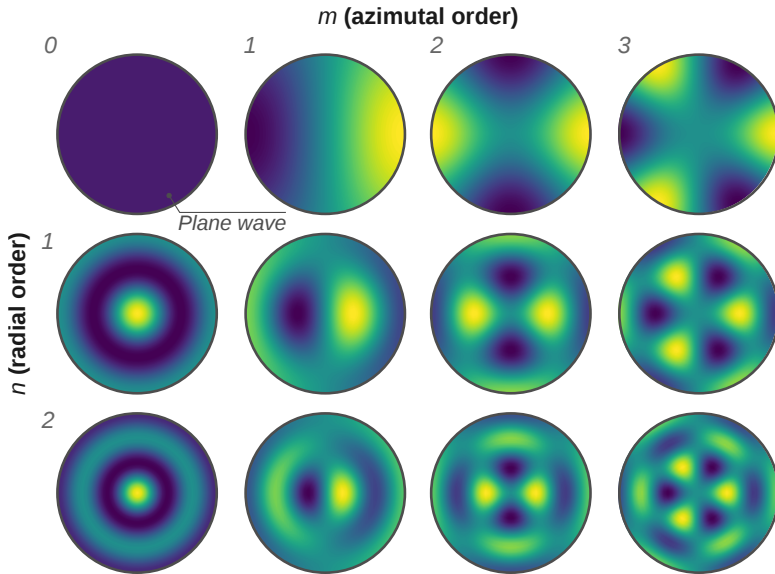
Figure 2.1: *Cross-sectional views and notation of classical acoustic modes in combustion chambers [50].*

The potential of computational methods (CFD) for analysing combustion chamber resonance modes was first demonstrated by Torregrosa, Broatch et al. [52, 53]. However, although wave motion across the chamber was successfully resolved and compared with theoretical cylinder modes, no realistic initial flow field or combustion model were used, introducing instead small regions of high pressure simulating the ignition points.

Furthermore, Torregrosa et al. [52] showed through calculations based on acoustic modal theory [54] how the acoustic excitation point –in this case the ignition location– has an impact on the high frequency pressure response. This effect was reproduced later by Broatch et al. [53] using CFD simulations.

They also suggested that the amplitude of pressure oscillations is linked to the intensity and relative location of the excitation, that in engine words are equivalent to the spatial pressure gradients achieved and to the relative position of the ignition zones in the chamber.

2.3. Phenomenological description of the CI combustion

Compression-ignited engines traditionally operated with diesel-like fuels, characterized by a high cetane index to assure the auto-ignition of the air-fuel mixture.

After the ignition, two different phases can be distinguished within the combustion process [55]. During the first phase, the charge is burned in premixed conditions at different locations inside the combustion chamber. The burning rate is primarily controlled by chemical kinetics, causing an abrupt energy release. In the second phase, a diffusion flame is established and the energy may be assumed to be released at the same rate as the fuel mixes with air. The rate of heat release (RoHR) is smoother than in the previous phase, and local heat fluctuations appear as a consequence of the interaction between turbulent transport and combustion.

Although the analysis of the pressure signal obtained from experiments clearly evidences how the unsteady oscillations arise just before once the premixed combustion begins, there is no consensus about which combustion stage is contributing to this phenomenon in a greater extent.

While Schuller [56], in collaboration with PSA group, defends that resonant oscillations are caused only by the stochastic fluctuations produced in the flame surface stabilized in the diffusion phase, the hypothesis taken by Torregrosa, Broatch et al. [52, 53] in their CFD simulations suggest that pressure instabilities generated during the premixed combustion are significantly larger, and they dominate the acoustic source by far.

2.3.1. Towards lean combustion concepts

In the past two decades, CI Diesel engines have become the leading power plant of light-duty vehicles in Europe and probably worldwide. However, the increase of CO_2 emissions together with other pollutants, specially Nitrous Oxides (NO_x) and particulate matter, have been forced to explore new technological solutions to ensure the fulfilment of emissions standards, while improving engine performance.

In spite of managing pollutant emissions can be reasonably easy by a combination of close control of the combustion and the newest exhaust after-treatment devices, these solutions worsen fuel consumption and increase engine costs.

Advanced low temperature combustion (LTC) concepts arise as a solution to reduce after-treatment costs and fuel consumption. They have been thoroughly investigated for their advantage in reducing NO_x and soot emis-

sions simultaneously. In homogeneous charge compression ignition (HCCI) [57–62] or premixed charge compression ignition (PCCI) [63–65], fuel is ignited in highly premixed conditions to avoid soot formation, whereas NO_x production is inhibited by decreasing the local temperatures with large amounts of exhaust gas recirculation [66, 67].

The main issues with these concepts concern the over-mixed blend and the liquid fuel impingement on the cylinder/piston walls, which increase the unburned hydrocarbons (HC) and carbon monoxide (CO) emissions [64, 68].

Newest combustion concepts, such as gasoline partially premixed combustion (PPC) [69–71] operate with partially premixed charges, between completely premixed and fully diffusive conditions. Investigations have confirmed the suitability of combining this combustion concept with gasoline-like fuels to achieve really low emissions of both NO_x and soot particulates, while keeping the engine indicated efficiency [72, 73].

Nonetheless, important technological drawbacks inherent to the combustion process must be solved; among others, the accurate control of the combustion phasing [74] and the combustion noise. The main issue lies probably in the combustion control, as the injection event alone does not ensure combustion [75]. This fact added to the narrow operation margin defined by the combustion limits, i.e. high combustion (knock) and unstable combustion (misfire), lead to a reduced load operation range.

In a recent research developed at Universitat Politècnica de València [75–82], it appears that an innovative 2-stroke high speed direct injection (HSDI) CI engine could represent a promising solution to control the combustion timing and to extend the load range [83]. Indeed, as proven by these investigations, the ability of this engine to control the cylinder conditions through the air management settings, allows to fix the local fuel concentration at the start of combustion. This means that it is possible to keep the local equivalence ratios in the most reactive band, so as to avoid the production of soot precursors while ensuring combustion efficiency and stability [79–81]. However, by delaying the combustion start, the increased HC and CO amounts in the exhaust cause important efficiency losses of the combustion process and this evidences a new trade-off between combustion efficiency and NO_x-soot emissions [80–82].

Despite the significant advances in the gasoline PPC concept, the increase in combustion noise also compromises the compliance with future and even current legislations on noise levels [84]. Moreover, the customers' sense of comfort is strongly influenced by how they perceive the engine

noise. Therefore, current research efforts are focused on reducing the overall combustion noise levels [47, 85, 86] and improving the sound quality of the engine noise [23, 48, 87, 88]. However, research on combustion acoustics of this particular concept is very limited and only a few authors included noise analysis in their works [81, 82].

Since there is no mixing-controlled phase in gasoline PPC, it is obvious that noise emissions are a direct consequence of the premixed or partially pre-mixed burning, without any additional contribution. Moreover, the fact that resonant oscillations are also present in these kind of combustion modes[1] sug-gests that Schuller's statement [56] is, at least, questionable and premixed combustion plays a non negligible role in the chamber resonance.

2.4. Techniques for combustion noise analysis

Pressure instabilities induced by combustion resonate inside the chamber, interacting with the chamber walls and behaving as acoustic sources. The acoustic perturbations are then transferred through the engine block into the vehicle and its environment. Thus, another relevant aspect in the combustion noise arises: the radiation of the acoustic perturbations through the engine structure and towards the cabin.

A first division can be made between those studies aiming to analyse the radiation of acoustic perturbations and those works focused on characterizing the source of noise emissions.

Following a similar analogy, there are two different strategies to reduce the noise levels and modify the acoustic signature of the engine so as to improve the impact on the user. The first, commonly known as passive solutions, is related to the modification of the acoustic response of the source by combining a proper engine block design and encapsulation. The second option, denoted active solutions, consists in optimizing the hardware design and the operation settings to act directly on the combustion noise source. Research efforts have therefore been directed towards both options, and have led to several experimental and theoretical approaches for assessing and understanding combustion noise.

---

[1]They can be easily identifiable in any of the cited documents

2.4.1. Impact on external-radiated field

Passive solutions have been thoroughly explored due to the inherent simplicity of the concept. The main idea lies in 'blocking' or attenuating the frequency contents, which have an undesired effect on NVH.

Since the early eighties, many studies have focused on establishing a relation between the combustion noise source and the end user, thereby estimating how source phenomena translate to the externally-radiated noise and also taking into account the attenuation due to the engine structure where NVH analysis has evidenced completely different propagation patterns of the acoustic energy [89–92].

For qualitative analysis many research works estimate the acoustic path between the source and free-field conditions by a transfer function. This simplification does not allow an accurate prediction of the radiated noise level [47, 93], but it is extremely useful for relative comparisons. Besides, several combustion noise metrics are defined following this method. In this case, the acoustic path was estimated with the classical approach proposed by Austen and Priede [38], which assumes a linear behaviour between the source and the observer.

According to this theory, the engine structural attenuation curve can be calculated as the difference between the in-cylinder pressure and the radiated noise 1/3-octave band spectra. Among all structural attenuation curves available in the literature [47, 94, 95], the one obtained by Anderton [94] is the most commonly used and also considered the standard.

Since it has been demonstrated that the acoustic response of the engine is highly non-linear and it is mainly related to the working condition [47], engine block design and the acoustic insulation [89, 90], further studies assessed the radiation through the engine by different approaches.

For instance, Torregrosa, Payri et al. [47, 48] found correlations between typical engine output parameters and both objective and subjective effects on noise. After a complete statistical analysis, they proposed a simple model to estimate both the overall noise and sound quality of a given CI Diesel engine with only three and two parameters, respectively.

Other authors on the other hand, dedicated efforts on identifying which are the main sources within the engine structure [92, 96]. For instance, Zhao et al. [96] proposed a close loop control for identifying the combustion parameters through the vibration signal of several accelerometers located at the engine surface.

A larger number of works are also focused on applied solutions [87, 97, 98] rather than analysing the acoustic path purely. While Mao et al. [87] optimized the engine block design using a finite-element model to improve the acoustic signature of a Diesel engine, other authors such us Duvigneau et al. [98] resorted to CFD and simplified acoustic models to reach an improved design.

2.4.2. Combustion as a source of noise

From the point of view of active solutions, the in-cylinder acoustic field recreation, as being spatially and time variable, demands multiple measurement points across the combustion chamber [99].

Instead of performing complex and expensive engine modifications, most of the experimental studies are focused on analysing the pressure signal registered by a unique transducer. Indeed, practically all the classical papers cited above [38, 44–46] are based on this approach. The available data, although incomplete, offers enough information to link some parameters related to the engine operation with their respective acoustic response.

The decomposition pressure method, developed for the first time by Priede [44] and further expanded by Payri et al. [49], allowed Torregrosa et al. [47] to establish dependences between three characteristic parameters and their excited harmonics.

Figure 2.2 summarizes the state-of-the-art on combustion noise source research. As can be seen from Priede, Torregrosa et al. research, low frequency span is dominated by the engine speed, the pressure rise rate caused by combustion is responsible for medium frequency range changes whereas high frequencies are a direct consequence of the chamber resonance.

Combining these statements with the advances described in Section 2.2, it is possible to go further and to determine the original causes of the spectrum behaviour. In that sense, low frequencies are fixed by the engine speed operation, the medium range is controlled by the combustion law or RoHR [47, 49] and, finally, the higher frequencies are managed by the chamber geometry, the intensity of pressure perturbations (due to combustion) and the relative position of the ignition points within the chamber [52, 53].

Nonetheless, resonance phenomenon in CI engines is still the most unexplored field related to combustion noise emissions. Since there is very scarce literature on the subject, its fundamentals are not well established yet and further efforts should be taken in order to identify its origins.
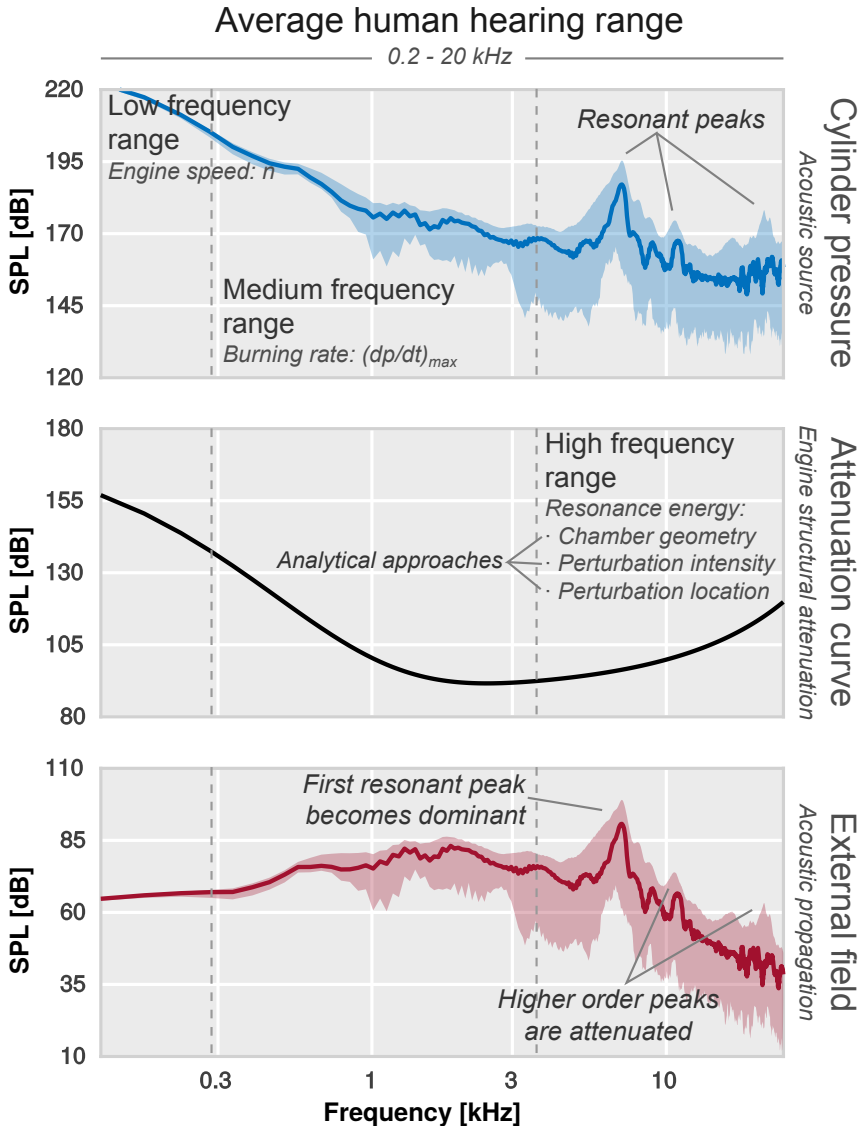
Figure 2.2: *Synthesis of combustion noise characterization based on the decomposition pressure signal [44, 49] and further experimental studies [47, 50, 52, 53].*

One of the main concerns about resonance phenomena is to determine an adequate metric to quantify its effects. Several metrics are available in the literature and most of them are based on correlations. The peak pressure rise rate (PPRR) or the ringing intensity (RI), are such examples widely extended

[100]. However, Shahlari et al. [93] have evidenced their weakness for characterizing the resonance phenomenon when the combustion strategy, engine platform or operating conditions change.

In front of this, Broatch et al. [53] defined a metric, named energy of resonance or E_{res}, that appeared to offer the best reliability for the quantification of the amplitude of the pressure oscillations because it is based on the pressure trace and not on indirect parameters. Additional information about this parameter is included in Appendix 3.4.

2.4.2.1. Numerical simulations

Another relevant approach that many authors traditionally adopt to assess noise sources [50, 54] is to use numerical simulations in an attempt to overcome single-point measurements limitations. In particular, CFD has become one of the most useful tools for typical engine flow applications. Indeed, once the model is set-up to reproduce adequately the phenomena involved, any number of parameters can be modified and quickly tested [101, 102].

However, the complexity of the phenomena involved in the noise generation is such that hard hypotheses have to be assumed in order to reduce computational time. For instance in some noise studies the combustion is approached by a local increment of pressure [53, 103]. Nowadays, the increase in computational power coupled with the development of reacting flow codes allows simulating the combustion process, thus contributing to the understanding of the combustion dynamics and its effects on efficiency and pollutants production [82]. The maturity of these methods opens new ways to explore the acoustics of ICE engines.

When preparing a CFD simulation, one of the most crucial decisions is how the turbulence will be modelled. While several approaches can be found in the literature, three "families" enjoy greater popularity. The most simple, Reynolds-Averaged Navier-Stokes (RANS), aims to model the mean flow disregarding the fluctuation component of the flow variables. However, velocity fluctuations still appear in the Reynolds stress tensor, which has to be modelled through different approaches for the closure of the turbulence problem: Spalart-Allmaras, $k - \varepsilon$ [104], $k - \omega$ [105], etc., each of them in turn comprising a large amount of variants and refinements.

This first approach is the most commonly used in engineering applications, as it offers a reasonable solution for typical flows while not being as computationally intensive as the more advanced turbulence modelling techniques. In order to apply this method to transient flows, Unsteady RANS (URANS)

is used: a series of consecutive RANS simulations are performed, each one starting from the previous solution. However, this does not account for the loss of the true fluctuating terms in the equations and so, a quasi-steady process is in fact assumed, where only external perturbations are resolved.

In order to address this shortcoming, Large Eddy Simulations (LES) [106] approach the turbulence problem by performing instead a low-pass spatio-temporal filtering of the Navier-Stokes equations. In contrast with URANS, this keeps the fluctuation information (although only up to the size of the chosen filter), so more realistic unsteady situations, where the turbulence itself plays a relevant part in the behaviour of the flow, can be resolved [107, 108]. LES is, however, much more computationally expensive than RANS.

Finally, Direct Numerical Simulation (DNS) of the Navier-Stokes equations can be attempted, where no simplifications are performed and all the scales of the flow are resolved, from the integral scale to the Kolmogorov microscale. However, this requires an extremely large amount of computational capacity, and DNS remains confined to fundamental research on turbulence or, at most, simple cases for validation of other numerical models [109].

This last option is not suitable yet for engine combustion simulation, and thus a choice must be made between URANS and LES models. Nonetheless, high computational requirements associated to LES schemes can compromise their application to a specific field of study. Then, it is crucial to establish what demands must be covered by the simulation and which hypotheses can be considered admissible to achieve them. Involved phenomena and their corresponding effects must be therefore deeply studied and understood.

2.4.2.2. Modelling internal combustion engines

In the framework of engine combustion simulations, the URANS approach has being employed for the majority of the applications. For example, URANS simulations have been used for enhancing the understanding of the flow motion during the gas exchange process [110] or the generation of pollutants [111], for optimizing the combustion system design [112, 113] and for simulating the spray and flame structure, ignition delay and lift-off length [114].

Regarding specifically noise emission, the noise contributions due to the mechanical compression-expansion process are easy to model analytically [81], and the mean combustion contribution is relatively simple to reproduce by an adequate modelling of the low to middle frequency rise in pressure and temperature [101, 115], however the combustion chamber acoustic resonance remains a more elusive phenomenon to characterize.

On the other hand, LES models have received an increasing interest during the last years and they have become the most explored methods for modelling the turbulent flow properties in a wide range of automotive applications. They allow to potentially increase the accuracy of simulations, resolving flow details and phenomena not accessible with URANS due to its simplicity for approximating the turbulent field. For instance, Vermorel et al. [116] observed cyclic pressure variations produced by misfires and large scales fluctuations in a 4-valve SI engine.

Application of LES schemes in CI engine simulations is more limited, although for instance Tillou et al. [117] proposed a numerical study of the pressure field variability of a single spray combustion into a constant-volume chamber under diesel-like conditions. The results give an idea of the variability of the combustion, specifically on that related to the effect of the stochastic fluctuations in the turbulent flow field.

While the aforementioned studies have shed some light to the main sources of the combustion noise, clear evidence is still lacking about the advantages of LES in the simulation of this particular issue in CI engines. Specifically whether or not stochastic fluctuations can play a significant role in the acoustic response of the combustion, arises as an important question to answer. Thereby, a consensus on the best way to model combustion noise does not yet exist.

2.5. Conclusions

After a detailed review of the existent literature of different aspects of combustion noise, some important conclusions should be pointed out from the state of the art of combustion noise sources in CI engines:

- Combustion noise in ICEs is generated by periodic combustion oscillations and local heat release fluctuations due to the interaction between turbulence and burning process. In addition, thermoacoustic instabilities are not relevant since the establishment period of the combustion is extremely short and the magnitude of these perturbations are really small if they are compared with the overall pressure rise.

- Nonetheless, being purely direct, combustion noise can be generated by distinct phenomena. In conventional Diesel combustion, the origin of acoustic perturbation can be the premixed burning or the stochastic heat release fluctuations during the mixing controlled combustion phase.

- However, in highly premixed combustions as it happens in new LTC concepts, the absence of other combustion stages concentrates the noise generation only in the premixed combustion.

- There are two traditional strategies to deal with the combustion noise: while passive solutions are focused on attenuating the undesired acoustic effects by modifying the path among the source and the observer, active solutions try to promote lower acoustic levels by acting on the source directly.

- Experimental studies consistently identified, through the in-cylinder pressure signal registered at a single location, three operating parameters that condition the acoustic signature of the combustion.

- Although low-to-medium frequencies are spatially uniform inside the chamber, high frequency components oscillate following particular spatial patterns. As a consequence, single location measurements does not allow a complete reconstruction of the in-cylinder pressure field.

- Computational Fluid Dynamics simulations appear as an interesting solution to reconstruct the in-cylinder pressure field completely, thereby overcoming experimental limitations of single-location measurements and avoiding to perform expensive and intricate engine modifications to measure the pressure evolution at several points.

- Turbulence modelling is the main bottleneck in acoustic engine simulations since it has not been demonstrated that URANS approaches, simpler than sophisticated LES models, are capable of capturing all relevant phenomena in the combustion acoustic response of CI engines.

Experimental characterization of combustion noise

As starting point, the analysis of the combustion noise source is addressed by experimental techniques. The target here is to give a first characterization of this matter but also to confirm the conclusions shown in the prior chapter.

This chapter is therefore devoted to the results of applying the described acoustic methods to several measurements already performed. The application of these methods is presented step-by-step, including some relevant examples to understand the procedure easily. Finally, results are utilized to establish the following research directions while identifying the main limitations of the experiments.

3.1. Experimental facilities

Experimental activities, including all measurements, acquisition system design, engine instrumentation, apparatus calibration, etc. were performed prior to this thesis, in the framework of the doctoral theses of L. Monelletta [118] and D. de Lima [119]. Therefore, only a brief description of the

---

Work in this chapter has been partly published in the following papers:

- *Development of a Virtual CFR Engine Model for Knocking Combustion Analysis* [10]
- *Experimental analysis of cyclical dispersion in CI vs. SI engines and its significance for combustion noise numerical modelling* [8]
- *Combustion noise analysis of partially premixed combustion concept using gasoline fuel in a 2-stroke engine* [1]

Table 3.1: *Main specifications and injection system characterisation of the Diesel engine.*

Engine type	HSDI CI Diesel engine
Fuel [-]	Conventional Diesel
Number of cylinders [-]	4 in line
Displacement [cm^3]	1600
Bore – Stroke [mm]	75.0 – 88.3
Connecting rod length [mm]	137.1
Compression ratio [-]	18:1
Number of valves [-]	2 intake and 2 exhaust
Injector nozzles [-]	6
Nozzle holes diameter [μm]	124
Included spray angle [deg]	150

experimental facilities and engine configurations will be presented in this section. Full details about the experimental facilities can be found in both documents [118, 119].

Since an inherent goal of this research is to contribute to combustion noise fundamental knowledge in automotive engine applications, the engines were conscientiously selected for dealing with current design tendencies of the automotive industry for compression-ignited engines.

3.1.1. Engine for conventional Diesel combustion

The experimental characterization of Diesel combustion was carried out in a light-duty DI Diesel engine. This is a 1.6 l, four-cylinder, turbo-charged engine equipped with a common rail injection system. All tests were performed with a 6-nozzle injector with hole diameters of 124 μm and an included spray angle of 150°. The combustion chamber has a conventional head design with a re-entrant bowl geometry. This piston design provides a geometric compression ratio of 18. The main specifications of the engine and the injector are presented in Table 3.1.

The gear box was assembled with the engine block in order to maintain the vibration patterns as close as possible to real operation. In addition, an asynchronous electric brake was directly coupled with the engine for controlling the engine speed. The latter was physically and acoustically isolated with sound damping panels so as to prevent possible interferences in the engine noise measurements. The test bench was installed inside of an anechoic chamber located at laboratory 5K of Universitat Politècnica de València, which offers free-field conditions for frequencies above 100 Hz.

Table 3.2: *Engine specifications and injection system characterization of the 2-Stroke engine.*

Engine type	2-stroke HSDI CI engine
Fuel [-]	RON95 gasoline
Number of cylinders [-]	1
Displacement [cm^3]	365
Bore – Stroke [mm]	76.0 – 80.5
Connecting rod length [mm]	143.2
Compression ratio (geometric)	17.8:1
Compression ratio (effective)	From 13.0:1 to 8.8:1
Number of valves [-]	2 intake and 2 exhaust
Type of scavenge	Poppet valves with scavenge loop
Injector nozzles [-]	8
Nozzle holes diameter [μm]	90
Included spray angle [deg]	118

In-cylinder pressure signals were measured in the four cylinders with Kistler 6055Bsp piezoelectric transducers placed in the middle of the intake valves at the glow plug location. Although not being used directly in the following studies, the noise radiated by the engine block was measured using a free-field microphone to calibrate the acoustic models described in Appendix 3.4. The pressure and noise signals were sampled using a dedicated acquisition system and recorded during 50 consecutive engine cycles. All signals were also registered with a sample frequency of 50 kHz, ensuring a free-aliasing bandwidth similar to the human hearing domain –20Hz to 20kHz– according to the Nyquist criterion [120].

3.1.2. Engine for advanced LTC combustion

In this case, experimental activities have been carried out in a single-cylinder research version of an innovative engine concept characterized by a 2-stroke HSDI CI engine with poppet valves scavenge loop. The main specifications of this engine are included in Table 3.2.

A particular design of the cylinder head, shown in Fig. 3.1, was adopted to optimize the scavenging of burnt gases while keeping short-circuit losses as small as possible during the 2-stroke cycle. The cylinder head geometry exhibits a staged roof for baffling the air flow between intake and exhaust valves, directing the air to the cylinder wall toward the bottom of it. This geometry represents the best compromise between scavenging efficiency, acceptable permeability, and favourable combustion chamber design [83].
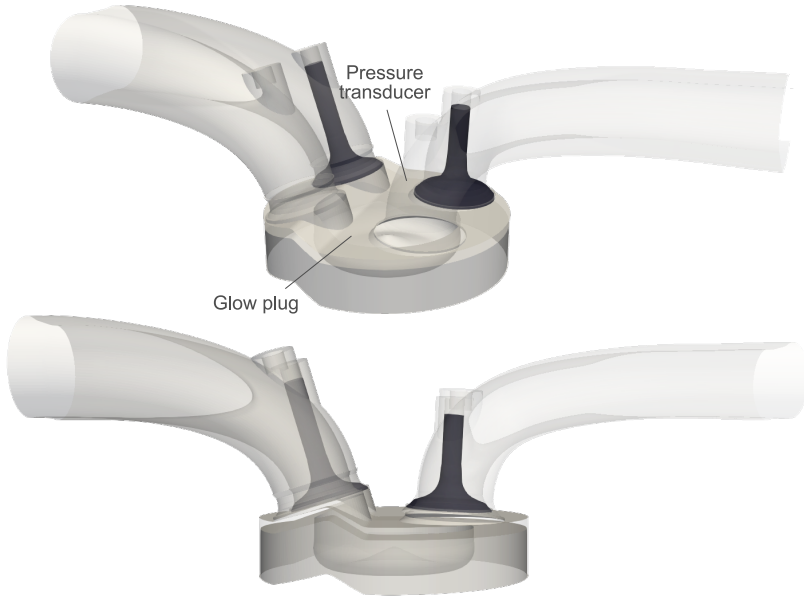
Figure 3.1: *Combustion chamber geometry of the 2-Stroke engine.*

The timing control of the four poppet valves actuated by double-overhead camshafts relies on a hydraulic cam-driven Variable Valve Timing (VVT) system, which allows delaying both intake and exhaust valve timings up to +30 degrees from the base cam phasing. This system is well adapted for modifying the air management characteristics, due to its flexibility to adjust the overlap period between intake and exhaust, but also the effective compression and effective expansion ratios.

The engine is equipped with a common rail prototype fuel injection system, which grants a maximum rail pressure of 1100 bar when operates with gasoline fuel. All tests were performed with a nozzle configuration of 8 holes of 90 μm of diameter, and with an included angle of 148°. The piston bowl geometry employed was of a conventional design, optimized for operating with the Conventional Diesel Combustion (CDC) concept, and provided a geometric compression ratio of 17.8.

The engine was assembled in a fully instrumented test cell equipped with all auxiliary devices required for engine operation. An external compressor supplied the intake air and simulated the boost conditions. The exhaust back-pressure produced by the turbine was generated and controlled by means of

a throttle valve located downstream of the exhaust settling chamber. The installation also included independent water and oil cooling circuits, and an additional low EGR system to provide arbitrary levels of cooled exhaust gas even at very high intake boost pressures.

The in-cylinder pressure was measured with a Kistler 6061B pressure transducer placed between the intake and exhaust valves opposite to the glow plug location, while a different piezo-resistive pressure sensor was used to reference this pressure signal. Instantaneous high frequency signals, such as cylinder pressure were sampled using a dedicated acquisition system and recorded during 100 engine cycles for each operation condition. These signals were also registered with a sample frequency of 45 kHz, ensuring a free-aliasing bandwidth similar to the human hearing domain.

The most relevant combustion parameters, such as maximum pressure time-derivative, maximum cylinder pressure, rate of heat release and combustion phasing angles were calculated from the in-cylinder pressure by means of the energy equation and some simplifications [121, 122]. This equation was solved assuming uniform pressure and temperature throughout the whole combustion chamber volume and yielded the instantaneous mean temperature and the heat release.

3.2. Conventional Diesel combustion

In this section, the source of combustion noise in compression-ignited (CI) Diesel engines is characterized through in-cylinder pressure signals obtained from the measurements performed by L. Monelletta [118]. This character-ization not only allowed a first approximation to relieve noise emissions produced by combustion but also permitted to recognize which are the most critical conditions within the whole operating map.

To begin with, experimental pressure data was processed, decomposing the raw pressure trace of each cycle into its components following the technique already pioneered by Priede [44] and further extended by Payri et al. [49]. This is done, first, by subtracting the low-frequency "pseudo-motored pressure trace", exclusively caused by the compression-expansion process itself. Although this signal can be theoretically obtained, it was measured in this work by switching off fuel injection in just the studied cylinder during one isolated cycle while the combustion was kept in the other cylinders [49]. This procedure was repeated ten times through the 50 recorded cycles, thereby allowing to estimate an average pseudo-motored signal whereas the operating conditions were maintained.
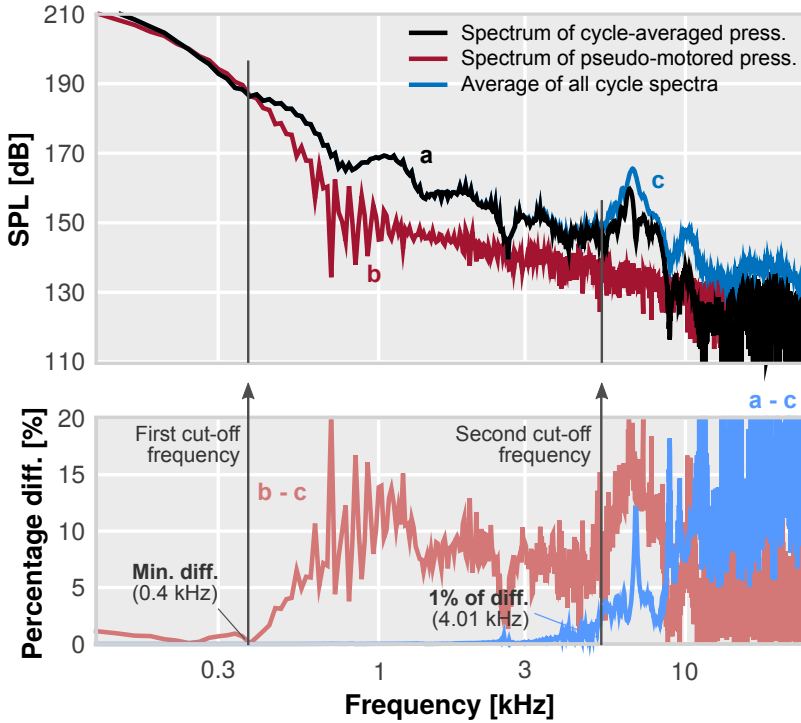
Figure 3.2: *Visual representation of the frequency cut-off determination following the selected pressure decomposition algorithm.*

Once that this purely mechanical contribution is subtracted, the "excess" pressure signal that remains is then related to the combustion process [123, 124]. From the point of view of the frequency, now it is possible to determine a cut-off frequency between both signals. As can be seen in Fig. 3.2, in which data from a given operating condition is plotted as example, the spectrum of pseudo-motored signal practically matches the averaged spectrum in the low frequency range. The difference among both traces (b-c) plotted in the bottom graph of this figure, reveals that the minimum gap is around 0.4 kHz and therefore this point was considered as the first cut-off frequency.

An additional difference must be established however between the homogeneous pressure rise caused by the heat release of the combustion, and the resonant gas oscillations inside the chamber caused by the reflections of the pressure waves [47, 52].

This resonance-dominant part of the pressure spectra can be isolated through a high-pass filter, the cut-off frequency of which can be determined following the method suggested by Strahle [46] for Diesel engines, where

the spectrum of the cycle-averaged pressure trace (instantaneous average of all recorded cycles) is compared to the average of all cycles. When a significant difference appears between both traces at a certain frequency, then this can be regarded as the start of the frequency range dominated by the resonant pressure wave oscillations. As can be seen in Fig. 3.2 again, this frequency was determined by the point at which the gap between both traces exceeds 1% of difference.

The result of applying this decomposition procedure to the experimental engine data can be seen in Fig. 3.3. In the first two plots, the in-cylinder pressure trace and its components in the time and frequency domains are shown in order to easily see the cause-effect relationship among temporal and frequency domains. Raw pressure from a selected test is divided in its corresponding components: mechanical compression in red, mean combustion pressure in black, and the chamber resonant oscillations in blue. The cycle-to-cycle variation (CCV) has been included in these curves by shading representing the standard deviation (SD) at each crank angle. Moreover, the radiated spectrum of these signals is included in the bottom graph of this figure to analyse the external field response.

Adding a further step, the spectrum of the radiated sound pressure can be obtained by applying the classical approach proposed by Austen and Priede [38] and the engine attenuation curve obtained by Anderton [94]; both procedures are widely explained in Chapter 2. As can be seen in the bottom plot of Fig. 3.3, the radiated spectrum can be separated in the same three frequency regions previously delimited. Now, it is thus possible to obtain the overall amplitude of each band of frequencies to determine which is the contribution of each frequency range to the overall radiated noise.

In this procedure, the overall amplitude of the whole broadband is calculated with the method described in Appendix 3.4 and then converted to a linear scale. Repeating this procedure for each one of the bounded regions, their overall amplitudes can be obtained. Thus, the ratio between these values expresses the contribution of each band of frequencies to the overall noise, thereby revealing which part of the spectrum is conditioning the noise emission to a greater extent.

Recalling the bottom plot of Fig. 3.3, the contribution of each band of frequencies is labelled in percentage of the overall noise level. It can be seen that while the low frequency range represents only a negligible part of the overall engine noise level or ON ($<$ 1%), the main contribution is thus shared between the medium-high frequency regions ($\sim$ 55 – 45%).
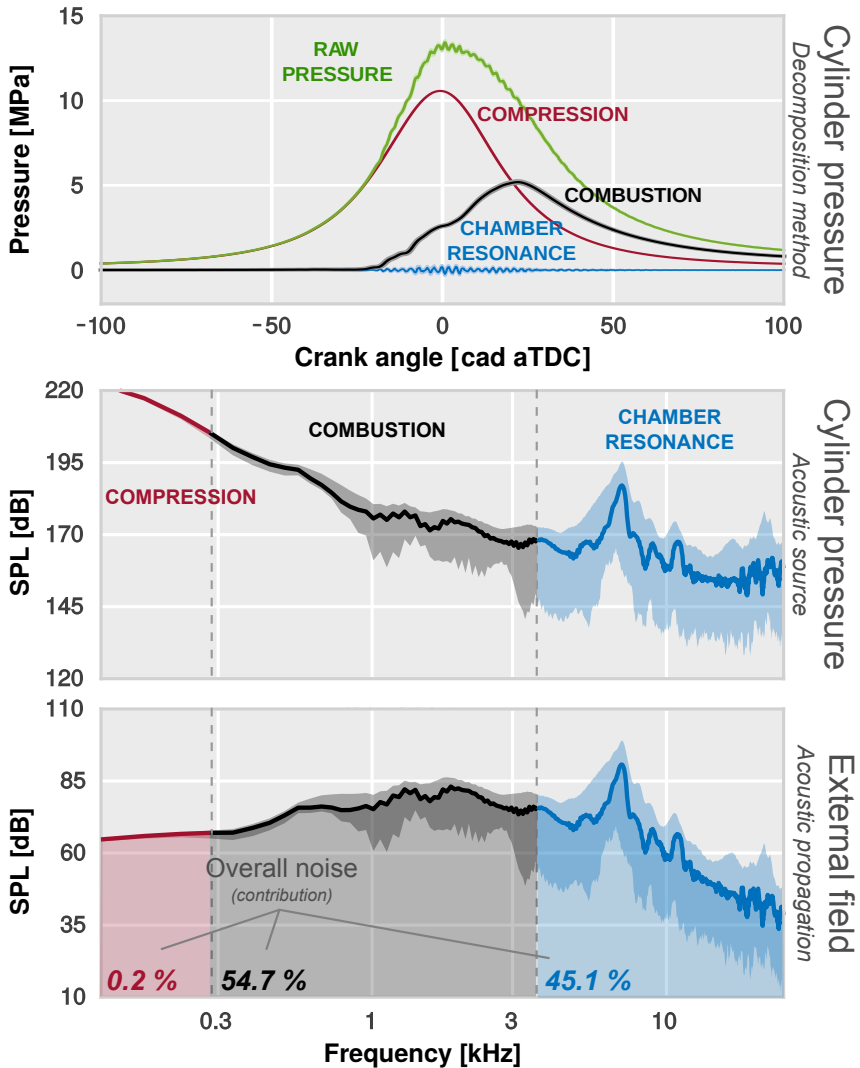
Figure 3.3: *Example of the pressure decomposition technique application. In-cylinder pressure is drawn along with each contribution in the time domain (top plot). Pressure spectral density: in-cylinder pressure (middle plot) and radiated sound pressure (bottom plot). Spectra have been separated based on the prevalence of each source mechanism, including the mean sound pressure level (SPL) and cyclic spread (shaded) along all experimental cycles of a given operating condition.*

This fact reveals two distinct strategies to act on the emission source. On the one side, the combustion can be modified through the operating settings (injection parameters, EGR, etc.) to reduce the contribution of the middle
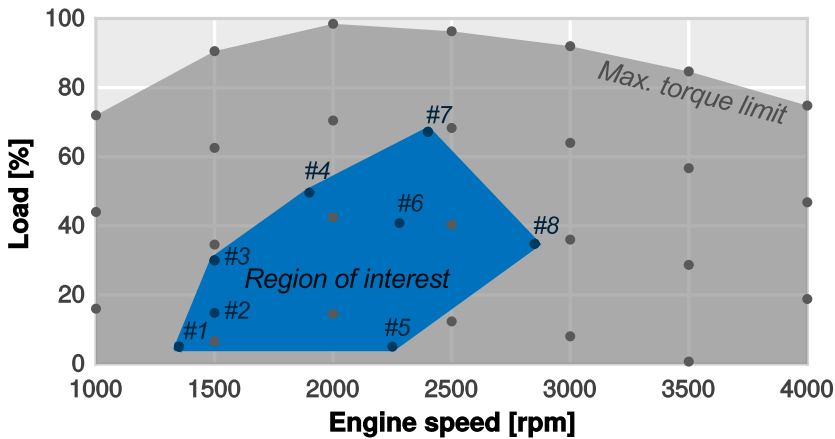
Figure 3.4: *Operating points chosen for the noise characterization analysis of CDC.*

frequency region. On the other side, the resonant gas oscillations inside the chamber due to reflections of the pressure waves can be mitigated by modifying the combustion system design.

The review of the available literature on combustion noise characterization done in Chapter 2 revealed that resonant behaviour only depends on the geometric design of the chamber, thus being independent from the combustion law. Therefore, it is possible to decrease, at least theoretically, the resonance intensity and, subsequently the overall noise emissions, without any remarkable change in the combustion process. This has positive implications from the point of view of engine efficiency but also of pollutant emissions.

Although this is an extended belief, the impact of both strategies on the whole operating range has not been well established yet. Therefore, the methodology presented so far is used to identify and characterize the origin of the combustion noise in the most relevant operating range.

On the engine operation map, the region framed in the low-medium speed and low-medium load is traditionally accepted as the most critical operation range since it is the region in which the engine operates most frequently under standard driving conditions. Moreover, usual and future homologation driving cycles are specifically focused on this region [125].

Hence, the region highlighted in Fig. 3.4 was chosen to quantify both the overall noise emissions and the relevance of the resonance. In this figure, blue dots correspond with the operating conditions used in this study and shown in Table 3.3, in which the main running settings are summarized.

Table 3.3: *Main running settings of the operation points considered for the noise characterization of CDC.*

Point	#1	#2	#3	#4
Engine speed [rpm]	1350	1500	1500	1900
Torque [Nm]	12.3	36.9	75.2	123.9
Number Injections [-]		3 (2 pilots + main)		
Injection pressure [MPa]	40	65	87	105
Intake pressure [MPa]	0.104	0.107	0.118	0.161
Point	**#5**	**#6**	**#7**	**#8**
Engine speed [rpm]	2250	2280	2400	2850
Torque [Nm]	12.7	102.1	168.3	87.0
Number Injections [-]		3 (2 pilots + main)		
Injection pressure [MPa]	40	95	80	92
Intake pressure [MPa]	0.111	0.168	0.206	0.181

Besides the identification of the region of interest, the metrics related to the noise characterization were included in Fig. 3.5 using a cubic polynomial fit for the visualization. As can be seen from contours plotted on the top graph, ON levels monotonically increase with the engine speed and also with the load, evincing that the most serious issues are focused on the top-right region of the map considered.

However, the relevance of the resonance is not correlated to neither the engine speed nor the load, as shown by the random behaviour of the contours plotted on the bottom graph of the previously referred figure. The colour scale shows the contribution of the resonant oscillations, this is the aforementioned overall amplitude of the high frequency content, in front of the medium frequency range. Thus, as illustrated the sketch attached to this figure, a value of 0.45 means that the ON level is 45% influenced by the resonant frequency content and 55% affected by the medium range of frequencies. Note that the contribution of the low range of frequencies is not considered due to its small significance ($< 1\%$).

It becomes readily apparent that different mechanisms are influencing the noise generation due to combustion as the operating point is changing along the map. For instance, noise generation is clearly dominated by the resonant phenomena within the zone of lower engine speeds and loads gathered by 50 and 100 Nm of torque whereas the highest speed region (Point #8) is mostly controlled by the homogeneous pressure rise rate due to combustion, which covers the middle frequency range.
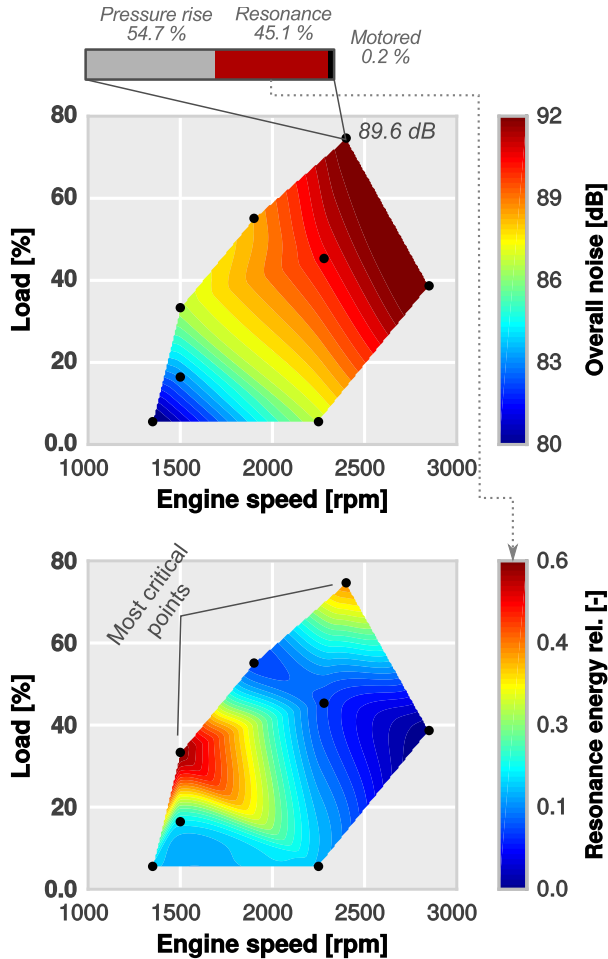
Figure 3.5: *Noise and resonance contribution maps for CDC operation. The overall noise and the contribution of resonance energy maps are interpolated and plotted using contour plots.*

Aside from these opposed zones, there are other points in which a resonance lowering could mean a significant noise reduction. In this sense, Point #7 which is the most interesting since a small resonance lowering could significantly reduce the high levels of ON exhibited.

Once that origin of combustion noise has been characterized in a wide operating range, it is time to gain further insight about the noise generation mechanisms and their connection with the combustion. However, the limitations in experimental techniques described in Chapter 2 prevent going further in the investigation of this matter.

Table 3.4: *Main running settings of the operation points considered for the noise characterization of PPC gasoline concept.*

Point	#1'	#2'	#3'	#4'	#5'	#6'
Engine speed [rpm]	1250	1250	1250	1500	1500	1500
IMEP [MPa]	0.31	0.55	1.04	0.10	0.31	0.55
Number Injections [-]	2	2	3	2	2	3
Injection pressure [MPa]	40	60	85	30	40	60
Intake pressure [MPa]	0.150	0.170	0.276	0.125	0.150	0.180
Point	**#7'**	**#8'**	**#9'**	**#10'**	**#11'**	**#12'**
Engine speed [rpm]	1500	1750	1750	1750	2000	2500
IMEP [MPa]	1.04	0.31	0.55	1.04	0.31	0.55
Number Injections [-]	3	2	3	2	3	3
Injection pressure [MPa]	85	40	60	40	80	60
Intake pressure [MPa]	0.275	0.150	0.170	0.150	0.180	0.170

3.3. Advanced LTC combustion concepts

Owing to the clear propensity to generate extremely high burning rates, LTC concepts are inherently noisy and the acoustic emissions are an important constraint for their application to commercial vehicles. The study presented in the previous section is expanded here to the PPC gasoline mode described in Chapter 2, being an interesting concept from the point of view of both emissions and efficiency and enough representative of noise issues shown by new LTC concepts.

Although being a single-cylinder engine particularly designed for research purposes, it has been tried to measure an operating region equivalent to that considered in the previous section with the CDC study. Therefore, twelve tests were carried out with the specifications shown in Table 3.4.

Figure 3.6 displays the results obtained from PPC gasoline measurements. Following a similar representation of Fig. 3.5, the overall noise level is shown at the top and the resonance relevance at the bottom. As can be seen, combustion noise is now highly correlated to the engine load rather than the engine speed. Apart from this, noise levels are considerably higher if they are compared with CDC; points with low acoustic levels exhibit around 90 dB in PPC gasoline whereas their corresponding points in CDC rarely exceed 81 dB.

Regarding the resonance contribution, it is not correlated to any of the operating parameters plotted in the graph, showing an arbitrary pattern along the measured map as in Diesel combustion. However, some significant
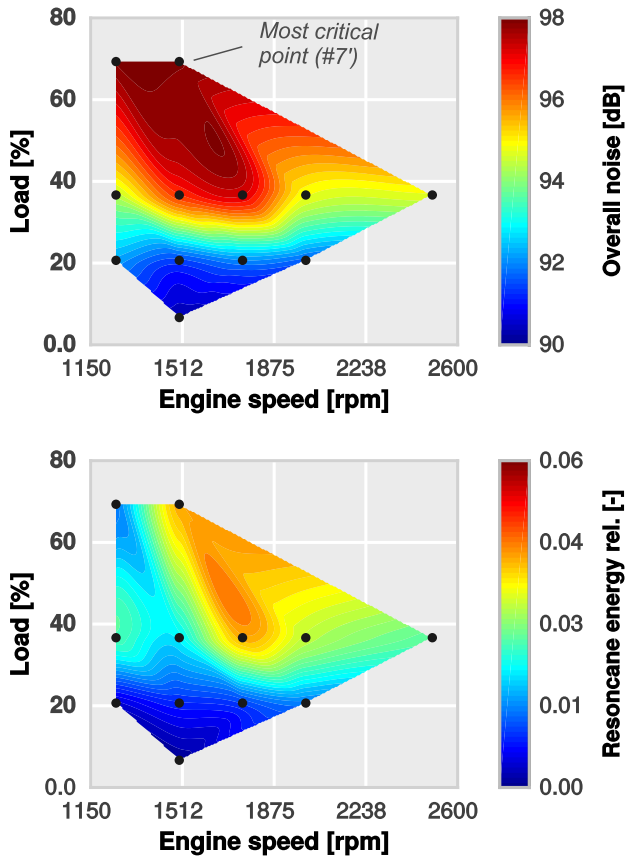
Figure 3.6: *Noise and resonance contribution maps for gasoline PPC operation. The overall noise and the contribution of resonance energy maps are interpolated and plotted using contour plots.*

differences are also observed; the most evident, the maximum values of the resonance contribution. While these values reached 45% in several Diesel operating points, they do not surpass 5% in the whole PPC gasoline map, thereby suggesting that resonant constitution in this combustion concept is almost negligible.

Nonetheless, since the air management and injection settings were not optimized for each operating condition (they were adjusted just to provide the fixed outputs), there is no way to assure if the measured conditions are representative enough of the regular engine operation. For this reason a further step should be taken to verify that the resonance contribution can be disregarded.

In order to achieve this target, Point #7' was selected to perform additional measurements since it has proved as the most unfavourable operating condition from the perspective of noise emissions. Moreover, a preliminary analysis revealed that the main injection timing, commonly referred by the start of energizing of the injector (SoE), has the most notable impact on combustion features. Therefore, an additional study was performed by sweeping SoE_{main} each 2 cad between -42 and -34 cad aTDC with the settings of Point #7'.

Once the measurements were finished, a frequency analysis was performed with the aim of finding significant differences. Results are shown in Fig. 3.7 (top), in which the average spectrum of all measured tests are plotted together for comparison. An extra test was carried out operating with CDC, optimized settings and providing the same outputs to easily and fairly compare both combustion modes. As it can be seen, all PPC tests exhibit very similar SPL traces, with only a few differences in the middle range of frequencies (0.2 – 2.9 kHz). This gap becomes notably larger if we compare PPC with CDC. However, resonant amplitudes are very similar even in both combustion modes, showing some kind of independence from the combustion.

The bottom plots also included in this figure are the result of a subsequent study performed to check the validity of the relationships between combustion parameters and the amplitude of specific frequency bands reported by Torregrosa et al. [47] for CDC combustion. Following the procedure described in previous section for estimating the contributions of ON, it is possible to obtain the overall cylinder pressure level (CPL)[1] assigned to a given frequency range by using the spectrum of the in-cylinder pressure instead. In this way, noise parameters –$(dp/dt)_{max}$ and E_{res}– can be related to their frequencies of excitation. In Fig. 3.7 (bottom-left) the relation between the peak pressure rise rate and the CPL evaluated in the medium range of frequencies is plotted for all measured cycles in PPC tests. On the other hand, the bottom-right plot of Fig. 3.7 shows the link between the energy of resonance and the CPL in the high frequency range. In both cases each of the characterization parameters has been normalized using its maximum value. Results confirm that the maximum pressure rise rate

---

[1]CPL is obtained by applying the same procedure described on Section 3.A.1 of the Appendix 3.4 for the ON estimation but considering the in-cylinder pressure trace instead of the radiated engine signal.
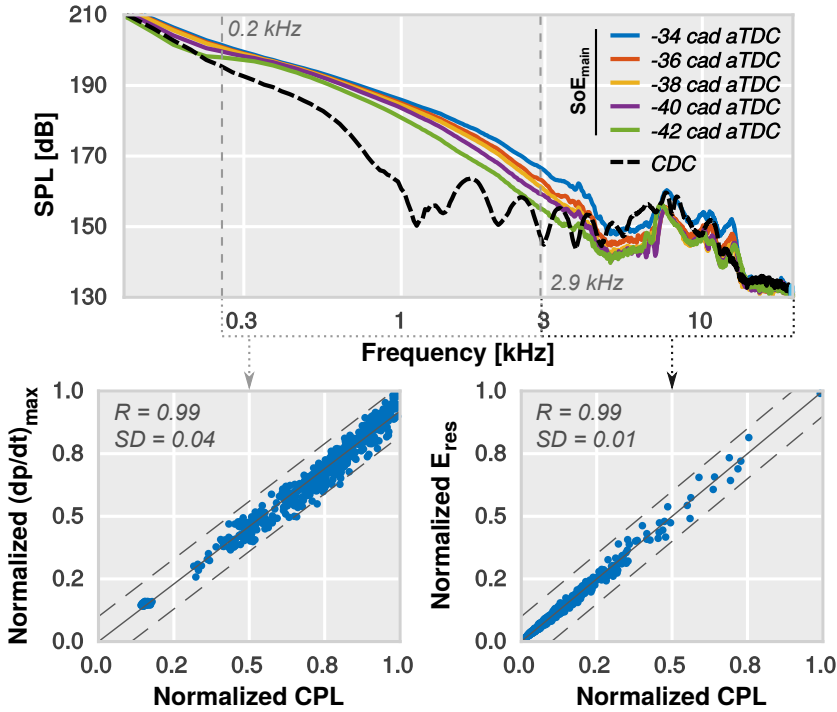
Figure 3.7: *Frequency analysis of PPC gasoline concept sweeping the timing of the main injection. In-cylinder pressure spectra comparison is plotted at top whereas the correlation between the characterisation noise parameters (maximum pressure rise rate and energy of resonance) and CPL evaluated in distinct frequency bands.*

affects the CPL generated in the medium band of frequencies whereas the energy of resonance influences the CPL related to the high frequency band, thereby confirming the conclusions remarked for CDC.

Returning to the previous study, Fig. 3.8 is included to analyse the influence of SoE_{main} in $(dp/dt)_{max}$ and E_{res}. As these graphs shown, both parameters tend to increase as the SoE_{main} is delayed towards the Top Dead Centre (TDC). The maximum pressure rise rate increases monotonically, whereas the energy of resonance evolution tends to be exponential. The comparison of these results with those obtained with CDC shows that the significant differences observed in the medium range of frequencies are related to the important variations in the pressure rise rates. When operating with PPC gasoline, $(dp/dt)_{max}$ is one order of magnitude larger compared to that obtained when operating with CDC even at earlier values of SoE_{main}. The extremely high burning rates generated by PPC gasoline combustion
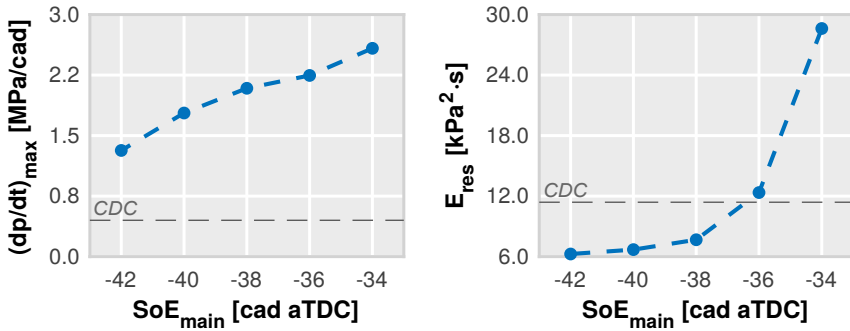
Figure 3.8: *Influence of SoE$_{main}$ on maximum pressure rise rate and energy of resonance.*

explains this fact, as indeed the pressure rise rate is strongly influenced by this parameter [126]. On the contrary, resonance levels are reasonably similar until a certain SoE$_{main}$ (-36 cad aTDC). However, additional shifts in SoE$_{main}$ towards the TDC result in a notable increase of the resonant energy.

At this point it seems that the lower contribution of resonance to the overall noise already observed in Fig. 3.6 is a consequence of the higher pressure rate of change achieved during the combustion rather than a resonance reduction. This fact can be demonstrated by applying again the method for determining the contribution of each frequency band to the total ON.

Figure 3.9 compares the contribution of each frequency band to the calculated ON level for all tests performed sweeping SoE$_{main}$. CDC test is also included for reference.

The extremely different contribution of medium-high frequency bands to both combustion concepts is evident. As can be seen the contribution of the resonance phenomena to the engine noise is again here almost negligible (< 5 %) when operating with PPC gasoline while modifying the operating settings, thereby showing that the maximum pressure rise rate is the major influencing parameter in engine noise radiation. Consequently, results displayed in Fig. 3.6 can be considered representative of the engine operation.

On the other hand, the proportions showed by CDC in the single-cylinder engine are more comparable and very similar to those observed in the multi-cylinder engine.
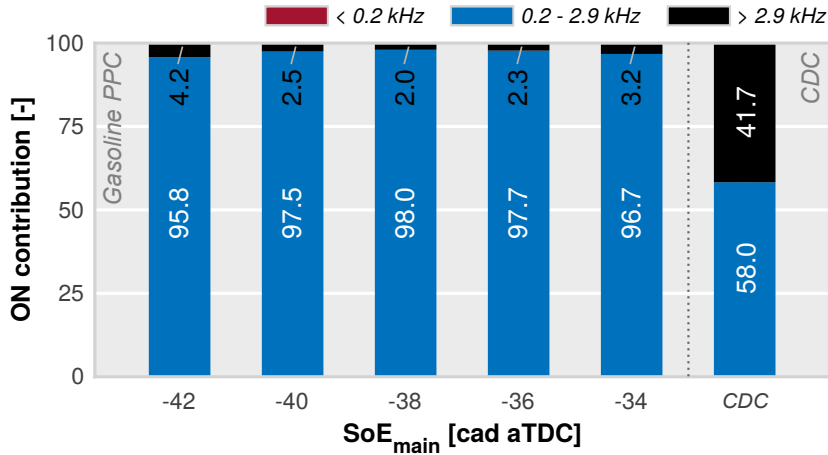
Figure 3.9: *Contribution of each band of frequencies to ON level estimation.*

3.4. Conclusions

In this chapter a characterization of combustion noise generated in CI engines has been performed by means of experiments.

Analysis was first done by considering in-cylinder pressure data of a DI CI engine operating with conventional Diesel combustion. Results confirmed two different paths to act on combustion noise actively: the management of the combustion through the operating settings that helps to reduce the amplitude of the medium range of frequencies, and the mitigation of high frequency harmonics due to the resonant gas oscillations.

Moreover, the study revealed which operating regions are more sensitive to resonant oscillations since depending on the engine operation the contribution of resonance in the external-propagated field it can be completely different.

In this sense, regions with low resonance contributions, mostly focused on high engine speeds and low loads, are more favourable for applying the first strategy. However, the second strategy seems to be more appropriate for the rest of the regions with elevated levels of resonance.

Concerning the partially premixed combustion with gasoline fuel, the contribution of resonance to the noise emissions is clearly lower than in Diesel combustion, even having similar levels of resonance. Thus, combustion noise is unquestionably dominated by the medium band of frequencies which, in turn, is controlled by the maximum pressure rise rate. Consequently, in this case it does not make sense to apply the second strategy to reduce noise

emissions by a resonance lowering, evincing the need to resort to the first strategy and therefore including noise emissions in the optimization loop of this particular combustion mode.

As it has been seen, pressure measurements allow to identify which are the causes of acoustic emissions due to the combustion, either focusing them on the combustion itself or on the chamber resonances. Nevertheless, data available from this experimental approach is not enough to reconstruct the spatial distribution of the unsteady pressure field, showing the need to assess the resonant phenomena through other approaches and go further in the investigation of this phenomenon.

In view of this constraint, numerical simulations have demonstrated their capabilities to enhance the comprehension of local phenomena. Therefore, a numerical model will be implemented and validated in the following chapters in order to provide more insight about the local mechanisms of combustion noise generation in CI engines.

3.A. Appendix: metrics for noise characterization

This appendix to Chapter 3 shows the two procedures used to compute the desired overall noise level, using different approaches. Subsequently a brief validation, based on external-microphone measurements, is presented to give an idea about the accuracy in the estimations.

3.1.1. Classical method

The fist method is based on the classical approach proposed by Austen & Priede [38] and the structural attenuation curve suggested by Anderton [94]. Thereby, the ON level of a given operating condition can be obtained by

$$\mathrm{ON\,(dB)} = 10 \cdot \log_{10} \frac{P_N^2}{p_0^2} \tag{3.A.1}$$

where p_0 is a reference sound pressure of $20\,\mu\mathrm{Pa}$, which corresponds to the minimum human hearing threshold. Besides P_N is defined as

$$P_N = \frac{1}{N} \cdot \sum_{f=f_1}^{f_N} P(f) \tag{3.A.2}$$

where N is the number of harmonics between f_1 and f_N, and P(f) represents the Fast Fourier Transform (FFT) of the engine radiated signal, which is obtained by subtracting the structural attenuation curve from the in-cylinder pressure spectrum following Austen's approach [38].

3.1.2. Method of three-parameters

Torregrosa et al. [47] proposed a three-parameters model for estimating the overall noise

$$\mathrm{ON} = C_0 + C_n I_n + C_1 I_1 + C_2 I_2 \tag{3.A.3}$$

where C_i are coefficients which depend on the engine concept and size. These coefficients were also determined by Torregrosa et al. [47], whose obtained the most convenient correlation coefficients to link the noise source with the engine radiated noise through a multiple regression analysis.

The indicators I_i are considered as fundamental noise parameters and are linked to a specific band of frequencies in the response of the source. The operation indicator (I_n), associated with the low frequencies, depends on

both the engine speed (n) and the idle speed (n_{idle}) as

$$I_n = \log\left[\frac{n}{n_{idle}}\right] \tag{3.A.4}$$

The combustion indicator (I_1) characterizes the sudden pressure rise due to the combustion and it is related to the medium band of frequencies. Hence, it is defined as

$$I_1 = \frac{n}{n_{idle}}\left[\frac{(dp/dt)_{max_1}^{comb} + (dp/dt)_{max_2}^{comb}}{(dp/dt)_{max}^{comp}}\right] \tag{3.A.5}$$

where $(dp/dt)_{max_1}^{comb}$ and $(dp/dt)_{max_2}^{comb}$ are the two maximum peak values of the pressure rise rate during the combustion, and $(dp/dt)_{max}^{comp}$ is the highest peak of the pressure rise rate during the compression-expansion phase.

Finally, the resonance indicator (I_2) represents the contribution of the resonance phenomena inside the chamber. It is mathematically expressed as

$$I_2 = \log\left[E_0\frac{E_{res}}{E_{comp}}\right] \tag{3.A.6}$$

Here E_0 is a convenient scaling factor and E_{res} is the signal energy of the resonance pressure oscillations. This parameter characterizes the global amplitude of the pressure oscillations due to the resonance phenomenon and its definition, as usual in the field of signal processing, is

$$E_{res} = \int_{IVC}^{EVO} p(t)_{res}^2\, dt \tag{3.A.7}$$

where $p(t)_{res}$ is the resonance pressure signal, which is integrated between intake valves closing (IVC) and exhaust valves opening (EVO). Similarly, E_{comp} can be obtained by integrating the compression-expansion pressure signal.

This latter parameter was defined for the first time by Broatch et al. [53] and it has to be understood in the sense of the energy on an electrical signal, as is usually defined in the field of signal treatment. In this context, the dissipated power ($\dot{W}$) in a resistive electric circuit can be defined as

$$\dot{W} = \frac{V^2}{R} \tag{3.A.8}$$

where V is the voltage and R is the circuit impedance. Therefore, the electric energy emitted from 1 Ohm resistive circuit is obtained from

$$E = \int_{t_0}^{t_1} \dot{W}\,\mathrm{d}t = \int_{t_0}^{t_1} \frac{V^2}{R}\,\mathrm{d}t \xrightarrow{R=1\Omega} \int_{t_0}^{t_1} V^2\,\mathrm{d}t \qquad (3.A.9)$$

According to this, the energy of reso-
nance signal can be characterized con-
sidering the measured pressure as elec-
tric signal: $V \to p(t)$.

3.1.3. Methods validation

Figure 3.10 shows a simple validation of
both methods expressed above. In this
figure predicted levels are contrasted
against the measured values. As can be
seen, the method of three-parameters
has a correlation coefficient (R) of 0.98
with a less than 1 dB of standard devi-
ation, offering a good estimation of the
noise level. The classical method, on

Figure 3.10: *Validation for the overall noise level prediction methods.*

the other hand, also shows an acceptable coefficient of correlation; however, SD is higher than 2 dB.

Thus, while the method of three-parameters is an appropriate approach to asses the real ON level of any operating condition, the classical approach should be utilized only for qualitative studies in which the exact value of the noise level is not critical.

Numerical model implementation

Prior to setting up and executing a CFD simulation there are many aspects that must be taken into account to guarantee the quality of the information generated by CFD. Therefore, a previous stage of identification and characterization of the problem while analysing the involved phenomena is demanded. Whether to model a problem in two or three dimensions, how to create an adequate mesh or which is the correct time discretization are typical decisions that might be addressed.

The singularity of the in-cylinder pressure field responsible for noise emission makes this a complicated choice that could compromise both the validity of the obtained conclusions and the attainment of the planned targets.

In this chapter the implementation of the numerical model is presented and discussed, paying special attention to the evaluation of the impact of the most relevant calculation parameters on the frequency content of the in-cylinder pressure. General features of the CFD model are firstly outlined together with an extended study about the effects of the turbulence approach election. The following two studies focus on establishing the optimum value

---

Work on this chapter has been partly published in the following papers:

- *Numerical approach for assessing combustion noise in compression-ignited Diesel engines* [6]

- *Understanding the unsteady pressure field inside combustion chambers of compression-ignited engines using a CFD approach* [11]

- *Experimental Analysis of Cyclical Dispersion in Compression-Ignited Versus Spark-Ignited Engines and Its Significance for Combustion Noise Numerical Modeling* [8]

of two calculation parameters, the mesh size and the time step. Finally, the last analysis evaluates the impact of the domain definition, the sensitivity of the initialization and the effect of injection-combustion uncertainties.

4.1. Description of the numerical model

The objective of this chapter is to implement a CFD model capable of reproducing the acoustic response of combustion while overcoming the drawbacks of prior works performed by Torregrosa, Broatch et al. [52, 53]. Consequently, complete engine cycles should be simulated, including the scavenging process, piston movement and valve movement profiles. Moreover, a realistic flow field recreation including the swirling air motion must be obtained, in which the injection and combustion processes should also be modelled.

Therefore, a numerical model of the engine was developed using the commercial CFD code CONVERGE [127]. The numerical solution of the 3D domain was obtained by using the finite volume method. A second-order central difference scheme was used for spatial discretization and a first-order implicit scheme was employed for temporal discretization. The species transport was also calculated by the mass fraction governing equations of all considered species in the domain.

The Redlich-Kwong equation [128] was selected as the equation of state for calculating the compressible flow properties. Pressure-velocity coupling was achieved by using a modified Pressure Implicit with Splitting of Operators (PISO) method [129].

The geometry of one cylinder of the Diesel HSDI CI engine used in the previous chapter (see Table 3.1 for additional details) was obtained by means of reverse engineering. The numerical domain, as shown in Fig. 4.1, included the complete single cylinder geometry and the intake/exhaust ports, allowing to perform either complete or closed cycle simulations. It also offers the chance to create a sector grid by considering periodic symmetry.

The mesh discretization, summarized in Table 4.1, was done using the cut-cell Cartesian method available in the code. The base mesh size was 3 mm throughout the domain in the reference grid configuration. Three levels of fixed embedding (0.375 mm of cell size) were added to the walls of the combustion chamber, ports and region near the fuel injector, to improve boundary layer prediction and the accuracy of spray atomization, droplet breakup/coalescence, etc. Mesh size in the chamber was reduced by two levels of embedding (0.75 mm of cell size) after the start of combustion, for

Velocity-based AMR
(intake valves flow)

Intake
ports

General view of
the numerical
domain and mesh
configuration

Mesh details at
intake valves

Spray and chamber
embbeding

Exhaust
ports

Temperature-based AMR
(combustion process)

Squish
region

Bowl
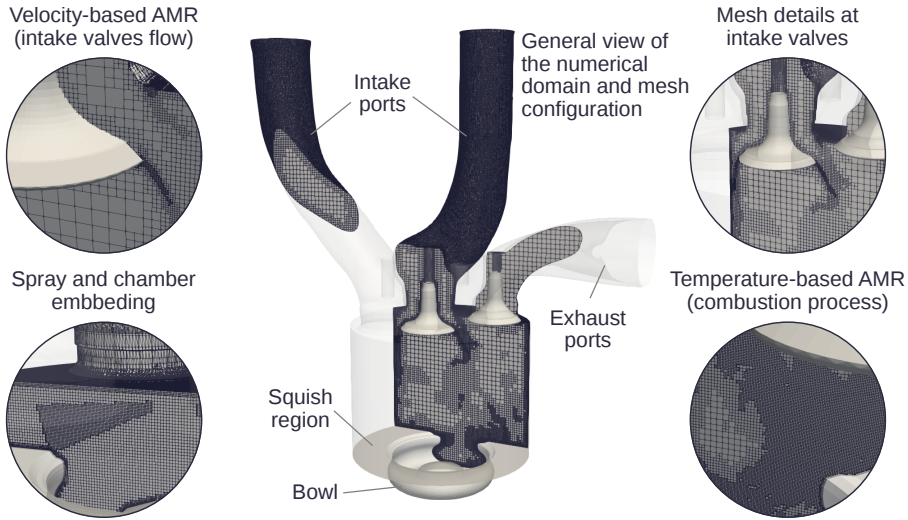
Figure 4.1: *Numerical domain and mesh characterization of the Diesel engine architecture.*

an improved recreation of the interaction and reflection of the pressure waves while avoiding undesired spatial aliasing effects. The code also employed adaptive mesh refinement (AMR) to increase grid resolution by three levels of additional refinement (up to 0.375 mm minimum cell size) based on the velocity and temperature sub-grid scales of 1 ms^{-1} and 2.5 K, respectively. As a result, the total number of cells varied between 1.5 million at Bottom Dead Centre (BDC) and 0.5 million at TDC.

This mesh configuration was selected after a broad literature review. In this task, recommendations about the grid resolution [130–134] and temporal discretization [52, 103] were taken into account in order to ensure a correct capture of the main features of Diesel combustion [135, 136] and its subsequent unsteady pressure oscillations [10, 137].

In the present work, the base mesh size and the level of grid refinement used in the AMR algorithm were utilized to either increase or decrease the grid resolution. Although the reference values were used for the majority of the simulations, both parameters were modified in some specified cases.

Several monitor points were distributed across the combustion chamber, including a monitor at the same location as the pressure transducer, in order to analyse the location of the standing waves. Moreover, the computed pressure was recorded at a sampling frequency of 50 kHz so as to provide an aliasing-free bandwidth, sufficient to cover the human hearing range [120].

Table 4.1: *Characterization of the reference grid selected for the model implementation after the literature review.*

Domain	Full geometry[a]
Base size	3 mm
Walls refinement	3 levels (0.375 mm)
Spray refinement	3 levels (0.375 mm)
Chamber refinement	2 levels (0.750 mm)
AMR	3 levels (up to 0.375 mm)
Turbulence modelling	URANS RNG k-ϵ

[a] This domain configuration can be used either for full and closed cycles.

The fuel injection was described by the standard Discrete Droplet Model (DDM) [138] and Kelvin Helmholtz (KH)-Rayleigh Taylor (RT) breakup model was employed to model spray atomization [139]. Droplet collision and coalescence were modelled by O'Rourke's model [140]. Moreover, the Frossling correlation [141] was used to model fuel evaporation. The drag coefficient of the droplets was calculated by the dynamic drag model of Liu et al. [142]. Following the extensively accepted standard approach [115], Diesel fuel physical properties were given by the *diesel2* fuel surrogate [143], which is known to provide suitable estimations of key spray parameters such as liquid length [143].

For combustion modelling, the SAGE detailed chemistry solver [130] was employed along with a multi-zone (MZ) approach, with bins of 5 K in temperature and 0.05 in equivalence ratio [144]. Although it doesn't utilize an explicit turbulent combustion closure [145, 146], the SAGE-MZ model has been demonstrated to perform well for simulating spray combustion in the context of both RANS and LES in previous studies [147, 148].

SAGE solver computes the source term of the energy equation by the approach proposed by Turns [149]. As he describes, the net production rate of all species considered in the calculation can be estimated by a multi-step chemical reaction mechanism where forward rate coefficients are expressed by the Arrhenius form whereas the reverse ones can be calculated from the equilibrium coefficient. All the necessary parameters to define the Arrhenius expressions, being different for each considered surrogate, are stored in tables, usually named chemical kinetic/reaction mechanisms, and loaded in runtime as the calculation progresses.

A reduced chemical kinetic mechanism for primary reference fuels (PRF) based on Brakora et al. [150] was used in this work to account for fuel chemistry and pure n-heptane was used as the Diesel fuel surrogate. The referred PRF mechanism was originally developed for approximating the

kinetic properties of several mixtures of Diesel, biodiesel (MD/MD9D) and gasoline fuels, allowing to perform a fair comparison between several blends of those fuels. In this way, iso-octane reactions were deactivated so as to predict the Diesel ignition features whereas the whole mechanism was considered in gasoline fuel simulations. In this way, the oxidation mechanism for diesel-like applications resulted in 42 species and 168 reactions. Using this approach, Senecal et al. [130] made a fundamental analysis of the spray features of the Diesel injection process, obtaining good results in terms of lift-off length. Later, other authors, such as Wang et al. [135] and Taglialegami et al. [136] demonstrated the suitability of n-heptane for predicting ignition delay in engine-like conditions.

Regarding emissions, soot formation and oxidation were determined by the empirical Hiroyasu soot model [151] whereas NOx formation was modelled by the extended Zel'dovich mechanism [152].

Cylinder wall temperatures were assumed to be constant and estimated using a lumped heat transfer model [153]. The inflow/outflow boundaries placed at the end of the intake and exhaust ports were prescribed by the cycle-averaged values of the corresponding measured pressures and temperatures for the most of the simulations in this work (unless otherwise specified). Finally, all turbulence approaches were coupled with the wall heat transfer model developed by Angelberger et al. [154].

4.2. Turbulence modelling evaluation

In the frame of CFD simulations, the characterization of the turbulence is still the main limiting factor for reproducing the flow field accurately. As commented in Chapter 2, there are many approaches to assess this regard.

Unsteady Reynolds Averaged Navier-Stokes is the standard approach in most practical ICE flows. The low computational time demanded has promoted its wide usage in the automotive industry. URANS methods assume that velocity variations around the mean value are small and due to turbulence, thereby it simulates the whole range of turbulence scales [104, 105].

Large-eddy simulation methods appeared as a partial solution to overcome some limitations of URANS models, such combustion instabilities due to the large turbulent scales. These techniques decompose the flow field into large and small scales; large scales are solved exactly whereas the small ones are approached by several Sub-grid Scale (SGS) stress models [106–108].

Table 4.2: *Characterization of the grid used in the turbulence model evaluation. Only changes respect to the reference grid configuration showed in Table 4.1 are presented.*

Domain	Full geometry[a]
Base size	2 mm
Walls refinement	3 levels (0.25 mm)
Spray refinement	3 levels (0.25 mm)
Chamber refinement	2 levels (0.50 mm)
AMR	4 levels (up to 0.125 mm)
Turbulence modelling	URANS RNG k-ϵ and dynamic structure LES

[a] Intake/exhaust ports were not utilized.

Lastly, DNS solves all turbulent scales, allowing to reach very accurate results, but the prohibitive computational costs make it improper for most of the engineering applications.

In this section, the performance of URANS modelling is evaluated against LES turbulence modeling. Specifically the re-normalized group (RNG) $k - \epsilon$ model [104] is compared with the dynamic structure LES model [108] for the same mesh resolution. Although the grid resolution was not optimized for any of both cases, the goal of this study is to determine if the differences in the rate of heat release arising from capturing large-scale turbulence structures with LES (unsteady flame instabilities) contribute to the in-cylinder pressure field modification in a significant way.

Two closed-cycle simulations with the reference mesh configuration (described in the previous Section 4.1) with the grid resolution displayed in Table 4.2 were performed using both turbulence models. The injection settings of a real operation condition were utilized together with the original configuration of the injector in order to assure the validity of the results. Initial conditions at IVC were obtained by a previous gas exchange process (GEP) simulation using URANS. Since there are no clear indications about how the time discretization could affect to the pressure oscillations estimation in the literature, the sonic CFL number was kept below one during the combustion, resulting in a minimum time step of 10 nanoseconds approximately.

Results of both simulations are shown in Fig. 4.2 (top), where in-cylinder pressure traces are plotted together with the rates of heat release. It can be seen how even though the gap between the RoHR traces in the diffusive combustion phase, the pressure is not excessively affected. Only a slight difference in the mean pressure level can be appreciated from 20 cad aTDC up to the end of the closed-cycle, where the pressure decays first in LES
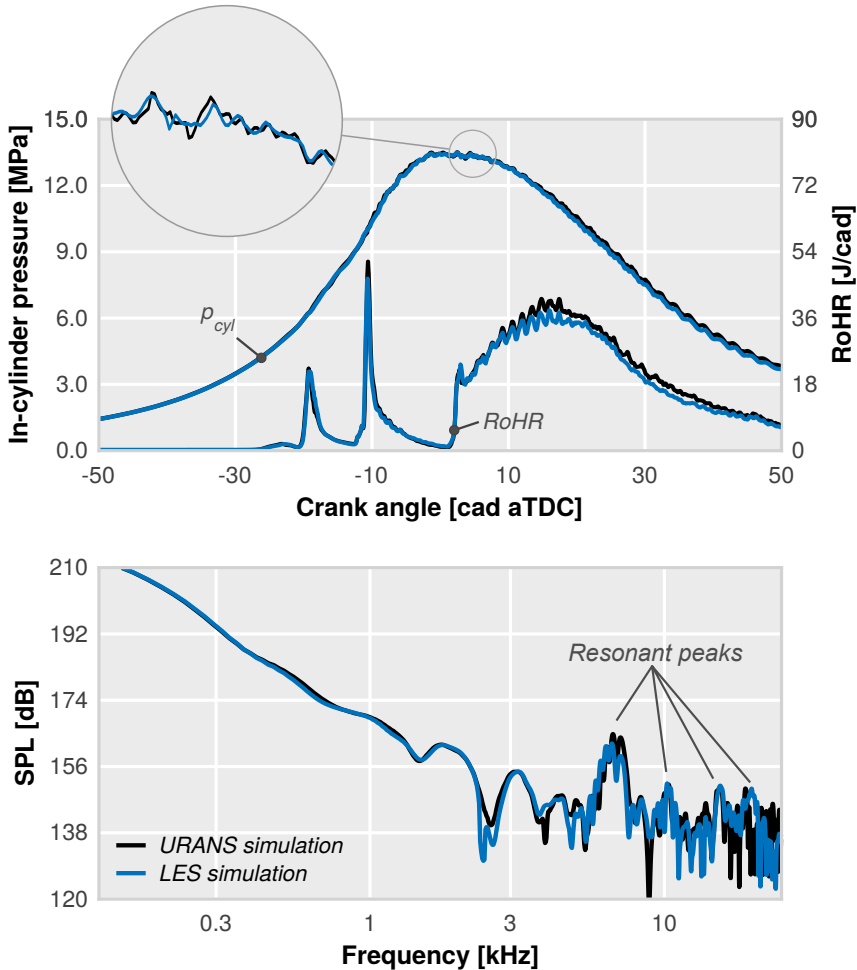
Figure 4.2: *Comparison between URANS and LES modelling in terms of in-cylinder pressure and RoHR (top), and frequency content of the pressure signal (bottom). The in-cylinder pressure were registered by a monitor point placed at the experimental transducer location.*

simulation. Besides, from the zoomed-in detail view included in the figure, it can be seen that pressure oscillations do not show relevant differences since they display a highly resemblant pattern.

In Fig. 4.2 it can be also observed that the heat release linked to the premixed combustion is practically identical in both simulations, and what is more interesting, the maximum values of RoHR and the ignition delays are replicated.

Now, in order to check the coherence of pressure signals in the frequency domain, the sound pressure level of both signals were computed and presented in Fig. 4.2 (bottom). As expected from the observations commented before, both spectra practically coincide in the whole broadband. Although there are minimal differences, the spectra traces follow the same trends and they show the same amplitude-frequency values for all resonant peaks. The overall noise calculated from the spectra does not show a significant difference: 88.4 dB were featured by the URANS simulation whereas LES predicted 88.3 dB.

Thus, there is no clear evidence that combustion instabilities, captured by LES modelling during the mixing-dominated burning phase, contribute to the acoustic signature or to the resonant mechanisms occurred within the chamber in a significant way. Consequently, it is possible to claim that phenomena involved in combustion noise generation are clearly dominated by the pressure leap achieved during the premixed burning, in which URANS provide the same results as LES.

Furthermore, although the difference in terms of computational effort is not significantly high, many cycles or realizations must be computed to extract statistically valid results in a LES simulation, thereby increasing the return time of a single simulation and decreasing the number of potential studies to perform.

All these reasons led to choose URANS as the reference turbulence model for the following studies in this chapter, and also in the majority of the analyses presented in this work. Nonetheless, a detailed comparison of the results obtained by multi-cycle URANS/LES simulations were included in Chapter 6 in order to provide a further understanding of this regard.

4.3. Mesh independence study

One of the most critical aspects in a CFD simulation is to define a mesh that assures an accurate solution while the computational time remains under reasonable values. As commented above, the code uses an internal algorithm to create a structured mesh based on hexaedrons that ensures high mesh quality, but the size of the grid must be selected by the user depending on the application. Therefore, a mesh independence study is performed in this section in order to ensure that the domain discretisation does not affect the in-cylinder pressure field estimation.

Table 4.3: *Characterization of the grid used in the mesh independence study. The changes respect to the reference grid configuration are presented.*

Domain	Full geometry[a]
Base size	2 to 4 mm (every 0.5 mm)
Initialization	Uniform
Injections	1
Injector nozzles	1

[a] Intake/exhaust ports were not utilized.

As in the previous study, closed-cycle simulations were performed with the reference grid configuration and some modifications shown in Table 4.3. Again the complete geometry domain was considered without utilizing the intake/exhaust ports since they were not necessary. The calculations were initialized with a uniform spacial distribution of thermodynamic properties (temperature, pressure, turbulent kinetic energy and turbulent dissipation) and species concentration. The number of injections were reduced to one and a single-nozzle injector, which sets a unique excitation source, was utilized to simplify the simulation as much as possible while keeping the phenomena related to noise emissions. Lastly, five different mesh sizes were defined with the base cell size parameter varying from 2 to 4 mm.

Figure 4.4 shows the most relevant results of the mentioned simulations. Here, the SPL of each pressure signal registered at the same location of the pressure transducer is plotted in order to visualize the effects of the grid resolution in the pressure frequency content.

On the bottom plot of this figure, the source mechanism of each part of the spectral signature is also indicated, following the method explained in Chapters 2 & 3 and originally presented by Priede [44], where the mechanical compression-expansion and mean combustion pressure trace are subtracted to identify the cut-off frequency (in this case $\sim$ 3 kHz) above, in which the unsteady pressure oscillations are predominant. This allows to identify that mesh resolution has a direct impact on the
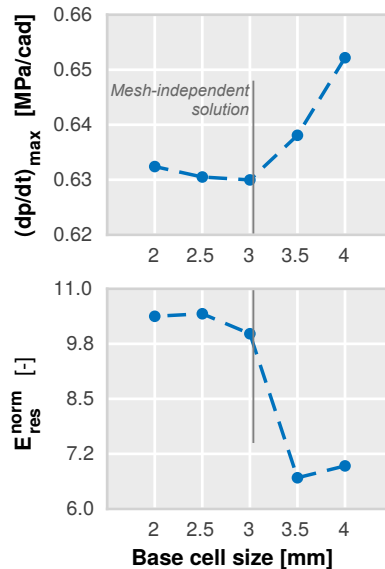
Figure 4.3: *Results of the independence mesh study. Trends of $(dp/dt)_{max}$ and E_{res}^{norm} are plotted to identify a mesh-independent solution.*

mean combustion pressure evolution
and on the overall resonant contribu-
tion.

It can be seen in this figure that while SPL values are coincident at frequen-
cies below 0.7 kHz, the traces slightly diverge at frequencies gathered within
0.7 and 3 kHz. Besides, the results evidence no influence of the mesh size
on the frequency-amplitude pair values of the resonance modes highlighted
in the figure. However, the noticeable dispersion observed in the amplitude
of the transition frequencies between the oscillation modes within the high
frequency span (> 3 kHz) does not show a clear convergence.

In Fig. 4.3 $(dp/dt)_{max}$ and E_{res} parameters, that define the behaviour of
both the mean combustion pressure and the resonance phenomena, are
plotted against the base mesh size in order to identify at which grid size the
solution could be considered independent from the spatial discretization.
The idea is to achieve similar levels of both parameters, even if the spectra
do not collapse completely.

In this case, the resonance energy is normalized (E_{res}^{norm}) by a reference
value E_{comb} defined as

$$E_{res}^{norm} = \frac{E_{res}}{E_{comb}} \tag{4.3.1}$$

$$E_{comb} = \Delta p_{comb}^2 \Delta t \tag{4.3.2}$$
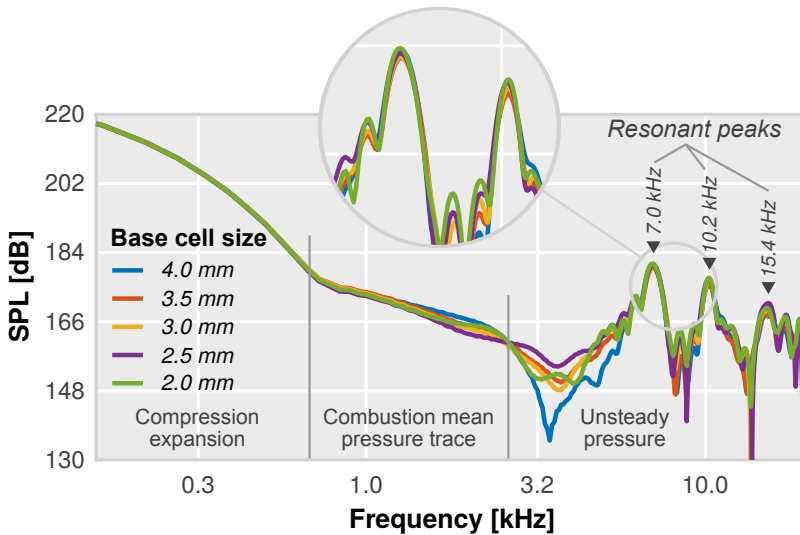
Figure 4.4: *Results of the independence mesh study. The spectral signature of
each simulation is plotted to identify the effects of the grid resolution in the
in-cylinder pressure field prediction.*

where Δp_{comb} is the maximum increase of the mean pressure due to the combustion event and Δt is the time span in which this maximum is achieved. Since in most cases the RoHR and therefore the intensity of the acoustic perturbation changed significantly, this normalization became required to dismiss the effect of this variation and only take into account the modification of the resonant conditions.

This figure confirms that neither the maximum pressure rise rate due to the combustion nor the global amplitude of the resonant oscillations do not excessively change with grids of base sizes close to 3 mm. Thus, this grid resolution offers a grid-independent solution for the combustion acoustic signature.

4.4. Temporal discretization

As explained in Section 4.2 the CFD model uses the sonic CFL number to fix the calculation time step during the combustion event. This mathematical procedure establishes the number of cells swept by a pressure wave between two consecutive time steps of the calculation. Although there are no studies that directly evaluate the effect of this parameter in the CFD solution, some authors [155, 156] claimed that it could severely affect the numerical dissipation of pressure waves and thereby, compromising the prediction of the stationary waves due to the resonance inside the chamber.

In this way, the following study analyses the impact of the time discretization of the Navier-Stokes equations on the spectral signature to establish the dissipation rate of pressure waves provoked by the combustion.

The same considerations taken in previous Section 4.3 about the mesh configuration were taken in this study to perform a new set of closed-cycle simulations varying the sonic CFL number during the combustion. On this occasion the grid base size was fixed to the optimum length (3 mm) and the time discretization was determined by maintaining the sonic CFL number close to 0.5, 1, 2, 10 and 50, respectively.

Once more, the pressure spectra of the pressure signal registered at the monitor placed in the transducer location are shown in Fig. 4.5. This figure shows that the most relevant discrepancies are focused in the high frequency range. The amplitude of the standing waves due to the resonance phenomena is attenuated as the sonic CFL number increases. Besides, SPL traces become smoother, diminishing most of the secondary high frequency peaks.
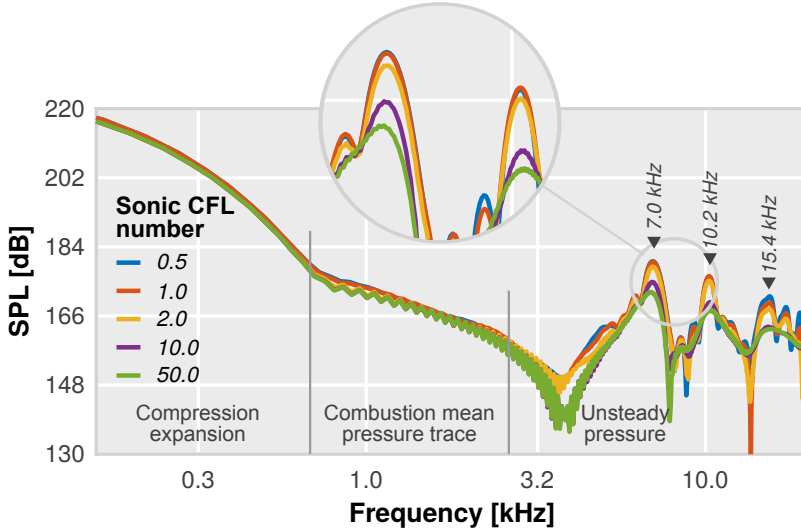
Figure 4.5: *The spectral signature of each simulation is plotted to show the effects of the time discretization of Navier-Stokes equations.*

These trends are also reproduced by the behaviour of E_{res}^{norm} displayed on Fig. 4.6 (top). While the overall amplitude of the pressure oscillations drastically decreases for sonic CFL numbers gathered within 5 and 50, it reaches a maximum and steady value for CFLs below one. However, the calculation time considerably increases as the time step is reduced, as the bottom graph shows.

The optimum time discretization that assures a suitable reproduction of the pressure wave interaction and reflection mechanisms is therefore that obtained by fixing the sonic CFL close to the unity.

It is important to remark that this temporal restriction was only applied during the combustion event due to the huge impact on the final calculation time. A dynamic time step strategy based on two different CFL numbers was used to overcome this limitation. The velocity
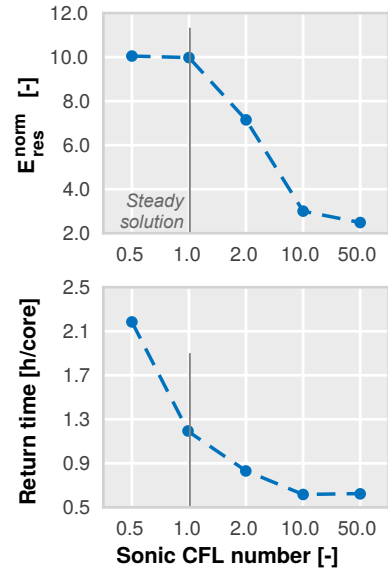
Figure 4.6: *Results of the time discretization study. Trends of E_{res}^{norm} and return time are plotted to identify the optimum time discretization. It should be noted that the scaling factor of the horizontal axis is not constant.*

Table 4.4: *Characterization of the grid used in the computational domain definition study. The changes respect to the reference grid configuration are only shown.*

Domain	Full geometry[a], 60° and 180° sectors
Initialization	Uniform
Injections	1

[a] Intake/exhaust ports were not utilized.

of the flow (u) was taken as the limiting
factor during the compression and injection phases, whereas the speed of sound (c) was considered during the combustion.

As a result, the computational time was reduced without loss of accuracy regarding the simulation of pressure oscillations that are produced by the combustion heat release, and are crucial in this investigation.

4.5. Definition of computational domain

Several numerical methods for analysing CI Diesel combustion in ICE are available in the literature. Some works [115, 130, 157, 158] focused on combustion diagnosis, performance and emissions, assume simplifications so as to reduce both the mesh size and simulation time. Some of those assumptions are mainly related to the definition of the boundary and the initial conditions. In particular, periodic suppositions and a uniform distribution of the thermodynamic variables for initialization were applied by utilizing angular sectors and simple thermodynamic models.

Most of these applications are supported by purely assessing physical properties and chemical reactions of the air-fuel mixture but none of them is based on simulating pressure waves interaction. Hence this study was devised to determine the best domain configuration for reproducing the acoustic field inside the chamber.

Three closed-cycle simulations were performed with the full geometry mesh, without using intake and exhaust ports, and with two angular sector grids of 60 and 180 degrees. Both sector meshes were built by assuming periodic symmetry, thereby including one and three sprays in the numerical domain, respectively.

Recalling the reference configuration showed in Table 4.1, these simulations used the same features with the changes shown in Table 4.4. Thus, the simulations started with uniformly-distributed thermodynamic conditions and the fuel was introduced in the chamber in a single injection.
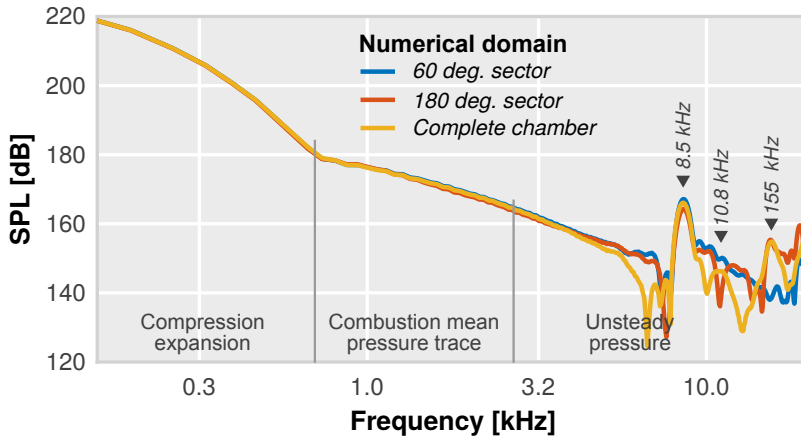
Figure 4.7: *Spectral signature of pressure signals registered with three different numerical domains (complete chamber, 180°. and 60° sectors).*

According to spectra shown in Fig. 4.7, the highest dispersion is again focused in high frequencies between 6 and 8 kHz. Although the first resonant peak located at 8.5 kHz is reproduced by all simulations, notable differences are observed in the second and third peaks. The second peak is clearly identifiable in the complete chamber simulation whereas it is not appreciable in any of both sector calculations. The third peak is however replicated by the 180°. sector simulation.

Results show the capability of the sector approaches to reproduce the pressure response at low to medium frequencies, allowing their application for performance or emission studies in which high frequency effects are negligible. However, assuming periodic symmetry through the boundary conditions definition compromises a correct estimation of the pressure waves interaction, thereby affecting negatively the estimation of the high frequency band of the pressure spectrum. Thus, a complete cylinder domain with non periodic assumptions must be considered for the assessment of the combustion as a noise source.

4.6. Initialization of the simulation

In this section two different but closely related studies are detailed, both are focused on analysing how the CFD solution is altered as the initialization of the simulation is modified. The first, evaluates the impact of considering uniform or non-uniform initial conditions on the prediction of the acoustic source. The final target of this study is to determine if it is necessary to

resort to full cycle simulations instead of using closed-cycle calculations, less expensive in terms of computational resources. On the other hand, the second study analyses the progress of the numerical solution as several consecutive cycles are simulated in order to determine if it is necessary to resort to simulate several cycles to achieve a representative solution.

4.6.1. Effects of initial conditions

In the first study two closed-cycle simulations with a different definition of the initial conditions at IVC were compared. For the first case, the initial conditions were taken from a previous GEP simulation, thereby considering the spatial non-uniformities. For the other case, the conditions at IVC were spatially averaged to use them as uniform initial conditions, emulating the initialization based on 0D models. This assumption allows a fair comparison of the results since both simulations kept the same mean values of thermodynamic conditions and species concentration.

Again, only the chamber region of the reference grid was utilized in the closed-cycle simulations. Nevertheless, GEP simulation used the full domain, including intake-exhaust ports and valves, to obtain flow field conditions at IVC. The simulation gathered a complete air management stage between EVO and IVC timings. Inflow and outflow boundaries located at the end of the intake-exhaust ports were established as the mean value of the measurements of instantaneous pressure and temperature.

This latter simulation was only performed to provide more realistic flow conditions for the closed-cycle simulation. Hence, the solutions obtained during the GEP were not directly considered for the following study.

Figure 4.8 shows the comparison between both closed-cycle simulations. In the top graph, in-cylinder pressure and RoHR traces are plotted against the crank angle degree. As it can be appreciated, there are no high differences among the solutions. While the ignition delay is practically replicated in both approaches, the mean behaviour of both pressure and heat release is almost the same. Nonetheless, from the top zoomed view of this graph, it can be observed how the maximum amplitudes of pressure osculations seem to be lower in the uniform-initialized solution. The bottom graph confirms this effect since there are significant differences in the high frequency band of the pressure spectra, especially in the first resonant peak. The latter is practically attenuated and trends of high order peaks (>10 kHz) are not exactly equal. As expected from the previous graph, lower differences are however observed in the low-medium frequency range (< 3 kHz).
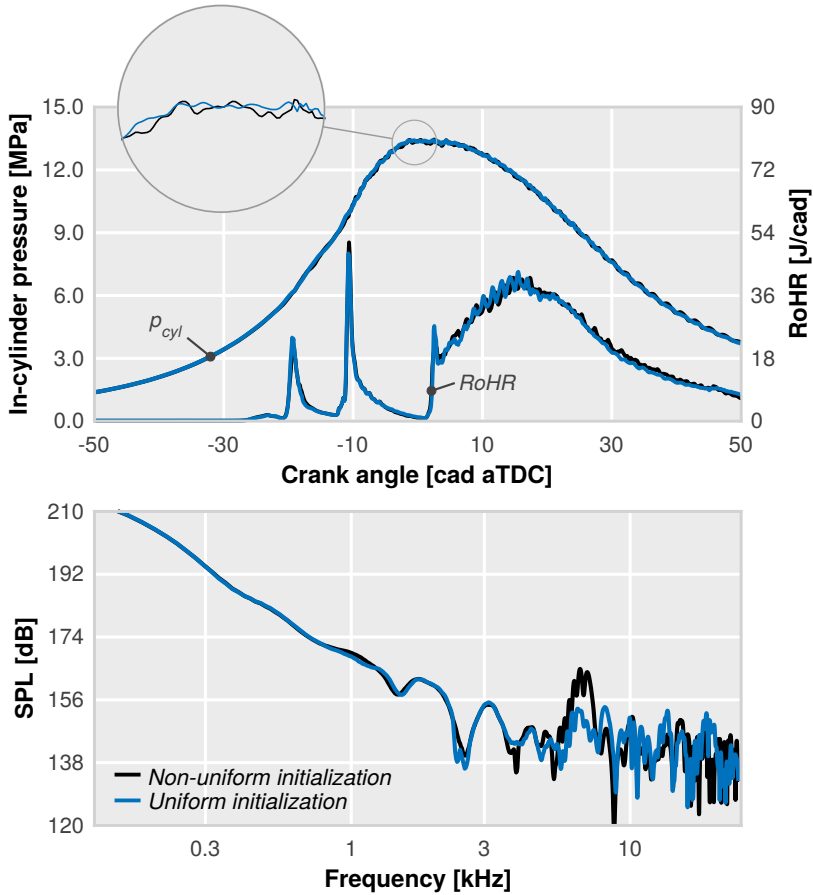
Figure 4.8: *Effects of the initialization in the numerical solution. In-cylinder pressures are plotted together with RoHR traces at top whereas the frequency content of pressure signals are compared at bottom.*

Since it has been demonstrated that very close solutions in the time domain may lead to an extremely different spectral signature of the pressure signal, an in-depth analysis of the main physical mechanisms of combustion was performed to identify which are the differences that condition the singular behaviour of the pressure field.

First, the spatial features of the combustion were studied by an analysis of the heat release at specific stages of combustion. In Fig. 4.9 six snapshots of the accumulated RoHR contours along the axial dimension of the cylinder at the start of each ignition in both considered simulations are shown. This procedure is also known as *line of sight* since it approximates a perpendicular
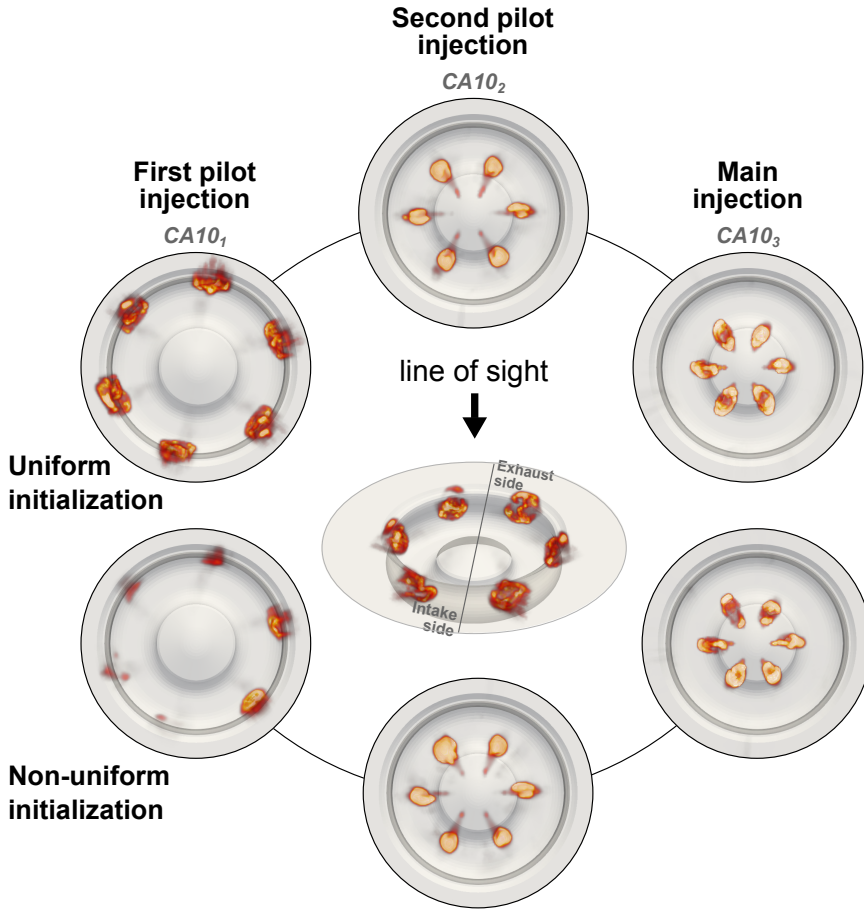
Figure 4.9: *Effects of the initialization on the numerical solution. The spatial heat release spreading is plotted at different stages of the combustion process for the two initialization hypotheses.*

view of any process from an external observer point of view. The plotted instants correspond with the time step at which 10% of the fuel of each injection is consumed ($CA10_i$).

Analysing the location of self-ignition zones, no remarkable differences are observed between both solutions at the same stage of combustion. The higher temperatures achieved as the chamber volume is reduced provoke a lower ignition delay that brings the burning regions towards the cylinder centre.
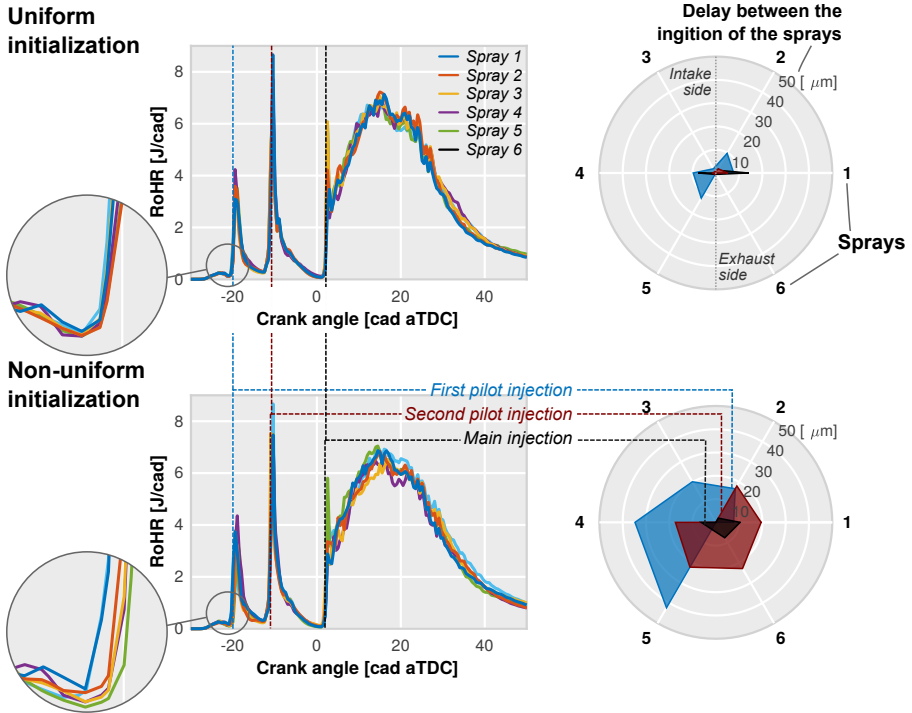
Figure 4.10: *Spreading of local features of combustion. RoHR profiles of each spray region are plotted at top whereas the delay between the ignition of sprays is drawn at bottom.*

However, energy release distributions reveal that the combustion is more or less uniformly distributed between all sprays in the top solution while it has a higher spreading in the bottom one. This suggests that it is possible to find important dissimilarities in the spray ignition sequence and energy allocation, especially during the ignition of the first injection.

Hence, the combustion chamber was divided into six sectors (one for each injector nozzle), and the RoHR profile was obtained for each one in order to analyse both aspects. In addition, these profiles were used to estimate the start of the combustion in all sectors by means of the CA10 parameter. Results of this study are presented in Fig. 4.10 where RoHR traces of each spray region are plotted at top and the delay among the ignition of each spray is presented at bottom.

Zoomed views of the left graphs confirm that ignition spread of the first injection is clearly higher if it is considered a non-uniform initialization. Inspecting the sequence of the sprays ignition in the right graphs, in which the polar axis symbolizes the number of sprays and the radial axis represents

the delay between combustion onsets (with respect to the first ignition), it can be observed that there is scarcely temporal scatter among sprays in the uniform initialization case. A certain symmetry is also observed in the combustion onsets of the first injection burning: the sprays located in opposed sides of the chamber have practically the same ignition delay. For instance, sprays 3 and 6 show a delay of 6 μs with respect to the first ignition event whereas the ignition of sprays 2 and 5 is postponed 8 μs.

This singular behaviour is not reproduced by the other simulation, for which the ignitions follow a random timing sequence due to the non-uniform local thermodynamic conditions and species concentration at the start of combustion. In addition to this spread, the combustion onset is produced in the exhaust side where local temperatures are higher.

As a brief summary of this section, it is possible to claim that physical mechanisms observed may influence the spectral content of the in-cylinder pressure in a significant way. Besides, the differences on the local features of the combustion, a closed-cycle simulation initialized by a spatial-averaged uniform conditions lead to an unrealistic interaction of pressure waves that condition the spectral content of the pressure field. These phenomena are only reproduced by simulating the flow field accurately in terms of local thermodynamics and species, thereby resorting to an initialization based on a previous GEP simulation. From the practical point of view, it is thus necessary to calculate the complete engine cycle to asses the combustion noise source.

4.6.2. Simulation of multiple engine cycles

In the second study, the reference configuration of the model (see Table 4.1) were utilized with the complete geometry, including intake/exhaust ports and valves, in order to perform a single simulation of several consecutive engine cycles.

The calculation started at EVO with uniform initial conditions at the whole domain in terms of pressure, temperature, turbulence and species concentration, and the velocity field was fixed as null at the start of the simulation. These flow conditions were determined by a combination of 0D modelling [122, 159] and direct measurements. In the subsequent cycles, the initial conditions were determined as a result of the previous cycle. Figure 4.11 illustrates the proposed methodology by the in-cylinder pressure evolution along the three consecutive cycles.
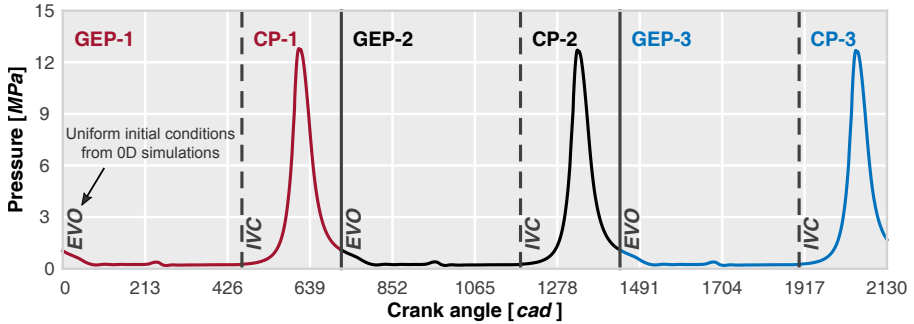
Figure 4.11: *A schematic representation of the calculation methodology followed in this section. In-cylinder pressure evolution of three consecutive cycles.*

Once the three subsequent cycles were calculated, the global thermo-dynamic conditions and the energy release were obtained and shown in Fig. 4.12. Here, the signals were separated in single cycles and superposed for comparison. Top graph displays the in-cylinder pressure of each simulated cycle during the GEP. There are not significant gaps between all the cycles. However, the thermodynamic conditions predicted by the CFD model at EVO after the first cycle are not exactly the same as those predicted by the 0D model for initializing the simulation. This causes slight differences between the first and the subsequent cycles during the opening phase of the exhaust valves. In spite of this disagreement, the prediction of the in-cylinder pressure at IVC is not significantly affected.

The same graph also shows the dispersion of the spatial-averaged temperature. While the first cycle exhibits a higher deviation from the other ones, the second and third cycles follow similar trends. Besides, the estimation of the mean temperature at IVC show a significant deviation between the first and the subsequent cycles ($\simeq 15$ K), influencing the charge mass available for combustion.

In the following graph (middle) it is possible to see the effects on the heat release of the mentioned disagreement. The ignition delay in the combustion of the first pilot injection is decreased in the second and third cycles and the maximum value of the RoHR is increased due to the higher mean temperatures and the lower mass trapped inside the cylinder. The maximum RoHR produced by the second ignition is larger in the first cycle than in the subsequent ones. During the main injection the differences are scarce and only the maximum RoHR presents a slight disagreement during the mixing controlled combustion.
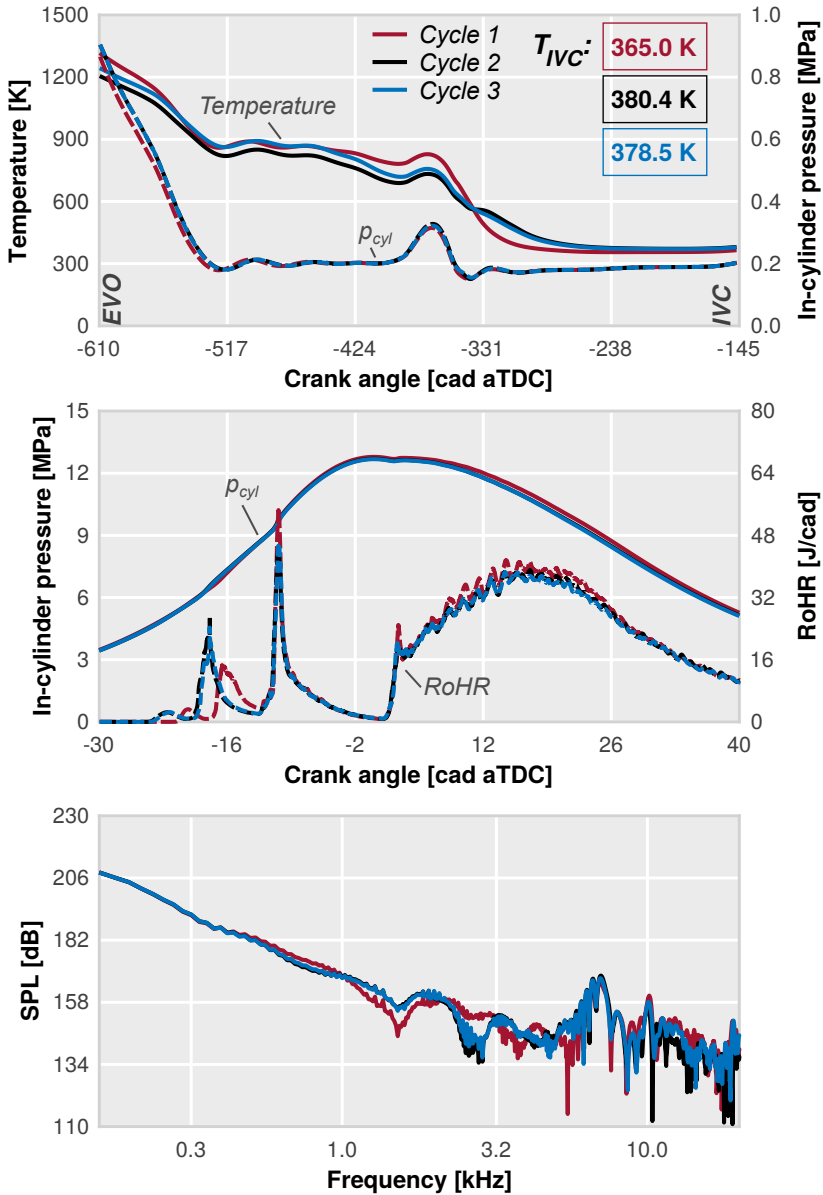
Figure 4.12: *Analysis of the solution dispersion between three consecutive engine cycle calculations. In-cylinder average pressure and temperature during the GEP are plotted at top. In-cylinder mean pressure and RoHR during the combustion are drawn at middle and the spectral density of the pressure signal at the transducer location is displayed at bottom.*
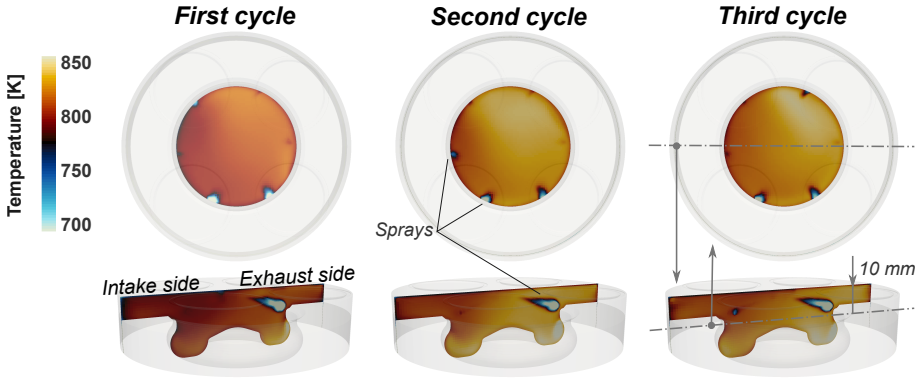
Figure 4.13: *Changes in the local temperature distribution at the start of combustion ($\simeq$ -25 cad after TDC). Snapshots of temperature contours at two different planes.*

As described in the previous Section 4.6.1, the differences observed are not only related with the global thermodynamic conditions, but with the local conditions that also play a relevant role in the prediction of the combustion features and its effects. Figure 4.13 shows a series of snapshots of temperature contours just at the combustion onset of each engine cycle. As it can be observed, there are considerable gradients of temperature inside the combustion chamber, showing a hotspot located on the side of the exhaust valves. The simulation of the first cycle allows to reproduce the in-cylinder temperature gradients but it does not achieve the same value of those predicted by the subsequent simulated cycles.

The in-cylinder mean pressure evolution does not change significantly among the three cycles during the combustion. However, there are noticeable differences in the estimation of $(dp/dt)_{\max_1}$ and $(dp/dt)_{\max_2}$, as it is observed in Table 4.5. Their close relation with the maximum heat release values achieved during the combustion of the two pilot injections explains the higher deviation of the first cycle. In addition, the last graph (bottom) shows that the dispersion in those parameters gives rise to relevant differences in the middle frequency band of the pressure spectra. In contrast, the resonance energy shows similar values between all cycles and the high frequency pressure spectra does not display remarkable differences.

Table 4.5 also presents the evolution of some acoustic parameters as the engine operation progresses so as to quantify the impact of the Sound Pressure Level (SPL) dispersion in both the internal and external propagation fields. Despite the differences observed in the pressure spectra, none of these parameters are notably affected, and no relevant dispersion is observed.

Table 4.5: *Comparison of the estimated metrics related to internal and external acoustic fields.*

Parameters	Cycle 1	Cycle 2	Cycle 3
$(\mathrm{d}p/\mathrm{d}t)_{\mathrm{max}_1}$ [MPa/cad]	0.922	0.815	0.824
$(\mathrm{d}p/\mathrm{d}t)_{\mathrm{max}_2}$ [MPa/cad]	0.453	0.548	0.514
E_{res} [kPa^{2}s]	29.93	30.55	27.60
ON [dB]	91.14	91.12	90.96

Although these acoustic metrics are not excessively altered, the spectral content of the pressure signal predicted in the first cycle is clearly distinct within the medium frequency range. Therefore, it must be resorted to calculate further cycles to ensure an accurate solution of the in-cylinder unsteady processes since the prediction of the first simulated cycle is influenced by the simplistic initial conditions.

In this case, the solution convergence was established after the simulation of two subsequent cycles, when the dispersion in the main thermodynamic parameters, such as pressure and temperature, was significantly reduced and the pressure spectral content achieved an unvarying solution.

4.7. Effects of injection and combustion uncertainties

The simulation of the injection event is known to play a crucial role in determining combustion in Diesel engines. From the primary breakup to the end burning, the spray features are numerous and involves many physical phenomena that must be accurately simulated to capture the main combustion traits.

Previous studies revealed that such combustion attributes may condition the in-cylinder acoustic field signature in a relevant way. For instance, Torregrosa et al. [52] and Broatch et al. [53] showed the impact of the energy release amount and the location of the ignition onset. They demonstrated how the amplitude of the resonant modes is enlarged as the maximum energy release increases. Moreover, they claimed that the location of the auto-ignition zones can influence the spectral content between two consecutive resonant peaks and therefore, changing the overall amplitude of the pressure oscillations.

Since these studies were made by assuming no piston motion and they did not consider the effect of the expansion stroke on in-cylinder temperature, one of the aims of this section is to reproduce the latter studies with

Table 4.6: *Grid characterization for the injection-combustion uncertainties study.*

Domain	Full modified geometry[a]
Base size	3 mm
Walls refinement	3 levels (0.375 mm)
Spray refinement	3 levels (0.375 mm)
Chamber refinement	2 levels (0.75 mm)
AMR	3 levels (up to 0.375 mm)
Sonic CFL number	< 1
Initialization	Uniform
Injections	1
Injector nozzles	1
Turbulence modeling	URANS RNG k-ϵ

[a] Intake/exhaust ports and valves were not utilized.

a moving piston mesh and a coupled injection-combustion approach, both assumptions of capital importance when addressing realistic engine simulations. Nonetheless, the principal objective is to evaluate the impact of the ignition location in the behaviour of the in-cylinder pressure field, thereby establishing the relevance of the injection-combustion uncertainties in the acoustic response of the combustion.

The idea lies on modifying the combustion onset location artificially while keeping the exact RoHR profile. The main and imperative condition in those simulations was therefore to reproduce an analogous energy release while the location of the auto-ignition is varied by the injector position.

Hence a series of closed-cycle simulations with the configuration shown in Table 4.6 were performed. They were initialized by the same uniformly-distributed thermodynamic conditions to keep the ignition delay whereas a simplified piston version, presented in Fig. 4.14, of the original geometry is used to avoid possible spray-wall interactions which could influence the fuel energy release. In addition, an injector with only one nozzle is considered to easily control both the ignition location and energy release.

Two variations of a reference position were considered in both cylindrical coordinates (radial and axial). Therefore, the radial position of the injector was conveniently modified in Figs. 4.14b and 4.14c to change the location of the spray ignition. On the other hand, Figs. 4.14d and 4.14e display the results of modifying the ignition position along the axial coordinate of the cylinder. All these graphs show snapshots of RoHR contours at the middle spray plane and at the same percentile of the heat release (10% of fuel burnt

Simplified full cylinder domain
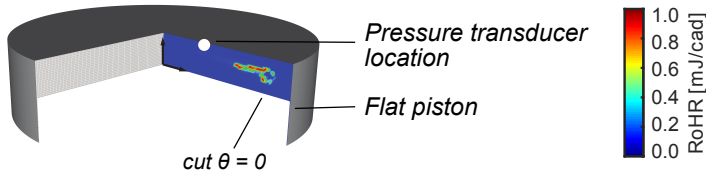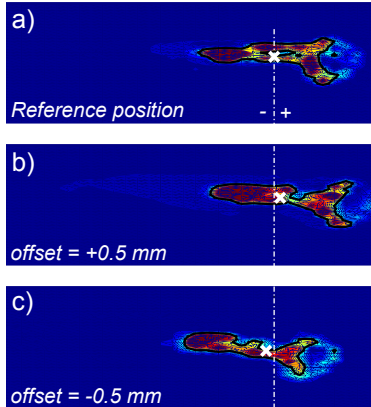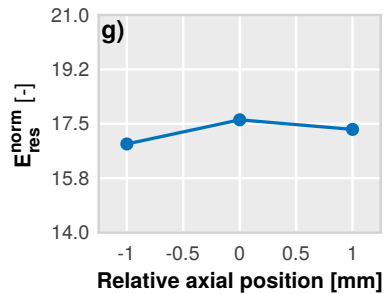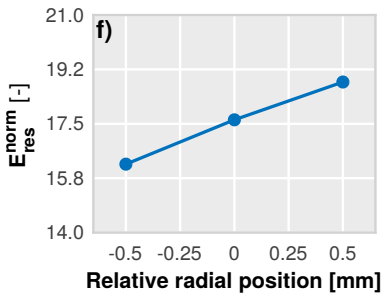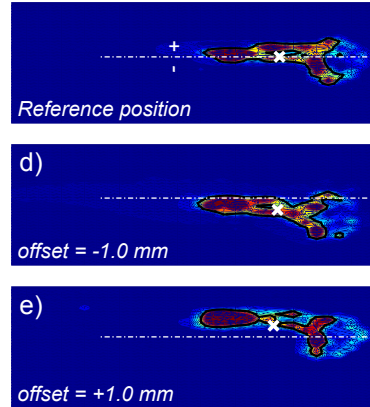
Figure 4.14: *Results of the auto-ignition location analysis. a) to e) Snapshots of RoHR contours at the middle spray plane for 3 different radial and axial positions, f) Differences in the global amplitude of the pressure oscillations along the radial dimension, g) Differences in the global amplitude of the pressure oscillations along the axial dimension*

or CA10) that, in this case, almost coincide with the same crank angle since the RoHR is practically identical. Lastly, Figs. 4.14f and 4.14g show how these modifications change the energy of resonance within the chamber.

As can be seen form these snapshots series, the centroid of combustion (obtained from the RoHR mass-weighted averaged along the chamber) was modified ±0.5 mm in the radial dimension and ±1 mm in the axial one, allowing to correlate the ignition location and its effect on the in-cylinder pressure field.

Examination of the two latter graphs reveals the effect of varying the self-ignition location in the global amplitude of pressure oscillations along both cylindrical coordinates. The resonance energy rises as the combustion is moving towards the cylinder walls, increasing the global amplitude pressure oscillations (E_{res}). By contrast, the variation of the E_{res} is lower and presents a nearly constant trend when the ignition zone moves along the cylinder axis. Both trends, especially the first one, remark the relevance of the injector geometry (number of nozzles, included angle, nozzle diameter, nozzle angle, etc.) and spray characterization (lift-off length, spray length, liquid length, spray angle, etc.) on the combustion and subsequently, on the resonant behaviour of the combustion chamber.

4.8. Conclusions

In this chapter, a numerical model for assessing combustion noise in CI Diesel engines has been presented. With the target of understanding how the unsteady pressure field behaves inside the combustion chamber, special attention has been put on evaluating the impact of the most relevant calculation parameters in the spectral content of the pressure instabilities.

The basis of the numerical model, especially those traits related to the spray and combustion modelling and inspired in previous works available in the literature [10, 52, 103, 130–137], has been also described.

The performance of URANS modelling has been evaluated against LES to identify the differences in the energy release that could condition the spectral content of the pressure field. Results revealed a slight disagreement among both predicted RoHR profiles specifically within the diffusive stage of the combustion. Although these dissimilarities, there is no clear evidence that combustion instabilities, captured by LES modelling during this latter burning phase, significantly contribute to the acoustic signature of the combustion.

Since cycle-to-cycle variations in the in-cylinder acoustic field cannot be reproduced due to the simplistic features of the proposed study, a further analysis is however needed to establish the contribution of the pressure instabilities generated at the standing flame reached in the diffusion stage in the overall spectral content.

The mesh independence study has shown that the interaction and reflection mechanisms of the travelling pressure waves within the chamber can be captured with a minimum grid size of 0.75 mm during the combustion or 3 mm of base cell size.

Analysis of the temporal discretization of Navier-Stokes equations has demonstrated how the CFL number based on the speed of sound has a direct impact on the high frequencies of the pressure spectrum. This parameter must be set close to unity during the combustion to ensure that only one cell is swept by a pressure wave between two consecutive time steps of the calculation, reducing the numerical attenuation of standing waves. However, the calculation time considerably increases due to the small time step.

Periodic boundary conditions applied to angular sector domains cannot reproduce the pressure wave interaction and reflection mechanisms correctly, thereby affecting negatively to the high frequency band of the pressure spectrum.

More complex simulations have shown how local thermodynamic conditions and species distribution determine the spatial and temporal features of the fuel ignition, both aspects of capital importance in the unsteady pressure behaviour within the combustion chamber. These particular circumstances are only achievable by simulating subsequent engine cycles with their correspondent gas exchange processes.

Lastly, it has also been proved that the overall spectral amplitude, specifically the high frequency range, depends on the fuel self-ignition location, thereby remarking the importance of the spray characterization in the pressure field estimation.

Validation of the numerical results

After understanding in detail how the numerical solution behaves against the most relevant calculation parameters, it is of the utmost importance to properly validate the obtained results in order to ensure that they correspond accurately enough to the physical reality.

An exhaustive experimental validation of CFD solutions is described in this chapter, including both qualitative and quantitative comparisons. As in Chapter 3, two distinct CI engines were selected for this purpose, being sufficiently representative of current design trends in the automotive market. Moreover, they were operated with two combustion concepts that have demonstrated important issues of noise.

5.1. Methodology

The usual validation method in CI engines is based on reproducing the in-cylinder pressure trace averaged from a given number of experimentally recorded cycles. However, simple cycle averaging is not suitable for providing a pressure trace representative of the average unsteady features of

---

Work on this chapter has been partly published in the following papers:

- *Combustion noise analysis of partially premixed combustion concept using gasoline fuel in a 2-stroke engine* [1]

- *Impact of the injector design on the combustion noise of gasoline partially premixed combustion in a 2-stroke engine* [2]

- *Understanding the unsteady pressure field inside combustion chambers of compression-ignited engines using a CFD approach* [11]

- *Development of a Virtual CFR Engine Model for Knocking Combustion Analysis* [10]

combustion noise (overall noise, energy of resonance, etc.) because cycle averaging smoothers out local pressure fluctuations. Therefore, a novel methodology was developed to identify the most representative cycle of a specific operating point. The main principle behind this technique lies in preserving the average characteristics of the high frequency content of the pressure signal.

The selection procedure aimed at choosing the cycle which showed least deviation from the average values of two characteristic parameters of combustion noise. While the maximum pressure rise rate ($(dp/dt)_{max}$) was used to characterize the uniform in-cylinder pressure rise, the unsteady pressure field was described by the energy of resonance (E_{res}). Considering these two parameters, a cost function (CF) was defined for each cycle i as follows:

$$CF_i = \frac{\left|(dp/dt)^i_{max} - (dp/dt)^{avg}_{max}\right|}{(dp/dt)^{avg}_{max}} + \frac{\left|E^i_{res} - E^{avg}_{res}\right|}{E^{avg}_{res}} \qquad (5.1.1)$$

Cost function was calculated using Eq. 5.1.1 for all the experimental cycles and the top cycle having the lowest cost function value was chosen as potential candidate for the most representative cycle. After the selection procedure, the only missing step is to check if this choice is also representative of the main behaviour of the pressure evolution.

An example of this procedure is shown in Fig. 5.1 in which the candidate cycle is highlighted. In addition, all the experimental cycles, the cycle-averaged pressure trace and standard deviation band around the cycle-averaged pressure are also depicted in temporal and frequency domains. It is evident that the picked cycle 37 correctly captures the main traits of the pressure trend and the spectral content in the whole broadband. Therefore, cycle 37 was considered to be the most representative pressure trace for this operating point.

On account of the particular behaviour of the pressure field within the chamber, traditional in-cylinder pressure measurements through a single transducer do not provide enough information for characterizing all resonant phenomena. The oscillation patterns observed in the pressure cause distinct local pressure distributions that condition the signal registration. Hence the simulated and measured signals must be recorded at the same location if we want to ensure a fair comparison among them. The experimental pressure trace registered by a piezoelectric sensor is therefore compared to that obtained by a point monitor at the same location of the transducer in order to check the consistency of numerical results. In addition, both signals were captured at a sample frequency of 50 kHz so as to provide an
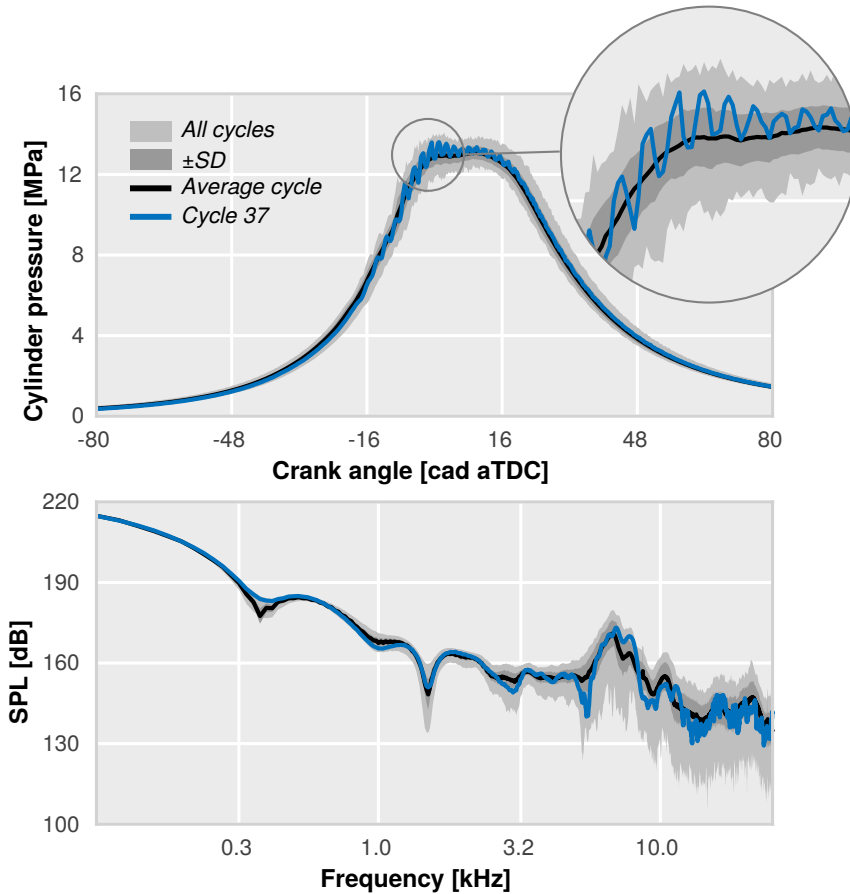
Figure 5.1: *Example of selection procedure application. The candidate for the most representative pressure trace are highlighted among all experimental cycles.*

aliasing-free bandwidth comparable to the average human hearing range [120]. If the comparison of these signals in temporal and frequency domains success, the solution can be considered to be suitable for extrapolation to the entire chamber domain.

The energy release of the combustion is also included for a deeper validation of the combustion process. Since this parameter was obtained by solving the energy equation by direct measurements and assuming several simplifications [122], the experimental RoHR must only be considered as a reference not as a direct measurement that has to be reproduced perfectly.

Table 5.1: *Operating settings used for the model validation in CDC mode.*

Point	#1	#3	#7	#8
Engine speed [rpm]	1350	1500	2400	2850
Torque [Nm]	12.3	75.2	168.3	87.0

Besides to this qualitative analysis, several acoustic metrics related to both internal and external propagation fields were considered to check the suitability of the model for predicting noise emissions. All these metrics and their calculation methods were described in Appendix 3.4.

Furthermore, in some specific cases in which other metrics can be considered relevant for the targets of the study, additional parameters such as performance or pollutant levels were incorporated for validation.

Finally, to ensure that representative data was captured by the simulation, the described methodology was applied to different engine platforms operating with CDC and gasoline PPC concepts.

5.2. Conventional Diesel combustion

In order to check the suitability of the model to predict the Diesel combustion features, the 4-stroke Diesel CI engine utilized in most of the studies presented so far and data available after the experimental campaign performed by L. Monelletta [118] were used for validation.

First, a steady operation condition defined by a medium speed/load (Point #7 of Table 3.3) was selected. This operating point has showed, in Chapter 3, the most critical conditions in terms of overall noise level and resonant contribution within the whole considered operation map. The recommendations obtained as a result of the study presented in the previous chapter where applied to implement a model set-up which was used as a reference.

In addition to this base configuration, two additional set-ups were built in order to perform more complex simulations able to reproduce, unless *a priory*, the cyclical dispersion registered in the measurements. A deeper analysis of considering a more elaborated turbulence scheme (LES) is therefore included to shed some light in CCV and their effects on noise emissions.

Lastly, the validation will be extended to additional operating points that have also revealed, through the analysis presented in the same Chapter 3, an undesired impact on combustion noise. Within all operating points used in that study, Points #1, #3 and #8 were only selected for simulating, being sufficiently representative of all noise issues present in the whole operating

Table 5.2: *Configurations of the CFD model used in the validation.*

Configuration	URANS-Coarse[a]	URANS-Fine	LES
Domain	Full geometry[b]		
Base size	3 mm	3 mm	2.2 mm
Walls refinement	3 (0.375 mm)	3 (0.375 mm)	3 (0.275 mm)
Spray refinement	3 (0.375 mm)	3 (0.375 mm)	3 (0.275 mm)
Chamber refinement	2 (0.75 mm)	2 (0.75 mm)	2 (0.55 mm)
AMR	3 (0.375 mm)	4 (0.188 mm)	4 (0.138 mm)
Sonic CFL number	< 1		
Initialization	Non-uniform[c]		
Turbulence modelling	URANS RNG k-ϵ		Dynamic structure LES

[a] Reference configuration.
[b] Including intake/exhaust ports and valves.
[c] Obtained from a previous URANS simulation of the GEP.

map while showing completely different frequency band contributions (low, medium and high frequency) to the overall engine noise. Although being already shown in Table 3.3, all operating conditions used in this chapter are summarized again in Table 5.1 for an easy identification of the conditions simulated in this chapter.

5.2.1. Validation of a single operation condition

The steady operation condition defined by an engine speed of 2400 rpm and 168 Nm of torque, which corresponds with the point number #7 in Table 5.1, was selected in the first place to validate the numerical methodology.

In Table 5.2 the three model set-ups used in this section can be seen. The guidelines introduced in Chapter 4 were taken as a reference to build the baseline configuration, named URANS-Coarse. The other two configurations have essentially the same set-up with only few changes in the grid resolution to enhance a better match with the turbulence model utilized. The second URANS configuration, denoted as URANS-Fine, was specifically included to verify that the potential improvements of the LES set-up are only due to the turbulence approach rather than the progress in the mesh quality. The LES mesh resolution was increased taking into account the recommendations found in the literature [160, 161].

Three simulations of four consecutive engine cycles were performed utilizing these model set-ups. All of them started from the same thermodynamic conditions to allow a fair comparison of all simulated cycles.
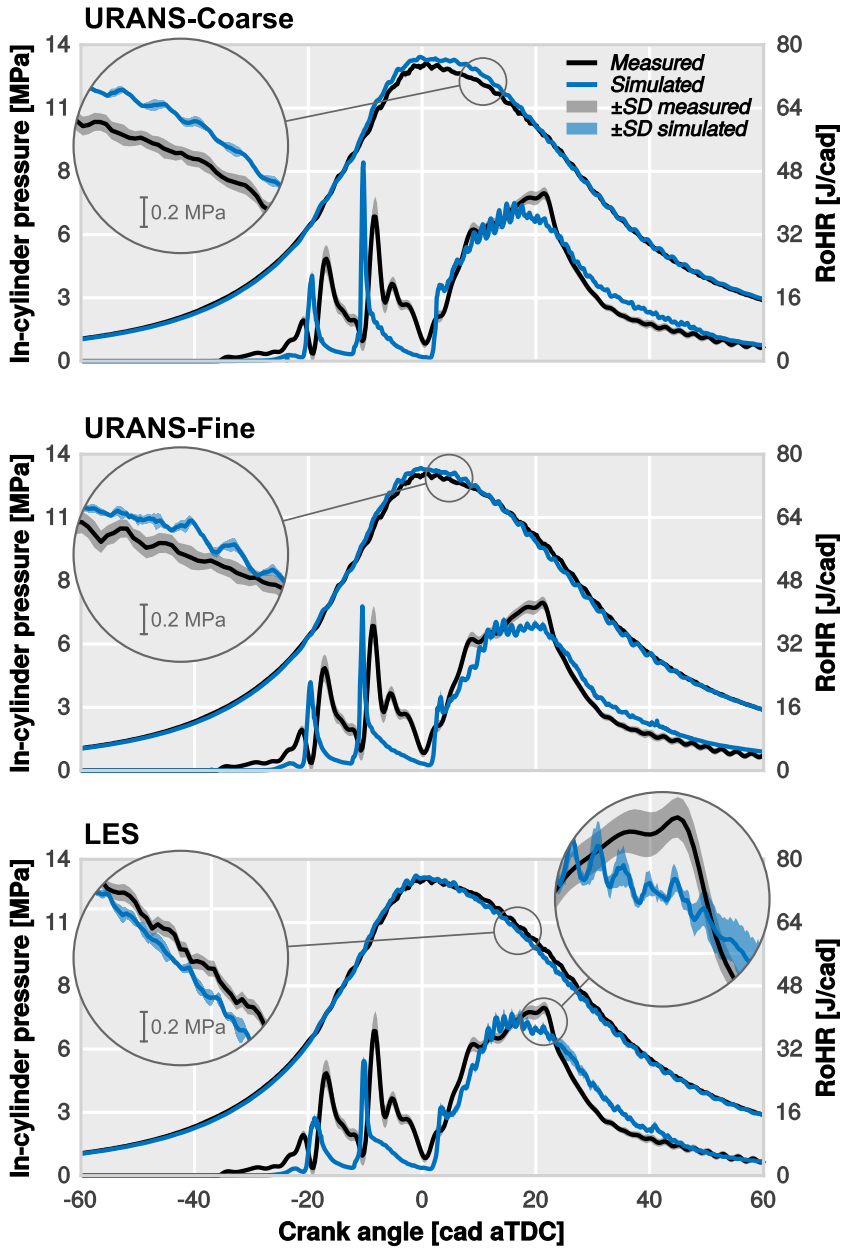
Figure 5.2: *Validation of the numerical models in terms of in-cylinder pressure and rate of heat release.*

In Fig. 5.2, the in-cylinder pressure data from the selected experimental cycle, including the experimental standard deviation data, is plotted against the numerical solution obtained from the three approaches. In general, all

the models offer a good estimation of the in-cylinder pressure behaviour since all simulated cycles are gathered within the experimental dispersion. Only a slight overestimation is observed in the reference solution after top dead centre when the energy release of the mixing-controlled combustion phase enhances its maximum value. Nonetheless, the gap among the experimental standard deviation and simulated cycles is very reduced, thereby the solution can be considered sufficiently accurate. Focusing in the zoomed views, it is possible to see how the resonant oscillation is self-similar from cycle to cycle: the cyclical dispersion is very small and the same oscillation peaks can be consistently identified. Moreover, this cyclical variation is apparently reproduced only by LES approach, without reaching the experimental levels though.

In addition to the in-cylinder pressure comparison, the RoHR is also included in Fig. 5.2 for deeper validation of the combustion process. Again a good match between experimental and simulated data is obtained. Although there are some differences among them, specially during the diffusion combustion phase, trends are reasonably reproduced and ignition delays are well-captured in all approaches. Moreover, the cyclic dispersion, more apparent during the main combustion where turbulent spray interactions have a direct impact on the energy release, is again solely imitated by LES modelling.

In Fig. 5.3, pressure spectral density is shown, indicating the source mechanism of each part of the spectral signature, following the method presented by Strahle [46] where the mechanical compression and mean combustion pressure trace are subtracted to identify the cut-off frequency (in this case ~ 4 kHz) above which the unsteady pressure oscillations are preponderant.

It can be seen in the plot that all simulated data in this last part of the spectrum, which constitutes our range of maximum interest, is within the experimental standard deviation, suggesting that CI combustion-generated wave interaction is well captured by every numerical scheme considered in this study. The medium frequency range, gathered by 0.4 and 4 kHz, evidences a certain degree of disagreement. However, both the main trend and the average spectral content are similar, thus validating the CFD solution.

Apart from the general trends of the selected cycle, it is evident, from the zoomed-in views, that URANS-Fine and LES approaches captured the dispersion due to the CCV, being more apparent in the LES one.

Overall noise was computed for all experimental cycles, resulting in a mean value of 89.61 dB with a standard deviation of 1.47 dB. As can be seen in Table 5.3, the mean values obtained from all simulated cycles (including the
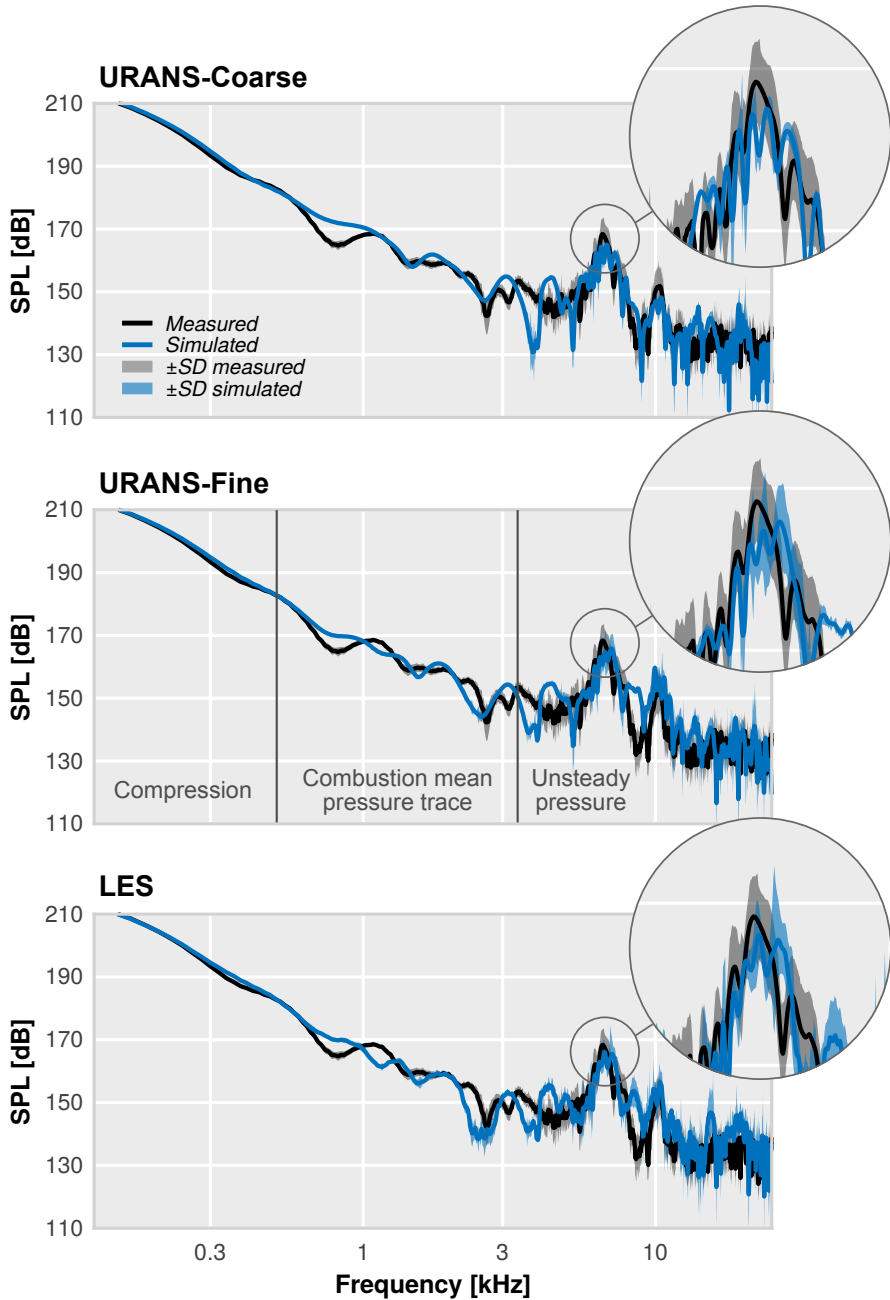
Figure 5.3: *Validation of the numerical models in terms of frequency content of the pressure signal.*

Table 5.3: *Validation of estimated acoustic metrics.*

	Experiment		URANS-Coarse		URANS-Fine		LES	
	Mean	±SD	Mean	±SD	Mean	±SD	Mean	±SD
ON [dB]	89.61	1.47	89.86	0.32	89.01	0.82	89.20	1.23
E_{res} [kPa²·s]	27.34	16.33	25.83	3.32	24.87	9.05	29.86	13.16

three approaches) are within the aforementioned experimental deviation. For instance, URANS-Coarse approach was rated at ON = 89.86 dB of mean value, this is, a difference of only 0.25 dB against the experimental value, thus capturing the average behaviour of the most relevant noise sources. Inspecting standard deviation values shown in the same table, a clear relationship can be found between the cyclical dispersion and the complexity of the model. LES approach is able to reproduce comparable values of ON dispersion whereas URANS show lower variation. Nonetheless, it is possible to capture some cyclic deviation with URANS schemes by increasing the mesh resolution.

Recalling the pressure spectra shown in Fig. 5.3, it can also be seen that the combustion contribution to the noise spectra CCV is very low and not excessively relevant in the overall noise. Thus, a well-configured[1] URANS simulation can offer a representative pressure spectra. This is of special relevance when addressing, as in automotive sector, highly complex problems in a limited time span.

Similar trends are observed if we compare the values of energy of resonance, showing that noise cyclical dispersion is produced fundamentally due to the alteration of the high frequency pressure field.

5.2.2. Validation of additional operation conditions

Three additional steady operating conditions, also included in Table 5.1, were selected to further validate the numerical model. These conditions were sufficiently representative of all noise-issue points identified in the whole operating range and the contribution of each frequency band (low, medium and high frequency) to the overall engine noise was completely different among these operation points (see Section 3.2 of Chapter 3 for further details).

---

[1]This is, with a space and time discretization small enough to correctly resolve the pressure waves travelling and interacting within the chamber.
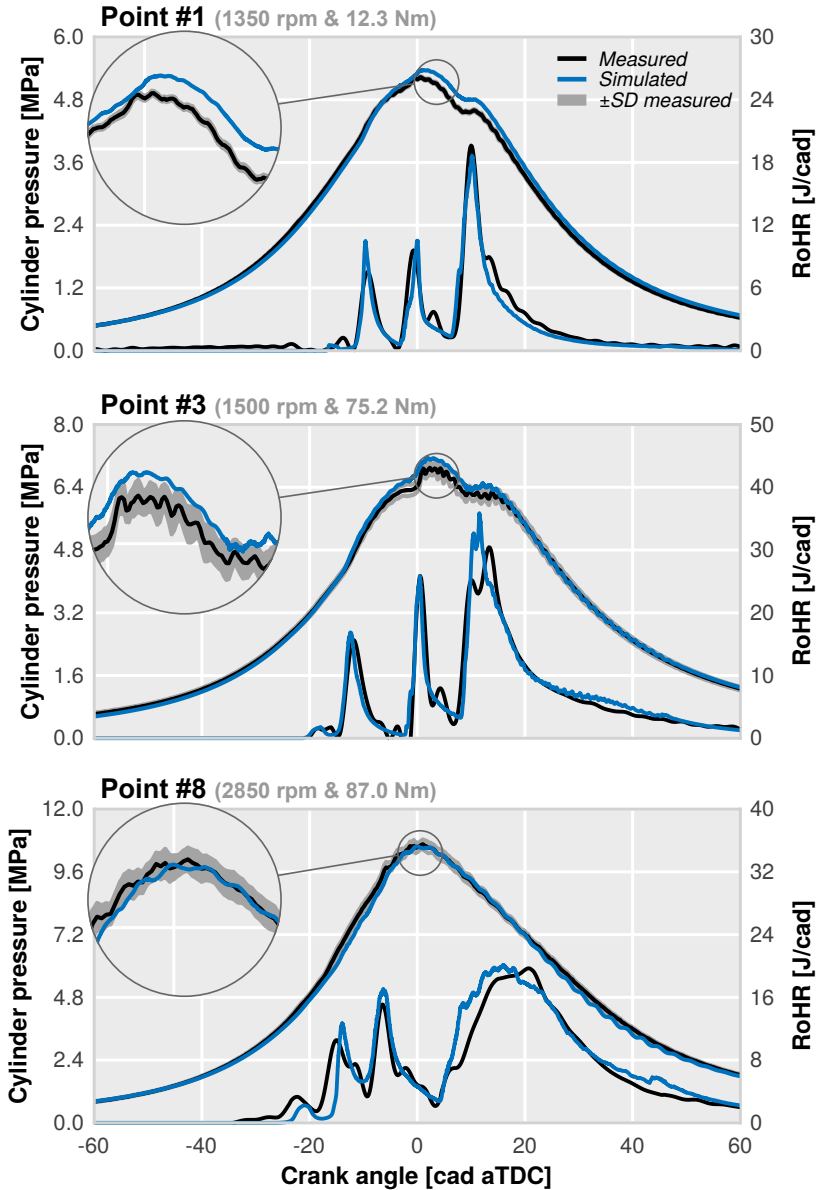
Figure 5.4: *The pressure signals registered at the transducer location are shown together with the estimated RoHR. The standard deviation (SD) of the measured cycles is included in order to compare the numerical solution with the measurement dispersion due to cycle-to-cycle variations.*

Since it has become clear that URANS modelling provide a coherent solution of the in-cylinder pressure field, URANS-Coarse configuration was used in the further steps of the validation. This will allow a more rigorous analysis that could confirm the suitability of URANS simulations to predict combustion noise features by enhancing its prediction confidence.
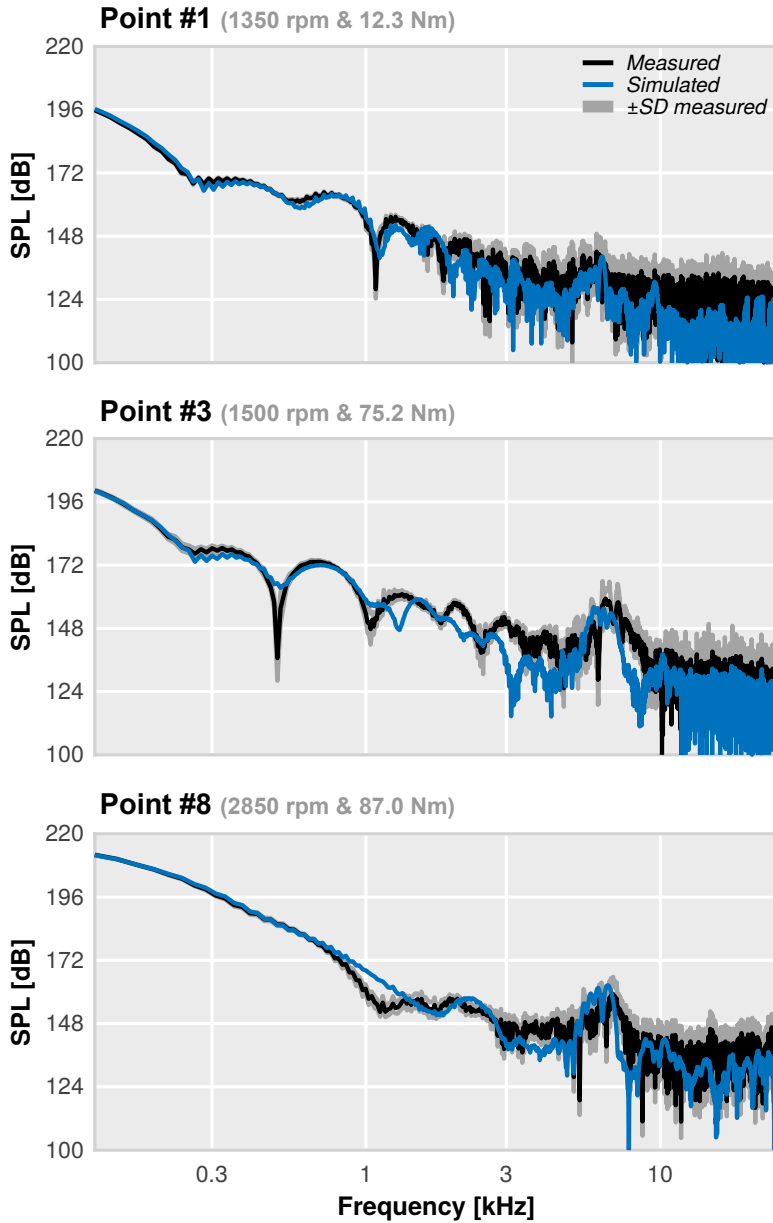
Figure 5.5: *The spectra of the pressure signals registered at the transducer location are shown. The standard deviation (SD) of the measured cycles is included in order to compare the numerical solution with the measurement dispersion due to cycle-to-cycle variations.*
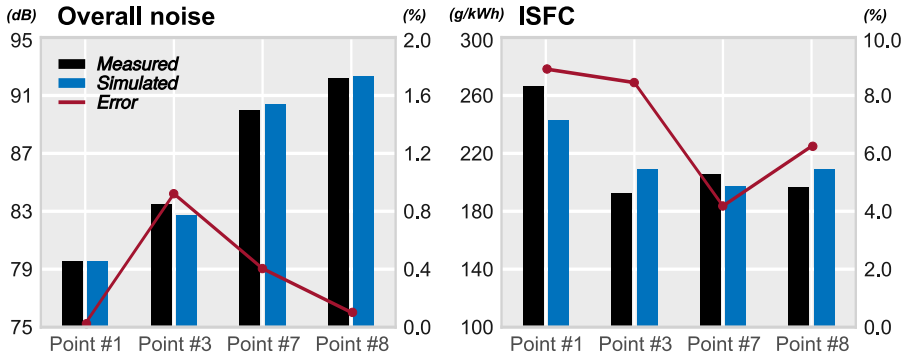
Figure 5.6: *Results of the extended validation considering additional engine outputs. The numerically estimated values of the overall noise (top) and ISFC (bottom) are compared against those obtained from the experiments.*

Figure 5.4 shows the comparison between simulations and experiments at the three additional conditions considered for validation. The pressure traces registered at the transducer location in experiments and simulations are plotted along with the corresponding rates of heat release. In general, a good agreement is obtained with experiments for all three operating points. As observed in the previous section, the ignition delay is remarkably well captured while the maximum values of energy release during the premixed combustion is also adequately reproduced. More difficulties are however observed to reproduce the heat release during the mixing-controlled phase, the main trend is roughly followed though. Zoomed views also show that the resonant oscillation process is consistently reproduced by the simulations.

The pressure spectral density of all operation points, shown in Fig. 5.5, shows how numerical results overlap with measurements in almost the whole frequency range, with only a slight disagreement observed for the medium frequencies in points number #3 and #8.

The suitability of the model for predicting noise emissions and performance levels was also assessed. The overall noise and indicated specific fuel consumption (ISFC) were selected for validation. Figure 5.6 shows that both parameters prediction are quite reasonable, since errors between the simulations and experiments are below 1% and 10%, respectively. Thus, although there was a slight disagreement in the medium frequency range of the spectrum of some of the operating points, the model ensures an accurate prediction of the external engine acoustic field and fuel consumption for all the operating conditions considered.
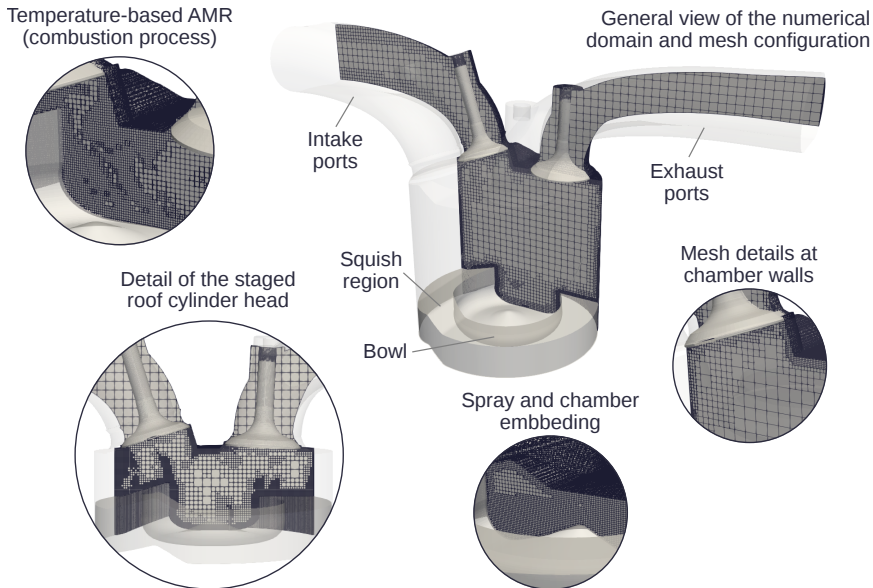
Figure 5.7: *Computational domain and mesh characterization of the 2-Stroke engine architecture.*

5.3. Gasoline Partially Premixed Combustion

As commented in Chapter 3, the experimental data for this study comes from a parallel research developed in the framework of the doctoral thesis of D. de Lima [119]. The 2-Stroke engine, also detailed in Chapter 3, was utilized during this study since it offers higher flexibility to operate under gasoline PPC conditions.

The numerical model used here is based on the grid configuration and the models utilized in the previous section (URANS-Coarse) while considering the 2-Stroke engine geometry displayed in Fig. 5.7. Nevertheless, a few changes where made in some injection-combustion parameters in order to asses the gasoline ignition features:

- A blend of 5% n-heptane and 95% iso-octane was utilized for predicting the physical properties of the gasoline fuel, being a suitable surrogate for predicting the ignition features of the RON95 gasoline used in experiments. Activating iso-octane reactions, the chemical mechanism resulted in a 45 species and 152 reactions.

- The injection rate was determined by the experimental data obtained with the injector characterization. This process measures the mass flow rate and spray momentum flux in a dedicated test rig [162, 163] for the injection configurations defined *a priory* in similar test conditions, in order to provide the most realistic injection characteristics.

Coupled with appropriate turbulence models, Kodavasal et al. [134] demonstrated that a similar combustion approach allows an accurate reproduction of gasoline autoignition, while other researchers [79, 82] established realistic rates of heat release under gasoline compression-ignited conditions.

5.3.1. Validation of a single operation condition

An operation condition defined by a medium speed and medium-high load, which corresponds with Point #7' in Table 3.4, was selected as a baseline for the model validation (further details about the engine settings are summarized in Table 5.4). This operating point was specifically chosen for the extremely high levels of noise registered during the tests.

A unique engine cycle was calculated in this case since the particular 2-stroke scavenge increases the simulation uncertainties. Although the need of performing several subsequent cycles to ensure a correct convergence of the fluid flow solution has been shown, the extremely sensitivity of the model to the scavenging parameters (instantaneous intake/exhaust pressures, valve timings, etc.) causes an unrealistic overestimation of the trapped mass after the simulation of the first cycle. Therefore, it was resorted to calculate a

Table 5.4: *Operating settings used for the model validation in gasoline PPC mode.*

Point	#7'[a]	#7$_1$	#7$_2$
Engine speed [rpm]	1500	1500	1500
Torque [Nm]	51.0	49.9	50.1
IMEP [MPa]	1.04	1.02	1.03
Number Injections [-]	3 (pilot + main + post)		
SoE$_{main}$ [cad aTDC]	-40.0	-42.0	-34.0
Injection pressure [MPa]	85	85	85
Intake pressure [MPa]	0.275	0.275	0.275
EGR [%]	43.53	43.66	43.56

[a] Baseline test.

complete single cycle but always assuring that the simulated trapped mass inside the cylinder at IVC is comparable to that estimated directly from the measurements.

The experimental and the simulated in-cylinder pressure traces of the baseline test are compared in the top graph of Fig. 5.8. As it can be seen, the CFD model correctly predicts the in-cylinder pressure. Indeed, the pressure prediction shows a similar deviation as measurements dispersion. The RoHR profiles show that the combustion phasing is slightly delayed and its peak value is minimally overestimated. However, these differences do not affect the maximum peak pressure in a significant way. This effect may be attributed to a minor underestimation of the effective compression ratio, given that the calculation of this parameter depends on material deformations and blow-by losses that the model does not take into account.

From the pressure spectrum side, included in the bottom graph of Fig. 5.8, the model is also capable of reproducing experimental trends in the whole broadband. Moreover, the characteristic frequency and the amplitude of the two first transversal modes are accurately estimated.

Due to the nature of subsequent studies presented in Chapter 8, an analysis of performance and pollutant emissions levels estimated by the CFD model has been included in Table 5.5. In general all simulated levels are in the same order of magnitude of experimental data. Soot values are, however, highly overestimated due to the simplicity of the soot oxidation model [151], thereby they will not directly be used in any of the studies that involve this specific engine and combustion mode.

The main limiting aspect of the methodology used here for the gasoline PPC concept validation is the incapacity to assess the cyclical deviation and its subsequent effects on the acoustic field.

In addition to the aforementioned restriction of a single cycle URANS simulation, the huge increase of computational burden hardly compromises the application of LES modelling in this situation. Furthermore, it is not clear that pure stochastic fluctuations could explain the whole variation of flow conditions among consecutive cycles in gasoline PPC mode.

Recalling the LES simulation used in Section 5.2, CCV effects are only remarkable when the diffusion flame is completely established and turbulent fluctuations provoke different heat release profiles from one cycle to other. A scarce dispersion is however observed during the auto-ignition event and later premixed combustion. Based on these observations, LES would neither be able to capture all CCV sources, thus evincing the existence of another relevant origin probably linked to operation conditions variability.
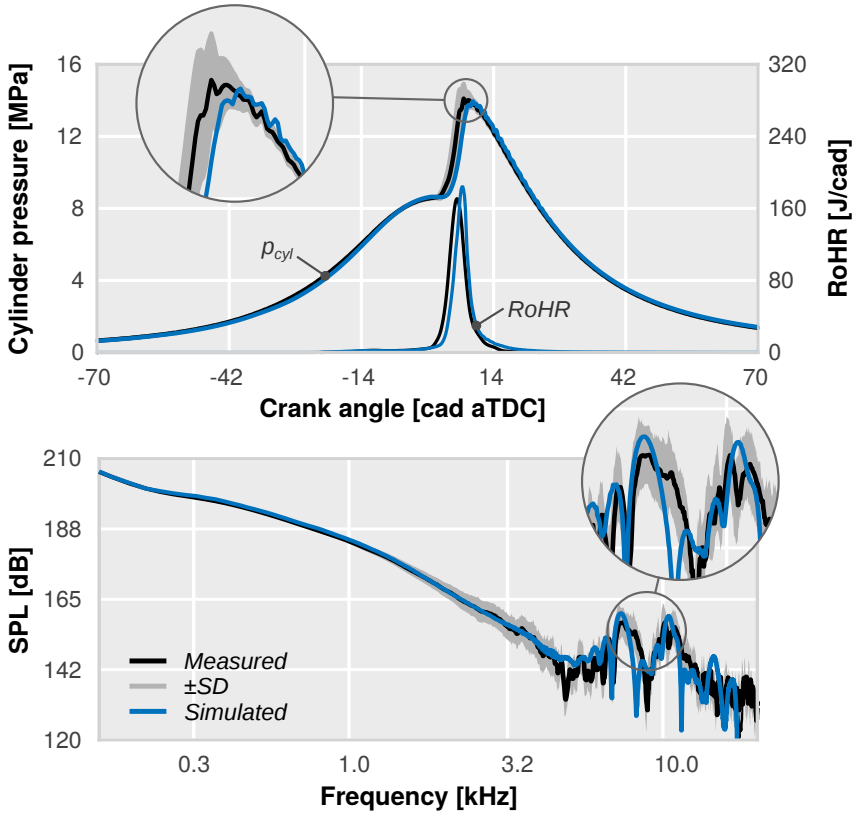
Figure 5.8: *Comparison between measured and CFD calculated results of baseline test, measurements dispersion is represented by their standard deviation (SD). In-cylinder pressure and RoHR traces are plotted at top whereas pressure spectra are drawn at bottom.*

Previous researches [164] claimed that CCV observed in CI engines is very low, if it is compared with SI engines, and mostly originated from the casuistic variability in fuel mass or trapped-gas conditions, rather than from arising in random variations in the turbulent flow and combustion process.

Hence, in a combustion process where the burning is essentially determined by the autoignition and premixed combustion without an established jet that could generate instabilities in the energy release, the application of LES models does not imply a significant advantage.

Other authors [65, 165] employed URANS to analyse CCV sources in several LTC strategies, where CCV is larger than CDC but still far from SI engines. They investigated the cyclical dispersion from the point of view of

Table 5.5: *Comparison of performance and pollutant emissions levels.*

	CFD	Experiment
η_i [%]	46.92	46.76
NO$_x$ [mg/s]	0.61	0.60
Soot [mg/s]	0.007	0.035
HC [mg/s]	12.03	9.14
CO [mg/s]	18.01	16.51

the operation uncertainties. The basis of their approach is to perform many parallel URANS simulations in which one or more key operating conditions are perturbed about the reference conditions.

Here, a new methodology based on this approach was used in an attempt of reproducing the experimental CCV and its effects on the acoustic field. Therefore the conditions at IVC of the baseline operating point were considered as the reference. Then, these conditions were artificially modified in order to imitate the variation of fuel mass, trapped mass, injection timing, etc.

In order to reduce the number of parallel simulations as much as possible, the selection of those parameters that significantly affect the combustion was made by taking into account the conclusions obtained by Klos and Kokjohn [165]. They found clear relationships among the dispersion of three operating parameters (EGR, mean gas temperature at IVC and fuel mass) and the combustion behaviour. Thus, these parameters and their recommended variations were utilized for modifying the IVC baseline conditions.

Nonetheless, an additional parameter must be considered in this study since the 2-stroke engine has a particular in-cylinder flow motion. While in traditional CI engines the flow spins in a plane parallel to the cylinder head (swirl motion), the flow describes a rotational path between intake and exhaust valves similar to that observed in SI engines (tumble motion). As reported by Vermorel et al. [116], tumble intensity significantly changes among consecutive cycles. They observed from LES simulations data that the magnitude of this rotational velocity could vary up to 25% at IVC. Therefore, this parameter was also included together with the other three determined by Klos. The parameters and their maximum variations used to perturb baseline conditions are displayed in Table 5.6. Note that EGR value was replaced by the percentage of combustion products within the cylinder at IVC, this is an equivalent parameter that define the amount of inert gases during the closed-cycle.

Table 5.6: *Baseline operation parameters and ranges of variation for the alteration of the IVC conditions.*

Parameter	Baseline	±	[%]
Combustion products [%]	36.70	1.0	2.7
T_{IVC} [K]	406.30	2.0	0.5
Tumble intensity [-]	4.31	1.1	25.0
Fuel mass [mg/cyc]	19.07	0.191	1.0

In addition to the baseline case, ten parallel closed-cycle simulations were performed. The initial conditions at IVC were accordingly perturbed by randomly distributed variations to sample the four-dimensional domain.

In Fig. 5.9, the same comparison previously done in Fig. 5.8 can be seen but including now the CCV spread of the simulations. The standard deviation of simulations is similar to that observed in the measurements in both temporal and frequency domains, proving the validity of the methodology in this particular case of study.

However, the interest of the analysis is not only to check the performance of the methodology to reproduce a realistic CCV but also to examine the effects of this variability on the acoustic field parameters. In order to accomplish this target, the overall noise and both maximum pressure rise rate and energy of resonance are plotted at each measured and simulated engine cycle in Fig.5.10. The standard deviation is also included to evaluate the capability of the methodology to reproduce CCV acoustic effects. Accurate results were obtained in terms of mean and dispersion levels for the overall noise. While the cycle-averaged noise level is almost coincident, the cyclical dispersion shows comparable values. Internal-related field parameters show similar encouraging results, without the same degree of exactitude, though.

The proposed methodology allows a realistic estimation of both the cycle-averaged and dispersion values of the main acoustic metrics. Thereby it offers the chance to include these parameters in the design process, optimizing them altogether with the rest of relevant emissions and performance metrics. However, further efforts must be taken to confirm, through LES simulations, that URANS is capturing all relevant phenomena in the combustion noise generation.
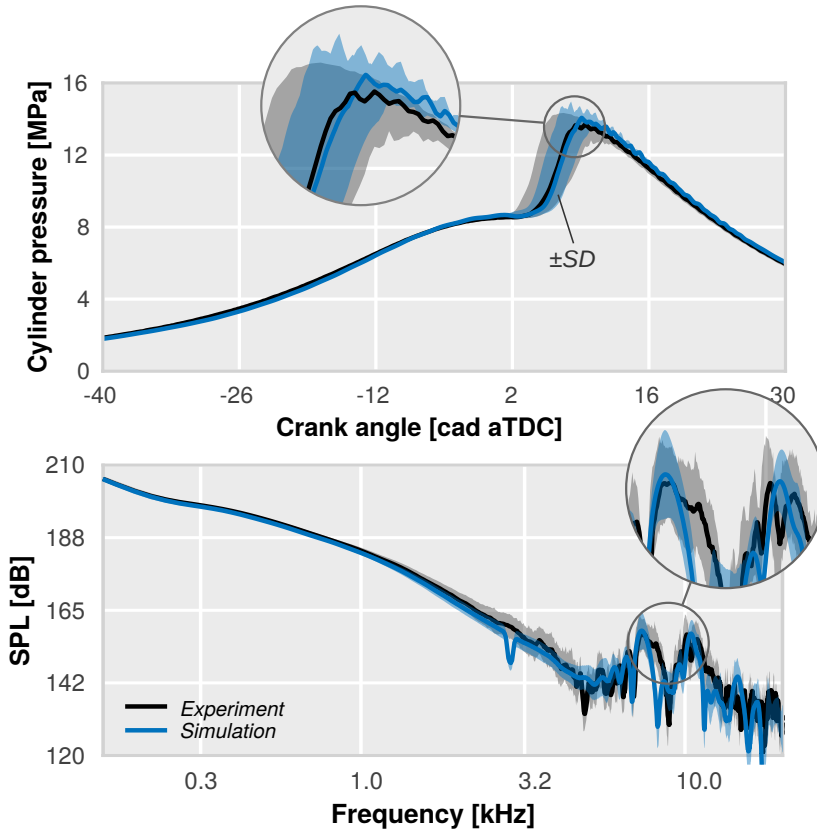
Figure 5.9: *Comparison between measured and CFD calculated results of baseline test, dispersion due to CCV is represented by their standard deviation value. In-cylinder pressure traces are plotted at top whereas pressure spectra are drawn at bottom.*

5.3.2. Validation of additional operation conditions

Two additional tests, also included in Table 5.4, were incorporated to evaluate the model performance in several operation conditions. In these two experiments, the timing of the main injection –defined by the Start of Energizing the injector (SoE)– was varied while the operation conditions were kept similar to the baseline.

Results were analysed through the three parameters shown in Fig. 5.11. These parameters, related to both the internal and external acoustic field, were plotted together with the experimental data obtained after the signals processing. This figure gives an overview of the trends followed by both results, specifically in terms of overall noise, maximum pressure rise
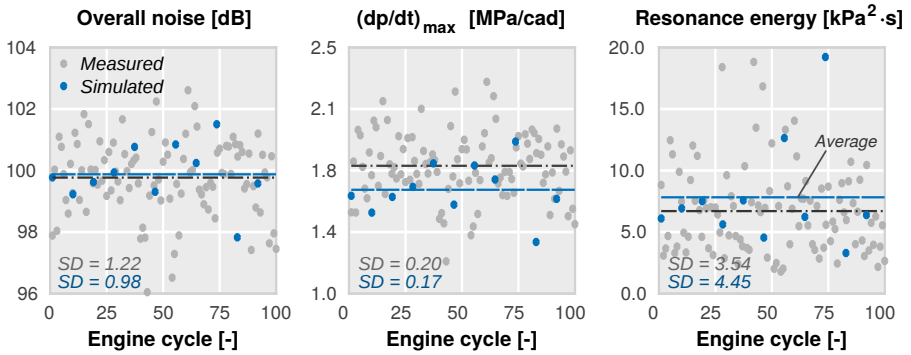
Figure 5.10: *Comparison between measured and CFD calculated results of base-line test, dispersion due to CCV is represented by their standard deviation value. Overall noise, $(dp/dt)_{max}$ and E_{res} are plotted to compare experimental and simulation results.*

rate $((dp/dt)_{max})$ and resonance energy at the transducer location (E_{res}). As it can be seen trends are reasonably captured by the model but some differences can be seen in point number #7_1 (SoE$_{main}$ = -42 cad aTDC). This could be attributed to the overestimation of the $(dp/dt)_{max}$ observed in the middle graph and its indirect effect on the rest of the parameters. However, taking into account that the model was not adjusted for the two extra operation points, the validation results are reasonably consistent with the trends followed by the measurements.

5.4. Conclusions

In this chapter numerical simulations of two different CI engines have been validated paying special attention to the spectral signature of the in-cylinder pressure field and its effects on the acoustic propagation, both regards usually overlooked in the majority of the works concerning the simulation of internal combustion engines.

An elaborated method to process the experimental data has also been presented in order to provide coherent-averaged data, being representative enough of the operating conditions, for the model validation.

It has been shown how URANS simulations offer a good estimation of in-cylinder acoustic field, resolving not only the pressure spectral content accurately but also predicting similar noise levels emitted by the engine. On the other hand, LES simulations have shown enhanced estimation of the cycle-to-cycle dispersion, especially when the fuel burning is dominated by the turbulent interaction within the spray, with an important counterpart in

terms of computational requirements. However, although URANS schemes are not able to reproduce the chaotic behaviour of the larger turbulent structures in the spray, an increase of the grid resolution specifically focused on these regions could help to capture some random combustion instabilities.

Further discussion on this regard suggests that the potential advantages of using LES as a turbulence approach to predict combustion noise in ICEs is, at least, questionable. Specifically in those combustion modes in which the burning rate is clearly controlled by chemical reaction timings (auto-ignition, premixed combustion, etc.), turbulence does not play a significant role and thus the use of more sophisticated models may not suppose a relevant advantage, especially in pure engineering applications.

In consequence, an alternative methodology has been developed to overcome the limitation for predicting CCV of URANS simulations. Examination of the results provided by this methodology, which is based on performing several parallel closed-cycle executions with different initial conditions, revealed really encouraging predictions of CCV in PPC conditions. Nonetheless, a further validation must be done by comparing URANS solution with LES results.

In summary, it has been proven that URANS simulations can be a useful tool to predict the noise generated by the combustion in CI engines, thereby using them together different optimiza-

Figure 5.11: *Validation trends of some relevant acoustic metrics for gasoline PPC concept. Overall noise, $(dp/dt)_{max}$ and E_{res} are plotted to compare experimental and simulation results.*

tion techniques for defining new combustion system designs, with optimal trade-off between consumption and both pollutant and noise emissions.

A detailed analysis of the local features and their contribution to the noise generation mechanisms of both URANS and LES solutions is nonetheless needed in order to further confirm the conclusions reached in this chapter

about the influence of CCV in acoustic prediction by numerical simulations, especially in the case of CI engines where the cost of multi-cycle LES appears to be questionable due to the extremely low cyclical dispersion.

Noise in conventional Diesel combustion

Once that the CFD model has been validated, the CFD solution can be used to visualize some physical phenomena that are impossible to be seen experimentally. For instance, numerical solutions traditionally allowed an easy visualization of elusive processes inside combustion chambers where it is extremely complex to access by optical techniques.

Here, the numerical model is utilized to provide more insight about combustion noise issues in CI Diesel engines and therefore, to give an enhanced comprehension of noise generation mechanisms. In the first place, an extended analysis of the in-cylinder pressure spectral content is presented in order to identify the principal sources of noise within the chamber. After that, CFD simulations are used to further understand such combustion related phenomena that contribute to the noise generation. In order to reach these targets, the unsteady behaviour inside the combustion chamber is studied by analysing the numerical results through the application of different flow decomposition techniques, aiming to resolve the underlying modal structure of the process.

Work in this chapter has been partly published in the following papers:

- *Understanding the unsteady pressure field inside combustion chambers of compression-ignited engines using a CFD approach* [11]

- *Modal decomposition of the unsteady flow field in compression-ignited combustion chambers* [5]

- *Experimental Analysis of Cyclical Dispersion in Compression-Ignited Versus Spark-Ignited Engines and Its Significance for Combustion Noise Numerical Modeling* [8]

6.1. Analysis of combustion noise origin

Using the LES model set-up described in Chapter 5, a simulation of the operating point number #7 was performed to further analyse the origin of combustion noise. Four consecutive cycles were computed in order to assure statistically valid results. Although it may seem a low number, it has been demonstrated how four realizations show CCV levels comparable to those displayed by the experiments.

Moreover, since there is still no certainty that URANS is capable of reproducing all phenomena involved in the combustion noise generation, it was deemed LES as the appropriate approach for characterizing the noise source. Nonetheless, a comparison of the solution achieved by both approaches will be done in a following section in order to establish which are the possible advantages of using URANS instead of LES modelling.

6.1.1. Identification of combustion noise sources

A series of snapshots were conscientiously chosen and plotted together in Fig. 6.1 for studding the combustion process and its effects on the internal pressure field. They were specifically selected considering different stages of combustion to allow a better comprehension of the interaction between pressure waves and the combustion process itself.

In this figure, the pressure field (pressure oscillation) is depicted in a slide perpendicular to cylinder axis and located 5 mm away from cylinder head. The colour scale was carefully fixed for a proper visualization of every pressure fluctuation. In addition, the blue edge also included establishes the borderline from which the pressure oscillation is bounded between 0.1 and 0.15 MPa, both values were subjectively selected by taking similar values to the oscillations observed in the raw pressure trace to ensure a clear visualization of those waves which become dominant. This helps to easily identify and compare the magnitude of each pressure fluctuation observed inside the chamber. The sprays are visualized by clipping the temperature at 2200 K and colouring them by the same temperature field, thus showing the reaction surface enclosing the spray. Finally, the energy release profiles are also plotted to distinguish at which step of the combustion is each snapshot it can be seen.
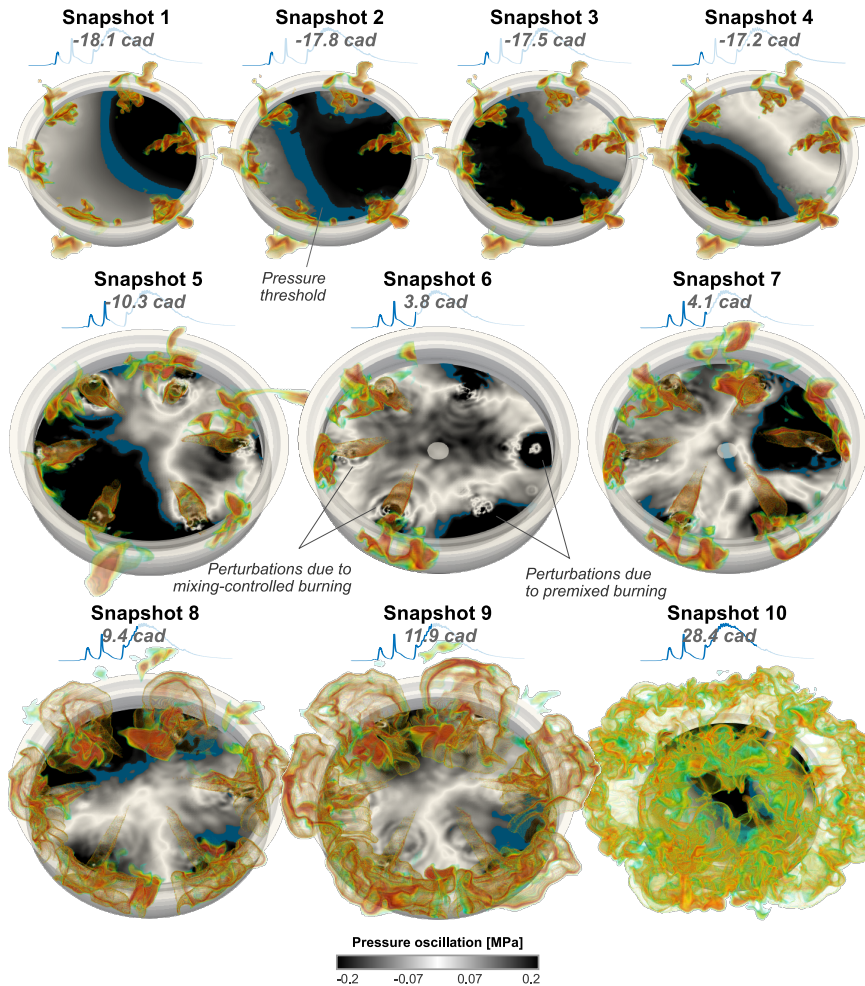
Figure 6.1: *Pressure field visualization along the combustion process. The spatial averaged pressure evolution in the chamber is subtracted in order to clearly observe the unsteady pressure fluctuations. The spray plumes are also included by clipping the temperature at 2200 K to identify the origin of pressure oscillations.*

Once fuel is injected inside the chamber, a region with high reactivity is formed at the end of the spray plume. The air-fuel mixture within this region is rapidly consumed after the spontaneous ignition, causing a sudden energy release. Then, if the fuel is still being injected, a stationary jet is established and the burning rate is now dominated by the turbulent transport.

In both combustion stages, the energy release causes an increase of temperature that subsequently contributes to rise the mean pressure of the chamber whereas the structure of the pressure field is changed.

Snapshots displayed on the first row of Fig. 6.1 show the instants after the first pilot ignition, in which practically all fuel is consumed under premixed conditions. It can be seen from this sequence how a pressure wave is travelling from the top-right to the bottom-left side of the chamber. As soon as this wave reaches cylinder walls it is reflected, producing a standing wave that modifies local pressure magnitudes following the already known oscillation patterns [50]. It is important to note that this resulting wave collapses the colour scale, thus evincing that its amplitude is, at least, similar to the mean oscillation size observed in the transducer-registered signal.

After this first combustion stage, the second pilot burning, again mostly developing under premixed conditions, contributes to enhance the generated standing wave. As can be seen in the first snapshot of the second row, the narrowing of the blue borderline suggests an increase of the wave sharpness and consequently an increment of the maximum amplitude.

The following snapshot, which is focused on the premixed phase of the main injection burning, shows a particular and interesting phenomenon. Here, it is possible to identify the local pressure rise generated by the jets due to the premixed combustion.

Focusing on the right side of the snapshot, in which the sprays are removed for a better view of waves generation, it can be seen how pressure waves produced at this stage practically reach the amplitude of the borderline. The location of the referred sprays –within the exhaust side of the chamber– suggests that there are significant differences in the spray ignition sequence. The jets positioned at the exhaust side of the chamber ignites earlier contributing not only to the unsteadiness of the in-cylinder pressure field but also to generate multiple asymmetries.

From here to the end of combustion, the pressure field becomes slightly different and other acoustic sources appear. As it becomes evident in snapshots 6 to 10, the heat release by the stabilized flame results in a fluctuating density that generates additional pressure waves. The turbulent interaction between the chamber atmosphere and jets acts as a supplementary source of pressure perturbations which contribute to the combustion acoustics in a similar way to what occurs in continuous flux combustors [27, 40, 166]. While snapshot 6 show these secondary waves emerging from the residual jets of the second pilot injection, snapshots 7 to 9 depict the same structures during the main injection.

Nevertheless, the standing wave generated during previous stages clearly remains as the largest pressure perturbation inside the cylinder since the maximum amplitude of these secondary oscillations are almost an order of magnitude smaller. In addition, while the standing wave persist during the whole combustion process and even when the fuel injection has finished (see snapshot number 10), jet-induced oscillations are rapidly attenuated and they seldom reach to sweep the entire chamber.

Consequently, the contribution of these jet perturbations to the overall acoustics should be very small if it is compared not only with the uniform pressure rise but also with the resonant standing waves.

6.1.2. Effects of turbulence on combustion noise sources

Although in Chapter 5 it has been showed that URANS schemes offer a good estimation of in-cylinder acoustic field, it is still unclear if they are able to reproduce all combustion features previously seen in LES. Therefore, a comparison of both solutions is presented in this section with the target of determining the main differences among both modelling approaches.

As in Fig. 6.1, the pressure gradient at a given plane is again utilized to visualize the unsteady field in Fig. 6.2. Three snapshots were specifically chosen to compare both solutions. For this analysis, LES is contrasted against the URANS-fine configuration already described in Chapter 5. Since both configurations have similar grid sizes, this comparison assures that solution differences are only due to the turbulence modelling instead of grid resolution changes.

The first snapshot of this figure shows the spatial distribution of the pressure gradient after the first pilot burning. It can be seen how the standing wave is well-captured by both simulations, showing very similar spatial patterns.

However, the second set of snapshots which correspond with the transition between premixed and diffusion phases of the main injection burning evinces some relevant differences. As commented before for LES, the premixed combustion generates a rise of the local pressure at the end of spray plumes. Moreover, several sinks of pressure waves are located inside the jets. As the latter set of snapshots reveals, the number of these sinks increases within the spray as the diffusion flame is completely established, forming the oscillating structure already reported in several works [167, 168]. This structure is characterized by opposed amplitude regions along the spray axis as result of an helical 3D oscillation pattern [169, 170].
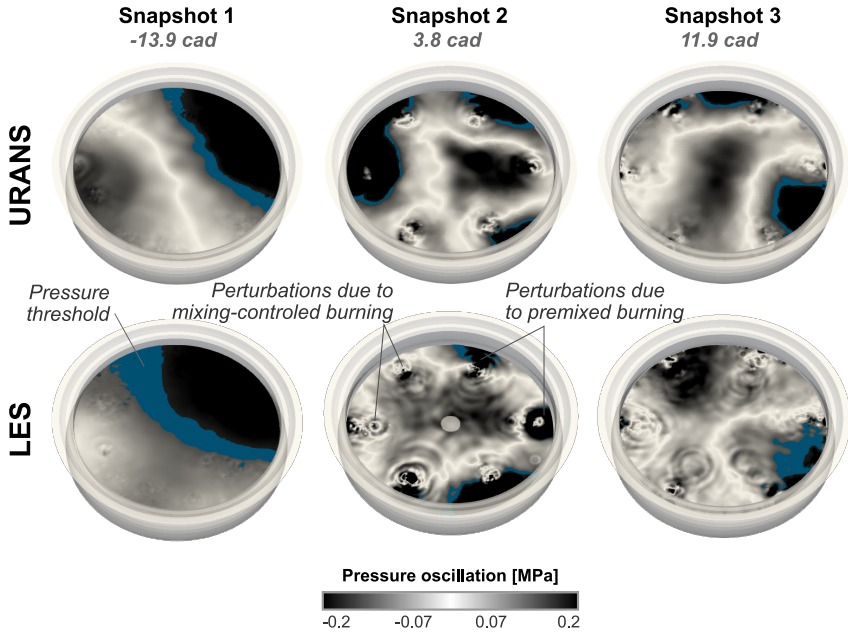
Figure 6.2: Comparison of pressure field prediction using URANS and LES simulations. The spatial averaged pressure evolution in the chamber is subtracted in order to visualize unsteady pressure fluctuations.

Focusing on URANS solution, the equivalent instants are slightly different. While the localized pressure increment as a result of the premixed burning closely resemble (in both pressure amplitude and location) to that observed in LES, spray pressure sinks are not clearly appreciated, at least during the transition between combustion regimes displayed in the second set of snapshots.

The internal structure of sprays are however quite similar once the diffusion regime is fully stabilized. As it can be seen from the last snapshot of the URANS solution, pressure patterns are comparable between both solutions.

Although these perturbations generate a series of small pressure waves in the spray surroundings of the LES solution, they are rapidly attenuated in the URANS case, being especially difficult to visualize them if the colour scale is kept between simulations. Since the grid resolution is similar in both set-ups, the reason behind this high dissipation rate is probably attributed to the traditional viscosity overestimation shown by URANS schemes.
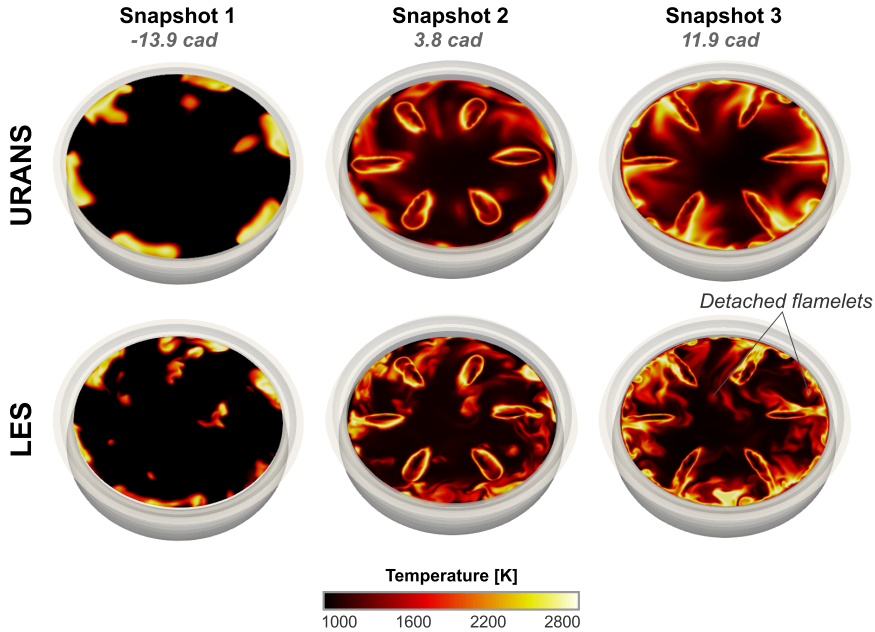
Figure 6.3: *Differences in local temperature field using URANS and LES approaches. Temperature contours are depicted at specific snapshots and planes.*

Despite this fact, the standing pressure wave developed during the first stages of combustion is still appearing in both solutions with similar magnitudes, evincing again the small relevance of these jet-induced perturbations in CI combustion acoustics.

In order to examine the differences in the combustion process itself, temperature contours at the same snapshots/planes considered in the previous figure are included in Fig. 6.3.

Here, the number of dissimilarities is considerably higher. While the flame movement owing to larger turbulent scales are clearly visible in LES, such details are smoothed out in the URANS solution being less evident.

A result of the interaction between the spray, in-cylinder flow and chamber walls, the flame structure is deformed in such a way that some flame sections come completely detached. As a consequence, the isolated hot spots are moved by turbulent vortexes, drawing the characteristic movement of the eddy wakes viewed in LES snapshots.

In the URANS case, these structures are not captured at the same level but they still give an idea about how the temperature field is changing. For instance, the anti-counter-clock wise swirl movement is evident in both solutions whereas flame frame at near-wall locations closely resemble.

6.2. Analysis of in-cylinder pressure field

Despite the fact that the previous study allowed to distinguish all combustion noise sources clearly, the contribution of each of them to the overall acoustic signature has not been appropriately quantified.

With the aim of establishing the significance of these noise sources, a detailed study of in-cylinder pressure field was carried out in order to support previous conclusions and to gain further knowledge about this elusive topic.

The singularity of in-cylinder field however demands a more complex analysis and very specific post-processing techniques which permit to link both the temporal and frequency variation of the pressure with a specific position inside the chamber.

Since there are several methods that specifically match with this kind of analyses, the formulation of each one and the results obtained from its application are included in the following sections with the purpose of evaluating their potential benefits.

6.2.1. Data preparation

Generally, the information on the flow field evolution coming from numerical simulations or experimental data[1] will be naturally presented in a sequence of N vectors $\mathbf{v}_i$ representing temporal snapshots that can be gathered in a matrix $\mathbf{V}$:

$$\mathbf{V}_1^N = \{\mathbf{v}_1, \mathbf{v}_2, \ldots, \mathbf{v}_N\} \tag{6.2.1}$$

Each snapshot contains a quantity M of scalar flow magnitudes which in the case of experimental results usually represent the velocity information. In the case of numerical simulations these snapshots may represent other useful information such as pressure, species, etc. These snapshots should be separated by a constant time step Δt.

Results from the simulation were exported by means of a custom UDF (User Defined Function). After each simulated time step converged, pressure data was saved to a text file, each row containing cell centroid coordinates x, y and z and corresponding pressure p.

---

[1]For instance, from experimental Particle Image Velocimetry (PIV) measurements that capture a sequence of velocity field snapshots.

However, it must be taken into account that the CFD code automatically refines or coarsens the mesh as the simulation advances, in order to optimize solving time. Cells are also dynamically created and destroyed as the cylinder moves. As a consequence, cells are not necessarily preserved across snapshots.

It was thus necessary to perform a preliminary post-processing step in order to obtain coherent pressure records. A reference snapshot was first chosen, and then a subset of 10^5 random cells was selected from it in order to speed computations while still ensuring a good spatial resolution.

The rest of the snapshot files were then scanned to find the best match for the selected reference cells. Given each snapshot i, this best match for each reference cell j was determined by calculating the squared Euclidean distance between the reference cell and the entire set of cells of the snapshot:

$$\mathbf{d}_{i,j}^2 = \left(\mathbf{X}_i - x_j^{\text{ref}}\right)^2 + \left(\mathbf{Y}_i - y_j^{\text{ref}}\right)^2 + \left(\mathbf{Z}_i - z_j^{\text{ref}}\right)^2 \qquad (6.2.2)$$

In the next step, $\min(\mathbf{d}_{i,j}^2)$ is evaluated. If $\min(\mathbf{d}_{i,j}^2) = 0$, at position k, a cell exists in snapshot i that exactly matches the reference cell j, and thus its pressure value p_k is added to the global snapshot matrix, $\mathbf{V}(j,i) = p_k$.

However, it could happen that $\min(\mathbf{d}_{i,j}^2) > 0$, this is, that no exact cell match is found for the previously mentioned reasons of mesh refinement or coarsening and of piston displacement. In order to differentiate between both issues, a maximum cell centroid displacement $d_{\text{c,max}}$ due to refinement and coarsening can be calculated taking into account CONVERGE input parameters L and r:

$$d_{\text{c,max}} = \sqrt{3\left(\frac{L}{2} - \frac{L}{2^{r+1}}\right)^2} \qquad (6.2.3)$$

The derivation of this expression is exemplified in Fig. 6.4. If $\min(\mathbf{d}_{i,j}^2) \leq d_{\text{c,max}}$, at position k, then cell k is related to reference cell j through a mesh refinement or coarsening process and its pressure value p_k is again stored at $\mathbf{V}(j,i)$.

If however $\min(\mathbf{d}_{i,j}^2) > d_{\text{c,max}}$, it can be concluded that the position of reference cell j has been blocked by the piston in snapshot i, and thus the pressure record at that location cannot be used. A NaN value is then stored in $\mathbf{V}(j,i)$.
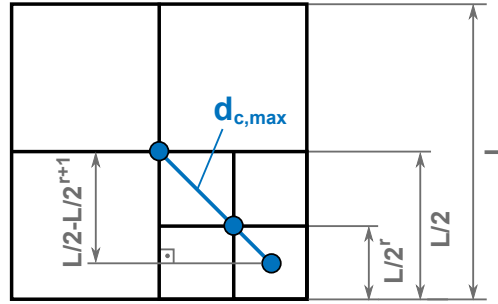
Figure 6.4: *Simplified example of the maximum allowable centroid distance during the cell search process, for the case of $r = 2$ in 2D. Extension to 3D cubic cells is straightforward.*

Finally, rows of **V** containing NaNs are culled, thereby obtaining an snapshot matrix **V** of continuous pressure records at approximately constant spatial positions, suitable to apply the discussed post-processing techniques. As CONVERGE may sometimes introduce NaNs as well, this step ensures that the data is valid for further post-processing.

It should also be mentioned that if the simulation was carried out with a variable time step to optimize the computation speed, an additional interpolating step must be then performed in each row of **V** to obtain snapshots that are equally sampled in time.

The use of monitor points randomly allocated in the combustion chamber may simplify this step, allowing an easy way to link the temporal pressure evolution with the location in which it is registered.

6.2.2. Fourier analysis

A way to explore the spatial distribution of the acoustic flow field for different frequency-related phenomena of interest is to perform the Fourier transform at each cell record in the considered domain. Then, the amplitude of the transformed signal at the frequency of interest is used to colour each cell, be it directly or through a smoothing interpolation.

This technique can be exploited in an attempt to identify the aforementioned actual modes of the combustion unsteady field. The spatial representation of selected Fourier traces that are manually selected based on inspection of the spectra can give a hint at the influence of the chamber geometry on the pressure oscillation patterns.
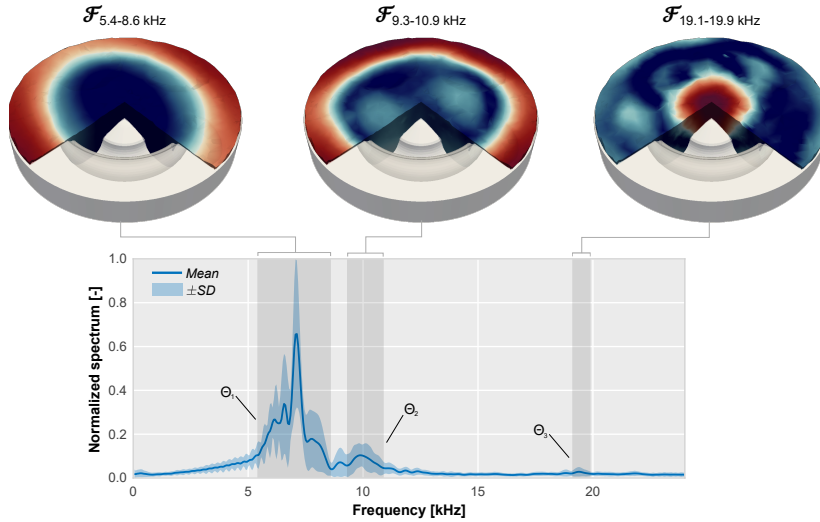
Figure 6.5: *Fourier analysis of the combustion pressure signal. Pressure spectrum, averaged across all selected cells in the domain, is plotted along its standard deviation (SD). Three characteristic "bumps" are identified and marked, accompanied by the spatial distribution of the Fourier transform restricted to each selected frequency range.*

However, while this Fourier analysis method allows the obtaining of interesting results in a simple, straightforward way which moreover can be found already implemented in some commercial CFD codes, it is not free of disadvantages.

Among them is the need to manually select the frequencies of interest, thereby having the risk of missing relevant frequencies, which are not known beforehand. Time evolution of these spatial features is also lost unless Short-time fast Fourier transform (STFFT) is attempted, at the cost of losing frequency resolution. Also, in more complex geometries or flow structures such as those of turbulent jet ignition (TJI) chambers, it could be difficult to exactly pinpoint relevant features, requiring specific and intricate visualization methods to reconstruct these modal structures.

Hence, with the aim of giving a first method to quantitatively examine the unsteady field responsible for acoustic emissions, a frequency analysis was performed by following the outlined procedure in which resonant modes and their spatial distribution are identified through pressure spectra inspection.

The interest of the analysis is focused on the medium-high frequencies, in whose spatial modes particular pressure distributions and their acoustic contribution can play an important role. Therefore, the homogeneously-

distributed, steady pressure evolution was subtracted from each cell pressure record in order to focus on the unsteady phenomena propagating in the chamber.

Once this procedure was applied to all rows of **V** matrix, the Fast Fourier Transform was applied to every resulting pressure signal at each considered cell. Results are presented in Fig. 6.5, in which pressure spectra were averaged across all selected cells in the domain and its standard deviation is displayed to denote the spatial variation of the pressure oscillations.

Three distinct "bumps" are noticed and their associated frequencies can be identified, similar to the work of Torregrosa et al. [52]. These allow to obtain the Fourier transform restricted to each cell and selected frequency band and, hence, the spatial distribution of the resonant modes can be visualized through the volume renders displayed in Fig. 6.5 (top).

Mode Θ_1, located between 5.7 – 8.5 kHz, is clearly the most relevant among all the identified ones. The reflection of the pressure waves in the transversal direction makes this mode essentially a transversal mode with a single node line. Therefore, the higher amplitudes are oppositely localized in the squish zone of the chamber.

The second (Θ_2) and third (Θ_3) resonant modes seem to be gathered at 9.3 – 10.9 kHz and 18.9 – 20.1 kHz, respectively. Their amplitudes are significantly lesser, especially in the case of Θ_3. The second resonant mode results from interaction among the oscillations which are excited in the squish and also inside the bowl. The higher amplitudes are established near the cylinder walls as in Θ_1, but in this case, an additional source of oscillations is located within the bowl.

In contrast with the previous modes, the highest frequency mode oscillations are aligned according to the symmetry of the combustion chamber, showing an annular node region, and its oscillation pattern seems to be focused inside the bowl.

6.2.3. Proper Orthogonal Decomposition

In order to address limitations evidenced by the Fourier analysis, more sophisticated analyses can be carried out to obtain the modal decomposition of the unsteady pressure field. One of the most used among these is probably the Proper Orthogonal Decomposition (POD), also called Principal Component analysis (PCA) or Karhunen–Loève expansion [171], which originated in the field of probability theory and was first applied to the analysis of tur-

bulent flow in 1967 [172]. As (rather poetically) put by Aubry in the aptly named paper *"On the Hidden Beauty of the Proper Orthogonal Decomposition"* [173], the objective of this technique is that:

> *"The flow is decomposed into both spatial and temporal orthogonal modes which are coupled: each space component is associated with a time component partner. The latter is the time evolution of the former and the former is the spatial configuration of the latter."*

Thereby, this decomposition allows the identification of which spatial structures comprise the most energy of the flow field, which is understood as the superposition of all modes. The ordering of the contribution of each mode however, allows in principle a simplified yet meaningful reconstruction of the flow field.

POD can then be realized by diagonalizing the time-averaged spatial correlation matrix $\mathbf{V}^\mathrm{T}\mathbf{V}$ [174, 175], by solving its associated eigensystem. However, $\mathbf{V}^\mathrm{T}\mathbf{V}$ can be very large, so an alternative approach is generally preferred, based on the Singular Value Decomposition (SVD) of $\mathbf{V}$: [176, 177]

$$\mathbf{V} = \mathbf{U}\mathbf{\Sigma}\mathbf{W}^\mathrm{T} \tag{6.2.4}$$

In this way, $\mathbf{U}$ is an $M \times N$ matrix[2] whose columns contain the so-called POD spatial modes $\mathbf{\Psi_i}$ (or left-singular vectors) that form an orthonormal basis of $\mathbf{V}$. These are also the eigenvectors of $\mathbf{V}^\mathrm{T}\mathbf{V}$, hence the validity of this alternate approach.

Next, $\mathbf{\Sigma}$ is an $M \times N$ diagonal matrix whose non-zero elements are the principal values σ_i of $\mathbf{V}$, which correspond to the squared eigenvalues of $\mathbf{V}^\mathrm{T}\mathbf{V}$. They represent the contribution of each mode $\mathbf{\Psi}_i$ to the total energy of matrix $\mathbf{V}$, defined by Nikiforov [178] as $\sum \sigma_i$. Thereby, they indicate the relevance of each orthonormal mode in the total flow field.

Finally, $\mathbf{W}$ contains the right-singular vectors of $\mathbf{V}$, so therefore the rows of $\mathbf{\Sigma}\mathbf{W}^\mathrm{T}$ describe the temporal evolution $\mathbf{a}_i(t)$ of the contribution of each spatial mode $\mathbf{\Psi}_i$, and thus the flow field can be described as a linear superposition of spatial and temporal information:

$$\mathbf{V}(\mathbf{x}, t) = \sum_{i=1}^{N} \mathbf{\Psi}_i(\mathbf{x})\, \mathbf{a}_i(t) \tag{6.2.5}$$

---

[2]If the "economy" version of the SVD algorithm is used in order to optimize computation time.

The main advantage of the POD method is its capacity for dimensionality reduction. If the total flow field is reconstructed following Eq. 6.2.5 but with a reduced $L < N$ number of modes, the reconstructed flow field $\widetilde{\mathbf{V}}$ is the closest one to the original, in the sense that the Frobenius norm of the difference between the original and the reduced field is the minimum achievable for a reduced $\widetilde{\mathbf{V}}$ of rank L.

This can be proved by realizing that the partial summary reconstruction is equivalent to forming a reduced $\widetilde{\mathbf{\Sigma}}$ with $\sigma_i = 0$ when $L < i < N$ and then obtaining $\widetilde{\mathbf{V}} = \mathbf{U}\widetilde{\mathbf{\Sigma}}\mathbf{W}^{\mathrm{T}}$. The Eckart–Young theorem [179] ensures that a matrix of rank L reconstructed in this way minimizes $||\mathbf{V} - \widetilde{\mathbf{V}}||_{\mathrm{F}}$.

For many applications, especially in the field of computational fluid dynamics where simulations feature very large matrices, dimensionality reduction is crucial in order to facilitate further use of the results such as vibroacoustic propagation, structural mechanics, aeroelasticity simulations, or preparing inlet conditions for Large Eddy Simulations [180, 181].

Principal drawbacks of this method include that in some cases energy may not be the most relevant metric in characterizing the relevance of flow structures [174], and that the use of second-order flow statistics can result in a loss of information such as phase [173], failing to capture the dynamics of the coherent structures of the flow [182].

Moreover, while modes resulting from POD exhibit spatial orthogonality, they can contain multi-frequency temporal content [183, 184]. This means that a particular flow structure can be excited by different phenomena and at different frequencies, yet remain spatially coherent in time and thus result in a higher energy POD mode.

Linking the unsteady spatial structures with a specific phenomena requires, as a consequence, some guesswork based on prior knowledge of the excitation mechanisms. A good example of this is the application of POD to the CFD simulation of an engine manifold presented by Sakowitz et al. [184], where it can be seen how the first POD mode contains different frequency content originated from both the engine firing and the valve opening. However, the combustion chamber itself is not included in their work.

Other authors have applied POD to combustion processes, be it through CFD simulations [185], or experimentally obtaining the flow snapshots with the aid of optical techniques such as PIV [186–189], chemiluminiscence [190] or raw luminosity [191], but most of these results are restricted to continuous combustion cases such as those of gas turbines or industrial
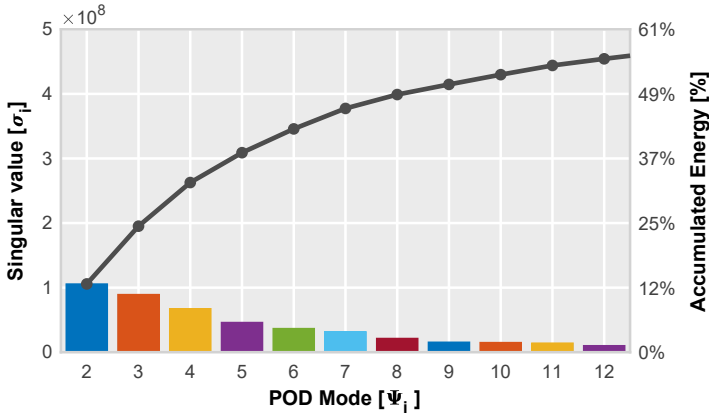
Figure 6.6: *Pareto chart showing the singular values associated to POD modes* Ψ_{2-12} *and the accumulated contribution to the remaining energy after* Ψ_1 *is disregarded (since it only contains the well-known information of the homogeneous mean pressure).*

burners, focusing on the thermoacoustics originated by the open flame oscillations and not on the more explosive, confined acoustics of reciprocating ICE combustion chambers.

Although some authors have specifically addressed ICE combustion issues through POD, these studies have been focused on cycle-to-cycle variation analysis [191–193], spark-ignition misfires [194] or the evolution of a particular species [195], whereas the pressure resonance issues of CI combustion chambers addressed in this work has not been yet investigated using this method.

Proper Orthogonal Decomposition was then performed as described above. Orthonormal POD modes Ψ_i and their corresponding principal values σ_i were obtained, together with temporal evolution coefficients $\mathbf{a}_i$.

In order to characterize the relevance of each mode, their contributions to the total energy of the snapshot matrix are computed with the help of the principal values. Since the mean pressure evolution in the chamber is not subtracted, the first spatial mode Ψ_1 is homogeneously distributed through the chamber, with its singular value σ_1 representing 97.5% of the matrix energy.

As in this section the main interest lies in extracting the unsteady behaviour of the combustion itself, rather than that of the compression-expansion cycle, the first mode related to the mean homogeneous pressure can be disregarded. The remaining energy is thus distributed among the subsequent modes as shown in the Pareto chart of Fig. 6.6.

It can be seen in this figure that POD modes Ψ_{2-12} gather approximately 54% of the remaining energy, with 50% being gathered by modes Ψ_{2-9}. Although not shown in the graph, 80% of the remaining energy is represented by modes Ψ_{2-32} and finally modes Ψ_{2-154} sum up to 99%. The rest of the modes $\Psi_{155-215}$ represent just 1% of the remaining energy, demonstrating the usefulness of POD for dimensionality reduction.

Besides the scrutiny of the singular values to measure the overall energy contribution of each mode, the information contained within the time coefficients $\mathbf{a}_i = \sigma_i \mathbf{W}_i^{\mathrm{T}}$ allows the analysis of the evolution of each mode in the time and frequency domains.

In Fig. 6.7 the normalized time coefficients $\mathbf{a}_i(t)$ of POD modes Ψ_{1-12} are plotted for each time step of the CFD simulation. Mode Ψ_1 has been independently scaled with $\max(\Psi_1)$ to allow its representation along the rest, while each remaining mode Ψ_{2-12} has been scaled with $\max(\Psi_{2-12})$ in order to preserve the scaling between them due to their corresponding singular values σ_i.

It is clear from the figure that, while Ψ_1 describes the smooth evolution of the mean pressure in the chamber, the rest of the modes describe the acoustic instabilities associated to the combustion process. This is made more evident in Fig. 6.8 where the frequency content associated to each mode is presented.

Inspecting the time evolution of the POD modes shown in Fig. 6.7, clear relationships can be found between the inception of the modes and the timing of the combustion of the different injections of the cycle, denoted in the figure by C_{1-3}. These instants have been found by calculating the time step at which 10% of the fuel of each injection is consumed.

From the zoomed-in detail view included in the figure, it can be easily seen how the onset of modes $\Psi_{2,3,4}$ is coincident with the time of C_1, although the amplitude rise is much more pronounced in the dominant mode Ψ_2 while in mode Ψ_4 the time evolution is more progressive. On the other hand, mode Ψ_5 shows little relevance after C_1, only exhibiting a sudden rise in amplitude at the precise time of C_2. None of these first 12 modes seems to be triggered by C_3, confirming the preponderance of C_1 and C_2, purely premixed burnings, in creating the resonant field.

This coupling between the different burning times and the onset of different POD modes offers valuable insight into the acoustic effect of each separate fuel injection into the chamber, which will be useful when combined with the analysis of the spatial distribution of the modal energy.

Regarding now the frequency domain, periodograms shown in Fig. 6.8 have been obtained from the right-singular vectors $\mathbf{W}^{\mathrm{T}}$ avoiding the scaling by σ_i, in order to better visualize the spectral content of the higher order modes that would appear flat if $F\{\mathbf{a}_i\}$ had been used instead. Again, mode Ψ_1 is scaled independently from the rest, being clear in this figure that it contains the frequency peak corresponding to the compression-expansion process.
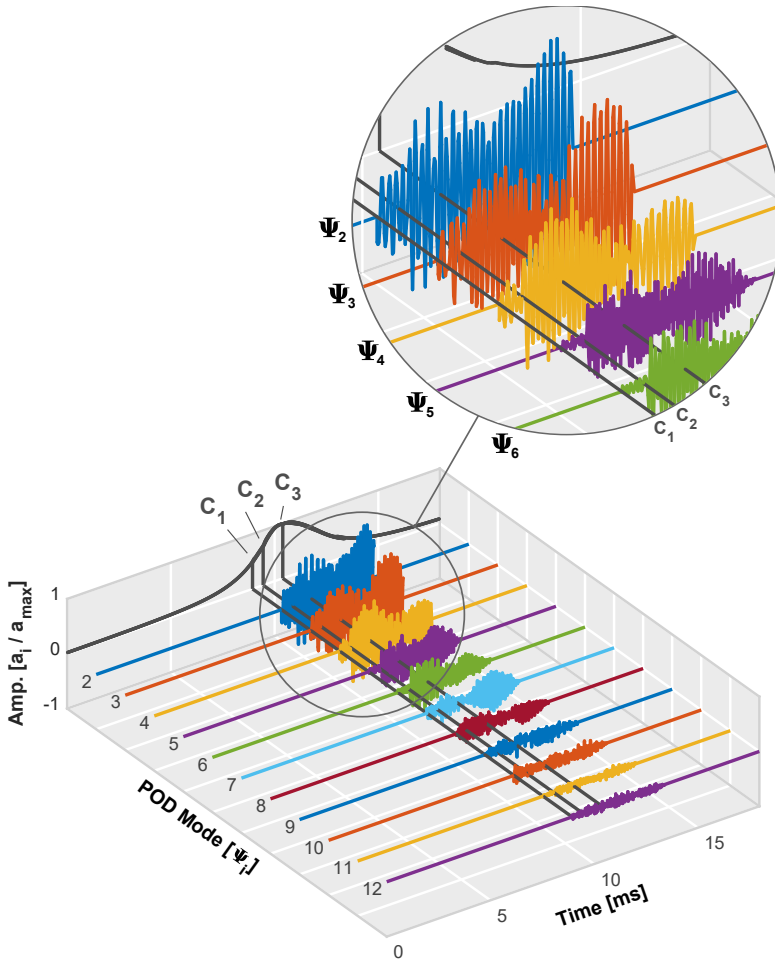
Figure 6.7: *Normalized amplitude of POD modes Ψ_{1-12} in the time domain, based on normalized time coefficients $\mathbf{a}_i$. Ten percent fuel burning times C_i for each of the three combustions are included for reference.*
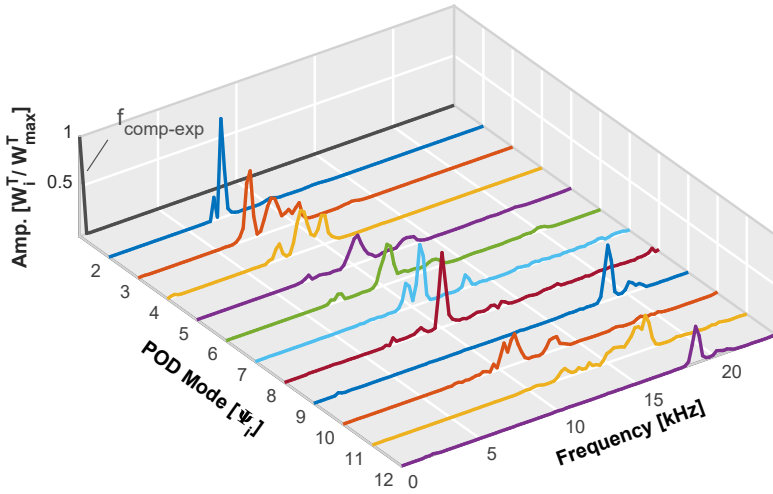
Figure 6.8: *Normalized amplitude of POD modes Ψ_{1-12} in the frequency domain, based on normalized periodograms of right-singular vectors $\mathbf{W}_i^T$. Scaling by singular values is avoided to allow a better visualization of the spectral content in higher order modes.*

For the majority of reciprocating thermal engines, this mean pressure pulsation Ψ_1 is of very low frequency, and thus near or even below the human hearing threshold, diminishing its relevance when analysing the acoustic output of the engine.

However, as seen in Fig. 6.8, the frequency content of the successive modes is concentrated well into the human hearing range, at 5 – 12 kHz in this particular simulation. It can also be seen how, as previously mentioned, each POD mode can feature various frequencies of interest, making it difficult to ascribe a particular mode to a given phenomenon of known frequency, except in the case of Ψ_1.

Finally, the spatial distribution of the POD modes can be inspected, by plotting the values of the left-singular vectors Ψ_i contained in the columns of $\mathbf{U}$ associated with each of the reference coordinates that were selected when building the snapshot matrix $\mathbf{V}$.

There are many ways of plotting the modal spatial information, such as slices at certain selected locations, isovolumes of a certain value, translucent volume rendering, etc. In Fig. 6.9, a set of isosurfaces is used to display POD modes Ψ_{1-12}, by showing the upper and lower 10% tails (this is, the 10% and 90% percentiles) of the distribution of their real values $\Re\{\Psi_i\}$.
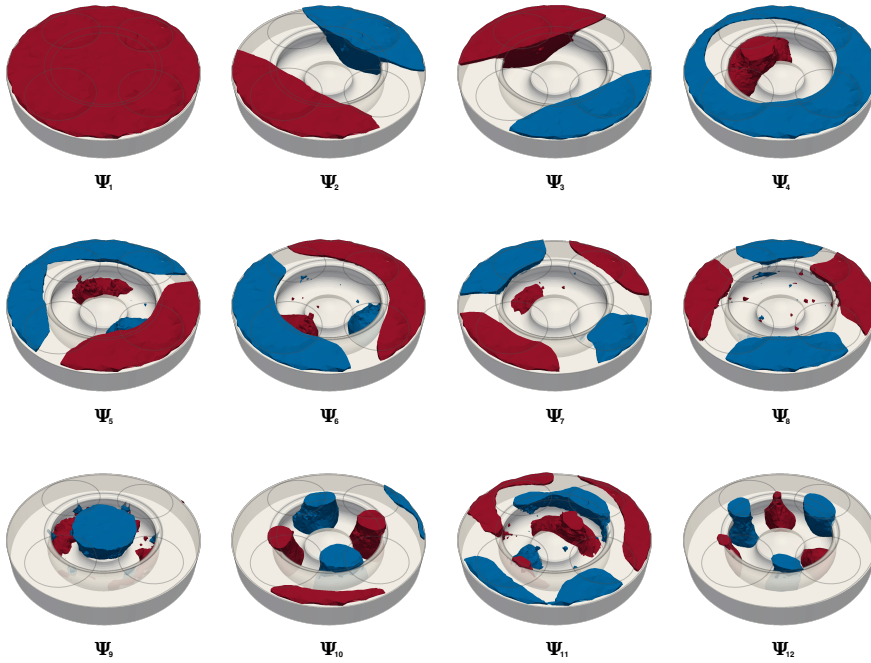
Figure 6.9: *Spatial distribution of POD modes $\mathbf{\Psi}_{1-12}$ across the simulated combustion chamber. Each mode except for the homogeneously distributed $\mathbf{\Psi}_1$ is represented by coloured isovolumes indicating the 10% (blue) and 90% (red) percentiles of the distribution of the real values of each individual mode $\Re\{\mathbf{\Psi}_i\}$. The geometry of the piston head and the position of the valves are added for reference.*

However, a previous step was necessary. The set of values $[\mathbf{x}^{\mathrm{ref}}, \mathbf{y}^{\mathrm{ref}}, \mathbf{z}^{\mathrm{ref}}, \Re\{\mathbf{\Psi}_i\}]$ forms essentially a point cloud randomly distributed across the combustion chamber, lacking any connectivity information. This was achieved by performing a 3D Delaunay triangulation [196, 197] using the open-source application ParaView [198], which includes an α-shape [199] related parameter to generate a more accurate reconstruction instead of just using the simple convex hull of the full dataset[3], and then extracting two clips.

In this figure, red and blue volumes thus indicate the distribution of the top 10% positive and negative real values of the mode. As seen in Fig. 6.7 time coefficients $\mathbf{a}_i(t)$ take positive and negative values along the simulation, so

---

[3]Note that this α parameter, which limits the valid search distance to connect vertices, is dependant on the particular geometry and sparsity of the point cloud, but in any case it must be higher that $d_{\mathrm{c,max}}$.

if the mode shape was animated by plotting $\mathbf{\Psi}_i \mathbf{a}_i$ the red and blue volumes would identify the regions oscillating with alternating higher amplitudes. The only exception is $\mathbf{\Psi}_i$ which would display the homogeneous rise and fall in mean pressure.

Inspecting the shapes of modes $\mathbf{\Psi}_1$ and $\mathbf{\Psi}_2$ in Fig. 6.9 it is clearly seen how the higher amplitudes are oscillating on opposite sides of the squish zone, in two different orientations. Not depicted in the figure are the nodal regions whose amplitude remains constant in time, which in these two modes consist of a slice of the chamber aligned in the middle of the two coloured isovolumes.

Furthermore, it can be seen that these two modes are reminiscent of classical acoustic transversal modes in opened combustion chambers, specifically mode ($m = 1, n = 0$) in the notation of Hickling et al. [50], also called first asymmetric mode.

Continuing this comparison, POD mode $\mathbf{\Psi}_4$ features a completely circular distribution between the squish zone and the bowl, with an annular nodal region instead of a straight one like in the previous modes, being similar to Hickling's first radial mode ($m = 0, n = 1$).

The next two modes $\mathbf{\Psi}_5$ and $\mathbf{\Psi}_6$ are interesting because they are remarkably three-dimensional. While they have shown again a straight nodal area, regions of higher amplitudes are crossed between the bowl and the squish area, something that would not be visible if only 2D slices of the chamber were being considered in this analysis.

Modes $\mathbf{\Psi}_7$ and $\mathbf{\Psi}_8$ are again similar to classical transversal asymmetric modes, in this case related to mode ($m = 2, n = 0$) shown by Hickling et al. Amplitudes in these two modes are again predominantly gathered in the squish area, but featuring two perpendicular nodal slices.

In contrast with previous modes, maximum amplitudes of $\mathbf{\Psi}_9$ are contained in the central region of the combustion chamber, alternating between a single region located immediately over the centre of the bowl and two opposite lower zones.

Recalling the spectrum trace of this node shown in Fig. 6.8, it can be seen how the frequency content of this particular mode, peaking around 19 kHz, is different from the previous squish-dominated modes in which the content was mainly spread between 6 and 11 kHz.

Subsequent mode $\mathbf{\Psi}_{10}$ presents again a pattern of mixed influence between the squish and the bowl contributions, in this case being similar to the previously discussed $\mathbf{\Psi}_5$ but with an added nodal slice as seen in modes $\mathbf{\Psi}_{7-8}$.

This mode, with bowl amplitudes again predominant, shows a frequency content centred around 11 kHz, thereby representing a transition from lower frequency squish-dominated modes and higher frequency bowl-dominated modes. Mode Ψ_{11} also contains information in both regions but since the energy of these modes is already low, it appears to contain not-so-clear residual information.

Finally, high amplitude isovolumes in mode Ψ_{12} are again confined in the bowl, in this case exhibiting a three nodal slices pattern reminiscent of Hickling et al. transversal asymmetric mode ($m = 3, n = 0$). As it was the case with Ψ_9, this bowl-dominated mode contains mainly high frequency content gathered around 19 kHz.

6.2.4. Dynamic Mode Decomposition

An alternative decomposition approach known as Dynamic Mode Decomposition (DMD) exists where instead of an optimal orthogonal basis, coherent flow phenomena at each frequency are sought. This is a relatively recent technique for modal flow decomposition [174, 200, 201] in which its application to combustion problems is still limited, and focused on the analysis of experimental PIV data [202, 203] such as velocity and vorticity fields in combustors.

This decomposition is realized by computing the eigenvalues and eigenvectors of a linear model which approximates the underlying dynamics of the system, which may not be necessarily linear [201]. The DMD modes (eigenvectors) calculated using this technique represent again coherent spatial structures of the flow, but in this case each one features a single temporal frequency [183], in contrast with POD modes. DMD eigenvalues represent the rates of decay and growth of these modes, along with their associated frequency.

Evaluation of the relevance of each mode to the dynamics of the system is usually performed by computing the norm of the mode, although Dahan et al. reported [204] that in some cases it may be preferable to order the modes attending to their frequency rather than their norm, as some modes may feature a growth rate of less than the unity, and thus they may be damped over time.

Furthermore, another advantage of the DMD and POD techniques is that it can be proved [174, 182] that processing only sub-domain data is possible, be it this sub-domain a small region of the domain or even a projection of the 3D field into a 2D plane, as no spatial arrangement is assumed by

either method. This is convenient when post-processing can be restricted to a region of the flow where relevant phenomena are expected, thereby saving computational effort.

As several variations for implementing a DMD strategy already exist in the literature only the basic concept originally proposed by Schmid [174] will be shown in this section.

We recall the matrix $\mathbf{V}_1^N$ introduced in Subsection 6.2.1 that contains N snapshots of the flow field. These are assumed to be linearly related through a certain matrix $\mathbf{A}$, which is assumed to remain approximately constant during the time $N\Delta t$ spanned by the sequence:

$$\mathbf{v}_{i+1} = \mathbf{A}\mathbf{v}_i \tag{6.2.6}$$

Even if the flow field is non-linear, matrix $\mathbf{A}$ will provide a linear tangent approximation of the dynamic characteristics of the flow. The objective is now to extract its eigenvalues and eigenvectors which, will be the DMD eigenvalues and the DMD modes of the flow. Combining both expressions in matrix form we can write that:

$$\mathbf{V}_2^N = \mathbf{A}\mathbf{V}_1^{N-1} \tag{6.2.7}$$

Where $\mathbf{V}_2^N$ contains snapshots 2 to N, and $\mathbf{V}_1^{N-1}$ contains snapshots 1 to $N-1$. As M for CFD simulations is usually in the order of 10^6 and N must comprise a sensible amount of time steps in order to ensure that the dynamic characteristics are well captured, directly performing the eigendecomposition of $\mathbf{A}$ is usually too computationally expensive.

In order to overcome this problem different strategies exist, such as reformulating 6.2.7 into a companion matrix that can be solved through a QR decomposition [175, 182, 200]. A more numerically stable method, however, is to make use again of the Singular Value Decomposition (SVD) [174, 183, 184, 201] to obtain $\mathbf{V}_1^{N-1} = \mathbf{U}\boldsymbol{\Sigma}\mathbf{W}^T$. Then, equation 6.2.7 becomes:

$$\mathbf{V}_2^N = \mathbf{A}\mathbf{U}\boldsymbol{\Sigma}\mathbf{W}^T \tag{6.2.8}$$

From this expression it is now possible to manipulate the terms that are already known in order to define a new matrix $\widetilde{\mathbf{S}}$, which will be, thus, related to $\mathbf{A}$ in the following way:

$$\widetilde{\mathbf{S}} \triangleq \mathbf{U}^T\mathbf{V}_2^N\mathbf{W}\boldsymbol{\Sigma}^{-1} = \mathbf{U}^T\mathbf{A}\mathbf{U} \tag{6.2.9}$$

It can be seen that this relationship between $\widetilde{\mathbf{S}}$ and $\mathbf{A}$ matches the definition of *matrix similarity*. Thus, $\widetilde{\mathbf{S}}$ is similar to $\mathbf{A}$ and as a consequence their eigenvalues λ_i are the same, with the advantage that $\widetilde{\mathbf{S}}$ is of reduced size

and easier to solve. The DMD modes Φ_i can finally be calculated from the eigenvectors y_i of $\widetilde{\mathbf{S}}$ as:

$$\Phi_i = \mathbf{U} y_i \tag{6.2.10}$$

The frequency associated with each spatial mode can be recovered by evaluating the imaginary part of each complex eigenvalue, and taking into account the time step Δt between snapshots:

$$f_i = \frac{\omega_i}{2\pi} = \frac{\mathfrak{I}\{\ln(\lambda_i)\}}{2\pi\Delta t} \tag{6.2.11}$$

Finally, the computed modes need to be ranked in importance. However, the procedure for doing so is not as clear cut as in the POD case, and several approaches can be found in the literature [174, 183, 205]. Here, the criterion proposed by Kou & Zhang [206] was used to rank the influence of each dynamic mode on the whole sampling space:

$$E_i = \sum_{j=1}^{N} \left| \alpha_i \lambda_i^{j-1} \right| \, \|\Phi_i\|_F^2 \, \Delta t \tag{6.2.12}$$

Where the modal amplitudes α_i can be recovered by solving the reconstructed flow field multiplied by the unknown amplitudes against, for instance, the first snapshot of the flow [205]:

$$\mathbf{V}_1 = \Phi \, \boldsymbol{\alpha} \implies \boldsymbol{\alpha} = \Phi^{-1} \mathbf{V}_1 = \mathbf{Y}^{-1} \mathbf{U}^* \mathbf{V}_1 \tag{6.2.13}$$

As discussed in the previous section, while it is possible to analyse the frequency content of POD modes and draw correlations between this content and the spatial distribution of each mode, Dynamic Mode Decomposition is a tool best suited for frequency analysis, as it forces each mode to contain a single frequency.

DMD was thus performed following the procedure outlined above. In order to assess the relevance of the different resulting DMD modes Φ_i, the relevance E_i of each mode was computed and then normalized with $\max_i(E_i)$. The magnitude of this metric for each mode can be seen in the chart of Fig. 6.10, where modes have been ordered according to their associated frequency.

It can be seen in this chart that three modes are peaking above those around them. Mode Φ_{381} at around 7.1 kHz is the most relevant mode in the range of 5 – 8.5 kHz, Φ_{803} is dominant among the 8.5 – 11 kHz and finally Φ_{584} appears as a single peaking mode at 19 kHz. The spatial distributions of these three modes have been included in Fig. 6.10 following the same procedure used in the POD case.
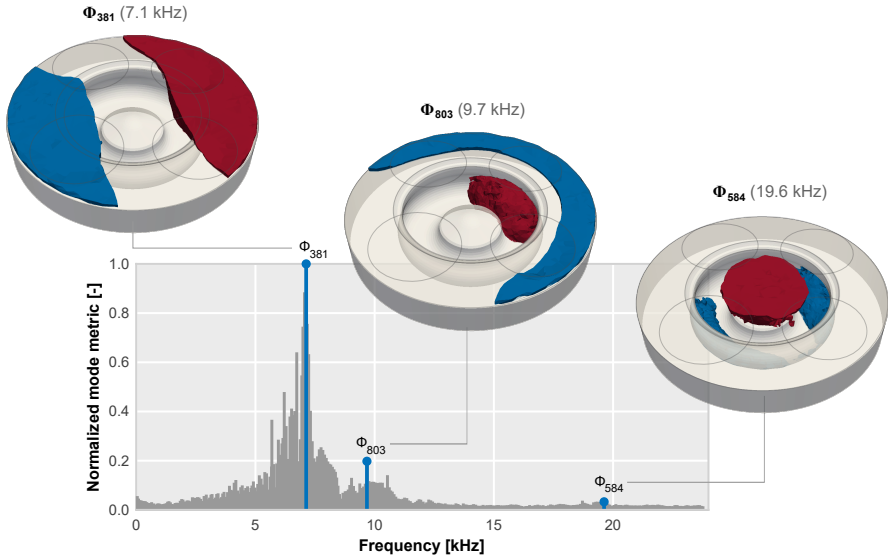
Figure 6.10: *Normalized relevance $E_i / \max_i(E_i)$ of all DMD modes, highlighting the most relevant modes at the frequencies of interest: $\boldsymbol{\Phi}_{381}$, $\boldsymbol{\Phi}_{803}$ and $\boldsymbol{\Phi}_{584}$ and including their spatial distribution. Each mode is represented by coloured iso-volumes indicating the 10% (blue) and 90% (red) percentiles of the distribution of the real values of each individual mode $\Re\{\boldsymbol{\Phi}_i\}$.*

These spatial distributions along with the modal relevance information offer a clearer view into the correlation between frequency content and spatial distribution that was already suggested by the POD decomposition. The first group of frequencies, exemplified by $\boldsymbol{\Phi}_{381}$, is the dominant in this combustion simulation, and it is clearly dominated by the reflections in the squish zone.

A second, smaller set of slightly higher frequency content is represented by mode $\boldsymbol{\Phi}_{803}$, which is related to the interaction of the pressure fluctuations between the squish zone and the bowl. Finally, higher frequency content near 20 kHz is linked to the pressure fluctuations contained within the bowl, as shown by the spatial distribution of DMD mode $\boldsymbol{\Phi}_{584}$.

It is important to remark the similarity shown between the most relevant DMD modes and those obtained by the Fourier method applied in Subsection 6.2.2. Despite the differences for visualizing the oscillation patterns, it is evident how both methods estimate comparable pressure behaviours at similar excitation frequencies.

After the results examination, modal decomposition techniques have proved to be a valuable tool to understand the resonant mechanisms within ICE chambers, allowing a complete connection between temporal, spatial and frequency features of this elusive phenomenon.

All methods of analysis, including Fourier's method, have shown that most of the acoustic energy is concentrated in macroscopic structures across the chamber, either in the squish or in the inner part of the bowl. Moreover, recalling the sequence of snapshots displayed in Fig. 6.1, it is obvious to claim that these structures are related to the standing wave generated during the premixed burning stages rather than induced by the inner jet perturbations, since none of the modes shown so far are specifically focused on the jet region itself.

This is the main reason why URANS solution is comparable to LES results, even without being able to reproduce all the sound generation phenomena seen in Section 6.2. Hence, all the results that are going to be shown from this point correspond to URANS simulations. In particular, the set-up denoted URANS-coarse in Chapter 5 was used in the following studies owing to its reasonably wall time and accurate prediction.

6.3. Conclusions

In this chapter a complete characterization of combustion noise source in CI Diesel engines has been performed. This concerns specially the analysis of phenomena involved in the noise generation and the comprehension of the unsteady behaviour caused by combustion.

The CFD model implemented and further validated in Chapters 4 and 5 was used in order to overcome experimental limitations while addressing the study of noise source in detail, thereby providing valuable insight about all involved phenomena.

They have been identified two different sources of acoustic perturbations caused by the combustion. The first, originated by the premixed combustion phase, produces sudden increase of pressure located at the end of the fuel spray plumes, that leads to generate a resonant wave inside the chamber. The second one, however, is not a fully localized source since it randomly appears along the stabilized flame during the mixing controlled combustion phase.

Inspection of the numerically obtained pressure field offers a way of characterizing the contribution of each source to the chamber acoustic signature. Thereby, it has been shown that these jet-induced oscillations are small and

rapidly attenuated if they are compared with the standing wave generated due to the premixed burning and, thus, they not contribute to the chamber sound level in a relevant way.

Besides to this qualitative characterization, more complex studies have been carried out in an attempt of verifying this deduction. Therefore, a methodology has been proposed to extract coherent time-spatial data from the simulation, even in cases where the mesh is changing due to moving components (cylinders, valves) or refining-coarsening optimizations designed to reduce the computation time.

Pressure data assembled in this way was post-processed using different techniques. A Fourier analysis was performed where the FFT of each cell was computed, and spatial features were extracted, filtering certain frequency ranges of interest selected manually based on idealized modes expected from the literature.

In order to automate this task and also to obtain a deeper insight into the time-spatial modal characteristics of the combustion unsteady flow field, POD was applied to the same pressure data. Clear three-dimensional pressure modes have been identified using this technique, reminiscent of classical open chambers acoustic modes but demonstrating for the first time the additional complex interaction of the pressure waves in the different zones in the chamber geometry.

Time evolution of these POD modes has been shown to correlate with the different phases of the combustion cycle, showing for instance how the annular resonance of the chamber is caused by the combustion of the second injection, thereby offering greater insight into the contribution of timing settings and geometric parameters to the overall acoustic resonance of the chamber by decoupling both time and spatial domains.

Another advantage of POD modes is their dimensionality-reduction optimality, allowing the pressure signals to be adequately reconstructed with only a low number of modes.

This optimum representation, however, implies that each mode carries a mixed frequency content. If the detailed analysis of the frequency domain is intended, the DMD technique is shown to provide a good identification of coherent spatial structures at each frequency of interest. Specifically, it has been shown how spectral content at 5 – 8.5 kHz is related to the squish-dominated pulsation, with the 8.5 – 11 kHz featuring squish-bowl interaction and the higher frequency content at 19 kHz being related to central top-down bowl oscillations.

Although data from LES simulations have demonstrated to be very useful to achieve an enhanced comprehension of in-cylinder phenomena, the computational requirements are extremely large and its application to practical cases is still being very limited. Consequently, the use of URANS schemes was again evaluated and compared to the LES solution in order to keep the CFD time resource within the limits of usual computational capacity without relevant accuracy losses.

Despite the incapacity for reproducing some secondary aspects such as those aforementioned jet-induced oscillations, URANS simulations can capture all relevant phenomena in combustion noise generation.

Noise optimization of conventional Diesel combustion

The very large number of parameters to be inspected after the model valida-tion demands to explore additional techniques for the identification of the optimizing paths in the configuration design or in the operation settings.

In this chapter, the numerical model is combined with optimization tech-niques in order to propose guidelines and potential alternatives to mitigate the undesired effects of noise. In the first place, the statistical approach De-sign of Experiments (DoE) has been applied to different operating settings to establish cause-effect relationships between the most influencing factors and their response. Next, the injector configuration is changed with the purpose of determining the effect of modifying the ignition location in resonant noise generation. Finally, a genetic algorithm optimization of the combustion sys-tem design –including chamber, injector and ports geometries– is performed considering the performance and both pollutant and noise emissions.

Work in this chapter has been partly published in the following papers:

- *Understanding the unsteady pressure field inside combustion chambers of compression-ignited engines using a CFD approach* [11]

- *Towards a Predictive CFD Approach for Assessing Noise in Diesel Compression Ignition Engines. Impact of the Combustion Strategies* [3]

- *Numerical Methodology for Optimization of Compression-Ignited Engines Considering Combustion Noise Control* [9]

Table 7.1: *Specified ranges for the input factors of both DoE plans.*

Study	Input parameter	Levels	Range
DoE$_1$	SoI$_1$ [cad aTDC]	4	[-33.8, -25.8]
	SoI$_2$ [cad aTDC]	6	[-23.6, -9.6]
DoE$_2$	EGR [%]	3	[0, 20]
	p$_{inj}$ [MPa]	3	[40, 107]
	p$_{int}$ [MPa]	3	[2.0, 2.5]

7.1. Strategies based on operating settings

In this section, CFD model was combined with the statistical technique DoE in order to estimate the relationships between influencing factors and outputs of the engine. This approach has been used in multiple engineering applications from ICE optimization [207] to injection molding [208]. The response variables such as noise level or efficiency were therefore analysed for several engine settings variations.

Two distinct studies were performed using the full factorial design method [209]. First, the different splits between pilots and main injections were chosen as input factors. The start of the pilot injections, SoI$_1$ and SoI$_2$, were selected with 4 and 6 levels of possible values. The EGR rate, intake and injection pressures were considered for the second study, with 3 levels for each parameter. Hence, both DoE plans result in 23 and 27 simulations, respectively. Additional details about the factor space, input factors and specified ranges are displayed in Table 7.1 and Fig. 7.1. Moreover, the operating point number #7 was again selected for both studies owing to the potential advantages for optimization described in Chapter 3.

Once all simulations were finished, data resulting from both two studies were presented and discussed. Thereby, noise emissions were compared with other relevant engine outputs, so as to identify general trends and optimum settings.

In a first step, all variables obtained at each point of the factorial space were interpolated using a cubic polynomial fit for visualization. In Fig. 7.2 the computed contours of overall noise and indicated efficiency of the DoE$_1$ are plotted together.

Several conclusions may be drawn from this picture. The timing of the pilot injections has only a slight impact on the indicated efficiency (±0.5% approx.), whereas it has noticeable influence on the overall noise (±0.75dB approx.). Also, the bottom-right hand side of the map is clearly identifiable as the optimum region, with low noise and high efficiency levels. The optimum
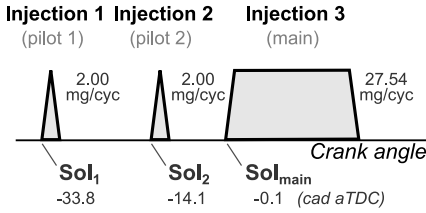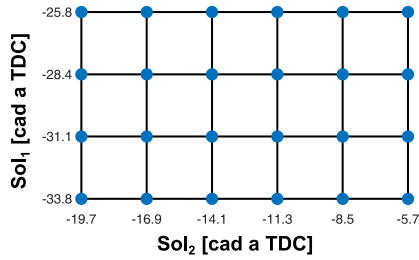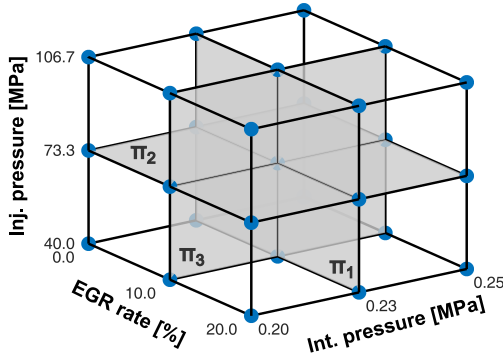
Figure 7.1: *Injection strategy scheme (top-left) and factor space of both full factorial designs: : DoE₁ (top-right) and DoE₂ (bottom).*

strategy is therefore to reduce the split between the second and the main injections, with the first injection happening as early as possible. The first injection earliest timing is limited to avoid an increase in soot emissions caused by the impingement of the excessive liquid fuel on the piston surface. In addition, it is clear that the second injection timing is the main controlling parameter and has a direct impact on both noise and efficiency. On the other hand, the first injection timing only has some relevant effect on noise.

This method not only allows an overall analysis of the results; it can also be used to better understand the connection between noise and efficiency. As reported before in Appendix 3.4, the noise indicators, I_1 and I_2, are related to the contributions of the rate of pressure change (due to the combustion) and of the resonance phenomena to the overall noise level. Thus, by plotting the ON and η_i against both indicators should provide additional details about the noise fundamental parameters and the cycle efficiency.
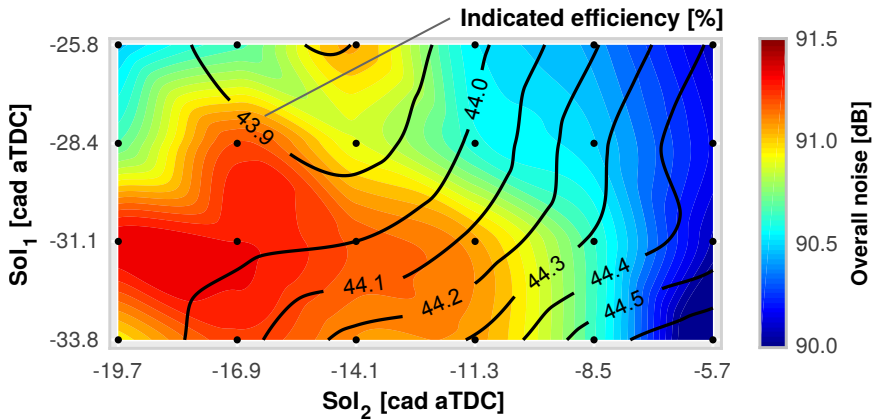
Figure 7.2: *Results of DoE$_1$, overall noise and indicated efficiency contours are superposed across the factorial space.*

DoE$_1$ results were interpolated, with the same method used before in order to obtain the maps shown in Fig. 7.3. In this case, from the worst (top-right hand side) to the better configuration (bottom-left hand side) it may be observed that the noise level drop is due to the mixed contribution of both indicators. This means that a noise reduction may be obtained if the pressure rise rate peak due to combustion and the resonance effects are both decreased.

An additional analysis was performed in order to examine how the noise may be mitigated by acting only on one of the noise indicators. The bottom graphs of Fig. 7.3 show the trends along the lines displayed in the prior contours. As can be seen, similar noise reductions are achieved when either indicators decrease. However, the indicated efficiency is only correlated with I$_1$, as is shown by its random behaviour when I$_2$ changes. According to this analysis, two different strategies may be used to decrease noise emissions, with differing impact on the efficiency.

To control the combustion by minimizing the contribution of I$_1$ is complicated due to the inherent relation between the rate of pressure change and the cycle efficiency. RoHR traces of the two extreme cases shown in Fig. 7.3 (bottom) are plotted in Fig. 7.4 in order to illustrate this issue. By moving the second pilot towards TDC the ignition delay is reduced, and this results in a smoother premixed combustion. Thus, noise is reduced while the indicated efficiency is increased.

The other strategy is based on controlling noise by reducing the contribution of resonance. This has an apparent advantage when compared with the previous one: its independence from cycle efficiency. Thus, as it already
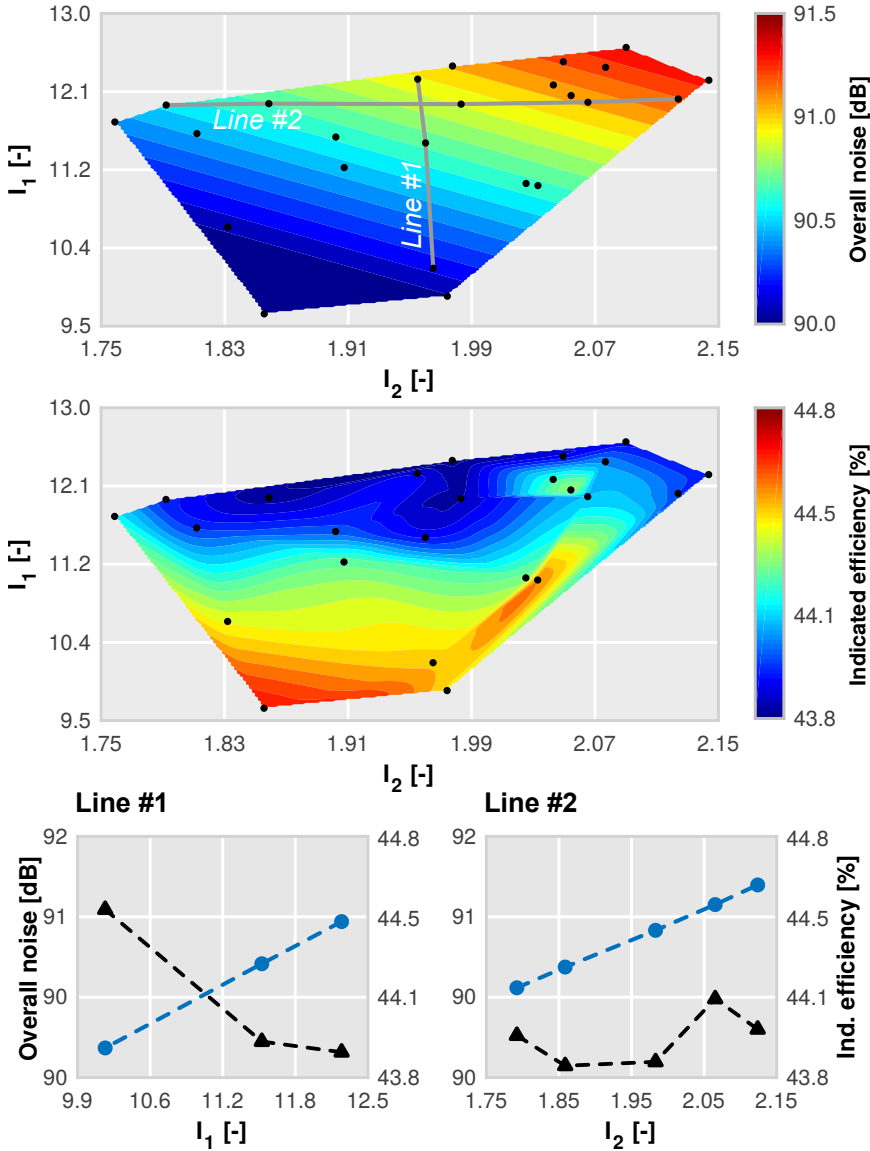
Figure 7.3: *Contours of overall noise (top) and indicated efficiency (middle) against the two noise indicators, I_1 and I_2. Trends along the two highlighted lines are also drawn at bottom.*

intuited in the literature review, the study of the resonant phenomena and their effects on the final noise perception is an interesting topic to develop in order to reduce noise emissions while maintaining, or even improving, the thermal efficiency.
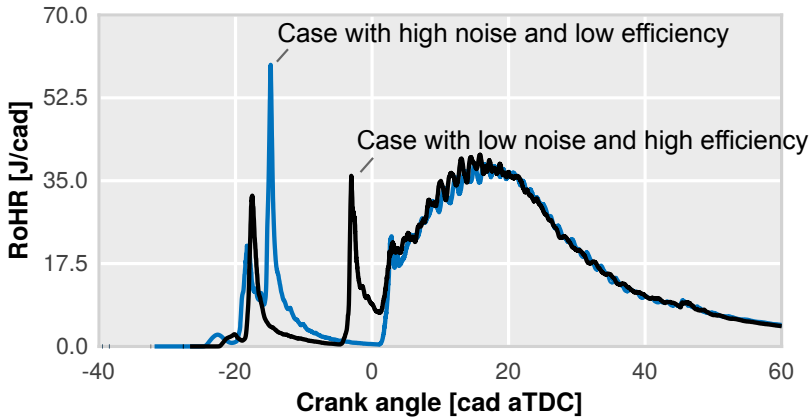
Figure 7.4: *Rate of heat release traces of the two extreme cases shown in Fig. 7.3 (bottom).*

Results of DoE_2 are presented in Fig. 7.5 following the same procedure described for DoE_1. In this case, the results are plotted at the three medium planes of the full factor space indicated in Fig. 7.1 (π_1, π_2 and π_3).

In the first plane (π_1), the well-known trade-off between EGR rate and injection pressure is clearly visible. The noise increases when the injection pressure rises and the EGR rate decreases. On the contrary, the indicated efficiency diminishes with high EGR rates and low injection pressures.

Examination of the second plane (π_2) reveals that the intake pressure can contribute to decrease the noise level and achieve higher values of efficiency. Hence, it is possible to mitigate the adverse effects of EGR on efficiency by increasing the boost pressure.

In the third plane (π_3), it is possible to observe again how the intake pressure helps mitigating the negative impact of the injection pressure increase on noise levels.

Therefore, when considering the EGR rate and the injection pressure separately it is only possible to achieve a compromise solution, which can be improved by increasing the intake pressure.

A similar analysis to that presented above in Fig. 7.3 was performed using DoE_2 results in order to establish the relationships between the noise indicators and the engine outputs. For this study, the overall noise is presented in Fig. 7.6. Additionally, the regions with higher levels of indicated efficiency are identified by a highlighted contour line.
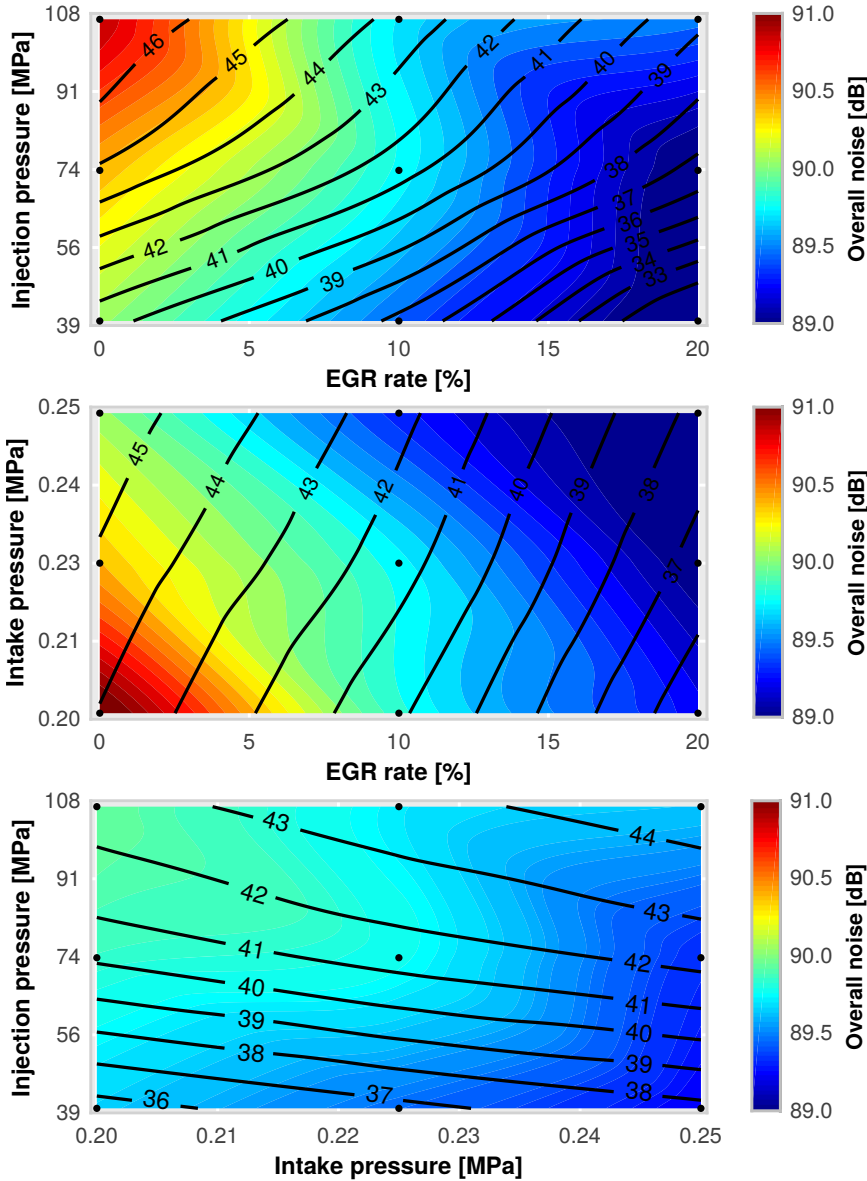
Figure 7.5: *Results of DoE$_2$, overall noise and indicated efficiency contours are superposed along the three different factorial planes. Plane π_1 (top), plane π_2 (middle) and plane π_3 (bottom).*

There are two distinct regions in which the efficiency is maximized. The largest region coincides with the highest values of I$_1$, which confirms the above mentioned relation between this noise indicator and the efficiency. The points located in the bottom left of the figure correspond to the highest EGR rate and lowest injection pressure configurations.
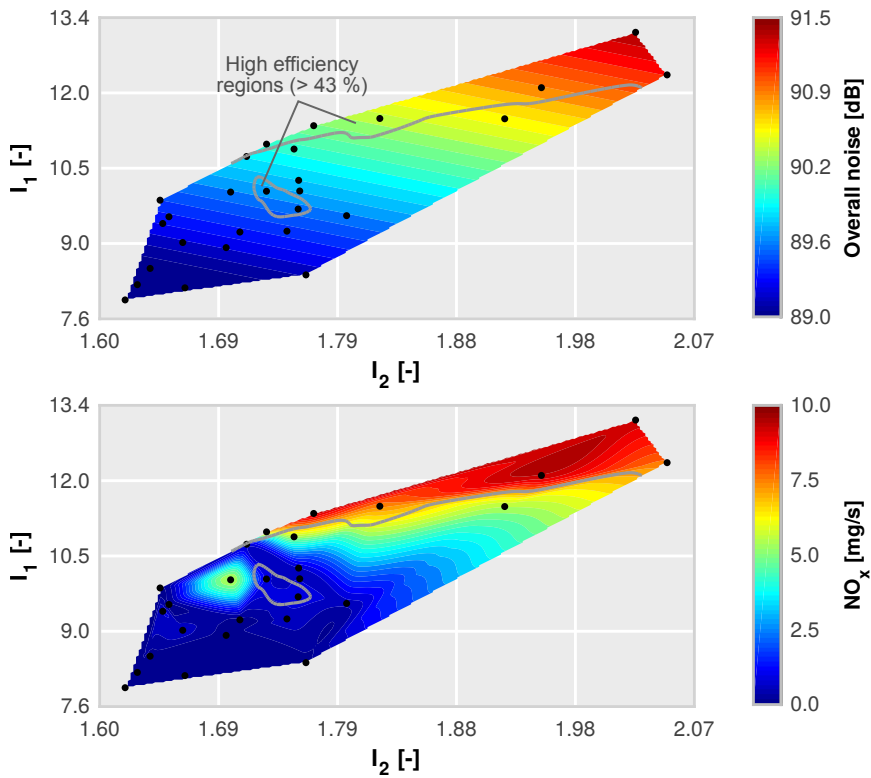
Figure 7.6: *Contours of overall noise (top) and NO_x emissions (bottom) against the acoustic indicators, I_1 and I_2. The regions with higher indicated efficiency (> 43%) are highlighted in both plots.*

The other region is delimited by low-medium values of both indicators. This matches with the optimum configurations, characterized by medium EGR rate, high pressure injection and medium-high intake pressure, representing a compromise solution between efficiency and noise. The bottom-left hand side of the map, with low noise and low efficiency, congregates configurations with high EGR rates and low injection pressures.

Finally, a map of NO_x emissions is also included in order to confirm the reliability of the proposed methodology when the analysis is extended to the pollutant emissions field. This shows the relevance of also including this kind of emissions in the analysis since positive effects on efficiency or noise, can mean increasing pollutants formation.

7.2. Strategies based on the injector configuration

Results obtained in the previous chapter highlight the advantages of the enhanced understanding of combustion chambers' time-spatial unsteady structures. Specifically, combustion acoustics can be improved by identifying and tackling the most relevant modes, allowing automated optimization algorithms to modify the combustion settings and/or chamber geometries in a more meaningful way, pursuant to the final objective of addressing the noise emission challenge faced by thermal-powered vehicles.

In this sense, the comprehension of how these structures are changing as the combustion features are modified through both the engine settings and design may shed light into this matter. In this section, changes in the in-cylinder pressure field are therefore analysed as the injector configuration is modified.

7.2.1. Frequency analysis

From Chapter 2 it can be recalled that several authors [52, 53, 103] have demonstrated theoretically that the relative position of the combustion excitation can determine the standing wave behaviour inside ICE combustion chambers by modifying the amplitude of the resonant modes. As these papers claim, the excitation of a specific resonant mode can be avoided by producing the flow disturbance at the same location of its node or zero amplitude region. Conversely, the same level of excitation enhances the contribution of a particular resonant mode as the application point is located away from the node.

Here, the procedure outlined in Section 6.2.2 was applied to three different combustion system configurations in order to evaluate the contribution of the ignition location to the resonance phenomenon. The combustion system was redesigned by decreasing the injector included spray angle (IA), whereas the engine operating conditions were maintained to 2400 rpm and 168 Nm (Point #7 from Table 3.3). The main idea of this study was to displace the ignition points towards the centre of the cylinder, while the excitation intensity or RoHR peaks was/were kept constant so as to reduce the amplitude of the most relevant mode (Θ_1).

Figure 7.7a show the maximum pressure rate of change reached during each combustion stage (first pilot, second pilot and main injection). The results indicate the consistency of $(dp/dt)_{max}$ for these three hardware
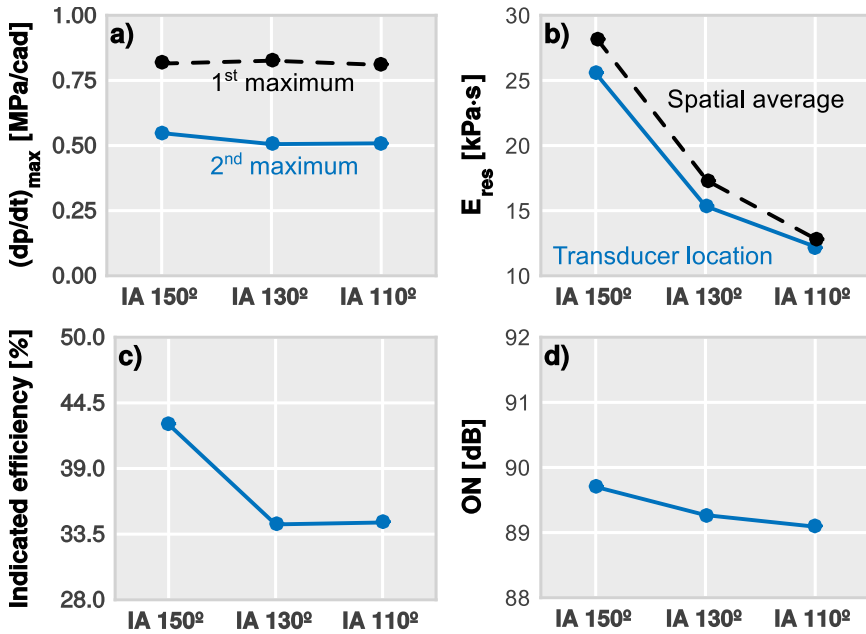
Figure 7.7: *Effects of the included spray angle variation. a) Maximum pressure rise rate due to each combustion phase, b) Energy of resonance at the transducer location and averaged c) Indicated efficiency and d) Overall noise (ON).*

configurations, demonstrating that the excitations were kept constant and ensuring that the impact on the resonance was only due to the change in the ignition position, not to the intensity of the excitation.

Trends in the energy of the resonance are presented in Fig. 7.7b. First, a comparison of the E_{res} obtained at the transducer location is shown. As expected, this parameter decreases with the included spray angle since, as it was intended, the ignition locations were moved towards the node of the first transversal mode. Secondly, an averaged value of E_{res} for all registration points was obtained in order to verify that the global resonance energy inside the combustion chamber follows the same trend.

Figure 7.7d shows the impact on the objective aspect of noise or overall noise (ON). A significant lowering of the overall noise was achieved (≈ 0.6 dB) by reducing the injector included angle. However, these improvements in terms of the unsteady response come together with important efficiency losses due to the worsening in spray/bowl matching, as can be seen in Fig. 7.7c.

The ignition areas can be identified by locating the places in which the fuel energy release is produced. Hence, taking advantage of the CFD results, the RoHR was numerically integrated along the whole domain with respect to the radial coordinate so as to analyse both the temporal and the spatial evolution of the combustion process. The solutions are presented in Fig. 7.8 in which the horizontal axis indicates the temporal evolution of the engine cycle, the vertical axis shows the integration variable –the normalized radial position R^{norm}– and finally the colour scale displays the energy release. Thereby, ignition locations were established by identifying the 99 percentile of the RoHR distribution values. This value guarantees that the energy release is sufficiently meaningful for its consideration as an ignition area. In addition, the RoHR associated with mixing-controlled combustion was neglected in view of its low contribution to the resonance phenomenon.

The energy distribution for the reference case (IA 150°) is displayed as an example in Fig. 7.8a. Then, the same method was applied to the rest of engine configurations and the position of the ignitions is presented in Fig. 7.8b. As it can be seen, the combustion of the first pilot injection is essentially located at the same radial position in all the cases. Poor density conditions cause a long ignition delay and a deep spray penetration, forcing the combustion to start close to the bowl limit even for the closest included spray angles. In the same way, the burning of the main injection does not present relevant differences in terms of radial location. However, in this case, fuel ignites very close to the injector nozzle due to the extreme thermodynamic conditions achieved close to TDC. By contrast, significant differences appear in the ignition location of the second injection. It is evident that the self-ignition event is moved towards the cylinder centreline as the included spray angle is reduced. The second combustion is therefore dominant in the resonance phenomenon due both to its highest intensity $(dp/dt)_{max}$ and to its ignition location.

In order to analyse the frequency distribution of in-cylinder pressure for each hardware configuration, the pressure spectrum averaged across all the monitors in the domain is plotted in Fig. 7.9. The mid-frequency range does not exhibit significant differences between all the cases considered, thus confirming again its relation with the $(dp/dt)_{max}$. The high frequency content varies with the engine configuration: the amplitude of the first mode is decreased and higher order modes are excited as the spray angle is reduced.
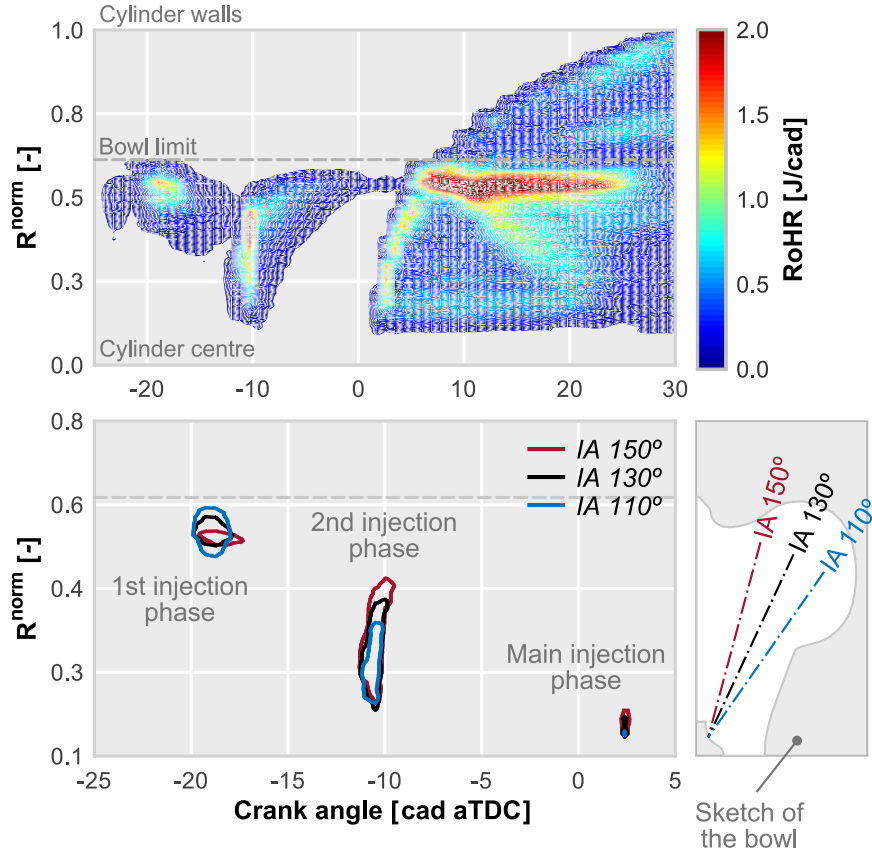
Figure 7.8: *Ignition areas identification and analysis. RoHR contours along the radial dimension of the engine cylinder for the reference case (top) and comparison of the ignition variation (bottom).*

The spatial distribution of the resonant modes can be examined by using the procedure described previously in Chapter 6. In particular, three different band-pass filters were applied to the pressure registered by all the monitors in order to inspect the most relevant modes for each hardware configuration (filter cut-off frequencies are also shown in Fig. 7.9). In the same Fig. 7.9 the spatial pressure distributions are displayed by plotting the SPL across a plane perpendicular to the cylinder axis rather than using volume renders as in Fig. 6.5. Moreover, SPL was normalized between the minimum and maximum values of each mode for proper scaling and visualization. It can be observed from these representations that the spatial distribution of the most energetic modes (Θ_1 and Θ_2) varies when the ignition location is moved whereas their characteristic frequencies do not change significantly.
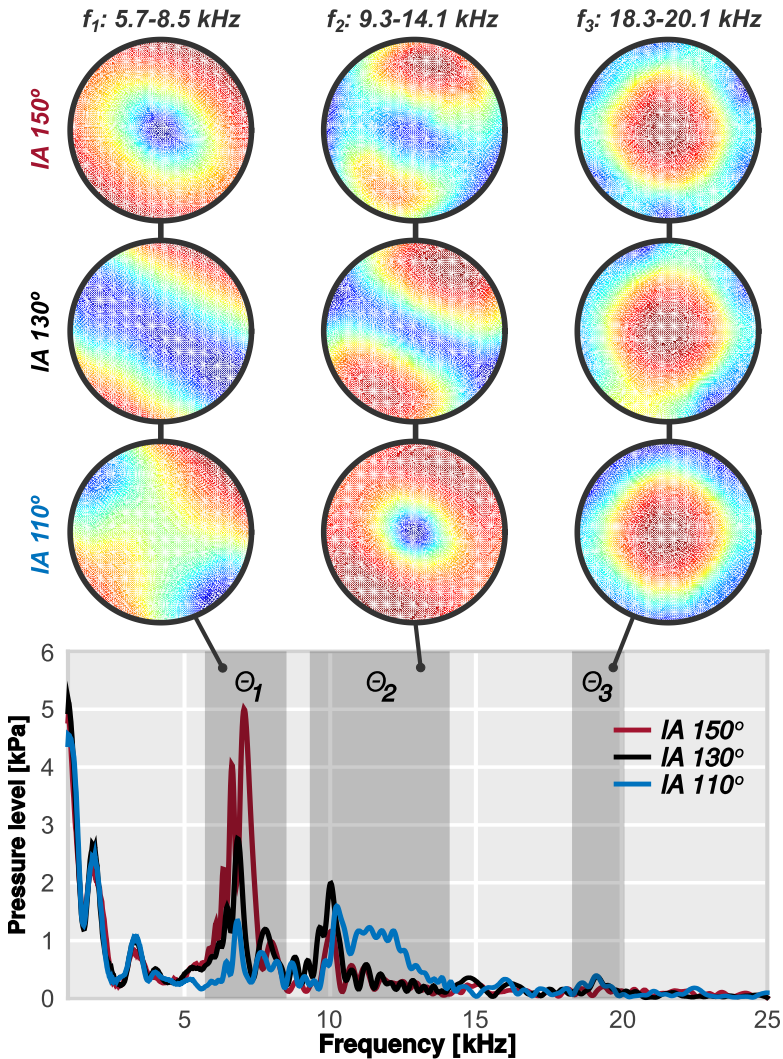
Figure 7.9: *A comparison of the pressure spectrum averaged across all considered monitors for the three combustion system configurations. Spatial pressure distribution of the most relevant modes of resonance are plotted at a perpendicular slide to the cylinder axis located at 2.5 mm of the cylinder head.*

However, the highest order mode (Θ_3), which has a symmetric distribution, does not exhibit any meaningful differences in its characteristic frequency and spatial distribution.

7.2.2. Modal decomposition analysis

The conclusions offered by the decomposition procedures about the correlation between spatial, temporal and frequency content of the unsteady flow field behaviour in the chamber can be applied to the practical optimization of the combustion process, in order to reduce the noise emission.

As seen in Fig. 7.9, in this combustion acoustic energy is mainly gathered in the 6 – 11 kHz band, which is coincidentally favoured by human hearing. An optimization strategy could consist in trying to demote this content shifting the acoustic energy to higher frequencies, which are naturally attenuated by the human auditory system. ITU-R BS.468-4 standard for instance quantifies this attenuation in 20.2 dB at 20 kHz [84].

Thus, if the energy represented by modes Θ_1 and Θ_2 could be shifted towards mode Θ_3 or, even better, independently reduced, the overall perceived noise level would be reduced. In order to do this, the information gained by means of the decomposition techniques can prove of utility.

Since it has been established that the 6 – 11 kHz content is mainly linked to the excitation in the squish area of the chamber, which is in turn caused by the location of the combustion energy release, a way to alter this dynamic behaviour could be to modify the angle of the fuel injection, directing the sprays slightly more towards the piston in order to promote bowl-dominated content against squish-dominated content.

To test this approach in more extremely conditions as those utilized in the previous section, another CFD simulation was carried out where the included spray angle was modified from 150° to 90°, keeping constant the remaining combustion parameters.

In Fig. 7.10 it is shown how the modified angle changes the impingement points of the sprays from the upper part of the bowl and the start of the squish in the original case, to near the bottom of the bowl wall in the 90° case.

The sprays are visualized in this figure by clipping the equivalence ratio ϕ at the unitary value, thereby showing the isovolume of stoichiometric conditions enclosing the spray. If C, H and O are the number of carbon, hydrogen, and oxygen atoms in a cell, the equivalence ratio is computed as:

$$\phi = \frac{2C + H/2}{O} \tag{7.2.1}$$

In order to understand how the spatial distribution of the unsteady pressure fluctuations has been affected by the new spray angle, POD was performed on the modified CFD results. Fig. 7.11 shows how the modal energy has shifted from the original to the modified combustion.

The energy share and spatial distribution of modified POD modes $\widetilde{\Psi}_{2-5}$ are plotted, along with that of the most closely resembling original mode. Again, mode $\widetilde{\Psi}_1$ is disregarded, and not considered for the analysis, since it is only related to the homogeneous compression-expansion pressure cycle. It can be seen how the circular ($m = 0, n = 1$) mode which was previously ranked fourth (Ψ_4) with 11.2% of the energy, is now the most relevant with an energy share of 18.25% ($\widetilde{\Psi}_2$).

Modified modes $\widetilde{\Psi}_{3-4}$ are shown to closely resemble the original Ψ_{2-3} modes, albeit with a rotation of the nodal plane, which is probably due to a different spray igniting first and thus initiating these squish-dominated propagating pressure oscillations. Their energy contents on the other hand have been diminished to less than half their previous ones. Lastly, the original bowl-dominated mode Ψ_9 has been promoted to the fifth place ($\widetilde{\Psi}_5$) with almost four times its previous energy.

To show how this shifting in the modal energy has affected the audible content, in Fig. 7.12 a comparison between the acoustic signature of the original and the modified combustions can be found. Decibel scale has been selected in order to better assess the difference at each frequency.

As predicted by the modal decomposition results, in-cylinder sound pressure levels at squish-dominated frequencies (6 – 8.5 kHz) are significantly reduced, by approximately 10 dB. Acoustic content in the 9 – 11 kHz band where a mixed influence of the squish zone and the bowl is also reduced, although not as much as in the previous band.

Original [150º]　　　　**Modified** [90º]
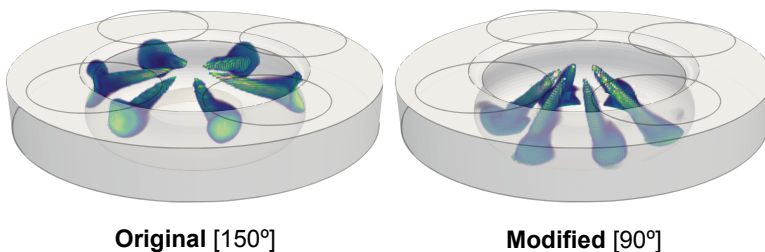
Figure 7.10: Original and modified sprays visualized as a clip of equivalence ratio $\phi > 1$ at approximately 7 cad after top dead center in both cases.
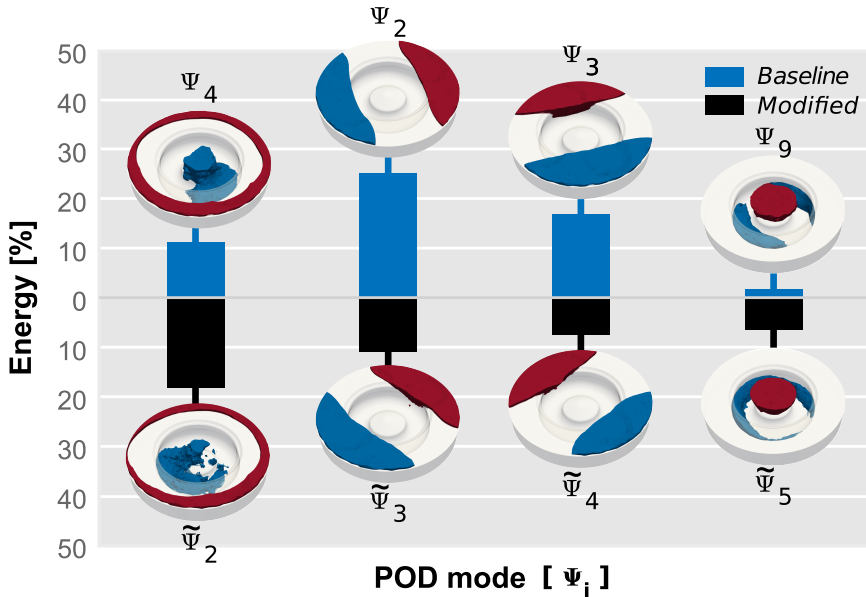
Figure 7.11: *Energy share and spatial distribution of the four most relevant modified modes $\widetilde{\Psi}_{2-5}$ (bottom), together with their most closely resembling original counterparts (top).*

On the contrary, and again as previously predicted, the shifting of the combustion excitation towards the bowl caused indeed an appreciable increase in the 19 kHz SPL content which is linked to this zone of the chamber. However, as can be seen in the bottom graph of Fig. 7.12, the natural human hearing attenuation mitigates the relevance of this increase since the content at this frequency is still masked by the medium-frequency noise emission.

It is true that this optimization of acoustic emission should not be performed on its own, as the possible increase in chemical pollutants and decrease of combustion efficiency is affected as well by other injector configuration parameters. However, modal decomposition is shown again to provide valuable information to better initialize and define a merit function for an optimization algorithm.

In-cylinder pressure spectrum

External noise spectra
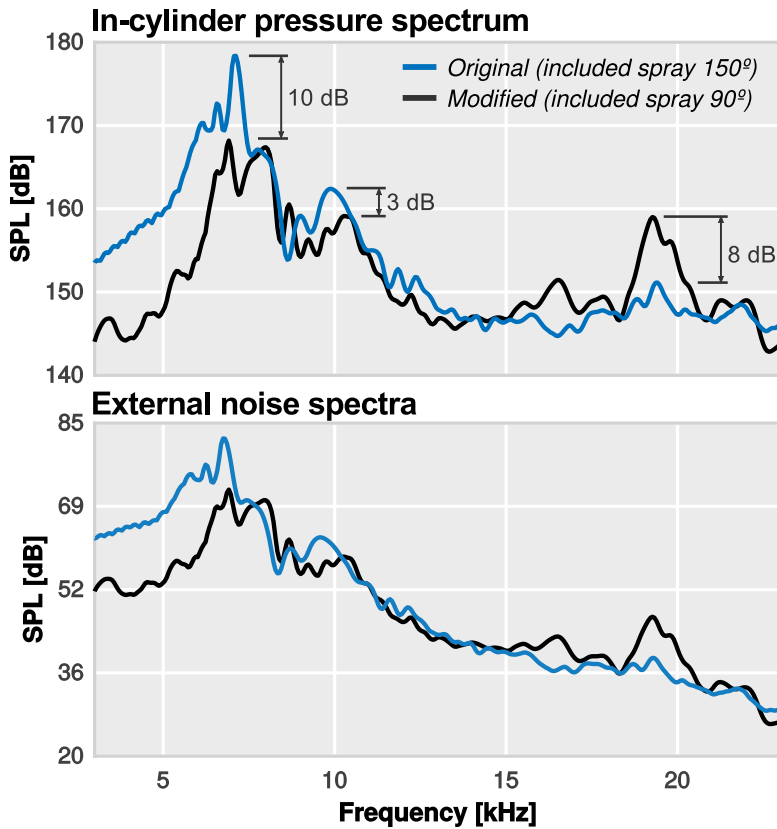
Figure 7.12: *Comparison between the averaged SPL of the original simulated combustion cycle and the SPL of the modified combustion with spray angle 90°, considering both in-cylinder (top) and radiated (bottom) field spectra.*

7.3. Design optimization strategies

As can be concluded from previous sections, in which several parameters either related to the engine operating settings and/or hardware configuration have been modified, parametric studies or DoE strategies have demonstrated to be a useful tool if they are combined with CFD to inspect main trends when only a few parameters, 3 or 4 as much, are changed.

However, some added difficulties appear when the number of parameters to be inspected grows, increasing the complexity of the analysis and therefore the workload of design engineers.

This encouraged development of additional techniques for the identification of optimization pathways with respect to combustion chamber design [102] or engine operating conditions [112, 113]. The interest in opti-

mization methods based on genetic algorithms (GA) has increased in the automotive industry over the last few years due to the wide range of solutions they offer in combination with CFD. Several studies [210, 211] have applied this technique to diverse engine applications in which the number of optimized parameters is relatively high. For instance, Senecal & Reitz [157] optimized the combustion chamber design of a CI Diesel engine with six design parameters considering emissions and performance. Sun & Wang [212] combined GA and artificial neural networks for optimizing the intake port design of a spark-ignited engine with four control parameters. However, till date, combustion noise control has not been employed as a criterion in engine design optimization studies.

In this section, a novel numerical methodology was implemented for optimizing the combustion system in the Diesel CI engine considered so far. Besides the performance and emissions (NO_x and soot), engine noise was also included as an objective parameter. In this regard, specific considerations were made pertaining to the CFD model parameters that could affect the estimation of the in-cylinder pressure field, and subsequently, the noise emissions. Although one of the objectives of this study is to contribute to the understanding of the relationship between noise emissions and chamber geometry in CDC, the subsequent goal is to develop a general technique which could also be applied to new combustion modes such as HCCI or PPC in different engine configurations.

It is noted that NO_x and soot emissions predicted by the CFD model could not be compared with direct measurements as it was not possible to measure these pollutant emissions inside the anechoic chamber. Nevertheless, based on the authors' experience, Hiroyasu soot model [151] and Zel'dovich mechanism [152] are expected to provide good estimations of soot and NO_x emissions, respectively. We employed them in various engine studies before and both emissions were reasonably well predicted when compared to exhaust analyser measurements. Examples of such validation can be found in Refs. [1] and [147]. Therefore, the CFD soot/NO_x predictions were considered to be sufficiently representative of the real emission levels in this study.

7.3.1. Simplified approach

Despite good agreement between simulations and experiments shown in Chapter 5, the CFD simulations were highly time consuming. This compromises their suitability for use with optimization techniques, such as genetic algorithms, that automatically refine the solution until an optimum is found after a large number of calculations.

Several modifications to the original model (using the URANS-Coarse setup) configuration were, therefore, made in order to minimize the calculation time while ensuring high accuracy.

First, the base mesh size was increased to 5 mm. All fixed embedding regions were maintained at the same levels of grid refinement. As a result, the walls, spray and AMR regions had a minimum cell size of 0.625 mm whereas the resolution of the mesh in the chamber was reduced to 1.25 mm during the combustion event. In addition, the maximum sonic CFL number was set to 2 during combustion.

Finally, the total simulation time was reduced to the closed cycle, encompassing only the time between IVC and EVO. Furthermore, the simulations were initialized by a non-uniform spatial distribution of thermodynamic conditions and species concentrations. This was obtained from a previous simulation of the gas exchange process using the original baseline model set-up. Although the calculation time is considerably reduced with these modifications, the conditions at IVC may notably change when the combustion chamber is modified. In view of this, a preliminary analysis was carried out to check the accuracy of the simplified model. In this case, the nominal injection specifications of operating Point #7 were varied to cause significant changes in emissions and ISFC levels. In order to calculate the ISFC parameter for closed-cycle simulations, results from the previous gas exchange process simulation were utilized, thereby using a common pressure trace from the BDC (compression stroke) to IVC and from EVO to the BDC (expansion stroke) among all calculated cases.

Figure 7.13 depicts the results of this study. It can be observed that the simplified model does not predict the exact values of all considered parameters. However, trends are properly reproduced, showing a reasonable level of agreement with the original model solution.

These modifications reduced the calculation time by almost 80% while ensuring a correct reproduction of the observed trends in the most relevant parameters. Nevertheless, any solution obtained by this simplified approach was later verified using the original model set-up.

7.3.2. Genetic algorithm optimization strategy

The combustion system optimization was performed using a genetic algorithm approach, which operates following the principles of evolution, where citizens in a population evolve over subsequent generations –with successful characteristics passing on genetically to children. This method has been demonstrated to be suitable for finding the global optimum solutions of complex multi-variable problems related to engine optimization, such as combustion chamber [102, 213] or intake port design [212].

Although there are many different styles of GA, they share a common underlying framework. The mathematical algorithm attempts to imitate the natural evolution by generating a population of candidates, or generation of citizens, which are subjected to a quality test. The best candidates are then selected to produce a new generation of citizens with better traits. In addition, it incorporates random variations of the best traits in order to mimic aleatory genetic mutations viewed in the nature.
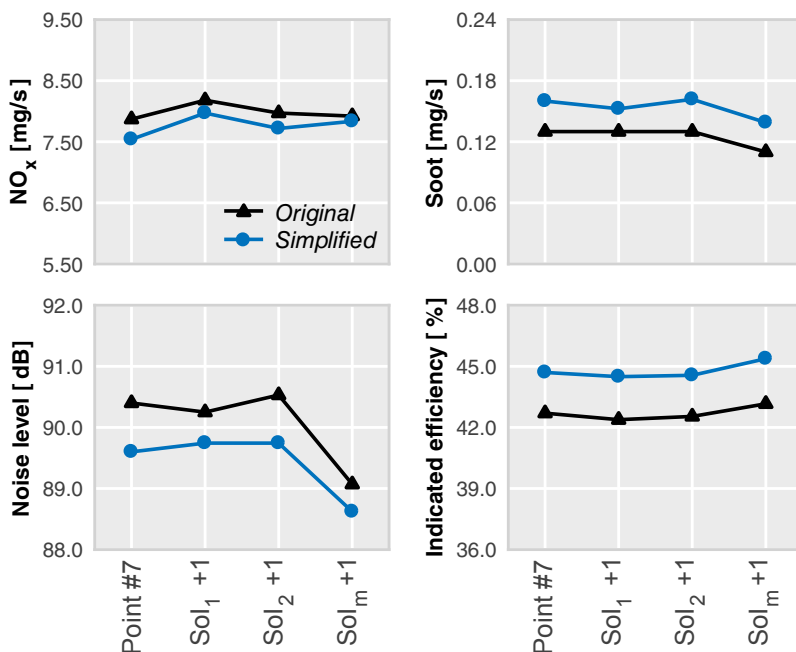
Figure 7.13: *Comparison between the solutions (emissions and ISFC) of the simplified model and the original model set-up. The injection settings of Point #7 were modified by delaying the start of each injection (SoI) timing: first pilot (1), second pilot (2) and main (m) injections, by 1 crank angle degree.*

Differences reside in which mathematical approaches are used to mimic these aspects. In the GA used in this study, each generation is produced by using the Punnett diagram [102, 214] where the best five citizens of the previous generation become the parents of the new generation. Consequently, the size of the population, which depends on the number of parents, is equal to 25 in this study.

Once the generation is created, each chromosome (optimizing parameter) of every citizen is then mutated. The original value of the chromosome is adjusted by a normally distributed random number. The standard deviation of this random distribution is exponentially reduced as the genetic algorithm progresses, thereby causing the mutation rate to decay. This approach allows exploration of the whole design space in the early steps of the GA, whereas in the final generations the solution is forced to converge.

The main goal of this optimization procedure is to reduce combustion noise and fuel consumption without any emission penalties. The optimization was approached from the point of view in which noise emissions are reduced by the effect of lowering the resonance. Again, the operating Point #7 used in the validation, was selected as the baseline for the optimization, since this point exhibited the most unfavourable conditions from the point of view of the resonant noise emission.

In order to be consistent with the second strategy, the energy of resonance (E_{res}), documented in Appendix 3.4, and ISFC were prescribed as the two main parameters to be minimized by the GA. In addition, NO_x and soot emissions were considered as the constraint variables. Thus, citizens which surpassed the emission constraints were penalized. All these considerations were mathematically expressed in the form of an objective merit function (MF) as follows:

$$
MF = \frac{0.3481 \cdot \sum\limits_{n=1}^{2} \alpha_n}{\sum\limits_{n=1}^{2} \left(\alpha_n \cdot e^{\beta_n \cdot \frac{x_n - x_n^{target}}{x_n^{target}}} \right)} - \sum\limits_{n=3}^{4} \left(\max\left(1, \frac{x_n - x_n^{limit}}{x_n^{limit}} \right)^{\gamma_n} - 1 \right) \quad (7.3.1)
$$

$$
x_1 \longrightarrow E_{res} \qquad x_2 \longrightarrow ISFC \qquad x_3 \longrightarrow NO_x \qquad x_4 \longrightarrow soot
$$

Where x_n is the value of each output parameter for a given engine design candidate, x_n^{target} is an optimistic estimation value of either resonance energy or ISFC, whereas x_n^{limit} refers to the emission levels achieved by the baseline configuration (emission constraints). Finally, α_n, β_n and γ_n are weighted constants for specifying the influence of each parameter on the merit function.

Table 7.2: *Summary of the constants and reference values in the merit function.*

Parameter	E_{res}	ISFC	NO_x	Soot
α_n	3.0	2.0	-	-
β_n	2.0	2.0	-	-
γ_n	-	-	15	0.5
x_n^{target}	0.1 kPa²·s	150 g/kWh	-	-
x_n^{limit}	-	-	7.54 mg/s	0.16 mg/s

Table 7.2 shows the constants and reference values considered in this study. All these constants were prescribed based on a previous sensitivity analysis and several simulations with the baseline configuration. A set of citizens were artificially created and ranked by taking into account several subjective factors. Then, different combinations of possible constants were applied to all individuals of the population. Finally, the set of constants that better recreated the defined ranking were considered in the merit function.

Eight parameters related to combustion system design were chosen as inputs for the GA. Five of them were related to combustion chamber geometry, two were related to injector configuration and the last one was associated with the design of intake ports.

The generation of realistic and coherent combustion chamber designs was one of the most complex steps in this procedure. Chamber geometry can be very intricate which, in turn, complicates its recreation with only few parameters. Here, a piston bowl profile generator was implemented using Bezier polynomial curves and five optimizing parameters [102, 207]. As can be seen in Figure 7.14, this method offers a wide range of possible chamber designs, from large open bowls to tight and highly re-entrant ones. The only restriction imposed on the chamber generation was the compression ratio, which was set to be the same as in the baseline case. The compression ratio was kept constant by adjusting the free squish height. However, in some cases where the proposed geometry couldn't match the specified compression ratio, it was discarded and a distinct set of random mutations were applied to the geometric parameters to generate a new one.

The two parameters considered to optimize the injector configuration were the spray included angle to guide the fuel within the piston bowl, and the number of injector nozzle holes. In all cases, the total fuel mass injected, total nozzle area and injection pressure were kept constant. Therefore, nozzle diameter of the injector holes were adapted to maintain the overall

Baseline geometry **Bowl geometry #2**

Bowl geometry #3 **Bowl geometry #4**
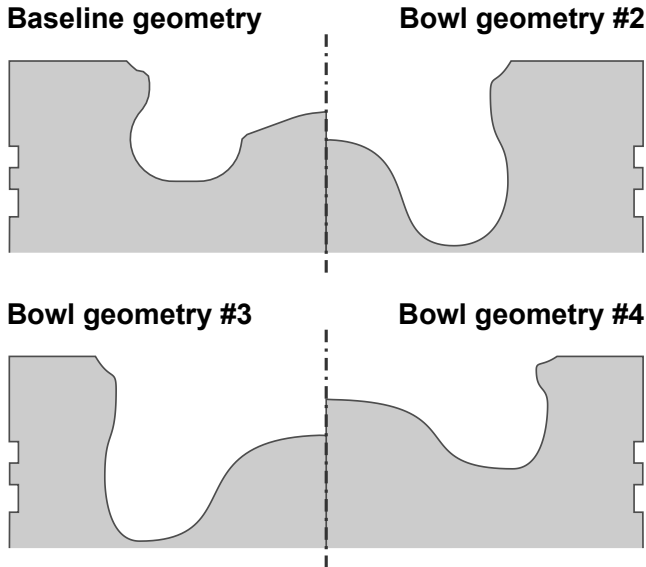
Figure 7.14: *Examples of different bowl profiles obtained by the Bezier polynomial method [102, 207].*

injection area, assuming that the discharge coefficient remains constant for every hole. Therefore, the nozzle diameter was decreased as the number of nozzle holes were increased.

The design of intake ports was indirectly optimized by considering the swirl number at IVC as an optimizing parameter in the GA loop. The magnitudes of the velocity components at initialization were accordingly adjusted so as to correspond to a given value of swirl number.

Table 7.3: *Ranges of the input parameters considered for GA optimization.*

Geometric parameter 1 [-]	0.01–0.99
Geometric parameter 2 [-]	0.01–0.99
Geometric parameter 3 [-]	0.01–0.99
Geometric parameter 4 [-]	0.01–0.99
Geometric parameter 5 [-]	0.01–0.99
Number of injector nozzles [-]	4–12
Spray included angle [-]	80–180
Swirl number at IVC [-]	0.0–2.0

The ranges of all the input parameters in the design space are listed in Table 7.3. These parameters and their ranges of variation were selected by taking into account possible technological limitations such as minimum injector orifice diameter and maximum bowl depth.

Results from the optimization procedure are then presented as follows:

- First, the convergence of the GA is verified and trends of the output parameters are analyzed.

- Then, the comparison of the results between the simplified and original model setups is inspected.

- Finally, the outputs of the optimized configuration are compared against the baseline case and in-cylinder acoustic effects are analyzed in detail to understand the noise generation mechanisms.

7.3.3. Optimization results

As the first step, algorithm convergence was verified to ensure that the GA reached a unique global optimum. Although convergence is mathematically determined since the mutation variability is reduced as the GA progresses, the attainment of the best solution after a given number of generations defined a priori is not guaranteed. For this reason, the progression of the merit function as the GA progresses was tracked as shown in Fig. 7.15. Besides the MF values for every simulation, the generation averaged value and the generation dispersion (±SD) are also included in the graph. It can be seen that the average and dispersion are significantly reduced after the 12th generation (300th simulation). Nevertheless, the solution continues to improve even after the 20th generation (500th simulation). After this point, the average remains practically constant. The dispersion however keeps oscillating until the 27th generation (675th simulation), after which it becomes reasonably constant. Observing this progress, the optimization was stopped after the 29th generation and the GA was considered to have converged.

Subsequently, the inspection of the target and constraint parameters was carried out in order to check the solution success and compliance with the constraints. Figure 7.16 shows the progress of these parameters during the optimization procedure. The graphs at the top show how both soot and NOx emissions move towards their respective constraint values, reaching a final solution which practically coincides with these values. The middle graphs show notable improvements in both the objectives: while the energy of
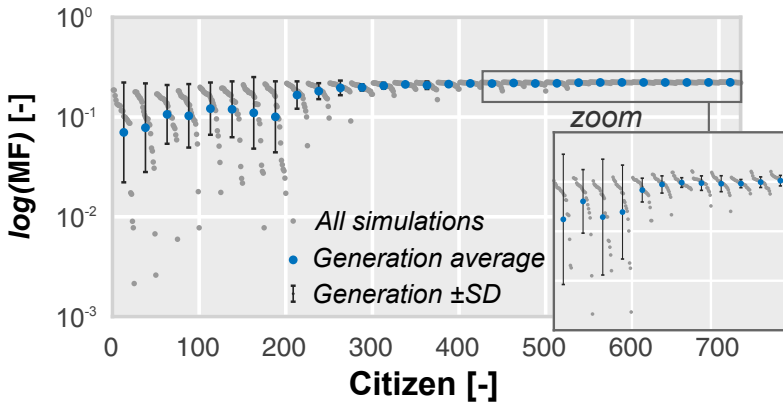
Figure 7.15: *Evolution of the merit function as the genetic algorithm progresses. An acceptable convergence is achieved after 29 generations.*

resonance is reduced by almost 70%, the ISFC exhibits an improvement of 2%. The bottom plots are included to illustrate how these improvements affect the overall noise and indicated efficiency. It can be observed that noise emissions are reduced by acting directly on the resonance phenomena whereas the indicated efficiency is increased. This fact confirmed the suitability of this strategy for lowering noise emissions as described in the previous section.

In addition to the general trends observed in these parameters, in Table 7.4, a comparison between the baseline and optimized specifications is included to quantify the maximum improvement in all the relevant output parameters. As observed in the previous trends, the energy of resonance is lowered the most, so the overall noise is reduced by more than 1 dB. Moreover, indicated efficiency increases by 1.8%, whereas both pollutant emissions are maintained below their baseline levels.

Table 7.4: *Comparison between the baseline and optimized configurations. All relevant parameters are included to observe the changes in the main engine outputs.*

Configuration	Baseline	Optimized
E_{res} [kPa$^2\cdot$s]	5.95	1.53
ISFC [g/kWh]	188.3	184.9
NO_x [mg/s]	7.54	7.48
Soot [mg/s]	0.16	0.12
Overall noise [dB]	89.6	88.2
Indicated eff. [%]	44.7	45.5

Constraints:
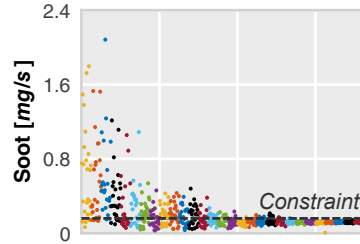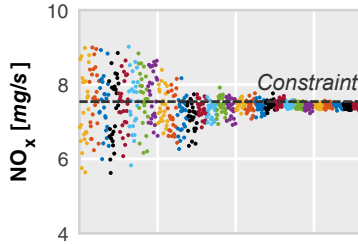
Objectives:
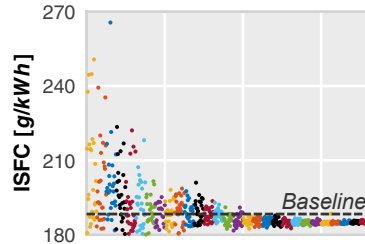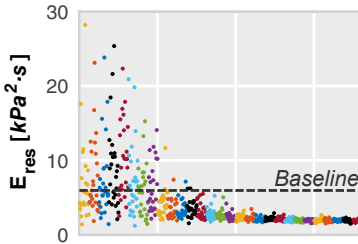
Indirect objectives:
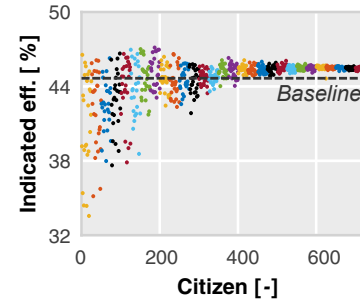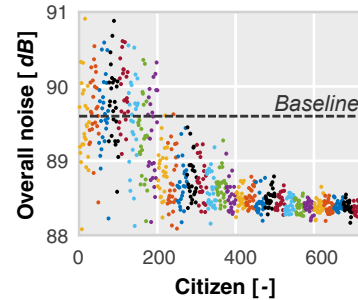
Figure 7.16: Progress of objectives and constraints towards the optimum solution. The final targets (indirect objectives) of the optimization are also included.

The optimized configuration was further examined to determine which design parameters had changed to a greater extent. Hence, all the design parameters of both specifications are included in Fig. 7.17 for comparison. The optimized geometry exhibits a deeper and tighter bowl profile with a less re-entrant shape. The number of injector nozzle holes increases up to 12, as a result the nozzle diameter is also reduced. Finally, the spray included angle is expanded by 13.4 degrees while the swirl number is slightly higher. These changes in the injector configuration and swirl would enhance the mixing rate and minimize spray penetration, thereby avoiding an excessive spray-wall impingement during the injection event.

7.3.4. Coherence of the results

As mentioned previously, certain modifications were made to the original model set-up in order to reduce the computational time for the optimization. Although results of this modified model were considered sufficiently accurate since it captured the main trends of the original solution, the coherence of this solution must be verified by simulating the optimized system with the original model set-up.

Therefore, a series of consecutive engine cycles using the optimized configuration were simulated with the original base mesh size (3 mm) and fixing the sonic CFL number to 1. As the design of the intake ports was indirectly optimized by the swirl number achieved after the gas exchange process, the velocity field was adjusted at IVC of each cycle to achieve the swirl number demanded by the optimized design. Following this approach, it was possible to modify the swirl motion during combustion without intake pressure changes, thereby allowing a fair comparison between the two combustion systems. It was thus assumed that the new design reaches a high swirl with the same intake pressure.

Baseline bowl geometry

Optimized bowl geometry

Configuration	Baseline	Optimized
Spray included angle [deg]	75.0	83.4
Number of nozzle holes [-]	6	12
Swirl number [-]	1.26	1.69
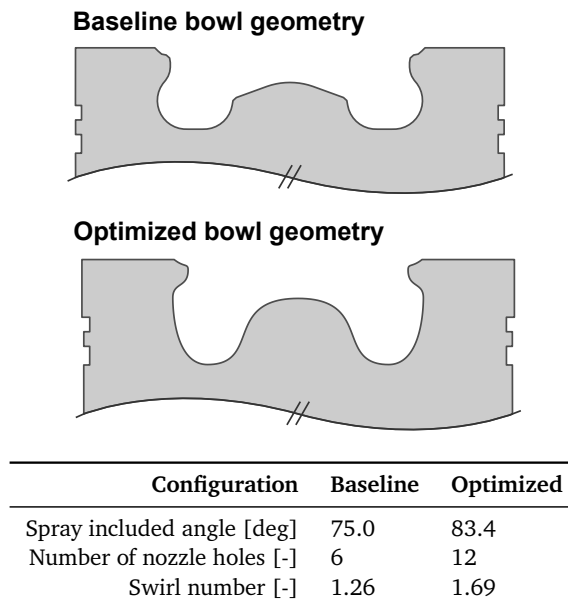
Figure 7.17: *Comparison of the baseline and optimized configurations. Baseline bowl profile is plotted together with the optimized bowl geometry (top) whereas the injector and flow motion parameters are shown in the table (bottom).*

Table 7.5: *Comparison of the predictions between the simplified and original model set-ups.*

Setup	Simplified model		Original model	
Configuration	**Baseline**	**Optim.**	**Baseline**	**Optim.**
NO_x [mg/s]	7.54	7.48	7.87	7.85
Soot [mg/s]	0.16	0.12	0.13	0.10
Overall noise [dB]	89.6	88.2	89.9	89.3
Indicated eff. [%]	44.7	45.5	42.7	43.6

The solution was considered converged after the third cycle, since the pressure trace and spectrum registered at the transducer location did not show any relevant dispersion.

Table 7.5 summarizes the results for the two model set-ups with both combustion system designs. It is evident how the simplified model causes the same effects on the solution in both designs. Every parameter which is overestimated in the baseline design (soot and indicated efficiency levels), is also overestimated in the optimized one, with the simplified model. In the same way, this behaviour is also replicated in every underestimated parameter (NO_x and overall noise levels). This fact evinces the consistency between both the numerical models, since they reproduce the trends even when the system configuration is completely modified.

Apart from this, the differences in NO_x, soot and efficiency levels between the two numerical models for the same engine configuration, show great similarity. For instance, between the two numerical set-ups, NO_x emissions vary by 0.33 mg/s for the baseline configuration whereas the difference for the optimized one is 0.37 mg/s.

However, this difference between the numerical set-ups is noticeably higher for noise levels. It is around 0.3 dB for the baseline, whereas in a case of the optimized configuration, a 1.1 dB of difference is seen. As it was emphasized in Chapter 4, local thermodynamic conditions before ignition govern the combustion phenomena and its subsequent in-cylinder pressure field effects. Therefore, limiting the simulation to the closed cycle and initializing the simulation with the results of the previous gas exchange process using the baseline configuration, may affect the prediction of noise levels when the geometry is highly modified, since local thermodynamic conditions can change notably.

Despite this slight discrepancy, the simplified solution offers a good prediction of the main parameters and it achieves the optimization objective: it gives a combustion system configuration which reduces noise emissions

while pollutant emissions and efficiency levels are maintained at the baseline level. Thus, even though not perfect in terms of prediction, the proposed approach is still a very reliable tool for incorporating combustion noise of CDC in optimization methods.

7.3.5. Acoustic analysis

In addition to consider combustion noise control in optimization strategies, another important aspect of this investigation is to reproduce the pressure oscillations that are present in a real engine and are responsible for resonant combustion noise. Again, the comprehension of such complex phenomena is critical to devise strategies for combustion noise mitigation.

The numerical pressure data available from the simulations, once validated, can then be analysed through different techniques to reveal the real behaviour of the in-cylinder pressure field, thus providing valuable information about pressure oscillation modes, their characteristic frequencies and their temporary evolution. However, the complexity of the resonant acoustic field complicates even a simple recreation for visualization purposes and hinders a correct interpretation of the involved phenomena.

The procedure followed in Section 6.2 was therefore applied here to examine the changes in the acoustic signature of combustion, thereby overcoming the inherent difficulties in the comprehension of such phenomena.

Hence, the first way to explore the spatial distribution of the acoustic pressure field for different frequency phenomena of interest is to perform FFT at each cell record in the considered domain. Then, the dispersion of the high frequency spectra gives an idea, at least in a qualitative way, about the variability of the pressure field in the combustion chamber.

Figure 7.18 exemplifies this procedure; the averaged pressure spectra are plotted together with the spatial variation, represented by the standard deviation (±SD), for both configurations considered so far. Interesting information can be obtained about the most excited modes from this comparison. It appears that the acoustic energy is shifted towards higher frequencies for the optimized configuration. Consequently, new resonant modes experience a notable lowering of amplitude, causing the reduction of the overall resonant noise. If we compare both external noise spectra, also included in the bottom graph of this figure, it is possible to notice that this acoustic energy is move towards frequencies less perceptible by the human hearing. Note that the increment of higher frequency amplitudes is heavily attenuated by the engine structure but also by the hearing system. The spatial variability
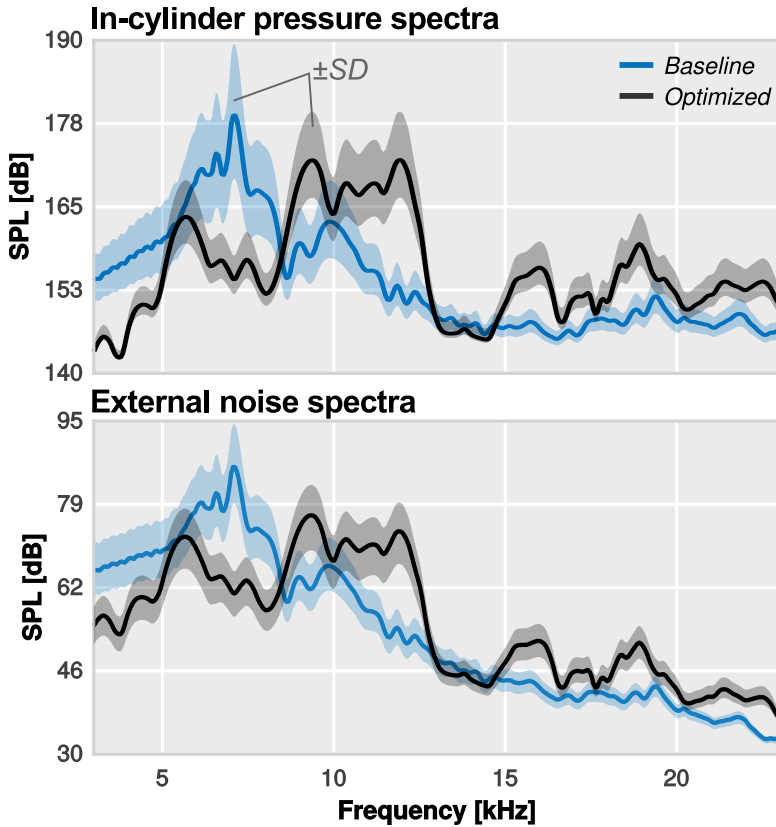
Figure 7.18: *Comparison of the in-cylinder pressure spectra trends. The pressure spectrum averaged over all cells in the domain is plotted with its standard deviation for both configurations (baseline and optimized).*

is also reduced in the frequencies for which the modes are attenuated (6 – 8.5 kHz) and, conversely, it is increased at the harmonics with higher level of excitation (8.5 – 13 kHz and 15 – 20 kHz).

Although this information sheds some light on the in-cylinder pressure field, it becomes impossible to imagine how this field is locally changing, given the limitations of this method. Some studies have taken a step forward by combining FFT, band-pass filtering and multiple monitor points in the combustion chamber in order to overcome these limitations. However, they still missed the temporal evolution of each acoustic mode. In this context, POD is a viable tool suitable for identifying which spatial structures comprise most of the energy of the flow field.
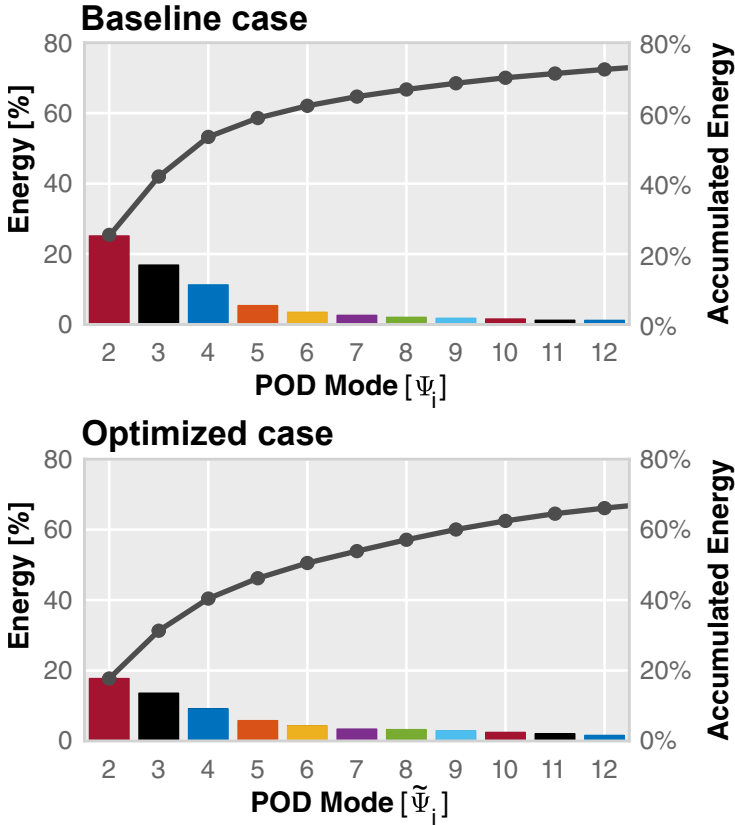
Figure 7.19: *Pareto charts showing the energy contributions of POD modes Ψ_{2-12} and the accumulated contribution to the resonance energy in each configuration: the baseline (top) and the optimized (bottom).*

A POD analysis of the in-cylinder pressure field was carried out to address the limitations of previous methods mentioned above. Orthonormal POD modes (Ψ_i) and their corresponding energy of excitation (obtained from their principal values σ_i) were obtained, together with the temporal evolution coefficients ($\mathbf{a}_i$).

In order to characterize the relevance of each mode, its contribution to the total resonance energy was analysed, as shown in the Pareto charts of Fig. 7.19. It can be seen that, for the baseline configuration, the first three modes Ψ_{2-4} account for the major part of this energy while the energy distribution for the optimized configuration is more equitable. Note that the first mode related to the mean homogeneous pressure is again disregarded in this study.

The pressure amplitude associated with each set of coordinates is plotted in Fig. 7.20 using a set of iso-volumes. POD modes Ψ_{2-6} are thus displayed by showing the upper and lower 10% tails (i.e., the 10% and 90% percentiles) of the distribution of their amplitudes. Only the five most energetic modes were included in the analysis since they exhibited the most meaningful differences between the two designs.

Inspecting the shapes of modes Ψ_2 and Ψ_3 in Fig. 7.20, it can be clearly observed how the higher amplitudes are oscillating on opposite sides of the squish zone, in two different orientations. In contrast to these, POD mode Ψ_4 features a completely circular distribution between the squish zone and the bowl, with an annular nodal region instead of a straight one like in the previous modes.

There is another interesting aspect in Fig. 7.20 which can provide additional information about the resonant modes' behaviour. It can be seen how the spatial distribution of the most energetic modes are remarkably different in both engine configurations.

Recalling the energy distribution of the modes plotted in Fig. 7.19, the energy share and spatial distribution of POD modes $\widetilde{\Psi}_{2-6}$ are plotted in Fig. 7.21, along with the corresponding most closely resembling modes of the baseline ($\Psi_{2,4,5,6,9}$). This figure shows how the modal energy has shifted from the original to the modified combustion, i.e., how the spatial distribution of the unsteady pressure fluctuations has been affected by the change in engine design. It can be seen that $\widetilde{\Psi}_{2-3}$ modes which were previously ranked fifth and sixth ($\Psi_{5,6}$) with 5.36% and 3.48% of the energy, are now the most relevant with an energy share of 17.73% and 13.57%, respectively. Modified mode $\widetilde{\Psi}_4$ is found to closely resemble the original Ψ_4 mode. Its energy content, on the other hand, has been slightly diminished. Finally, mode Ψ_9 for the original bowl has been promoted to the sixth place $\widetilde{\Psi}_6$ for the optimized configuration, with almost three times its previous energy. Therefore, it is possible to claim that the transfer of resonant energy to higher frequencies, which was observed in Fig. 7.18, is also accompanied by a change in the spatial distribution of the pressure field.

The information contained within the POD data also allows the analysis of the evolution of each mode in time and frequency domains. In Fig. 7.22, the frequency content associated to $\Psi_{2,5,9}$ and $\widetilde{\Psi}_{5,2,6}$ modes is presented. It is evident that each POD mode is associated with a specific frequency band. These modes were specifically selected to illustrate the effects described in Fig. 7.18. For instance, modes Ψ_2 and $\widetilde{\Psi}_5$ clearly mimic the reduction of the pressure spectra gathered between 5 and 8.5 kHz.
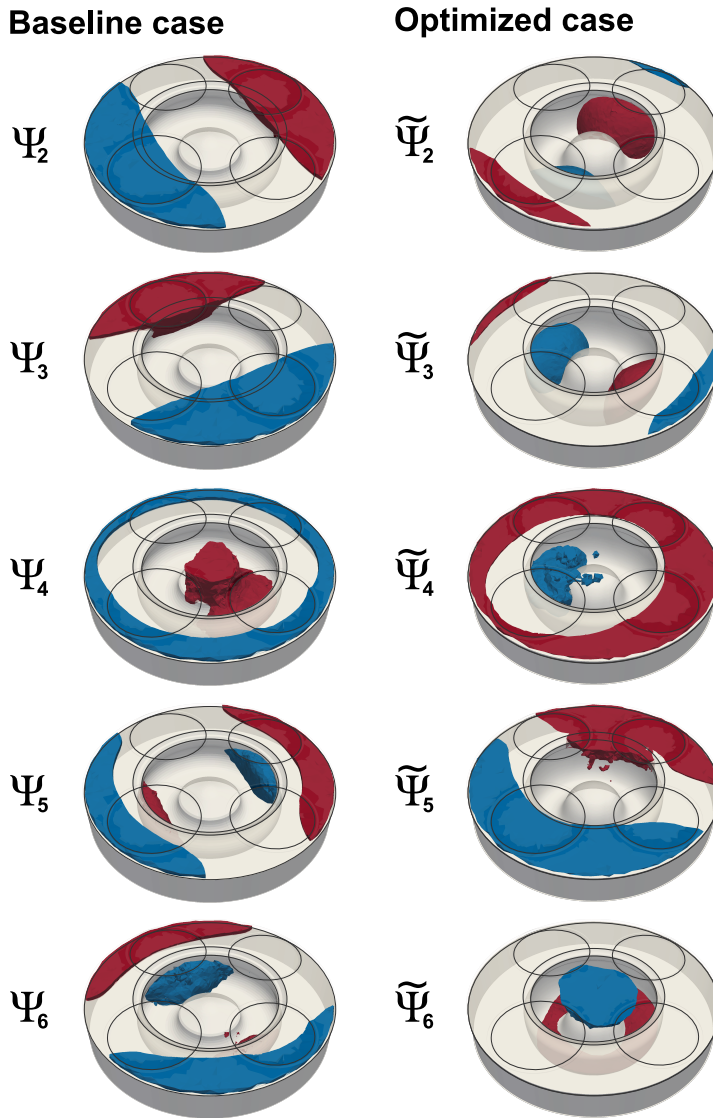
Figure 7.20: *Spatial distributions of the POD modes Ψ_{2-6} across the simulated combustion chamber. Each mode is represented by coloured iso-volumes indicating the 10% (blue) and 90% (red) percentiles of the distribution of the real values of each individual mode.*
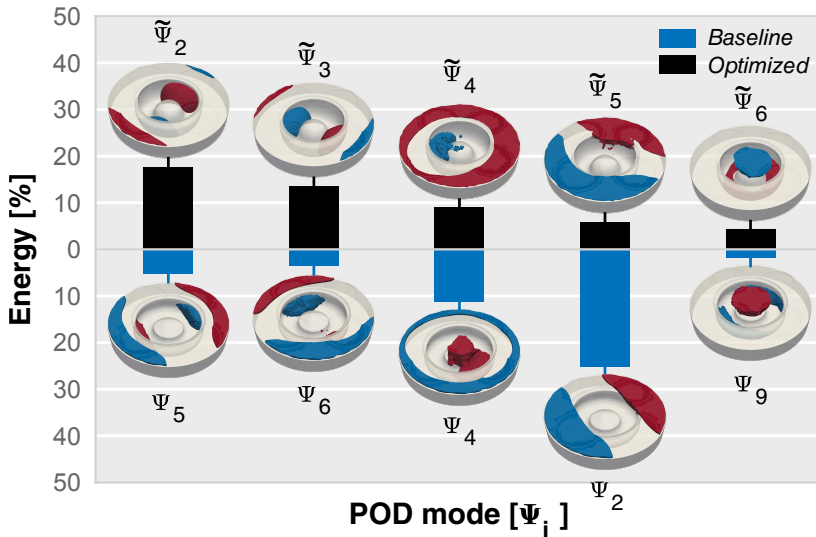
Figure 7.21: *Energy share and spatial distribution of the five most relevant optimized design modes $\widetilde{\Psi}_{2-6}$ (top), together with their most closely resembling baseline counterparts (bottom).*

In a similar way, the rest of the represented modes aim to reproduce the energy increase observed for the frequencies comprising 8.5 – 13 kHz and 15 – 20 kHz. Again, this clearly depicts how the pressure field changes its spatial distribution as the frequencies being excited vary. On the other hand, it is interesting to note that the energy of the modes is progressively concentrated within the bowl as the frequency increases, going from completely squish-dominated modes at 5 – 8.5 kHz to entirely inside-bowl oscillations at 15 – 20 kHz. Meanwhile a mixed effect of both is easily identifiable at 8.5 – 13 kHz.

Continuing this comparison, Fig. 7.23 displays the time evolution of these three specific modes, in an attempt to find possible relationships between the inception of these modes and different phases of the combustion process. The first plot depicts how the onset of mode Ψ_2 is coincident with the start of combustion of the first pilot. Moreover, the amplitude rapidly reaches its maximum value during the second pilot combustion phase. This mode is again excited during the diffusive combustion, with its amplitude increasing practically up to the highest value. Mode $\widetilde{\Psi}_5$ however, starts to develop after the onset of the second combustion phase and practically disappears very soon after the start of the third combustion stage. This indicates the relevance of the early pilot injections in the resonant noise generation, since they heavily contribute to the excitation of less energetic modes.
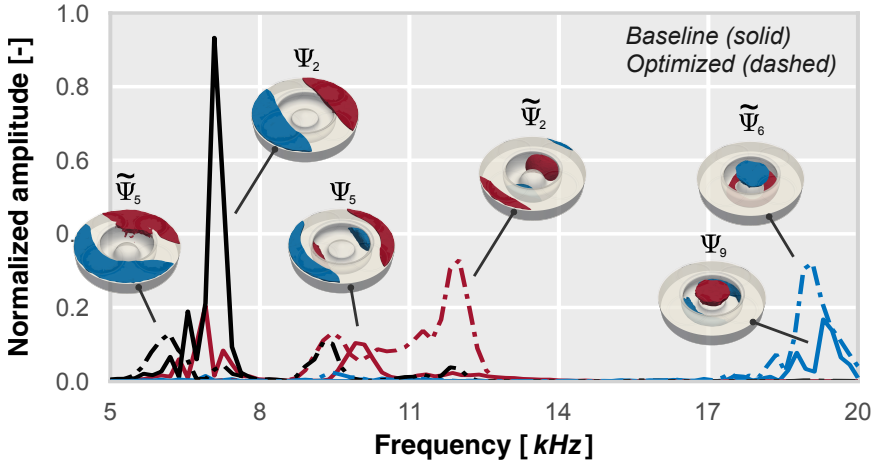
Figure 7.22: *Normalized amplitudes of POD modes $\Psi_{2,5,9}$ and $\widetilde{\Psi}_{5,2,6}$ in the frequency domain.*

In the second plot, both modes Ψ_5 and $\widetilde{\Psi}_2$ appear at the second ignition event, although the amplitude rise is much more pronounced for mode $\widetilde{\Psi}_2$ while for mode Ψ_5 the time evolution is essentially constant during the whole combustion. Furthermore, the amplitude of mode $\widetilde{\Psi}_2$ increases during the main combustion stage, reaching its maximum value at 10 cad aTDC.

Finally, the last plot shows the evolution of Ψ_9 and $\widetilde{\Psi}_6$ modes. Mode $\widetilde{\Psi}_6$ displays an amplitude rise at the start of the last two combustion phases but its intensity is severely attenuated due to its high characteristic frequencies. On the other hand, mode Ψ_9 shows little relevance after the second combustion onset, only exhibiting a significant amplitude during this short stage.

7.4. Conclusions

In this chapter a numerical methodology based on a combination of CFD modelling and optimization techniques, such as design of experiments or genetic algorithms, has been presented for the evaluation of combustion noise, efficiency and other relevant working parameters of a CI Diesel engine. With this, it has been possible to perform a qualitative analysis of the relationships between several engine settings, effects on combustion and response parameters, thus avoiding any costly experimental approaches.
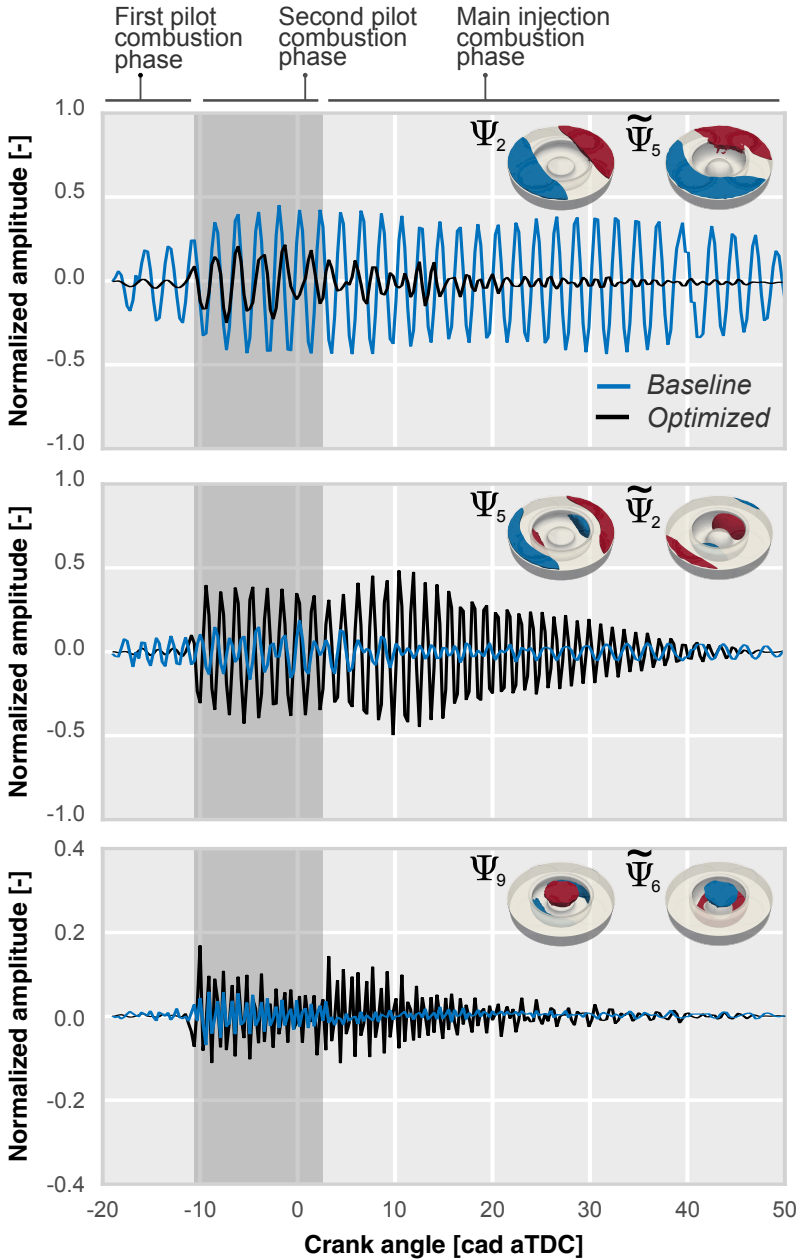
Figure 7.23: *Normalized amplitudes of the POD modes $\Psi_{2,5,9}$ and $\widetilde{\Psi}_{5,2,6}$ in time domain. The different combustion phases are also identified to connect possible combustion features with temporary changes in the time evolution of each mode.*

This work ratified again the two different paths, already deduced from chapters 2 and 3, to deal with the combustion noise issue. The first strategy consists in decreasing the maximum rate of pressure change by promoting smoother premixed combustions. As a counterpart, special attention must be paid to the cycle efficiency due to its direct connection with the combustion timing.

Results from the first DoE have revealed that the optimum configuration to maximize efficiency and minimize noise is to reduce the split between the second and the main injections, whereas the first pilot should happen as early as possible. On the other hand, the second DoE has shown a trade-off trend between noise and efficiency when the EGR rate and the injection pressure are varied. Additionally, the increase of the intake pressure allows a better compromise solution between noise, efficiency and NO_x emissions.

The second strategy is based on minimizing the contribution of the resonant oscillations. Its main advantage is that it offers independence of the cycle efficiency. However, a deep knowledge about the complex mechanisms related to resonance phenomena is required for its application. Therefore, techniques used in previous Chapter 6 have been applied again with the objective of providing better understanding of the source mechanisms of resonant oscillations and leading to some innovative way of addressing noise issues.

Advantage was taken of this spatial-frequency decomposition of the combustion to showcase a practical application where the spray angle was redirected in order to promote higher frequency bowl-dominated modes, since results have established these modes to feature higher frequency content, less perceptible by the human hearing. Results revealed an energy shifting between modes as the pressure excitation location is modified. The annular mode was promoted from third to first in combustion acoustic relevance, with the bowl-dominated mode almost quadrupling its energy share. Squish-dominated modal energy was however almost halved.

The intended effect of the modified modal content on the averaged acoustic levels of the combustion chamber was also validated, exhibiting a reduction of the sensitive mid-frequency content, at the cost of an increase in less adverse higher frequency content.

Despite the attractive benefits of reducing combustion noise by means of a simple modification in the injector design, the worsening attained in spray/bowl matching produces a drastic decrease in the indicated efficiency, and it also compromises the pollutant emissions levels.

As a consequence, a further step has been taken to optimize the combustion system design, with the target of controlling combustion noise while maintaining (or even improving) pollutant emissions and performance.

This methodology was employed to optimize the combustion system of a CI Diesel engine considering chamber geometry, injector specifications and in-cylinder swirl, in order to promote a quieter engine design by minimizing high frequency pressure oscillations. The new system was able to reduce noise emissions, owing to the lowering of resonance energy, since it modified the frequency content to feature higher frequencies, less perceptible by human hearing.

The optimized design included a deeper and tighter bowl geometry with higher swirl and greater number of nozzle holes with smaller nozzle diameters. The changes in the injector and swirl led to enhanced mixing rate and minimized spray penetration, thereby avoiding excessive spray-wall impingement during the injection event. Moreover, the spray included angle increased in order to match with the new bowl geometry.

In addition, a detailed analysis of the in-cylinder acoustic effects was carried out to understand the unsteady pressure field behaviour and to identify the most relevant noise issues. POD decomposition of the results for both the baseline and optimized designs was performed, revealing again the energy shifting between modes as a result of the different combustion system features. The most dominant mode, and thus the main source of resonant emissions, was significantly attenuated whereas the amplitudes of higher order modes were accordingly increased, albeit never reaching levels as high as the first one. Besides the frequency shift, the pressure field also experienced a change in spatial distribution. Specifically, the spectral content at 5 – 8.5 kHz was related to the squish-dominated pulsation, the 8.5 – 13 kHz frequencies featuring squish-bowl interaction and the higher frequency content at 15 – 20 kHz related to central top-down bowl oscillations. Finally, a relation between the inception of the modes and different phases of the combustion was identified, showing how early pilot injections significantly contributed to the excitation of less energetic modes.

These results highlight the advantages of the enhanced understanding of combustion chambers' time-spatial unsteady structures obtained in this work through frequency analysis and modal decomposition techniques. Specifically, combustion acoustics can be improved by identifying and tackling the most relevant modes, allowing automated optimization algorithms to

modify the combustion settings and/or chamber geometries in a more meaningful way, pursuant to the final objective of addressing the noise emission challenge faced by thermal-powered vehicles.

Noise in gasoline Partially Premixed Combustion

Contrary to what is observed in Diesel combustion, noise emission in gasoline PPC is principally managed by the combustion itself. The resonant oscillations within the chamber appear as a secondary source of noise that only constitutes a small part of the acoustic emissions caused by the combustion.

In consequence, the analysis showed in Chapter 6, in a successful attempt to identify all mechanisms present in noise generation and their impact on the resonant pressure field, can be avoided.

In this chapter the use of optimization techniques to find the most convenient design path is presented and discussed once again for the gasoline PPC concept. The objective here is to attain the noise problem from a practical point of view, instead of conducting complex phenomenological analyses. Prior to apply these techniques, a study of the operating outputs is shown in order to determine the principal constraints. Then, the numerical model is utilized to understand the trends observed experimentally. Thereafter, some injector configurations are suggested and further analysed to improve the concept capabilities, especially terms of noise emissions, performance and pollutants production.

Work in this chapter has been partly published in the following papers:

- *Combustion noise analysis of partially premixed combustion concept using gasoline fuel in a 2-stroke engine* [1]

- *Impact of the injector design on the combustion noise of gasoline partially premixed combustion in a 2-stroke engine* [2]

- *Potential of dual spray injectors for optimising the noise emission of partially premixed gasoline combustion in a 2-stroke engine* [7]

8.1. Main limitations of the concept

As stated in Chapter 3, the engine load and the acoustic emissions are closely connected, consequently operating at high loads entails serious noise issues. An operating condition defined by a medium speed and medium-high load (also denoted as operating point number #7' in Chapter 3) was chosen as baseline in the following studies.

A preliminary analysis was performed with the experimental results obtained with the SoE sweep of the main injection detailed in the same Chapter 3, in order to describe the gasoline PPC concept in terms of noise emissions but also in other relevant parameters such as efficiency or exhaust emissions.

Figure 8.1 shows the effect of shifting the main injection timing on some of these parameters. NO_x and soot results confirm the well-known simultaneous reduction in both pollutants with the advance of SoE_{main} as a consequence of delaying the combustion after TDC. This allows decreasing local temperatures, thus disabling NO formation, while lengthening mixture time and avoiding high local equivalence ratio zones. However, CO increases due to the lower local temperatures that hinder its oxidation reaction to CO_2 [79]. The low density conditions during early SoE_{main} also favour deeper spray penetration, and this results in more liquid fuel impinging the cylinder and piston surfaces. This fuel accumulation is the main source of unburned HC at the exhaust. So this simultaneous NO_x and soot reduction is attained at the expense of decreasing combustion efficiency.

Comparing the cycle efficiencies, the indicated power and combustion stability follow the same trend –i.e. they decrease when advancing SoE_{main}–, whereas the thermodynamic efficiency remains approximately constant. This indicates that the fraction of fuel that burns provides high thermal efficiency, but that it is not possible to burn all the injected fuel, due to the decrease in combustion efficiency. Therefore, the best way to obtain high indicated efficiency levels and low emissions is to keep the combustion efficiency as high as possible while delaying combustion.

On the other hand, combustion noise follows a trend similar to that of NO_x and soot emissions: in sudden and short combustion conditions with high local temperatures, the emitted noise is higher than that generated by soft and long combustions with low local temperatures.

As a result of the above discussion, there appears to be a new trade-off between combustion noise and combustion efficiency, which limits the applicability of the gasoline PPC concept. Significant reductions in engine noise –almost 6 dB in two extreme cases– can be achieved with a limited impact on combustion efficiency. However, even with this notable reduction,

noise levels are still so high and uncontrolled CO and HC emissions notably increase. Further analysis will be performed to understand why combustion noise generation is being changed while giving a comprehensive view of the connection among performance, noise and exhaust emissions.
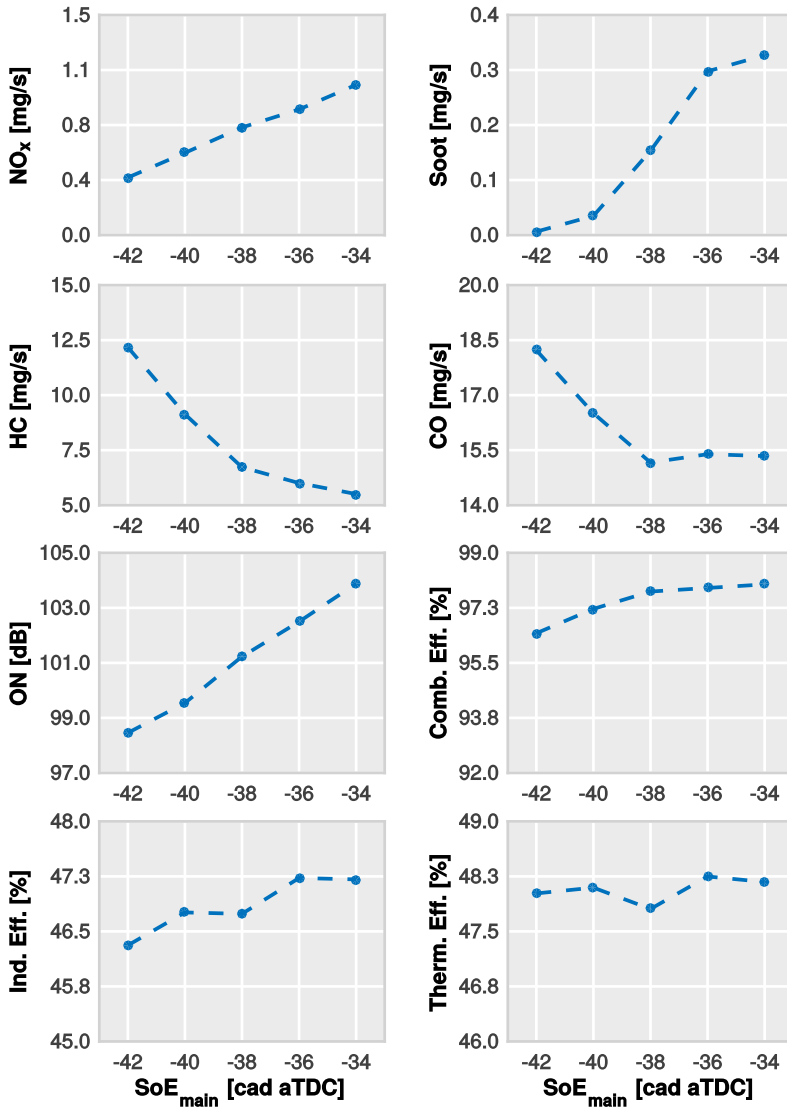
Figure 8.1: *Influence of SoE_{main} on exhaust emissions (NO_x, soot, HC and CO), engine noise (ON) and engine performance (combustion, indicated and thermodynamic efficiencies)*

Table 8.1: *Main running settings of the operation points considered for the* SoE_{main} *sweep.*

Point	#13'	#7'	#14'	#15'
Engine speed [rpm]		1500		
Number Injections [-]		3 (pilot + main + post)		
Injection pressure [MPa]		85		
Intake pressure [MPa]		0.275		
SoE_{main} [cad aTDC]	-34	-40	-46	-52

In the following studies, the CFD model is used to answer, or try it at least, the questions laid out so far. The idea lies on utilizing the model as a tool to complement experimental data. Then, with a better understanding of this matter, the study will be extended and the model will be used in numerical optimizations of the concept.

8.2. Analysis of an extended operating range

During the experimental tests the combustion stability was extremely deteriorated when advancing SoE_{main} beyond -42 cad aTDC to the point of reaching misfire conditions. The unfavourable gas thermodynamic conditions at this early injection timing, particularly in terms of pressure and temperature, increase both ignition delay and mixing time. As a result, local equivalence ratios tend to decrease down to very lean conditions, even achieving values below the ignition limit. This explains the deterioration in combustion stability and the misfiring observed experimentally.

An extended sweep of the SoE_{main} was performed using the CFD model and then presented in this section. In addition to point #7' conditions used as reference case, Table 8.1 shows the three additional cases calculated to complete the study. Two of these cases, designated as test #14' and #15' respectively, were simulated to extend the SoE_{main} range to -46 cad aTDC and -52 cad aTDC. A third case with late injection timing, designated as point #13', is included to extend the range to -34 cad aTDC and then beyond the knock-like combustion limit.

Both noise and efficiency results obtained from the SoE_{main} sweep described above are shown in Fig. 8.2, where experiments are also included to show the suitable agreement between both results.

As observed in the experimental study presented firstly in this chapter, ON reductions are achieved at the expense of engine efficiency losses. It is interesting to observe how decreasing the ON level down to the target
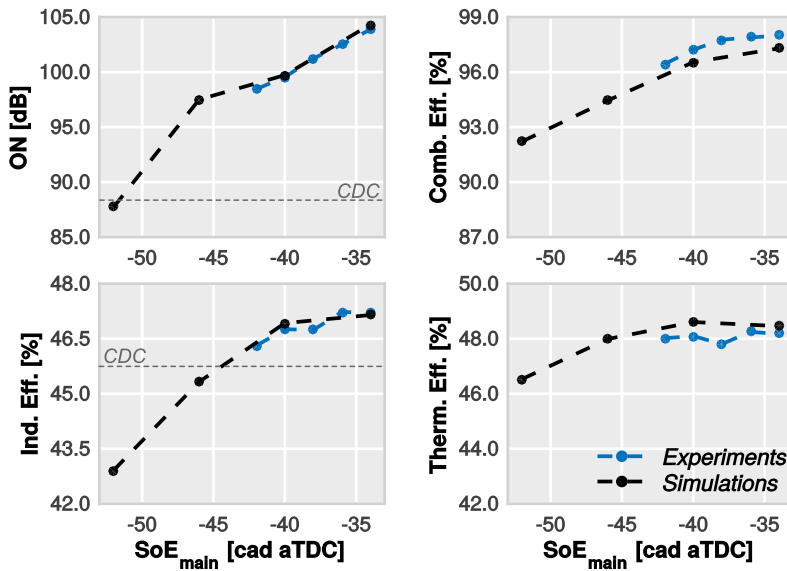
Figure 8.2: *Impact of SoE$_{main}$ on noise emissions (ON) and engine performance (combustion, indicated and thermodynamic efficiency)*

highlighted in the same graph –set on the basis of the equivalent running condition operating with the CDC concept– the indicated efficiency decreases to extremely low values, compromising the specific fuel consumption and consequently raising CO_2 emissions.

This figure also shows that this reduction in the indicated efficiency is mainly related to the combustion process deterioration in the SoE$_{main}$ range comprised between -46 and -34 cad aTDC.

In order to understand why combustion efficiency trends change when the main injection timing is modified, in Fig. 8.3 it is shown how the modified injection timing changes the impingement points of the sprays from the upper part of the bowl and the start of the squish in the baseline, to cylinder walls in the advanced injection timing.

As in previous studies, the sprays are visualized by clipping the equivalence ratio at the unitary value, enclosing the stoichiometric conditions within the spray.

Examination of the impingement points shows how a non depreciable amount of liquid fuel is deposited at cylinder walls. These deposits are not completely evaporated during the combustion, becoming sources of unburned HC and CO, since the temperature of cylinder walls is noticeably lower.

Baseline *(Point #7')*   **SoE$_{main}$ -52** *(Point #15')*

Excessive liquid film impingement at cylinder walls
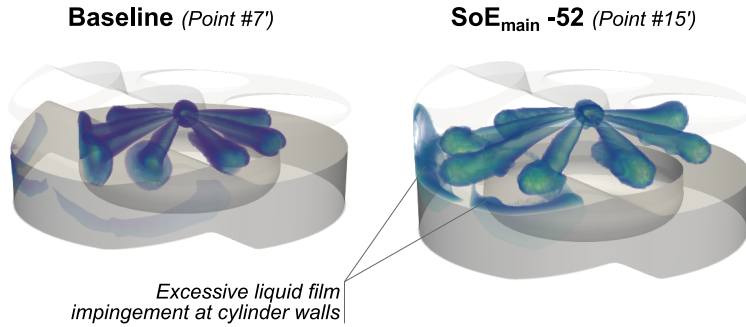
Figure 8.3: *Visualization of baseline and advanced SoE$_{main}$ sprays.*

However, as the SoE$_{main}$ is advanced beyond -46 cad aTDC, a secondary effect also contributes to the engine efficiency losses. In these cases the combustion takes place too late during the expansion stroke, producing less indicated work during the engine cycle and decreasing the thermodynamic efficiency.

In Fig. 8.4 in-cylinder pressure traces from both test #15' and baseline are compared in time and frequency domains. Examination of the top graph shows how the peak pressure decreases as the energy release rate is reduced by effect of the combustion delay. As can be seen, this burning rate lowering are also accompanied by an important reduction of both $(dp/dt)_{max}$ and E$_{res}$ parameters.

Focusing now on the spectra graphs, it is evident how the noise reduction is focused on medium-to-high frequency range. While the amplitude of medium frequencies is considerably reduced, the high frequency span shows a smaller attenuation.

This study confirms the narrow relation among the combustion noise and the burning rate in gasoline PPC: a less abrupt combustion process –characterized by smoother and longer RoHR profiles– results in lower combustion noise levels. Moreover, both experimental and numerical results showed a trade-off trend between ON and combustion efficiency, namely the increase in CO and HC emissions as the combustion becomes less noisy.

8.3. Conventional injector optimization

Being determined the operating limits, the injector configuration is modified in the subsequent study in an attempt of enlarging the operating range of the concept. This work was also made by using the CFD model operating with the baseline conditions (SoE$_{main}$ -40 cad aTDC).
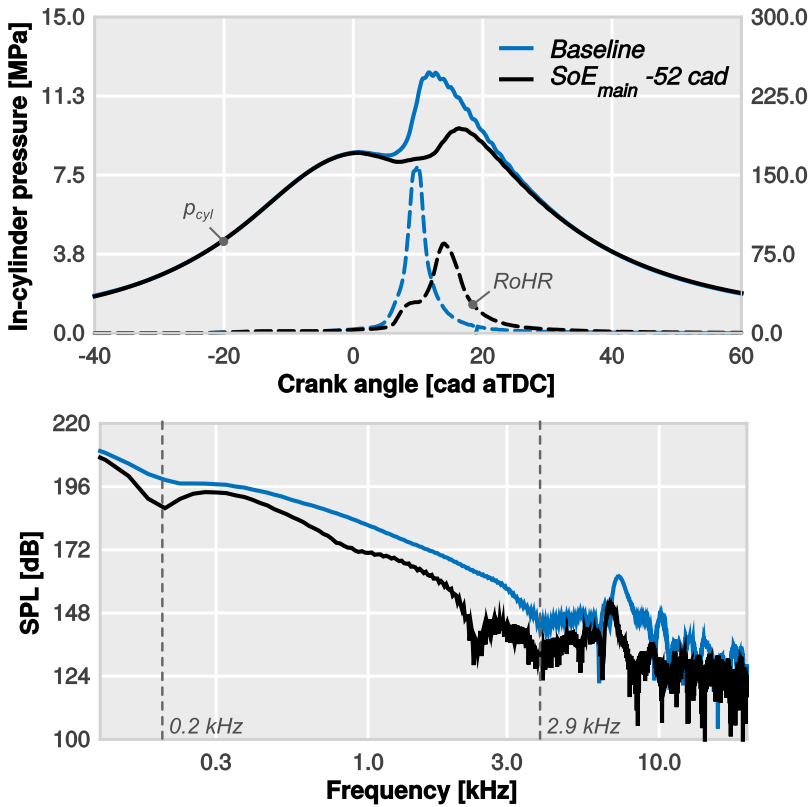
Figure 8.4: *Pressure trace comparison between baseline and early SoE$_{main}$ timings in gasoline PPC concept. In-cylinder pressure and RoHR traces are plotted at top whereas spectra are drawn at bottom.*

Two aspects were analysed according to injector modifications: in the first one the included spray angle (IA) was varied to guide the fuel to the centre of the bowl, and in the second the number of injector nozzles (NN) was modified, while the total injection area was kept constant. In both studies the injection rate remained fixed. Moreover, the nozzles diameter of the injector holes in the NN study was adapted to maintain the overall injection area, assuming that the discharge coefficient remains constant for every hole. Therefore, the nozzle diameter decreases as the number of nozzles increase. All details about both studies are included in Tab. 8.2.

Figure 8.5 shows the results of the two studies in terms of in-cylinder pressure and RoHR. Examination of IA study data (top graph) shows that the time delay is reduced for included spray angles below 148 degrees.

Table 8.2: *Injector configuration for all simulations studies in the conventional injector optimization.*

Set-up	IA [deg]	NN [-]	Nozz. diam. [μm]
#01[a]	148	8	90
#02	90	8	90
#03	110	8	90
#04	135	8	90
#05	148	12	60
#06	148	10	72

[a]Baseline configuration

With these values of IA the spray is fully directed towards the interior of the bowl where the local temperatures are higher and the spray mixing is more efficient. Since the mixing rate is increased, the ignition delay is too small to achieve lean mixtures, causing high reaction blends at the start of combustion. The combustion tends to become sharper and shows a maximum peak value for the RoHR approximately constant.

For the NN study, the ignition delay is reduced as the number of nozzle holes increases. Mixing conditions and local temperatures reduce this time gap by achieving more reactive blends. However, the duration of the combustion remains nearly constant while the maximum RoHR is increased. In addition, in comparison to the IA study, the combustion process is less abrupt with longer RoHR profiles.

Four typical acoustic parameters, widely used along this document and presented in Fig. 8.6 have been used to characterize the combustion noise behaviour in both studies.

Several effects can be observed in the in-cylinder acoustic field due to the combustion behaviour described above. The ON is significantly incremented if the IA is reduced below 148 degrees, achieving a steady value around 104 dB. This parameter rises as NN increases but, in this case reaches lower values.

If these parameters are compared with Fig. 8.6c, it is evident that the ON levels follow the same trends as exhibited by the maximum peak pressure rise rate. This replicates the conclusions obtained in Chapter 3, which claim that the main contribution to combustion noise radiation in gasoline PPC concept comes from $(\mathrm{d}p/\mathrm{d}t)_{\max}$ associated to the premixed combustion.
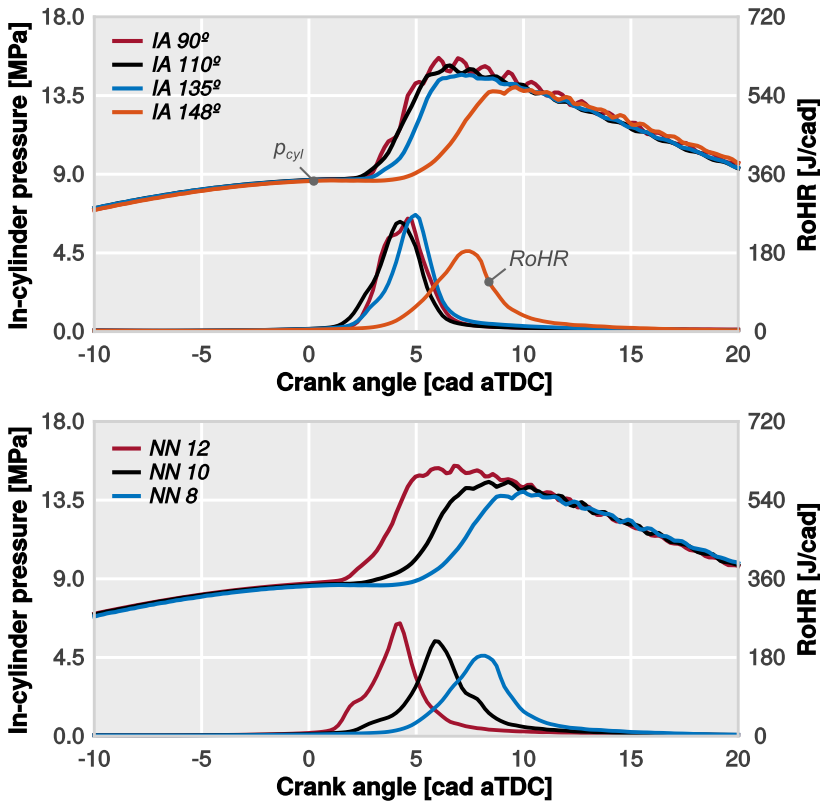
Figure 8.5: *Comparison of the in-cylinder pressure and RoHR traces. Data from the included spray angle study are plotted at top whereas the traces from the number of injector nozzles study are drawn at bottom.*

However, the similar $(\mathrm{d}p/\mathrm{d}t)_{\mathrm{max}}$ obtained in configurations #02 and #05 can produce different levels of overall noise. Indeed, set-up #02 and #05 present very close values of the maximum pressure rise rate, while the ON is almost 1.5 dB lower in configuration #05.

The analysis of Fig. 8.6d reveals that the energy of resonance is clearly higher in these two cases. Additionally, the gap between them is notable ($\simeq$32%) and it could explain the difference in the overall noise levels. Thus, contrarily to what was observed in Chapter 3, the resonance phenomenon can become an important aspect in some operation conditions, in which its high energy values affect the overall noise and also the acoustic signature.
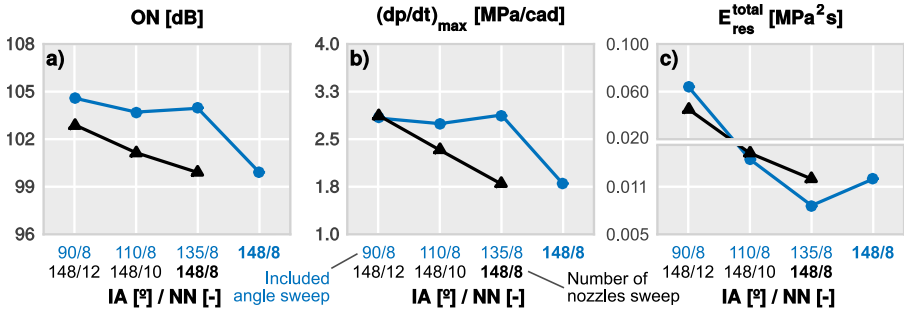
Figure 8.6: *Effects of the included spray angle and number of injector nozzles. a) Overall noise, b) Maximum pressure rise rate, c) Energy of resonance.*

Nonetheless, it is worth noting that these particular circumstances are produced under extreme conditions in which the burning rates are extremely large and noise levels widely exceed 100 dB.

Intuitively, the tendency is to think that the resonance phenomenon directly depends on the acoustic excitation intensity. In ICE this excitation is linked to the combustion process, with $(\mathrm{d}p/\mathrm{d}t)_{\max}$ considered as the main characterization parameter due to its direct relation with the fuel energy release.

However, it has been theoretically and numerically demonstrated that some additional parameters can determine the standing waves behaviour, modifying both the amplitude and the characteristic frequency of resonant modes. In fact, in Chapter 7 it has been shown how similar excitation levels obtained with different injector set-ups cause large differences in the energy of resonance. Moreover, recalling the previous figure it can be seen how tests #02 and #05 exhibit very high levels of resonance energy in comparison with tests #03 and #04.

As in prior studies, the RoHR was numerically integrated along the whole CFD domain with respect to the equivalence ratio (ϕ) and to the cylindrical coordinate (R^{norm}) in order to analyse both temporal and spatial features of the combustion process. The solutions are presented in Fig. 8.7 in which the horizontal axis of the contour plots represents the temporal evolution of the engine cycle, the vertical axis shows the integration variable (ϕ or R^{norm}) and the colour scale displays the RoHR.

The sequence of graphs displayed in the left column of this picture, describes the combustion process in terms of fuel stratification. In tests #02 (IA90° – NN8) and #05 (IA148° – NN12) the combustion starts in near-stoichiometric mixtures ($\phi \simeq 1$), causing high burning rates during this combustion phase. In addition, fuel in near-stoichiometric conditions is
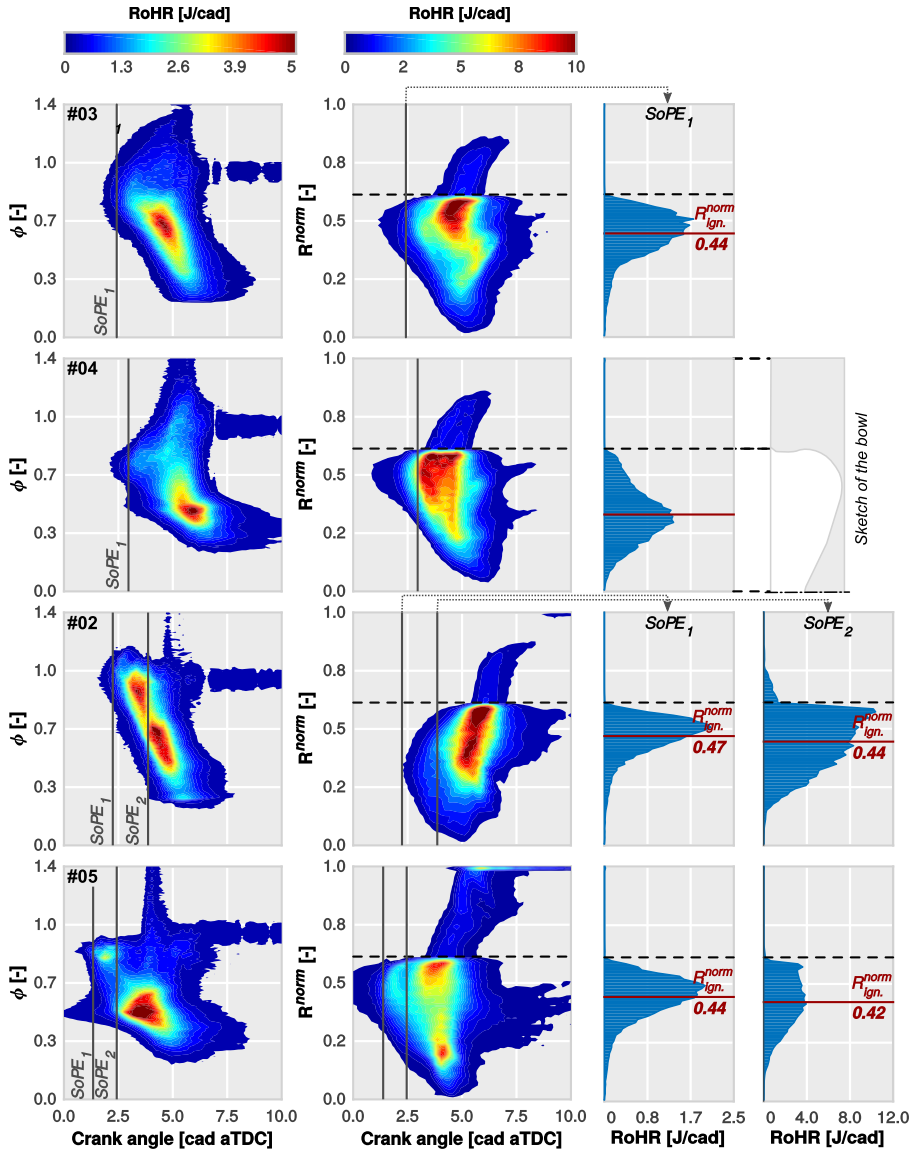
Figure 8.7: *Results of the combustion process analysis for set-ups #03, #04, #02 and #05. RoHR contours along equivalence ratio and crank angle degree are plotted at left, RoHR contours along the radial dimension of the cylinder engine at centre and histogram of RoHR along the radial dimension of the cylinder engine at the start of combustion (SoPE) are drawn at right.*

completely consumed before the leaner blends ($0.4 < \phi < 0.7$) achieve their ignition limits. Consequently, a second ignition of this lean mixture

generates an additional acoustic excitation, which increases the resonance level inside the combustion chamber. This effect is similar to that observed in CDC with multiple injection strategies 6. By contrast, tests #03 (IA110° – NN8) and #04 (IA135° – NN8) only show a single ignition located in the medium range of the equivalence ratio ($0.4 < \phi < 0.8$), with the resonance below limited values. Therefore, it is possible to claim that the large difference in the resonance energy between tests #02 – #05 and #03 – #04 is related with the number of sequential ignitions.

However, this conclusion does not explain the differences in E_{res} levels between tests #03 and #04, and also between #02 and #05. Comparing tests #03 (IA110° – NN8) and #04 (IA135° – NN8), both show a single ignition, but test #03 show a higher level of resonance with a somewhat lower $(dp/dt)_{max}$. Additionally, tests #02 (IA90° – NN8) and #05 (IA148° – NN12) display different levels of E_{res} with similar $(dp/dt)_{max}$ and the same number of sequential excitations.

Again, as it has been demonstrated in the previous chapter, the amplitude of the resonant modes is amplified as the maximum of the RoHR increases. Moreover, it is stated that the relative location of the ignition zones with respect to the nodes –or zero amplitude regions– can influence the frequency content of the spectrum between two consecutive resonant modes, and change the energy of resonance. In addition, since the contribution of the first resonant mode is the most relevant in the total energy of resonance, an analysis of the radial position of the ignition areas could contribute to understand why the resonant contribution is changing among both tests.

Figure 8.7 also shows the results of an analogous procedure presented above but, in this case, the cylindrical coordinate R^{norm} was selected as integration variable. R^{norm} is the radial position normalized by the radius of the cylinder; it is zero at the center of the bowl and one at the cylinder walls. These contour plots allow identifying where the energy release is located during the engine cycle. Nevertheless, it is necessary to establish a criterion to determine the start of combustion and thus obtain the position of the ignition area. The start of pressure excitation (SoPE) was considered, which is defined as the instant when the pressure wave due to the ignition event starts to develop. This moment practically coincides with the crank angle for 10% of fuel burnt (CA10). Finally, Fig. 8.7 (right histograms) also shows the distribution of the RoHR along the R^{norm} coordinate at SoPE timing and the red line represents the average position of the energy release.

Table 8.3: *Combustion characterization parameters (SoPE, $(dp/dt)_{max}$ and R^{norm}) in tests #02, #03, #04 and #05.*

Set-up	First ignition			Second ignition		
	$SoPE_1$ [cad aTDC]	$(dp/dt)_{max_1}$ [MPa/cad]	R_1^{norm} [-]	$SoPE_2$ [cad aTDC]	$(dp/dt)_{max_2}$ [MPa/cad]	R_2^{norm} [-]
#03	2.42	2.75	0.44	-	-	-
#04	2.96	2.88	0.33	-	-	-
#02	2.24	2.45	0.47	3.90	2.83	0.44
#05	1.34	1.54	0.44	2.40	2.88	0.42

Table 8.3 shows remarkable differences in the radial location of the ignition between tests #03 (IA110° – NN8) and #04 (IA135° – NN8). The local thermodynamic conditions cause a smooth combustion close to the bowl limits in test #03, whereas in test #04 the combustion law is sharper and located at the centre of the bowl. Thus, the energy of resonance can be mitigated by forcing the ignition to start in the middle of the cylinder near the node of the first resonant mode.

Focusing on tests #02 (IA90° – NN8) and #05 (IA148° – NN12), it is necessary to analyse both sequential combustions separately, obtaining the excitation intensity ($(dp/dt)_{max}$) and position (R^{norm}) of each one. Table 8.3 shows these parameters for these set-ups and for each ignition. Both present slight differences in the radial location, but these differences do not explain the gap observed in the E_{res} levels. A substantial difference is however observed between the $(dp/dt)_{max}$ of the first ignition; while test #02 exhibits 2.45 MPa/cad, #05 only achieves a value of 1.54 MPa/cad. Therefore, the gap in the resonance energy is explained not only by the position of the ignitions, but also by the intensity of all of them.

Although E_{res} was widely used in the literature for its correlation with engine noise, it does not provide a detailed information about the pressure spectrum in the high frequency range. Indeed, it does not report about the frequency distribution of the resonant modes and their spatial patterns. Therefore, the contribution of this parameter to the understanding of the in-cylinder acoustic field is very limited.

For this reason, Fig. 8.8 shows a pressure spectra comparison between tests #03 – #04 and tests #02 – #05 that provides more insight and overcomes this drawback. It gives an idea, at least in a qualitative way, about which are the most excited modes (mean spectrum) and also about their spatial variation (±SD).

As reported above, test #03 displays a higher value of E_{res} than test #04. According to the data presented in Fig. 8.8 (top), significant changes in the high frequency distribution are clearly visible. While the amplitude of the first mode is reduced, it is increased in higher order modes when the conditions change from test #03 to test #04. In addition, the spatial dispersion seems to be correlated with the relevance of each mode. On the other hand, Fig. 8.8 (bottom) shows that the differences in the pressure spectra of tests #02 and #05 are smaller. Both tests follow the same trend in terms of the relevance of the modes, whereas their amplitudes are scaled.
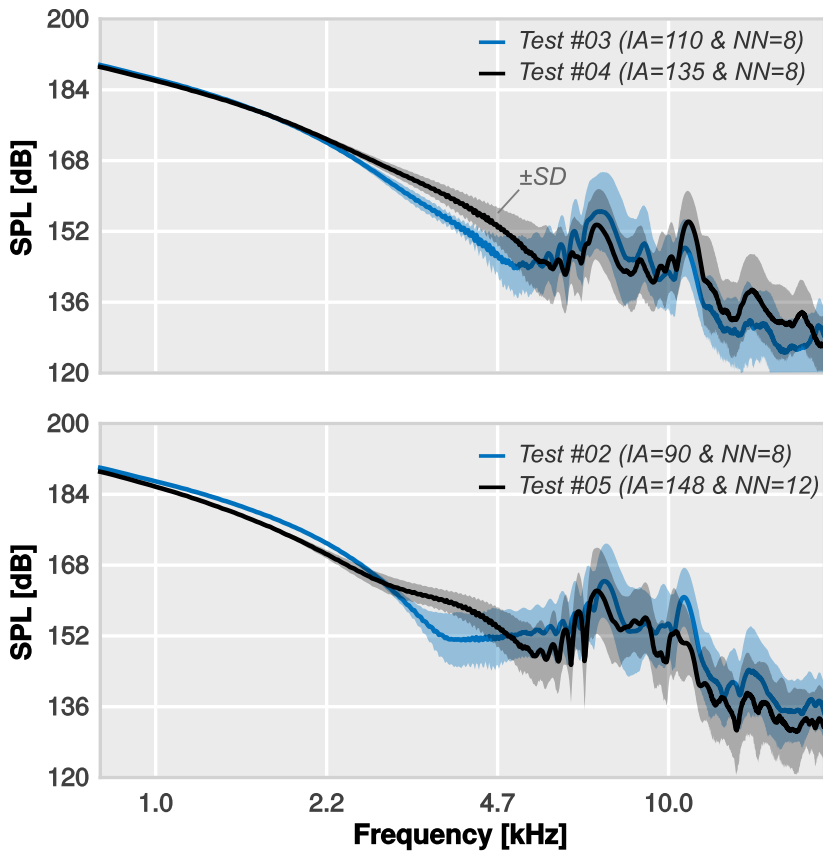
Figure 8.8: *Comparison of the in-cylinder pressure spectra trends. The pressure spectrum averaged over all monitors distributed in the domain is plotted with its standard deviation (SD). Tests #03 and #04 are compared at top while tests #02 and #05 are drawn at bottom.*

Further analysis of the results shows that the trend in the high frequency spectrum is similar in tests #02, #03 and #05 for which the position of the ignition is almost the same (see Tab. 8.3). Only in test #04 for which the ignition location is notably different, this trend changes and the second mode becomes the most dominant. Therefore, the ignition location has an impact not only on the global amplitude of the high frequency pressure spectra (E_{res}), but also on the relevance of the excited modes.

Lastly and extending the analysis to efficiency and pollutant emissions, Fig. 8.9 shows trends resulting when the injector configuration is modified. In this figure blue points reflect the evolution of NO_x, combustion and indicated efficiencies as the included angle is changed, while black ones show the effects of varying the number of nozzles. Contrary to what is observed for the overall noise, all considered parameters increase with the lower included angles and the higher number of nozzles. Thereby, the trade-off between combustion noise and combustion efficiency, already evinced by other researchers [79, 81] when the combustion law is managed through a multiple injection strategy [215], cannot be avoided using a conventional injector.

Nonetheless, these results show the benefits of using an injector with a high number of orifices and a small included spray angle in the combustion efficiency. This configuration reduces the spray penetration and, therefore, it minimizes the liquid fuel impingement during early and long injections. In contrast, the spray-bowl matching worsening in late injections decreases the efficiency and increases NO_x emissions. In these circumstances, a configu-
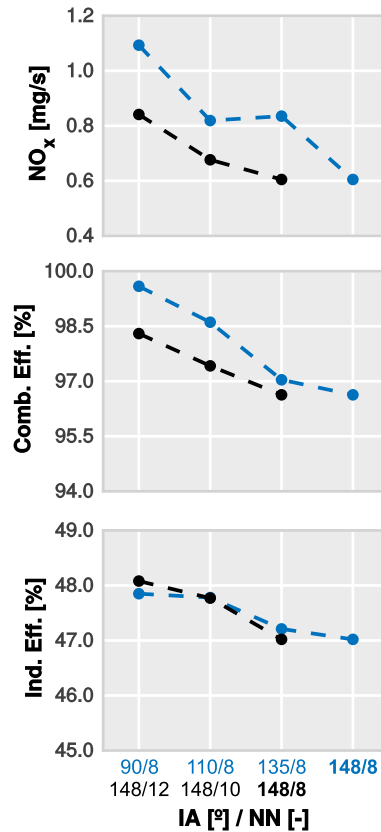
Figure 8.9: *Trends of nitrous oxides, combustion and indicated efficiencies for both injector studies.*

ration with a lower number of orifices and higher included angle can help to improve the spray-bowl matching, thus minimizing pollutant and noise emissions.

8.4. Advanced injector configuration

The next study explores the potential benefits of developing a combustion system able to combine both injector configurations described in the previous section, that is, to use the optimum configuration for each injection event. A possible physical implementation of such a system is the injector proposed by Perr [216], featuring dual actuators that allow switching between two sets (crowns) of orifices. The first actuator is connected to the first needle valve associated with a first set of injector orifices (crown 1), while the second actuator controls an additional concentric needle valve associated to a second set of orifices (crown 2).

Since the proposed configuration would add supplementary degrees of freedom to the intricate engine system, enlarging the number of parameters to be inspected, it is demanded to explore additional techniques for the identification of the optimizing paths in the configuration design. One of the most used methods for this purpose is the statistical approach known as Design of Experiments (DoE). This technique, coupled with the Response Surface Method (RSM), has been traditionally applied to multiple engineering design processes [101, 208] in order to establish cause-effect relationships between the influencing factors and their response.

8.4.1. Optimization methodology

The CFD model was combined with the statistical technique DoE in order to optimize the new injector configuration. According to the knowledge acquired during the previous section, a base configuration with three optimization parameters was defined . The test plan was based on a Central Composite Design (CCD) of three factors and it consisted in 15 simulations. In addition, RSM was used to determine the relationships between the injector parameters configuration and the output variables mentioned above.

Figure 8.10 shows the base configuration of the new injector. The first set of orifices, recommended for early injections, have an included angle of 90° (α_1) and 12 orifices whereas the second one is suggested for late injections with an included angle of 148° (α_2) and 8 holes. Although this system could operate such a double-row nozzle injector with a single needle
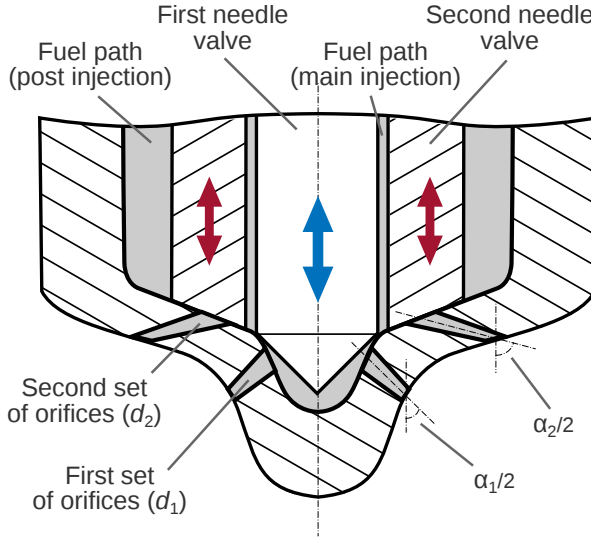
Figure 8.10: *Injector sketch based on Perr's patent [216]. The injector actuators are completely independent and they are connected to a specific set of orifices.*

actuator [217], the target of this study is not to evaluate a solution which could improve the sprays overlap. The main idea aims at exclusively utilizing a particular set of nozzles in each injection event, allowing the independent use of two conventional configurations in subsequent injections. Thereby, the fuel was injected through the first set of orifices during the pilot and main injections whereas the second set was only used for the post injection.

The total injection areas of both crowns of orifices, A_1 and A_2, were considered as optimization parameters. In both cases the number of orifices and the discharge coefficient for each hole remained fixed. Thus, the injection duration was adapted to maintain the injection pressure as well as the total injected mass between each configuration. The third optimization parameter was the split between the main and post injection masses ($\delta_{\text{main−post}}$); the mass of the pilot injection was maintained constant since it was experimentally observed that its effects were less significant than those of the other injections. This parameter represents the amount of fuel mass added or removed from the main injection. Thus, the fuel mass of each injection was obtained by

$$\text{MoI}_{\text{main}} = \text{m}_{\text{total}} \cdot \left(0.5 + \frac{\delta_{\text{main−post}}}{100} \right) \tag{8.4.1}$$

$$\text{MoI}_{\text{post}} = \text{m}_{\text{total}} \cdot \left(0.5 - \frac{\delta_{\text{main−post}}}{100} \right) \tag{8.4.2}$$

Table 8.4: *Values of the parameters used in each of the fifteen numerical simulations according to the test plan of the DoE study.*

Factor	1[a]		2[b]		3		
Param.	A_1 [%]	d_1 [μm]	A_2 [%]	d_2 [μm]	$\delta_{main-post}$ [%]	MoI_{main} [mg]	MoI_{post} [mg]
0	0.0	90.0	0.0	90.0	0.0	7.59	7.59
1	-17.8	81.6	-17.8	81.6	-11.9	5.78	9.39
2	-17.8	81.6	17.8	97.7	-11.9	5.78	9.39
3	17.8	97.7	-17.8	81.6	-11.9	5.78	9.39
4	17.8	97.7	17.8	97.7	-11.9	5.78	9.39
5	-17.8	81.6	-17.8	81.6	11.9	9.39	5.78
6	-17.8	81.6	17.8	97.7	11.9	9.39	5.78
7	17.8	97.7	-17.8	81.6	11.9	9.39	5.78
8	17.8	97.7	17.8	97.7	11.9	9.39	5.78
9	0.0	90.0	0.0	90.0	-20.0	4.55	10.62
10	0.0	90.0	0.0	90.0	20.0	10.62	4.55
11	-30.0	75.3	0.0	90.0	0.0	7.59	7.59
12	30.0	102.6	0.0	90.0	0.0	7.59	7.59
13	0.0	90.0	-30.0	75.3	0.0	7.59	7.59
14	0.0	90.0	30.0	102.6	0.0	7.59	7.59

[a] Pilot and main injections
[b] Post injection

where m_{total} is the available fuel amount for both injections. Additional details about the factor space, input factors and specified ranges are shown in Table 8.4.

8.4.2. Optimization results

Following guidelines defined by the RSM method, all variables obtained at each point of the DoE space were interpolated using a cubic polynomial fit for visualization. Results are plotted in Fig. 8.11 in which the computed contours of overall noise and indicated efficiency (η_i) are presented with the purpose of analysing the tendencies followed by both parameters.

It can be seen how the split between main and post injections is the most dominant parameter among those selected in the study. While the maximum change of $\delta_{main-post}$ modifies the overall noise in almost 14 dB, A_1 and A_2 parameters only produce a variation of 8 dB. In a similar way, the indicated efficiency varies 4.5 and 2 points, respectively. Also, contour distributions presented by both parameters, ON and η_i, are practically the same in the three considered planes. This behavior evinces again the trade-off trend observed by other authors [79] and it shows the close relationship between these parameters.

Focusing on the first plane, the evolution of combustion noise and indicated efficiency is plotted against the variation of A_1 and A_2. Both parameters decrease in the bottom-right hand side region, in which the total injection area of the first crown (A_1) is excessively increased. On the other hand, the higher levels are achieved by reducing the diameter of both sets of orifices.

In all these cases, both parameters show a monotonic trend, and thus only a compromise solution between performance and noise emissions seems to be achievable.

Nonetheless, a further examination of the complete DoE space shows that these trends change for certain configurations, allowing to improve the compromise solution of this particular system design. In particular, this behaviour can be clearly observed in the plane plotted in Fig. 8.12. This corresponds with a fixed split injection of -11.9% and different values of A_1 and A_2. While the bottom-left hand side of the map shows the lowest noise values, the region which maximizes the efficiency is located in the middle-right hand side.

In order to identify the optimum configuration within the whole DoE space, a merit function based on two parameters [218] was defined as

$$\text{MF} = \frac{1000 \cdot \sum\limits_{n=1}^{2} \alpha_n}{\sum\limits_{n=1}^{2} \left(\alpha_n \cdot e^{\beta_n \cdot \frac{x_n - x_n^{\text{target}}}{x_n^{\text{target}}}} \right)} \qquad (8.4.3)$$

$$x_1 \longrightarrow \text{ON} \qquad x_2 \longrightarrow \eta_i$$

where x_n is the value of each parameter at a given configuration (ON and η_i), x_n^{target} stands for these values achieved by the original configuration and both α_n and β_n are weighted constants for specifying the influence of each parameter in the merit function. For this particular study, the constants where fixed at 10 for ON parameter and at 8 for the indicated efficiency, giving more relevance to the combustion noise. This decision was made taking into account the extremely high levels of noise registered in this combustion concept.

Merit function values at each considered configuration are presented in Fig. 8.13 in which the optimum configuration can be identified. This configuration is therefore formed by two crowns with the same diameter of nozzle holes (97.7 μm) and an injection split displaced to the main injection event (62 – 38%).
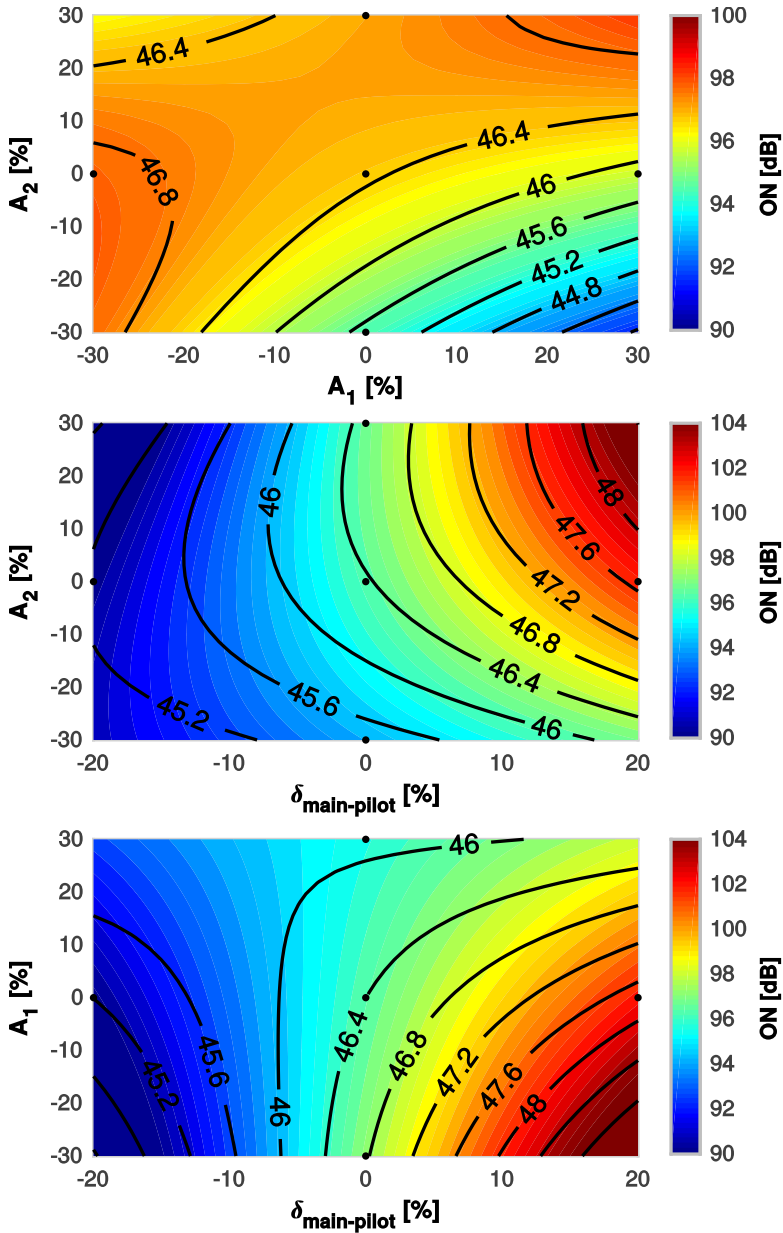
Figure 8.11: *Results of DoE interpolation procedure, overall noise and indicated efficiency contours are superposed along the three main DoE space planes. Plane 0-11-12-13-14 (top), plane 0-9-10-13-14 (middle) and plane 0-9-10-11-12 (bottom).*
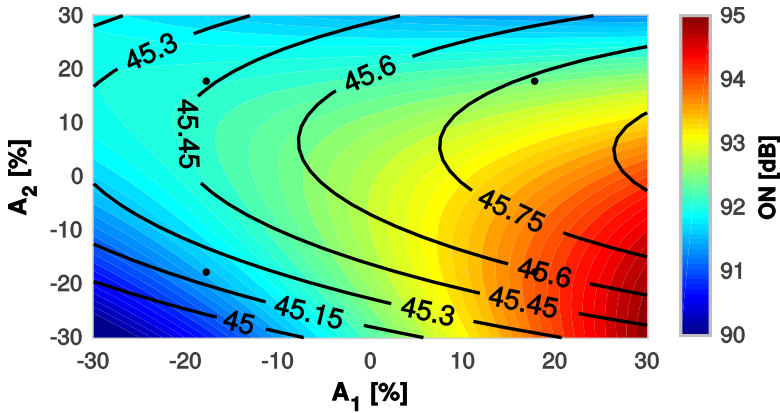
Figure 8.12: *Results of DoE interpolation procedure in terms of overall noise and indicated efficiency across the plane 1-2-3-4.*

In addition to the merit function, NO_x levels were restricted to the baseline configuration. In Fig. 8.13 those cases which do not comply with this constraint are identified in grey.

8.4.3. Optimized vs. baseline comparison

Once the optimum double crown configuration is identified, a direct comparison against the baseline can be performed for determining the most influencing parameters and their impact on the combustion. In a first step, the five relevant parameters shown in Table 8.5 were calculated. A noticeable
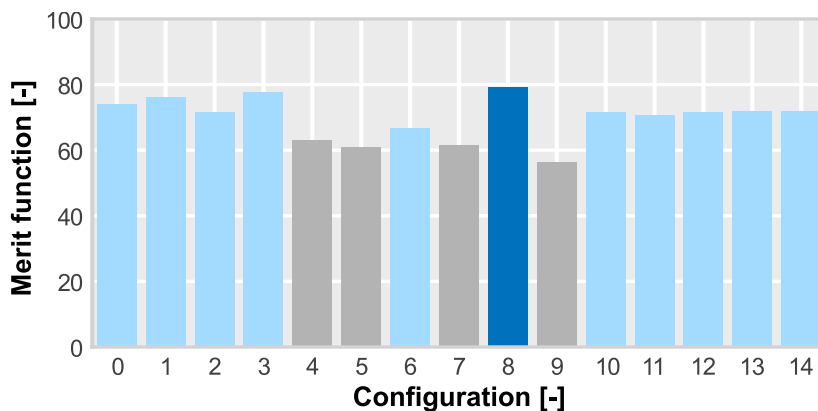
Figure 8.13: *Results of the selection procedure for choosing an optimum configuration. The optimum case (8) is distinguished in blue while configurations that do not comply with the NO_x constraint are identified in grey.*

Table 8.5: *Comparison of the estimated metrics related to the engine performance and emissions.*

Configuration	Original (baseline)	Optimum (double crown)
Overall noise [dB]	99.7	91.0
Indicated eff. [%]	46.9	45.0
Combustion eff. [%]	96.5	98.0
Thermodynamic eff. [%]	48.6	45.9
NO_x [mg/s]	0.60	0.31

reduction of the overall noise level is observed, going from 99.7 to 91.0 dB. Improvements in NO_x levels are even more remarkable, since these decrease from 0.60 mg/s to 0.31 mg/s (almost a 50% reduction).

However, despite the benefits of reducing both noise and NO_x emissions, a significant efficiency worsening is provoked. Table 8.5 shows a non-negligible reduction of 1.9 percentage points in the indicated efficiency levels.

Since this combustion mode tends to generate high levels of CO and unburned HC as the combustion stability is deteriorated, worsening then the combustion efficiency and subsequently, decreasing the thermal efficiency, the identification of the losses origin can provide additional insight on this regard.

As it can be seen in the same Table 8.5, this trend is not replicated by the optimum configuration. While the indicated efficiency is conditioned by the combustion stability in the baseline, it seems not influenced by thermodynamic losses in the optimum case.

In order to understand why efficiency trend changes when the injection system is modified, the evolution of the liquid film impingement at cylinder and piston surfaces is plotted in Fig. 8.14. Moreover, a visualization of the sprays at both pilot and main injection phases is provided in this figure. The sprays are visualized in this figure by clipping the equivalence ratio (ϕ) at the unitary value, thereby showing the iso-volume of stoichiometric conditions enclosing the spray.

Examination of the figure reveals that the baseline configuration tends to generate fuel liquid deposits at cylinder walls and squish regions. These fuel deposits, which are the main cause of the oil dilution, are maintained until the end of the closed cycle, increasing the unburned HC levels at the exhaust. The optimum configuration instead avoids these issues by leading the fuel into the piston bowl.

Original (baseline)
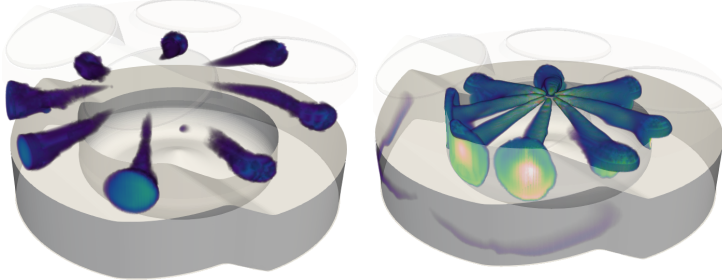
Optimum (double crown)
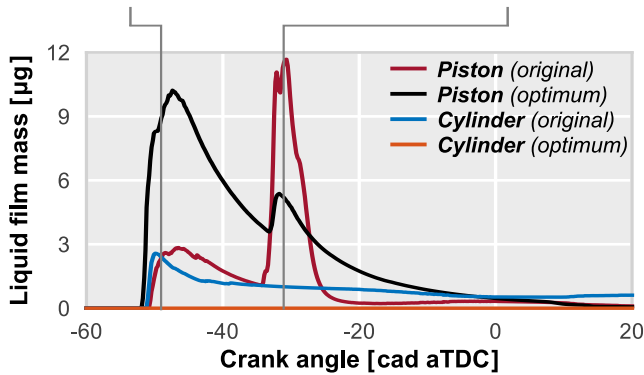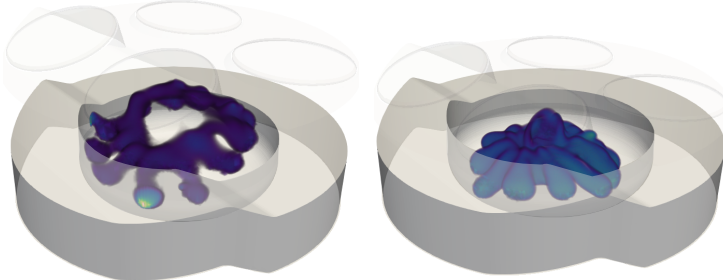
Figure 8.14: *Time evolution of the liquid film impingement at cylinder walls and piston surface in both considered injector configurations (bottom). Visualization of baseline and optimized sprays at two different instants during the pilot and main injections (top).*

Despite the gain in terms of combustion stability, losses due to the thermodynamic effects are so large that compromise thermal efficiency levels in a significant way. Thus, in-cylinder pressures of the two considered configurations are plotted together with the RoHR traces in Fig. 8.15 (top) in order to identify the source of these losses. As can be seen, the combustion phasing is excessively displaced towards the expansion stroke if the
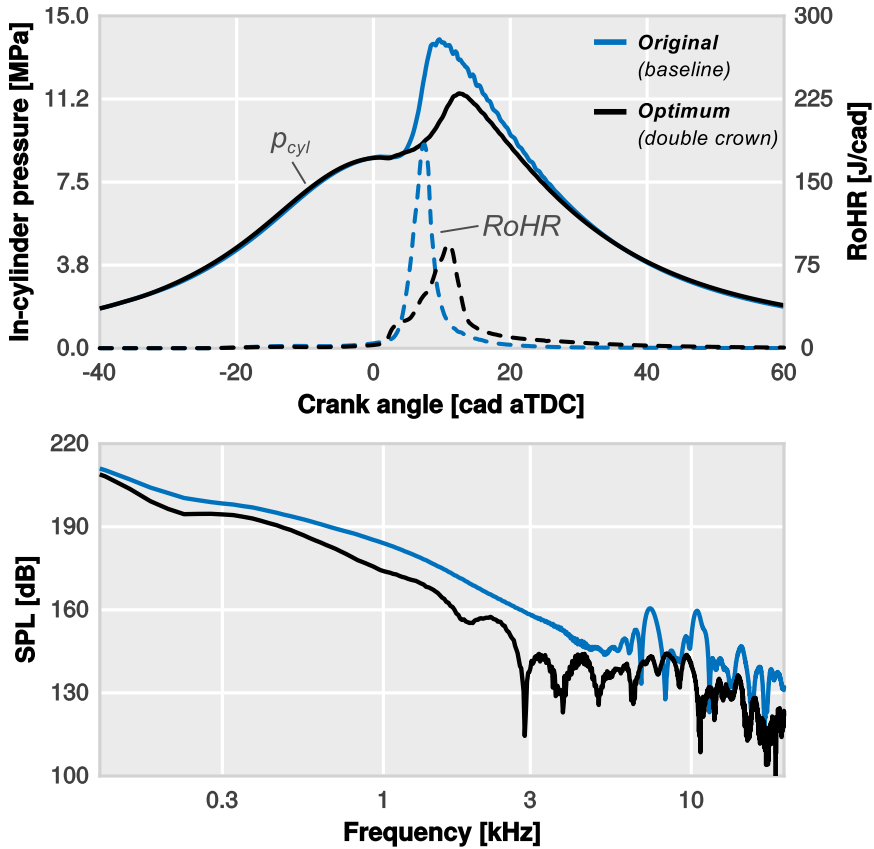
Figure 8.15: *Comparison between original (baseline) and optimum (double crown) injector configurations. Differences in terms of cylinder pressure (obtained at the transducer location) and rate of heat release are plotted at top whereas pressure spectra are presented at bottom.*

optimum configuration is compared to the baseline. This fact allows to recognize the combustion phasing as a possible shortcoming of this new system configuration, at least with the considered injection settings.

In addition to this fundamental analysis, it is important to understand how the fuel stratification modifies the reactivity of the charge. Hence, the RoHR was numerically integrated along the whole CFD domain with respect to the equivalence ratio (ϕ) in order to analyse the fuel stratification and its temporal evolution during the combustion. The solutions are presented in Fig. 8.16 in which the horizontal axis represents the temporal evolution of the engine cycle, the vertical axis shows the integration variable (ϕ) and the colour scale displays the RoHR.
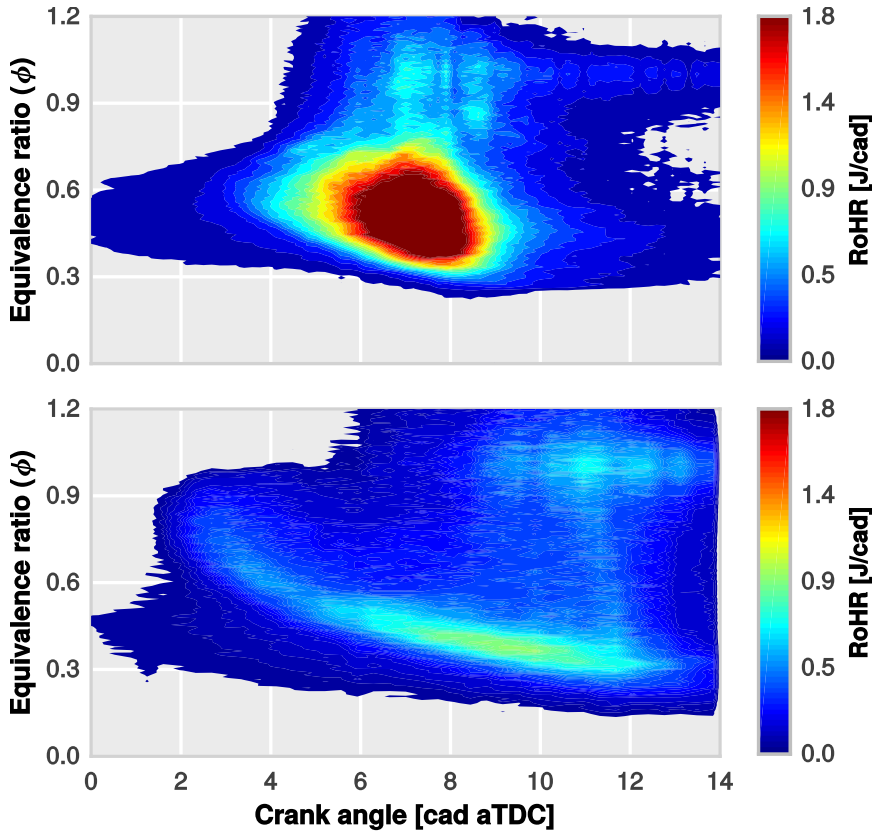
Figure 8.16: *Comparison of the fuel stratification. RoHR contours along the equivalence ratio (φ) and crank angle degree are plotted for the baseline (top graph) and for the optimum (bottom graph).*

It can be seen in this figure that the most reactive blend in the baseline case is focused on the middle range of equivalence ratios (0.35 – 0.7), causing a single-step combustion with high burning rates. In the optimum configuration however, the blend shows a higher level of stratification with mixtures gathered by 0.3 and 1.2 of equivalence ratios. Here, the combustion starts at near stoichiometric conditions (0.8 – 1.0), then it progresses toward lower equivalence ratios (0.5 – 0.3) and finally, it consumes the richest mixtures (1.0 – 1.2) within the chamber. This singular path leads to a progressive burn that results in a smoother combustion law.

From the in-cylinder pressure side, lower burning rates mean lower pressure rise rates. Consequently, the overall amplitude of the in-cylinder pressure spectrum is remarkably decreased in the whole broadband (see Fig. 8.15b).

The noise lowering associated to this effect is a straight consequence of two documented mechanisms. On one hand, the relaxation of the pressure rise rate produces a reduction of the SPL in the frequencies contained between 0.2 and 3.0 kHz. On the other hand, the contribution of the combustion chamber resonance is also reduced as the amplitude of high frequency oscillation modes (> 3.0 kHz) is notably decreased. Low frequencies (< 0.2 kHz) were excluded for the comparison since they mainly depend on the engine speed that, in this case, was kept constant among both configurations.

8.4.4. Sensitivity of the injection settings

With the aim of exploring the margin of improvement and the sensitivity of the new system configuration, an additional study was performed by sweeping SoE_{main} each 6 cad between -52 and -34 cad aTDC in both configurations. This injection parameter was specifically selected for its notable impact on the combustion phasing [80].

The interest of the analysis is focused on examining the emissions and performance parameters used before. Results, presented in Fig. 8.17, show the influence of varying SoE_{main} in the original and the optimum combustion systems.

Focusing on the baseline, a trade-off is evident between emissions (noise and NO_x) and efficiency. This was reported using direct engine measurements, and also supported by numerical simulations for providing a better understanding of the mixture stratification and the pollutants formation. Moreover, a more recent publication [82] shows how the main cause of these efficiency losses is the deterioration of the combustion stability due to an excessive fuel wall impingement.

Regarding the double crown configuration, Fig. 8.17 shows how it is less sensitive to SoE_{main} since all studied parameters present a lower maximum variation. For instance, while noise levels vary 5.7 dB for the new configuration, the baseline exhibit 16.6 dB of maximum difference. In addition, the proposed system is able to keep the combustion efficiency above the baseline even for extremely advanced SoE_{main}.
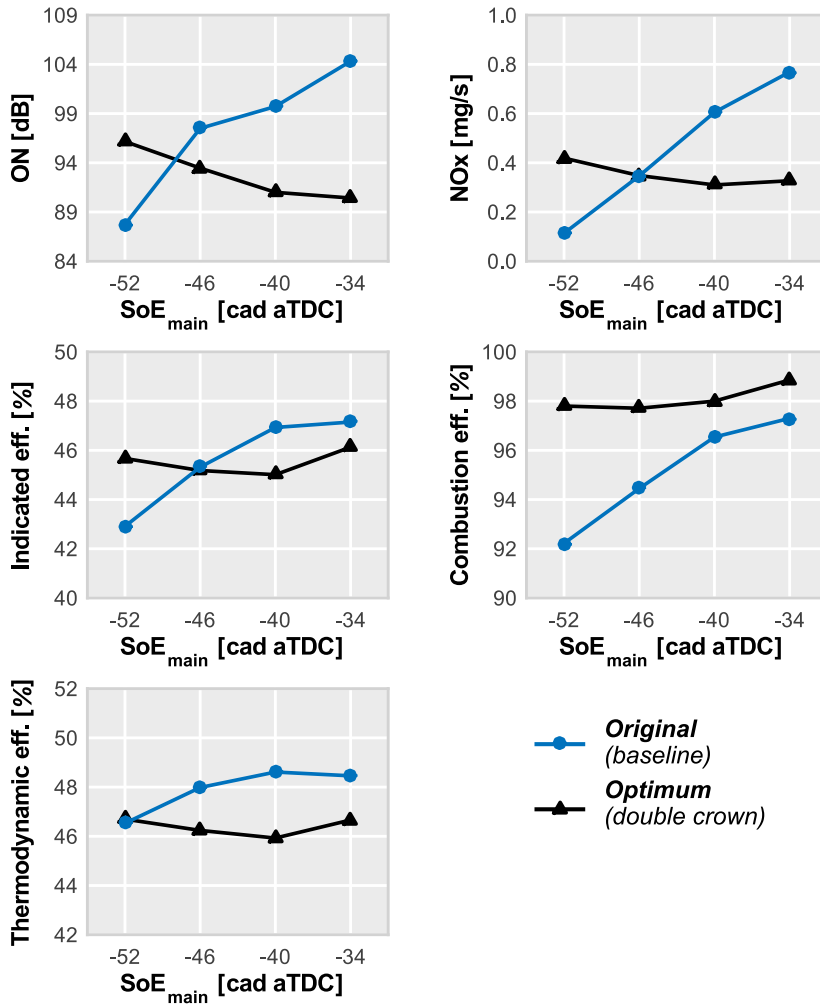
Figure 8.17: *Influence of SoE$_{main}$ on emissions (noise and NO$_x$) and engine performance (indicated, combustion and thermodynamic efficiencies) in the baseline and the optimum configurations.*

Thanks to this, the indicated efficiency is preserved at acceptable values despite the modest values of thermodynamic efficiency. Therefore, the improvement of the combustion stability seems to be the greatest improvement of the proposed configuration, making the new system potentially advantageous.

Finally, trends are reversed with respect to the baseline since, as it can be seen, both emissions and efficiency increase as SoE_{main} is advanced. Thus, a delay on the main injection timing improves the indicated efficiency whereas noise and NO_x emissions are kept at the lowest level.

8.5. Conclusions

An analysis of the combustion noise generated by a 2-stroke engine operated with the gasoline PPC concept has been presented in this chapter.

The experimental results have shown that it is possible to attain near zero levels of NO_x and soot emissions while maintaining reasonable combustion efficiency values. However, the engine noise remains at unacceptable levels. Indeed, the trade-off between combustion noise and indicated efficiency has been evidenced by the experimental work presented here and confirmed by the CFD results. In summary, the viability of the gasoline PPC concept requires promoting quieter combustions through the establishment of smoother and longer RoHR traces, but these are associated to high losses in the combustion process.

Since the management of these output parameters through the operating settings is not enough to improve the concept capabilities, a redesign of the engine hardware has been performed. Hence, the impact of the injector design on the combustion noise has been further analysed in this paper using CFD modelling.

The different injector configurations produce diverse fuel stratification conditions at the start of combustion, achieving higher reactive mixtures as the included angle decreases and the number of injector nozzles increases. This evidences that both the mixing conditions and local thermodynamic conditions are crucial in the combustion and its effects.

Results show how under certain conditions the resonance phenomenon can also play an important role. However, the noise exhibited at these particular conditions are extremely high and, even with an important lowering of resonance levels, the overall noise still remains at unacceptable values. The quantity of fuel in near-stoichiometric conditions mainly determines the acoustic excitation intensity, due to the high reacting rates linked to the stoichiometric mixtures. If the combustion process is divided in multiple ignition phases, the resonance level increases significantly, and becomes the most influential parameter in the amplitude of the resonance oscillations.

In addition, the relative position of the ignition also contributes significantly to the resonance level and influences the modes distribution of the high frequency pressure spectrum.

Furthermore, an injector with a high number of orifices and a small included spray angle has been shown as a good solution to relieve the efficiency losses owing to the combustion stability deterioration. This configuration reduces the spray penetration and, therefore, it minimizes the liquid fuel impingement during early and long injections. In contrast, the spray-bowl matching worsening in late injections increases NO_x emissions. In these circumstances, a configuration with a lower number of orifices and higher included angle can help to improve the spray-bowl matching, thereby minimizing pollutant emissions.

Despite the improvement in terms of combustion efficiency and pollutant emissions, the optimization of a conventional injector does not allow an accurate control of the reactivity of the charge through the operation settings, thereby it still compromises other important aspects such as noise emissions or knocking combustion.

In view of the challenges to manage combustion noise of partially premixed gasoline combustion in compression-ignited engines, an additional study to evaluate the potential of using dual spray injectors with a combination of numerical simulations and statistical design of experiments has been carried out. With this, it has been possible to perform a qualitative analysis of the relationships between several injector design parameters and their engine outputs, thereby contributing to the understanding of the combustion noise control in this singular combustion concept.

Results from this new injector optimization have revealed that the proposed configuration allows to decrease both noise and NO_x emissions while efficiency values decreases due to an excessively delayed combustion timing. The new configuration is composed by two crowns with the same diameter of nozzle holes and an injection split clearly displaced to the post injection. This helps to control the reactivity of the mixture and permitting a smoother combustion law which reduces the noise of the combustion in the whole broadband.

In addition to noise and NO_x emissions lowering, this new configuration present a less sensitive response to the injection timing, improving the combustion stability but declining the control of the combustion phasing. However, the considerable higher levels of combustion efficiency allow to maintain the performance at competitive values even with the poor achieved values of thermodynamic efficiency.

Conclusions and future works

The concluding remarks of this doctoral thesis are summarized in this final chapter in order to give an outline of the main findings obtained along this document and highlighting the original contributions of this research to the scientific community.

Some topics of interest are also suggested for possible future works that could extend the knowledge acquired, the rigour of the methodologies presented and their application to the industry requirements.

9.1. Conclusions

Having fulfilled the objectives proposed for this research, the conclusions summarize the main contributions of this thesis. Moreover, they can be divided into main contributions to the state of the art in the field of combustion noise characterisation in internal combustion engines and other findings related to the methodological procedures proposed along the different chapters of this document.

9.1.1. Original contributions

Results obtained from the application of aforementioned methods allowed an enhanced comprehension of the the physical phenomena involved in the acoustic response of combustion processes but also contributing to the alleviation of its undesired effects. The main contributions and conclusions can be enumerated as:

- Two distinct paths to deal with combustion noise have been identified. On the one hand, the first approach aim to decrease the amplitude of the medium frequencies by reducing the burning velocity. This strategy

may seem quite simple *a priori* (e.i. modifying the reactivity of the air-fuel blend by increasing the amount of EGR), however, special attention must be paid to the thermal efficiency due to its direct connection with the combustion features (burning rate and timing). On the other hand, minimizing the contribution of the resonant oscillations may offer independence from the thermal efficiency but a deep knowledge about the complex mechanisms related to resonance phenomena is required for its control.

- Analysis of simulation results revealed different sources of acoustic perturbations depending on the combustion features. While a pre-mixed combustion causes a sudden increase of pressure that generates a resonant wave inside the chamber, the heat release by the stabilized flame in a mixing-controlled combustion promote a fluctuating density that generates additional pressure waves along the flame.

- In-cylinder pressure field inspection shows that flame induced waves are an order of magnitude smaller than those originated by the pre-mixed burning and rapidly attenuated after their respective onsets, thereby barely contributing to the total energy of resonance. Indeed, modal decomposition results support this remark since the most energetic modal structures are squish-bowl dominated instead of focusing on those of the spray-jets structures.

- As a consequence of this, the choice of the turbulence model is not a critical aspect for noise modelling in CI engines. Although the incapacity for reproducing those jet-induced oscillations, URANS schemes predict results very similar to those seen in LES simulations with the added value of being computationally less expensive. Nevertheless, the use of more complex turbulence approaches offers a better prediction of the cyclical dispersion observed in the experiments.

- Experimental data from CDC operation have evinced that resonant oscillations constitute an important part of the acoustic emission. Moreover, simulations have shown that operating strategies such as injection specifications, EGR or intake pressure have shown a limited impact on the noise mitigation due to indirect effects on other relevant engine outputs. However, the complete redesign of the combustion system, including chamber, injector and intake ports geometry, has evinced potential benefits in noise reduction (basically due to a resonance lowering) while enhancing the thermal efficiency.

- Examination of all simulated engine configurations have shown a common feature in the resonant response. The location of the premixed combustion onset conditions the energy comprised by the resonant modes. Thus, moving these points to the centre of the cylinder the resonant energy is shifted towards higher frequencies less perceptible by the human hearing and also contributing to decrease the overall level of the radiated noise.

- Regarding the noise emitted by the gasoline PPC mode, it is worth to remark that the resonant oscillations only constitute a negligible component within the total acoustic emission, even showing absolute levels of resonance energy similar to those observed in CDC. Therefore, a noise reduction is only attainable by promoting lower burning rates while maintaining the combustion stability.

- Different optimization strategies, specifically focused on the injector configuration, have been applied to the gasoline PPC concept and it can be concluded that, even showing some relevant improvements, optimizing the injector design is not enough to significantly reduce acoustic emissions while maintaining the thermal efficiency.

9.1.2. Methodology findings

Since the main objective of this thesis was the development of a new computational methodology, other findings related to the method itself appeared that, although not being a pure contribution, may be interesting for the research community.

- Although traditional single-point pressure measurements allow a first characterisation of combustion noise, they fail when further insight about the physical origin of the acoustic instabilities is required to improve the comprehension of this regard. Nonetheless, the burning velocity and the resonant oscillations have been successfully correlated with their corresponding excitation frequencies, supporting the conclusions obtained by other authors.

- In order to highlight which operating conditions are more sensitive to a given frequency, a post-processing methodology has been developed on the basis of prior works. This technique has been applied to the experimental data available and used to build distinct noise and contribution maps that determine the most critical operation conditions along the region of interest of the engine operation.

- Numerical simulations have proved to be a valuable tool to extent the knowledge about all phenomena involved in the combustion noise generation, thereby overcoming experimental limitations while addressing this elusive phenomenon. The CFD solution allows a complete spatio-temporal recreation of the unsteady pressure field within the combustion chamber, which is the principal cause of the noise emission towards the cabin, but also of the spectral signature of the engine.

- However, special attention must be paid in several modelling parameters, specially in those related to the calculation set-up, because they strongly condition the final solution. Since the spatial and temporal discretization determines both the resolution and dissipation rate of pressure waves travelling across the chamber, simplification hypotheses of the physical domain (periodic or symmetry assumptions) and the simulated time span (only closed-cycle modelling) compromise the accuracy of the results.

- The robustness of the CFD model for reproducing the acoustic response of the combustion has been widely demonstrated in Chapter 5, in which several operating conditions, engine platforms and combustion modes have been considered. These results show that the model is consistent with both temporal and spectral content of experimental data and also it offers a reasonable prediction of some relevant external-propagated acoustic metrics.

- Several post-processing techniques such as Fourier's analysis and modal decomposition methods have been applied to extract coherent time-spatial data from the simulations. They offer helpful information regarding the behaviour of the combustion unsteady pressure field and how it affects the external-propagated noise perception.

- Advantage of combining CFD modelling with optimization techniques, specifically based on statistical methods or genetic algorithms, has also been shown regarding the search for appropriate operating strategies (injection timings or pressure, EGR amount, etc.) and optimal design paths for the combustion system (configuration of the injector, chamber and ports geometry). In some cases, the available information also allowed to stablish relationships between the influencing parameters and their acoustic response.

9.2. Future works

Some questions that have emerged along the execution of this thesis could not be accordingly answered during the investigation period, either owing to time constraints or budget limitations. This section includes several recommendations for future works motivated by all these arisen concerns.

- Further efforts should be taken to confirm the conclusions obtained by LES simulations in additional operating points. For instance, it would be interesting to check what happen when the number of pilot injections is reduced and, therefore, the premixed burning contribution is reduced.

- Simulation of additional operation conditions with the optimized solutions proposed in Chapters 7 and 8 would be interesting in order to evaluate the performance of these new configurations along the whole operating map.

- Additional analysis is nonetheless needed for a more complete optimization of the new systems, including additional design parameters that in this work were considered fixed. For instance, parametrising the chamber geometry with a higher number of parameters, increasing the number of injector specifications, etc.

- A validation of the optimization methodology should carry out by comparison with the experiments. The suggestions regarding the complete combustion system characterisation must be taken into account, therefore, the piston geometry and injector set-up should be manufactured and tested at the same conditions as in the baseline, thus proving the validity of the methodology.

- Extension of the optimization procedure for gasoline PPC concept by including the combustion chamber geometry. Since the particular design of the combustion chamber increases the complexity of the geometry parametrisation, a new approach for building the virtual design should be suggested and later tested.

Bibliography

[1] A. Broatch, X. Margot, R. Novella, and J. Gomez-Soriano. "Combustion noise analysis of partially premixed combustion concept using gasoline fuel in a 2-stroke engine". *Energy* 107, 2016, pp. 612–624 (cited in pp. 23, 73, 140, 163).

[2] A. Broatch, X. Margot, R. Novella, and J. Gomez-Soriano. "Impact of the injector design on the combustion noise of gasoline partially premixed combustion in a 2-stroke engine". *Applied Thermal Engineering* 119, 2017, pp. 530–540 (cited in pp. 73, 163).

[3] A. J. Torregrosa, A. Broatch, X. Margot, and J. Gomez-Soriano. "Towards a Predictive CFD Approach for Assessing Noise in Diesel Compression Ignition Engines. Impact of the Combustion Strategies". *International Conference on Modeling and Diagnostics for Advanced Engine systems: the 9th COMODIA, Okayama (Japan)*, 2017 (cited in p. 123).

[4] A. J. Torregrosa, A. Broatch, R. Novella, J. Gomez-Soriano, and L. F. Mónico. "Impact of gasoline and Diesel blends on combustion noise and pollutant emissions in Premixed Charge Compression Ignition engines". *Energy* 137, 2017, pp. 58–68.

[5] A. J. Torregrosa, A. Broatch, J. García-Tíscar, and J. Gomez-Soriano. "Modal decomposition of the unsteady flow field in compression-ignited combustion chambers". *Combustion and Flame* 188, 2018, pp. 469–482 (cited in p. 95).

[6] A. J. Torregrosa, A. Broatch, A. Gil, and J. Gomez-Soriano. "Numerical approach for assessing combustion noise in compression-ignitied Diesel engines". *Applied Acoustics* 135, 2018, pp. 91–100 (cited in p. 45).

[7] A. Broatch, R. Novella, J. García-Tíscar, and J. Gomez-Soriano. "Potential of dual spray injectors for optimising the noise emission of gasoline partially premixed combustion in a 2-stroke HSDI CI engine". *Applied Thermal Engineering*, 2018, pp. 369–378 (cited in p. 163).

[8] A. Broatch, J. J. López, J. García-Tíscar, and J. Gomez-Soriano. "Experimental Analysis of Cyclical Dispersion in Compression-Ignited Versus Spark-Ignited Engines and Its Significance for Combustion Noise Numerical Modeling". *Journal of Engineering for Gas Turbines and Power* 140, 10 2018, pp. 102808–102808–8 (cited in pp. 23, 45, 95).

[9] A. Broatch, R. Novella, J. Gomez-Soriano, P. Pal, and S. Som. "Numerical Methodology for Optimization of Compression-Ignited Engines Considering Combustion Noise Control". *SAE International Journal of Engines* 2018-01-0193, 2018 (cited in p. 123).

[10] P. Pal, C. Kolodziej, S. Choi, A. Broatch, et al. "Development of a Virtual CFR Engine Model for Knocking Combustion Analysis". *SAE International Journal of Engines* 2018-01-0187, 2018 (cited in pp. 23, 47, 70, 73).

[11] A. J. Torregrosa, A. Broatch, X. Margot, and J. Gomez-Soriano. "Understanding the unsteady pressure field inside combustion chambers of compression ignition engines using a CFD approach". *International J of Engine Research (available on-line)*, 2018 (cited in pp. 45, 73, 95, 123).

[12] A. Broatch, R. García-Tíscar, J. Gomez-Soriano, P. Pal, and S. Som. "Large Eddy Simulation for combustion acoustics in compression-ignited engines". *Submited to Combustion and Flame*, 2018.

[13] A. Broatch, R. García-Tíscar, J. Gomez-Soriano, P. Pal, and S. Som. "Advantages of Large Eddy Simulations in the prediction of compression-ignited combustion unsteadiness". *Submited to Applied Energy*, 2018.

[14] A. Broatch, R. Novella, R. García-Tíscar, and Gomez-Soriano. "On the shift of acoustic characteristics of compression-ignited engines when operating with gasoline partially premixed combustion". *Submited to Applied Thermal Engineering*, 2018.

[15] B. Masterton, H. Heffner, and R. Ravizza. "The Evolution of Human Hearing". *The Journal of the Acoustical Society of America* 45 (4), 1969, pp. 966–985 (cited in pp. 1, 4).

[16] I. Ekici and H. Bougdah. "A Review of Research on Environmental Noise Barriers". *Building Acoustics* 10 (4), 2003, pp. 289–323 (cited in p. 3).

[17] A. A. Saadu, R. O. Onyeonwu, E. O. Ayorinde, and A. Ogisi. "Road traffic noise survey and analysis of some major urban centers in Nigeria". *Noise Control Engineering Journal* 46, 1998, pp. 146–158 (cited in p. 3).

[18] V. R. Deulgaonkar, S. P. Kallurkar, and A. G. Mattani. "Review and Diagnostics of noise and vibrations in automobiles". *International Journal of Modern Engineering Research* 1 (2), 2011, pp. 242–246 (cited in p. 4).

[19] D. V. Matijević and V. M. Popović. "Overview of modern contributions in vehicle noise and vibration refinement with special emphasis on diagnostics". *FME Transactions* 45 (3), 2017, pp. 448–458 (cited in p. 4).

[20] H. Kanda, M. Okubo, and T. Yonezawa. "Analysis of Noise Sources and Their Transfer Paths in Diesel Engines". *International Congress & Exposition*, 1990 (cited in p. 4).

[21] S. A. Fausti, D. A. Erickson, R. H. Frey, B. Z. Rappaport, and M. A. Schechter. "The effects of noise upon human hearing sensitivity from 8000 to 20000 Hz". *The Journal of the Acoustical Society of America* 69 (5), 1981, pp. 1343–1349 (cited in p. 4).

[22] D. I. Nechaev and A. Y. Supin. "Hearing sensitivity to shifts of rippled-spectrum patterns". *The Journal of the Acoustical Society of America* 134 (4), 2013, pp. 2913–2922 (cited in p. 4).

[23] H. Liu, J. Zhang, P. Guo, F. Bi, H. Yu, and G. Ni. "Sound quality prediction for engine-radiated noise". *Mechanical Systems and Signal Processing* 56-57, 2015, pp. 277–287 (cited in pp. 5, 14).

[24] C. J. da Silveira Brizon and E. B. Medeiros. "Combining subjective and objective assessments to improve acoustic comfort evaluation of motor cars". *Applied Acoustics* 73 (9), 2012, pp. 913–920 (cited in p. 5).

[25] W. C. Strahle. "Combustion noise". *Progress in Energy and Combustion Science* 4 (3), 1978, pp. 157–176 (cited in pp. 8, 9).

[26] A. Schwarz and J. Janicka. *Combustion Noise*. Springer-Verlag, 2009 (cited in p. 8).

[27] F. Grimm, D. Ohno, S. Werner, M. Stöhr, et al. "Direct combustion noise simulation of a lean premixed swirl flame using stochastic sound sources". *54th AIAA Aerospace Sciences Meeting, AIAA SciTech Forum* (2016-1881), 2016 (cited in pp. 8, 98).

[28] E. Rolland, F. De Domenico, and S. Hochgreb. "Direct and indirect noise generated by entropic and compositional inhomogeneities". *Journal of Engineering for Gas Turbines and Power*, 2018 (cited in p. 8).

[29] D. G. Crighton, A. P. Dowling, J. E. F. Williams, M. Heckl, and F. G. Leppington. "Thermoacoustic Sources and Instabilities". In: *Modern Methods in Analytical Acoustics: Lecture Notes*. London: Springer London, 1992, pp. 378–405 (cited in p. 8).

[30] A. P. Dowling. "Acoustics of unstable flows". *Theoretical and applied mechanics 1996*, 1997, pp. 171–186 (cited in p. 8).

[31] C. L. Morfey. "Amplification of aerodynamic noise by convected flow inhomogeneities". *Journal of Sound and Vibration* 31 (4), 1973, pp. 391–397 (cited in p. 8).

[32] F. E. Marble and S. M. Candel. "Acoustic disturbance from gas non-uniformities convected through a nozzle". *Journal of Sound and Vibration* 55 (2), 1977, pp. 225–243 (cited in p. 8).

[33] W. Strahle. "A review of combustion generated noise". *Aeroacoustics Conference*, 1975, p. 1023 (cited in pp. 8, 9).

[34] F. D. Domenico, E. O. Rolland, and S. Hochgreb. "Detection of direct and indirect noise generated by synthetic hot spots in a duct". *Journal of Sound and Vibration* 394, 2017, pp. 220–236 (cited in p. 8).

[35] G. Persico, P. Gaetani, and A. Spinelli. "Assessment of synthetic entropy waves for indirect combustion noise experiments in gas turbines". *Experimental Thermal and Fluid Science* 88, 2017, pp. 376–388 (cited in p. 8).

[36] S. Busch, K. Zha, and P. C. Miles. "Investigations of closely coupled pilot and main injections as a means to reduce combustion noise in a small-bore direct injection Diesel engine". *International Journal of Engine Research* 16 (1), 2015, pp. 13–22 (cited in p. 8).

[37] S. Busch, K. Zha, A. Warey, F. Pesce, and R. Peterson. "On the Reduction of Combustion Noise by a Close-Coupled Pilot Injection in a Small-Bore Direct-Injection Diesel Engine". *Journal of Engineering for Gas Turbines and Power* 138 (10), 2016, p. 102804 (cited in p. 8).

[38] A. E. W. Austen and T. Priede. "Origins of diesel engine noise". *SAE Technical Paper* 590127, 1958 (cited in pp. 8, 9, 15, 16, 29, 41).

[39] S. A. Klein and J. B. W. Kok. "Sound Generation by Turbulent Non-premixed Flames". *Combustion Science and Technology* 149 (1-6), 1999, pp. 267–295 (cited in p. 8).

[40] F. Flemming, A. Sadiki, and J. Janicka. "Investigation of combustion noise using a LES/CAA hybrid approach". *Proceedings of the Combustion Institute* 31 (2), 2007, pp. 3189–3196 (cited in pp. 8, 98).

[41] S. Candel. "Combustion dynamics and control: Progress and challenges". *Proceedings of the Combustion Institute* 29 (1), 2002. Proceedings of the Combustion Institute, pp. 1–28 (cited in p. 8).

[42] S. Roux, G. Lartigue, T. Poinsot, U. Meier, and C. Bérat. "Studies of mean and unsteady flow in a swirled combustor using experiments, acoustic analysis, and large eddy simulations". *Combustion and Flame* 141 (1), 2005, pp. 40–54 (cited in p. 8).

[43] B. Higgins. "On the sound produced by a current of hydrogen gas passing through a tube". *Journal of natural philosophy, chemistry and the arts* 1 (129-131), 1802, p. 2 (cited in p. 8).

[44] T. Priede. "Relation between form of cylinder-pressure diagram and noise in diesel engines". *Proceedings of the Institution of Mechanical Engineers: Automobile Division* 14 (1), 1960, pp. 63–97 (cited in pp. 9, 10, 16, 17, 27, 53).

[45] T. Priede and E. C. Grover. "Paper 2: Noise of Industrial Diesel Engines". *Proceedings of the Institution of Mechanical Engineers, Conference Proceedings* 181 (3), 1966, pp. 73–89 (cited in pp. 9, 10, 16).

[46] W. C. Strahle. "Combustion randomness and diesel engine noise: theory and initial experiments". *Combustion and Flame* 28, 1977, pp. 279–290 (cited in pp. 9, 16, 28, 79).

[47] A. J. Torregrosa, A. Broatch, J. Martín, and L. Monelletta. "Combustion noise level assessment in direct injection Diesel engines by means of in-cylinder pressure components". *Measurement Science and Technology* 18 (7), 2007, pp. 2131–2142 (cited in pp. 9, 14–17, 28, 36, 41).

[48] F. Payri, A. Broatch, X. Margot, and L. Monelletta. "Sound quality assessment of Diesel combustion noise using in-cylinder pressure components". *Measurement Science and Technology* 20 (1), 2009, pp. 01–12 (cited in pp. 9, 14, 15).

[49] F. Payri, A. Broatch, B. Tormos, and V. Marant. "New methodology for in-cylinder pressure analysis in direct injection diesel engines – application to combustion noise". *Measurement Science and Technology* 16 (2), 2005, pp. 540–547 (cited in pp. 9, 16, 17, 27).

[50] R. Hickling, D. A. Feldmaier, and S. H. Sung. "Knock-induced cavity resonances in open chamber Diesel engines". *The Journal of the Acoustical Society of America* 65 (5), 1979, pp. 1474–1479 (cited in pp. 9–11, 17, 18, 98, 114).

[51] C. S. Draper. "Pressure waves accompanying detonation in the internal combustion engine". *Journal of the Aeronautical Sciences* 5 (6), 1938, pp. 219–226 (cited in p. 10).

[52] A. J. Torregrosa, A. Broatch, X. Margot, and V. Marant. "Combustion chamber resonances in direct injection automotive Diesel engines: a numerical approach". *International Journal of Engine Research* 5 (1), 2003, pp. 83–91 (cited in pp. 10–12, 16, 17, 28, 46, 47, 67, 70, 106, 131).

[53] A. Broatch, X. Margot, A. Gil, and C. Donayre. "Computational study of the sensitivity to ignition characteristics of the resonance in DI diesel engine combustion chambers". *Engineering Computations* 24 (1), 2007, pp. 77–96 (cited in pp. 11, 12, 16–18, 42, 46, 67, 131).

[54] L. J. Eriksson. "Higher order mode effects in circular ducts and expansion chambers". *The Journal of the Acoustical Society of America* 68 (2), 1980, pp. 545–550 (cited in pp. 11, 18).

[55] J. E. Dec. "A Conceptual Model of DI Diesel Combustion Based on Laser-Sheet Imaging". *International Congress & Exposition*, 1997 (cited in p. 12).

[56] T. Schuller, O. Sauvage, Z. Dimitrijevic, and G. Rymer. "Acoustic Analysis of Unsteady Diesel Engine Combustion Chamber Pressure Evolution". *11th AIAA/CEAS Aeroacoustics Conference*, 2005, p. 2910 (cited in pp. 12, 14).

[57] M. CANAKCI. "An experimental study for the effects of boost pressure on the performance and exhaust emissions of a DI-HCCI gasoline engine". *Fuel* 87 (8), 2008, pp. 1503–1514 (cited in p. 13).

[58] Q. FANG, J. FANG, J. ZHUANG, and Z. HUANG. "Influences of pilot injection and exhaust gas recirculation (EGR) on combustion and emissions in a HCCI-DI combustion engine". *Applied Thermal Engineering* 48, 2012, pp. 97–104 (cited in p. 13).

[59] S. GAN, H. K. NG, and K. M. PANG. "Homogeneous Charge Compression Ignition (HCCI) combustion: Implementation and effects on pollutants in direct injection diesel engines". *Applied Energy* 88 (3), 2011, pp. 559–567 (cited in p. 13).

[60] R. E. HEROLD, J. M. KRASSELT, D. E. FOSTER, J. B. GHANDHI, D. L. REUSS, and P. M. NAJT. "Investigations into the Effects of Thermal and Compositional Stratification on HCCI Combustion - Part II: Optical Engine Results". *SAE International Journal of Engines* 2 (1), 2009, pp. 1034–1053 (cited in p. 13).

[61] R. K. MAURYA and A. K. AGARWAL. "Experimental investigation on the effect of intake air temperature and air-fuel ratio on cycle-to-cycle variations of HCCI combustion and performance parameters". *Applied Energy* 88 (4), 2011, pp. 1153–1163 (cited in p. 13).

[62] R. K. MAURYA and A. K. AGARWAL. "Statistical analysis of the cyclic variations of heat release parameters in HCCI combustion of methanol and gasoline". *Applied Energy* 89 (1), 2012, pp. 228–236 (cited in p. 13).

[63] J. BENAJES, A. BROATCH, A. GARCIA, and L. M. MUÑOZ. "An experimental investigation of diesel-gasoline blends effects in a direct-injection compression-ignition engine operating in PCCI conditions". *SAE Technical Paper*, 2013 (cited in p. 13).

[64] W. L. HARDY and R. D. REITZ. "A Study of the Effects of High EGR, High Equivalence Ratio, and Mixing Time on Emissions Levels in a Heavy-Duty Diesel Engine for PCCI Combustion". *SAE Technical Paper* 2006-01-0026, 2006 (cited in p. 13).

[65] M. JIA, A. B. DEMPSEY, H. WANG, Y. LI, and R. D. REITZ. "Numerical simulation of cyclic variability in reactivity-controlled compression ignition combustion with a focus on the initial temperature at intake valve closing". *International Journal of Engine Research* 16 (3), 2015, pp. 441–460 (cited in pp. 13, 88).

[66] H. RYO and Y. HIROMICHI. "HCCI Combustion in a DI Diesel engine". *SAE Technical Paper* 2003-01-0745, 2003 (cited in p. 13).

[67] A. J. TORREGROSA, A. BROATCH, A. GARCÍA, and L. F. MÓNICO. "Sensitivity of combustion noise and NOx and soot emissions to pilot injection in PCCI Diesel engines". *Applied Energy* 104, 2013, pp. 149–157 (cited in p. 13).

[68] Y. Takeda, N. Keiichi, and N. Keiichi. "Emission Characteristics of Premixed Lean Diesel Combustion with Extremely Early Staged Fuel Injection". *SAE Technical Paper* 961163, 1996 (cited in p. 13).

[69] M. Lewander, B. Johansson, and P. Tunestål. "Investigation and Comparison of Multi Cylinder Partially Premixed Combustion Characteristics for Diesel and Gasoline Fuels". *SAE Technical Paper* 2011-01-1811, 2011 (cited in p. 13).

[70] H. Solaka, U. Aronsson, M. Tuner, and B. Johansson. "Investigation of Partially Premixed Combustion Characteristics in Low Load Range with Regards to Fuel Octane Number in a Light-Duty Diesel Engine". *SAE Technical Paper* 2012-01-0684, 2012 (cited in p. 13).

[71] P. Borgqvist, P. Tunestal, and B. Johansson. "Gasoline partially premixed combustion in a light duty engine at low load and idle operating conditions". *SAE Technical Paper* 2012-01-0687, 2012 (cited in p. 13).

[72] R. Hanson, D. Splitter, and R. Reitz. "Operating a Heavy-Duty Direct-Injection Compression-Ignition Engine with Gasoline for Low Emissions". *SAE Technical Paper* 2009-01-1442, 2009 (cited in p. 13).

[73] V. Manente, B. Johansson, P. Tunestal, and W. Cannella. "Effects of Different Type of Gasoline Fuels on Heavy Duty Partially Premixed Combustion". *SAE International Journal of Engines* 2009-01-2668, 2009, pp. 71–88 (cited in p. 13).

[74] J. Benajes, R. Novella, A. García, and S. Arthozoul. "Partially premixed combustion in a diesel engine induced by a pilot injection at the low-pressure top dead center". *Energy & Fuels* 23 (6), 2009, pp. 2891–2902 (cited in p. 13).

[75] J. Benajes, R. Novella, D. De Lima, V. Dugue, and N. Quechon. "The potential of highly premixed combustion for pollutant control in an automotive two-stroke HSDI diesel engine". *SAE Technical Paper* 2012-01-1104, 2012 (cited in p. 13).

[76] J. Benajes, R. Novella, D. De Lima, P. Tribotté, et al. "Analysis of the combustion process, pollutant emissions and efficiency of an innovative 2-stroke HSDI engine designed for automotive applications". *Applied Thermal Engineering* 58 (1), 2013, pp. 181–193 (cited in p. 13).

[77] J. Benajes, S. Molina, R. Novella, and D. De Lima. "Implementation of the Partially Premixed Combustion concept in a 2-stroke HSDI diesel engine fueled with gasoline". *Applied Energy* 122, 2014, pp. 94–111 (cited in p. 13).

[78] J. Benajes, J. Martin, R. Novella, and D. De Lima. "Analysis of the load effect on the partially premixed combustion concept in a 2-stroke HSDI diesel engine fueled with conventional gasoline". *SAE Technical Paper* 2014-01-1291, 2014 (cited in p. 13).

[79]   J. Benajes, R. Novella, D. De Lima, and P. Tribotte. "Investigation on multiple injection strategies for gasoline PPC operation in a newly designed 2-stroke HSDI compression ignition engine". *SAE International Journal of Engines* 8 (2015-01-0830), 2015, pp. 758–774 (cited in pp. 13, 86, 164, 177, 180).

[80]   J. Benajes, R. Novella, D. De Lima, and P. Tribotté. "Analysis of combustion concepts in a newly designed two-stroke high-speed direct injection compression ignition engine". *International Journal of Engine Research*, 2015 (cited in pp. 13, 188).

[81]   J. Benajes, J. Martín, R. Novella, and K. Thein. "Understanding the performance of the multiple injection gasoline partially premixed combustion concept implemented in a 2-Stroke high speed direct injection compression ignition engine". *Applied Energy* 161, 2016, pp. 465–475 (cited in pp. 13, 14, 19, 177).

[82]   J. Benajes, R. Novella, D. D. Lima, and K. Thein. "Impact of injection settings operating with the gasoline Partially Premixed Combustion concept in a 2-stroke HSDI compression ignition engine". *Applied Energy* 193, 2017, pp. 515–530 (cited in pp. 13, 14, 18, 86, 188).

[83]   P. Tribotte, F. Ravet, V. Dugue, P. Obernesser, et al. "Two Strokes Diesel Engine - Promising Solution to Reduce CO2 Emissions". *Procedia - Social and Behavioral Sciences* 48, 2012, pp. 2295–2314 (cited in pp. 13, 25).

[84]   ITU. *BS.468: Measurement of audio-frequency noise voltage level in sound broadcasting*. Geneva, CH, 1986 (cited in pp. 13, 136).

[85]   A. J. Torregrosa, A. Broatch, R. Novella, and L. F. Mónico. "Suitability analysis of advanced diesel combustion concepts for emissions and noise control". *Energy* 36 (2), 2011, pp. 825–838 (cited in p. 14).

[86]   A. Acri, E. Nijman, M. Klanner, G. Offner, and R. Corradi. "On the influence of cyclic variability on surface noise contribution analysis of internal combustion engines". *Applied Acoustics* 132 (Supplement C), 2018, pp. 97–108 (cited in p. 14).

[87]   J. Mao, Z.-y. Hao, G.-x. Jing, X. Zheng, and C. Liu. "Sound quality improvement for a four-cylinder diesel engine by the block structure optimization". *Applied Acoustics* 74 (1), 2013, pp. 150–159 (cited in pp. 14, 16).

[88]   T. Fuyuto and M. Taki. "Noise-canceling Spike between Pressure Rise Peaks of Pilot and Main Combustion in Diesel Engine". *International Conference on Modeling and Diagnostics for Advanced Engine systems: the 9th COMODIA, Okayama (Japan)*, 2017 (cited in p. 14).

[89]   L. Stanković and J. F. Böhme. "Time-frequency analysis of multiple resonances in combustion engine signals". *Signal Processing* 79 (1), 1999, pp. 15–28 (cited in p. 15).

[90]   J. M. Desantes, A. J. Torregrosa, and A. Broatch. "Wavelet Transform applied to Combustion Noise Analysis in High-speed DI Diesel Engines". *SAE Technical Paper* 2001-01-1545, 2001 (cited in p. 15).

[91]   J. Chang, M. Kim, and K. Min. "Detection of misfire and knock in spark ignition engines by wavelet transform of engine block vibration signals". *Measurement Science and Technology* 13 (7), 2002, pp. 1108–1114 (cited in p. 15).

[92]   F. Bi, L. Li, J. Zhang, and T. Ma. "Source identification of gasoline engine noise based on continuous wavelet transform and EEMD–RobustICA". *Applied Acoustics* 100, 2015, pp. 34–42 (cited in p. 15).

[93]   A. J. Shahlari, C. Hocking, E. Kurtz, and J. Ghandhi. "Comparison of Compression Ignition Engine Noise Metrics in Low-Temperature Combustion Regimes". *SAE International Journal of Engines* 6, 2013, pp. 541–552 (cited in pp. 15, 18).

[94]   D. Anderton. "Relation between combustion system and engine noise". *SAE Technical Paper* 790270, 1979 (cited in pp. 15, 29, 41).

[95]   M. F. Russell and R. Haworth. "Combustion Noise from High Speed Direct Injection Diesel Engines". *SAE Surface Vehicle Noise and Vibration Conference*, 1985 (cited in p. 15).

[96]   X. Zhao, Y. Cheng, and S. Ji. "Combustion parameters identification and correction in diesel engine via vibration acceleration signal". *Applied Acoustics* 116 (Supplement C), 2017, pp. 205–215 (cited in p. 15).

[97]   O. P. Singh, T. Sreenivasulu, and M. Kannan. "The effect of rubber dampers on engine's NVH and thermal performance". *Applied Acoustics* 75, 2014, pp. 17–26 (cited in p. 16).

[98]   F. Duvigneau, T. Luft, J. Hots, J. L. Verhey, H. Rottengruber, and U. Gabbert. "Thermo-acoustic performance of full engine encapsulations–A numerical, experimental and psychoacoustic study". *Applied Acoustics* 102, 2016, pp. 79–87 (cited in p. 16).

[99]   A. Vressner, A. Lundin, M. Christensen, P. Tunestål, and B. Johansson. "Pressure Oscillations During Rapid HCCI Combustion". *SAE Technical Paper* 2003-01-3217, 2003 (cited in p. 16).

[100]   M. Wissink, Z. Wang, D. Splitter, A. Shahlari, and R. D. Reitz. "Investigation of Pressure Oscillation Modes and Audible Noise in RCCI, HCCI, and CDC". *SAE Technical Paper* 2013-01-1652, 2013 (cited in p. 18).

[101]   J. Benajes, A. García, J. M. Pastor, and J. Monsalve-Serrano. "Effects of piston bowl geometry on Reactivity Controlled Compression Ignition heat transfer and combustion losses at different engine loads". *Energy* 98, 2016, pp. 64–77 (cited in pp. 18, 19, 178).

[102] J. BENAJES, R. NOVELLA, J. M. PASTOR, A. HERNÁNDEZ-LÓPEZ, and S. L. KOKJOHN. "Computational optimization of the combustion system of a heavy duty direct injection diesel engine operating with dimethyl-ether". *Fuel* 218, 2018, pp. 127–139 (cited in pp. 18, 139, 142–145).

[103] A. BROATCH, X. MARGOT, A. GIL, and J. C. DONAYRE. "A CFD approach to diesel engine combustion chamber resonance". *SAE Technical Paper* 2007-24-0043, 2007 (cited in pp. 18, 47, 70, 131).

[104] V. YAKHOT and S. ORSZAG. "Renormalization group analysis of turbulence." *Journal of Scientific Computing* 1 (1), 1986, pp. 3–51 (cited in pp. 18, 49, 50).

[105] D. C. WILCOX. "Formulation of the k-w turbulence model revisited". *AIAA journal* 46 (11), 2008, pp. 2823–2838 (cited in pp. 18, 49).

[106] S. B. POPE. "Ten questions concerning the large-eddy simulation of turbulent flows". *New Journal of Physics* 6 (1), 2004, p. 35 (cited in pp. 19, 49).

[107] J. SMAGORINSKY. "General circulation experiments with the primitive equations". *Monthly Weather Review* 91 (3), 1963, pp. 99–164 (cited in pp. 19, 49).

[108] E. POMRANING and C. J. RUTLAND. "Dynamic one-equation nonviscosity large-eddy simulation model". *AIAA journal* 40 (4), 2002, pp. 689–701 (cited in pp. 19, 49, 50).

[109] A. L. PILLAI and R. KUROSE. "Numerical investigation of combustion noise in an open turbulent spray flame". *Applied Acoustics* 133, 2018, pp. 16–27 (cited in p. 19).

[110] F. PAYRI, J. BENAJES, X. MARGOT, and A. GIL. "CFD modeling of the in-cylinder flow in direct-injection Diesel engines". *Computers & Fluids* 33 (8), 2004, pp. 995–1021 (cited in p. 19).

[111] J. BENAJES, J. J. LÓPEZ, R. NOVELLA, and P. REDÓN. "Comprehensive modeling study analyzing the insights of the NO–NO2 conversion process in current diesel engines". *Energy Conversion Management* 84, 2014, pp. 691–700 (cited in p. 19).

[112] H. HIROYASU, H. MIAO, T. HIROYASU, M. MIKI, J. KAMIURA, and S. WATANABE. "Genetic Algorithms Optimization of Diesel Engine Emissions and Fuel Efficiency with Air Swirl, EGR, Injection Timing and Multiple Injections". *SAE Technical Paper* 2003-01-1853, 2003 (cited in pp. 19, 139).

[113] M. COSTA, G. M. BIANCHI, C. FORTE, and G. CAZZOLI. "A Numerical Methodology for the Multi-objective Optimization of the DI Diesel Engine Combustion". *Energy Procedia* 45, 2014, pp. 711–720 (cited in pp. 19, 139).

[114] J. M. Desantes, J. M. García-Oliver, R. Novella, and E. J. Pérez-Sánchez. "Application of an unsteady flamelet model in a RANS framework for spray A simulation". *Applied Thermal Energy* 117, 2017, pp. 50–64 (cited in p. 19).

[115] S. Molina, A. García, J. M. Pastor, E. Belarte, and I. Balloul. "Operating range extension of RCCI combustion concept from low to full load in a heavy-duty engine". *Applied Energy* 143, 2015, pp. 211–227 (cited in pp. 19, 48, 57).

[116] O. Vermorel, S. Richard, O. Colin, C. Angelberger, A. Benkenida, and D. Veynante. "Towards the understanding of cyclic variability in a spark ignited engine using multi-cycle LES". *Combustion and Flame* 156 (8), 2009, pp. 1525–1541 (cited in pp. 20, 89).

[117] J. Tillou, J.-B. Michel, C. Angelberger, and D. Veynante. "Assessing LES models based on tabulated chemistry for the simulation of Diesel spray combustion". *Combustion and Flame* 161 (2), 2014, pp. 525–540 (cited in p. 20).

[118] L. Monelletta. "Contribution to the study of combustion noise of automotive Diesel engines". PhD thesis. Universitat Politècnica de València, 2010 (cited in pp. 23, 24, 27, 76).

[119] D. de Lima. "Analysis of combustion concepts in a poppet valve two-stroke downsized compression ignition engine designed for passenger car applications". PhD thesis. Universitat Politècnica de València, 2016 (cited in pp. 23, 24, 85).

[120] F. Ihlenburg. "The Medium-Frequency Range in Computational Acoustics: Practical and Numerical Aspects". *Journal of Computational Acoustics* 11 (02), 2003, pp. 175–193 (cited in pp. 25, 47, 75).

[121] M. Lapuerta, O. Armas, and J. J. Hernández. "Diagnosis of DI Diesel combustion from in-cylinder pressure signal by estimation of mean thermodynamic properties of the gas". *Applied Thermal Engineering* 19 (5), 1999, pp. 513–529 (cited in p. 27).

[122] F. Payri, P. Olmeda, J. Martín, and A. García. "A complete 0D thermodynamic predictive model for direct injection diesel engines". *Applied Energy* 88 (12), 2011, pp. 4632–4641 (cited in pp. 27, 63, 75).

[123] J. Yang and R. W. Anderson. "A new criterion for judging SI engine in-cylinder pressure development for its effect on combustion noise". *Journal of Engineering for Gas Turbines and Power* 120 (3), 1998, pp. 664–668 (cited in p. 28).

[124] J. Chung, J. Oh, and M. Sunwoo. "A real-time combustion control with reconstructed in-cylinder pressure by principal component analysis for a CRDI diesel engine". *Journal of Engineering for Gas Turbines and Power* 139 (6), 2017, p. 062802 (cited in p. 28).

[125] F. Steinparzer, P. Nefischer, and W. Stütz. "The future of the diesel engine as a means of propulsion in passenger cars". *15th Internationales Stuttgarter Symposium: Automobilund Motorentechnik*, 2015. Ed. by M. Bargende, H.-C. Reuss, and J. Wiedemann, pp. 1363–1380 (cited in p. 31).

[126] S. Rulik, W. Wróblewski, G. Nowak, and J. Szwedowicz. "Heat transfer intensification using acoustic waves in a cavity". *Energy* 87, 2015, pp. 21–30 (cited in p. 38).

[127] *CONVERGE 2.2 Theory Manual*. CONVERGENT SCIENCE Inc. 2015 (cited in p. 46).

[128] O. Redlich and J. N. S. Kwong. "On the Thermodynamics of Solutions. V. An Equation of State. Fugacities of Gaseous Solutions". *Chemical Reviews* 44 (1), 1949, pp. 233–244 (cited in p. 46).

[129] R. I. Issa. "Solution of the implicitly discretised fluid flow equations by operator-splitting". *Journal of Computational Physics* 62, 1986, pp. 40–65 (cited in p. 46).

[130] P. K. Senecal, E. Pomraning, K. J. Richards, T. E. Briggs, et al. "Multi-Dimensional Modeling of Direct-Injection Diesel Spray Liquid Length and Flame Lift-off Length using CFD and Parallel Detailed Chemistry". *SAE Technical Paper* 2003-01-1043, 2003 (cited in pp. 47–49, 57, 70).

[131] S. Som and S. K. Aggarwal. "Effects of primary breakup modeling on spray and combustion characteristics of compression ignition engines". *Combustion and Flame* 157 (6), 2010, pp. 1179–1193 (cited in pp. 47, 70).

[132] P. K. Senecal, E. Pomraning, K. J. Richards, and S. Som. "Grid-convergent spray models for internal combustion engine computational fluid dynamics simulations". *Journal of Energy Resources Technology* 136 (1), 2014, p. 012204 (cited in pp. 47, 70).

[133] P. K. Senecal, E. Pomraning, Q. Xue, S. Som, et al. "Large Eddy simulation of vaporizing sprays considering multi-injection averaging and grid-convergent mesh resolution". *Journal of Engineering for Gas Turbines and Power* 136 (11), 2014, p. 111504 (cited in pp. 47, 70).

[134] J. Kodavasal, C. P. Kolodziej, S. A. Ciatti, and S. Som. "Computational fluid dynamics simulation of gasoline compression ignition". *Journal of Energy Resources Technology* 137 (3), 2015, p. 032212 (cited in pp. 47, 70, 86).

[135] H. Wang, R. D. Reitz, and M. Yao. "Comparison of Diesel Combustion CFD Models and Evaluation of the Effects of Model Constants". *SAE 2012 World Congress & Exhibition*, 2012 (cited in pp. 47, 49, 70).

[136] J. TAGLIALEGAMI, G. BOGIN, E. OSECKY, and A. M. DEAN. "Simulation of n-Heptane and Surrogate Fuels for Advanced Combustion Engines (FACE) in a Single-Cylinder Compression Ignition Engine". *ASME 2013 Internal Combustion Engine Division Fall Technical Conference*, 2013 (cited in pp. 47, 49, 70).

[137] A. OYEDIRAN, D. DARLING, and K. RADHAKRISHNAN. "Review of combustion-acoustic instabilities". *American Institute of Aeronautics and Astronautics*, 1995 (cited in pp. 47, 70).

[138] J. K. DUKOWICZ. "A particle-fluid numerical model for liquid sprays". *Journal of Computational Physics* 35 (2), 1980, pp. 229–253 (cited in p. 48).

[139] R. D. REITZ and J. C. BEALE. "Modeling spray atomization with the Kelvin-Helmholtz/Rayleigh-Taylor hybrid model". *Atomization and Sprays* 9 (6), 1999, pp. 623–650 (cited in p. 48).

[140] P. J. O'ROURKE. "Collective drop effects on vaporizing liquid sprays". PhD thesis. Los Alamos National Laboratory, NM (USA), 1981 (cited in p. 48).

[141] A. A. AMSDEN, P. J. O'ROURKE, and T. D. BUTLER. *KIVA-II: A computer program for chemically reactive flows with sprays*. Tech. rep. Los Alamos National Laboratory, NM (USA), 1989 (cited in p. 48).

[142] A. B. LIU, D. MATHER, and R. D. REITZ. "Modeling the Effects of Drop Drag and Breakup on Fuel Sprays". *International Congress & Exposition*, 1993 (cited in p. 48).

[143] C. HABCHI, F. A. LAFOSSAS, P. BÉARD, and D. BROSETA. "Formulation of a One-Component Fuel Lumping Model to Assess the Effects of Fuel Thermodynamic Properties on Internal Combustion Engine Mixture Preparation and Combustion". *2004 SAE Fuels & Lubricants Meeting & Exhibition*, 2004 (cited in p. 48).

[144] A. BABAJIMOPOULOS, D. N. ASSANIS, D. L. FLOWERS, S. M. ACEVES, and R. P. HESSEL. "A fully coupled computational fluid dynamics and multi-zone model with detailed chemical kinetics for the simulation of premixed charge compression ignition engines". *International Journal of Engine Research* 6 (5), 2005, pp. 497–512 (cited in p. 48).

[145] P. PAL, S. KEUM, and H. G. IM. "Assessment of flamelet versus multi-zone combustion modeling approaches for stratified-charge compression ignition engines". *International Journal of Engine Research* 17 (3), 2016, pp. 280–290 (cited in p. 48).

[146] P. PAL. "Computational Modeling and Analysis of Low Temperature Combustion Regimes for Advanced Engine Applications". PhD thesis. University of Michigan-Ann Arbor, 2016 (cited in p. 48).

[147] P. PAL, D. PROBST, Y. PEI, Y. ZHANG, et al. "Numerical Investigation of a Gasoline-Like Fuel in a Heavy-Duty Compression Ignition Engine Using Global Sensitivity Analysis". *SAE International Journal of Fuels and Lubricants* 10 (1), 2017, pp. 56–68 (cited in pp. 48, 140).

[148] Y. PEI, S. SOM, E. POMRANING, P. K. SENECAL, et al. "Large eddy simulation of a reacting spray flame with multiple realizations under compression ignition engine conditions". *Combustion and Flame* 162 (12), 2015, pp. 4442–4455 (cited in p. 48).

[149] S. R. TURNS et al. *An introduction to combustion*. Vol. 499. McGraw-hill New York, 1996 (cited in p. 48).

[150] J. BRAKORA and R. D. REITZ. "A Comprehensive Combustion Model for Biodiesel-Fueled Engine Simulations". *SAE Technical Paper* 2013-01-1099, 2013 (cited in p. 48).

[151] H. HIROYASU and T. KADOTA. "Models for Combustion and Formation of Nitric Oxide and Soot in Direct Injection Diesel Engines". *SAE Technical Paper*, 1976 (cited in pp. 49, 87, 140).

[152] J. B. HEYWOOD. *Internal Combustion Engine Fundamentals*. McGraw-Hill Inc, 1998 (cited in pp. 49, 140).

[153] A. J. TORREGROSA, P. OLMEDA, B. DEGRAEUWE, and M. REYES. "A concise wall temperature model for DI Diesel engines". *Applied Thermal Engineering* 26 (11-12), 2006 (cited in p. 49).

[154] C. ANGELBERGER, T. POINSOT, and B. DELHAY. "Improving near-wall combustion and wall heat transfer modeling in SI engine computations". *SAE Technical Paper* 2003-01-0542, 1997 (cited in p. 49).

[155] E. GALLONI, G. FONTANA, and S. STACCONE. "Numerical and experimental characterization of knock occurrence in a turbo-charged spark-ignition engine". *Energy Conversion and Management* 85 (Supplement C), 2014, pp. 417–424 (cited in p. 55).

[156] A. MISDARIIS, O. VERMOREL, and T. POINSOT. "LES of knocking in engines using dual heat transfer and two-step reduced schemes". *Combustion and Flame* 162 (11), 2015, pp. 4304–4312 (cited in p. 55).

[157] P. K. SENECAL and R. D. REITZ. "Simultaneous Reduction of Engine Emissions and Fuel Consumption Using Genetic Algorithms and Multi-Dimensional Spray and Combustion Modeling". *SAE Technical Paper*, 2000 (cited in pp. 57, 140).

[158] S. CIATTI, M. JOHNSON, B. D. ADHIKARY, R. D. REITZ, and A. KNOCK. "Efficiency and Emissions performance of Multizone Stratified Compression Ignition Using Different Octane Fuels". *SAE Technical Paper*, 2013 (cited in p. 57).

[159] F. Payri, S. Molina, J. Martín, and O. Armas. "Influence of measurement errors and estimated parameters on combustion diagnosis". *Applied Thermal Engineering* 26 (2–3), 2006, pp. 226–236 (cited in p. 63).

[160] P. K. Senecal, E. Pomraning, K. J. Richards, and S. Som. "An Investigation of Grid Convergence for Spray Simulations using an LES Turbulence Model". *SAE 2013 World Congress & Exhibition*, 2013 (cited in p. 77).

[161] S. Som. "Development and validation of spray models for investigating diesel engine combustion and emissions". PhD thesis. University of Illinois at Chicago, 2009 (cited in p. 77).

[162] R. Payri, J. M. García, F. Salvador, and J. Gimeno. "Using spray momentum flux measurements to understand the influence of diesel nozzle geometry on spray characteristics". *Fuel* 84 (5), 2005, pp. 551–561 (cited in p. 86).

[163] R. Payri, F. J. Salvador, J. Gimeno, and G. Bracho. "A new methodology for correcting the signal cumulative phenomenon on injection rate measurements". *Experimental Techniques* 32 (1), 2008, pp. 46–49 (cited in p. 86).

[164] T. D. Fansler and R. M. Wagner. "Cyclic dispersion in engine combustion-Introduction by the special issue editors". *International Journal of Engine Research* 16 (3), 2015, pp. 255–259 (cited in p. 88).

[165] D. Klos and S. L. Kokjohn. "Investigation of the sources of combustion instability in low-temperature combustion engines using response surface models". *International Journal of Engine Research* 16 (3), 2015, pp. 419–440 (cited in pp. 88, 89).

[166] C. F. Silva, M. Leyko, F. Nicoud, and S. Moreau. "Assessment of combustion noise in a premixed swirled combustor via Large-Eddy Simulation". *Computers & Fluids* 78, 2013, pp. 1–9 (cited in p. 98).

[167] H. Chen, M. Xu, D. L. S. Hung, J. Yang, and H. Zhuang. "Development of a POD-Based Analysis Approach for Quantitative Comparison of Spray Structure Variations in a Spark-Ignition Direct-Injection Engine". *SAE/KSAE 2013 International Powertrains, Fuels & Lubricants Meeting*, 2013 (cited in p. 99).

[168] G. Tissot, L. Cordier, N. Benard, and B. R. Noack. "Model reduction using Dynamic Mode Decomposition". *Comptes Rendus Mécanique* 342 (6), 2014. Flow separation control, pp. 410–416 (cited in p. 99).

[169] T. Colonius and J. Freund. "POD analysis of sound generation by a turbulent jet". *40th AIAA Aerospace Sciences Meeting & Exhibit*, 2002, p. 72 (cited in p. 99).

[170] D. M. MARKOVICH, S. S. ABDURAKIPOV, L. M. CHIKISHEV, V. M. DULIN, and K. HANJALIĆ. "Comparative analysis of low- and high-swirl confined flames and jets by proper orthogonal and dynamic mode decompositions". *Physics of Fluids* 26 (6), 2014, p. 065109 (cited in p. 99).

[171] Y. C. LIANG, H. P. LEE, S. P. LIM, W. Z. LIN, K. H. LEE, and C. G. WU. "Proper orthogonal decomposition and its applications-Part I: Theory". *Journal of Sound and vibration* 252 (3), 2002, pp. 527–544 (cited in p. 106).

[172] J. L. LUMLEY. "The structure of inhomogeneous turbulent flows". *Atmospheric Turbulence and Radio Wave Propagation – Proceedings of the International Colloquium*, 1967, pp. 166–178 (cited in p. 107).

[173] N. AUBRY. "On the hidden beauty of the proper orthogonal decomposition". *Theoretical and Computational Fluid Dynamics* 2 (5-6), 1991, pp. 339–352 (cited in pp. 107, 108).

[174] P. J. SCHMID. "Dynamic mode decomposition of numerical and experimental data". *Journal of Fluid Mechanics* 656, 2010, pp. 5–28 (cited in pp. 107, 108, 115–117).

[175] S. BAGHERI. "Koopman-mode decomposition of the cylinder wake". *Journal of Fluid Mechanics* 726, 2013, pp. 596–623 (cited in pp. 107, 116).

[176] S. WOLD, K. ESBENSEN, and P. GELADI. "Principal component analysis". *Chemometrics and intelligent laboratory systems* 2 (1-3), 1987, pp. 37–52 (cited in p. 107).

[177] H. ABDI and L. J. WILLIAMS. "Principal component analysis". *Wiley Interdisciplinary Reviews: Computational Statistics* 2 (4), 2010, pp. 433–459 (cited in p. 107).

[178] V. NIKIFOROV. "The energy of graphs and matrices". *Journal of Mathematical Analysis and Applications* 326 (2), 2007, pp. 1472–1475 (cited in p. 107).

[179] C. ECKART and G. YOUNG. "The approximation of one matrix by another of lower rank". *Psychometrika* 1 (3), 1936, pp. 211–218 (cited in p. 108).

[180] P. DRUAULT, J. DELVILLE, and J.-P. BONNET. "Proper Orthogonal Decomposition of the mixing layer flow into coherent structures and turbulent Gaussian fluctuations". *Comptes Rendus Mecanique* 333 (11), 2005, pp. 824–829 (cited in p. 108).

[181] P. DRUAULT, S. LARDEAU, J. P. BONNET, F. COIFFET, et al. "Generation of three-dimensional turbulent inlet conditions for large-eddy simulation". *AIAA journal* 42 (3), 2004, pp. 447–456 (cited in p. 108).

[182] P. J. SCHMID, L. LI, M. P. JUNIPER, and O. PUST. "Applications of the dynamic mode decomposition". *Theoretical and Computational Fluid Dynamics* 25 (1-4), 2011, pp. 249–259 (cited in pp. 108, 115, 116).

[183] M. R. Jovanović, P. J. Schmid, and J. W. Nichols. "Sparsity-promoting dynamic mode decomposition". *Physics of Fluids (1994-present)* 26 (2), 2014, p. 024103 (cited in pp. 108, 115–117).

[184] A. Sakowitz, M. Mihaescu, and L. Fuchs. "Flow decomposition methods applied to the flow in an IC engine manifold". *Applied Thermal Engineering* 65 (1), 2014, pp. 57–65 (cited in pp. 108, 116).

[185] Y. Huang and V. Yang. "Dynamics and stability of lean-premixed swirl-stabilized combustion". *Progress in energy and combustion science* 35 (4), 2009, pp. 293–364 (cited in p. 108).

[186] A. M. Steinberg, I. Boxx, M. Stöhr, C. D. Carter, and W. Meier. "Flow–flame interactions causing acoustically coupled heat release fluctuations in a thermo-acoustically unstable gas turbine model combustor". *Combustion and Flame* 157 (12), 2010, pp. 2250–2266 (cited in p. 108).

[187] V. Caux-Brisebois, A. M. Steinberg, C. M. Arndt, and W. Meier. "Thermo-acoustic velocity coupling in a swirl stabilized gas turbine model combustor". *Combustion and Flame* 161 (12), 2014, pp. 3166–3180 (cited in p. 108).

[188] J. Meadows and A. K. Agrawal. "Time-resolved PIV of lean premixed combustion without and with porous inert media for acoustic control". *Combustion and Flame* 162 (4), 2015, pp. 1063–1077 (cited in p. 108).

[189] M. Fogleman, J. Lumley, D. Rempfer, and D. Haworth. "Application of the proper orthogonal decomposition to datasets of internal combustion engine flows." *Journal of Turbulence* 5 (23), 2004, pp. 1–3 (cited in p. 108).

[190] S. Kostka, A. C. Lynch, B. C. Huelskamp, B. V. Kiel, J. R. Gord, and S. Roy. "Characterization of flame-shedding behavior behind a bluff-body using proper orthogonal decomposition". *Combustion and Flame* 159 (9), 2012, pp. 2872–2882 (cited in p. 108).

[191] K. Bizon, G. Continillo, E. Mancaruso, S. S. Merola, and B. M. Vaglieco. "POD-based analysis of combustion images in optically accessible engines". *Combustion and Flame* 157 (4), 2010, pp. 632–640 (cited in pp. 108, 109).

[192] K. Bizon, G. Continillo, S. Lombardi, P. Sementa, and B. M. Vaglieco. "Independent component analysis of cycle resolved combustion images from a spark ignition optical engine". *Combustion and Flame* 163, 2016, pp. 258–269 (cited in p. 109).

[193] H. Chen, D. L. S. Hung, M. Xu, H. Zhuang, and J. Yang. "Proper orthogonal decomposition analysis of fuel spray structure variation in a spark-ignition direct-injection optical engine". *Experiments in fluids* 55 (4), 2014, p. 1703 (cited in p. 109).

[194] H. Chen, D. L. Reuss, and V. Sick. "Analysis of misfires in a direct injection engine using proper orthogonal decomposition". *Experiments in fluids* 51 (4), 2011, pp. 1139–1151 (cited in p. 109).

[195]   S. J. DANBY and T. ECHEKKI. "Proper orthogonal decomposition analysis of autoignition simulation data of nonhomogeneous hydrogen–air mixtures". *Combustion and Flame* 144 (1), 2006, pp. 126–138 (cited in p. 109).

[196]   J. R. SHEWCHUK. "Tetrahedral mesh generation by Delaunay refinement". *Proceedings of the fourteenth annual symposium on Computational geometry*, 1998, pp. 86–95 (cited in p. 113).

[197]   L. P. CHEW. "Guaranteed-quality delaunay meshing in 3d (short version)". *Proceedings of the thirteenth annual symposium on Computational geometry*, 1997, pp. 391–393 (cited in p. 113).

[198]   A. HENDERSON, J. AHRENS, C. LAW, et al. *The ParaView Guide*. Kitware Clifton Park, NY, 2004 (cited in p. 113).

[199]   H. EDELSBRUNNER, D. KIRKPATRICK, and R. SEIDEL. "On the shape of a set of points in the plane". *IEEE Transactions on information theory* 29 (4), 1983, pp. 551–559 (cited in p. 113).

[200]   C. W. ROWLEY, I. MEZIĆ, S. BAGHERI, P. SCHLATTER, and D. S. HENNINGSON. "Spectral analysis of nonlinear flows". *Journal of fluid mechanics* 641, 2009, pp. 115–127 (cited in pp. 115, 116).

[201]   K. K. CHEN, J. H. TU, and C. W. ROWLEY. "Variants of dynamic mode decomposition: boundary condition, Koopman, and Fourier analyses". *Journal of nonlinear science* 22 (6), 2012, pp. 887–915 (cited in pp. 115, 116).

[202]   F. RICHECOEUR, L. HAKIM, A. RENAUD, and L. ZIMMER. "DMD algorithms for experimental data processing in combustion". *Proceedings of the Summer Program 2012*, 2012, pp. 459–468 (cited in p. 115).

[203]   R. SAMPATH and S. R. CHAKRAVARTHY. "Investigation of intermittent oscillations in a premixed dump combustor using time-resolved particle image velocimetry". *Combustion and Flame* 172, 2016, pp. 309–325 (cited in p. 115).

[204]   J. DAHAN, R. FUTRZYNSKI, C. O'REILLY, and G. EFRAIMSSON. "Aero-acoustic source analysis of landing gear noise via dynamic mode decomposition". *21st International Congress on Sound and Vibration*, 2014 (cited in p. 115).

[205]   R. FUTRZYNSKI and G. EFRAIMSSON. *Dymode: A parallel dynamic mode decomposition software*. KTH Royal Institute of Technology. 2015 (cited in p. 117).

[206]   J. KOU and W. ZHANG. "An improved criterion to select dominant modes from dynamic mode decomposition". *European Journal of Mechanics - B/Fluids* 62, 2017, pp. 109–129 (cited in p. 117).

[207]   J. BENAJES, R. NOVELLA, J. M. PASTOR, A. HERNÁNDEZ-LÓPEZ, et al. "Optimization of the combustion system of a medium duty direct injection diesel engine by combining {CFD} modeling with experimental validation". *Energy Conversion and Management* 110, 2016, pp. 212–229 (cited in pp. 124, 144, 145).

[208] A. López, J. Aisa, A. Martinez, and D. Mercado. "Injection moulding parameters influence on weight quality of complex parts by means of DOE application: Case study". *Measurement* 90, 2016, pp. 349–356 (cited in pp. 124, 178).

[209] W. G. Box G. E. an Hunter and J. S. Hunter. *Statistics for Experimenters: Design, Innovation, and Discovery*. Wiley, 2005 (cited in p. 124).

[210] S. W. Park. "Optimization of combustion chamber geometry for stoichiometric diesel combustion using a micro genetic algorithm". *Fuel Processing Technology* 91 (11), 2010, pp. 1742–1752 (cited in p. 140).

[211] D. D. Wickman, H. Yun, and R. D. Reitz. "Split-Spray Piston Geometry Optimized for HSDI Diesel Engine Combustion". *SAE 2003 World Congress & Exhibition*, 2003 (cited in p. 140).

[212] Y. Sun, T. Wang, Z. Lu, L. Cui, and M. Jia. "The Optimization of Intake Port using Genetic Algorithm and Artificial Neural Network for Gasoline Engines". *SAE 2015 World Congress & Exhibition*, 2015 (cited in pp. 140, 142).

[213] A. Navid, S. Khalilarya, and H. Taghavifar. "Comparing multi-objective non-evolutionary NLPQL and evolutionary genetic algorithm optimization of a DI diesel engine: DoE estimation and creating surrogate model". *Energy Conversion and Management* 126, 2016, pp. 385–399 (cited in p. 142).

[214] A. J. F. Griffiths, J. H. Miller, D. T. Suzuki, R. C. Lewontin, and W. M. Gelbart. "Selective systems", 2000 (cited in p. 143).

[215] B. Yang, L. Wang, L. Ning, and K. Zeng. "Effects of pilot injection timing on the combustion noise and particle emissions of a diesel/natural gas dual-fuel engine at low load". *Applied Thermal Engineering* 102, 2016, pp. 822–828 (cited in p. 177).

[216] J. P. Perr, J. V. Perr, L. L. Peters, D. J. Benson, and J. T. Carroll. *Variable spray hole fuel injector with dual actuators*. US Patent 6.557.779. 2003 (cited in pp. 178, 179).

[217] S. Choi, S.-H. Shin, J. Lee, K. Min, and H. Choi. "The effects of the combustion chamber geometry and a double-row nozzle on the diesel engine emissions". *Proceedings of the Institution of Mechanical Engineers, Part D: Journal of Automobile Engineering* 229 (5), 2015, pp. 590–598 (cited in p. 179).

[218] S. Molina, C. Guardiola, J. Martín, and D. García-Sarmiento. "Development of a control-oriented model to optimise fuel consumption and NOx emissions in a DI Diesel engine". *Applied Energy* 119, 2014, pp. 405–416 (cited in p. 181).
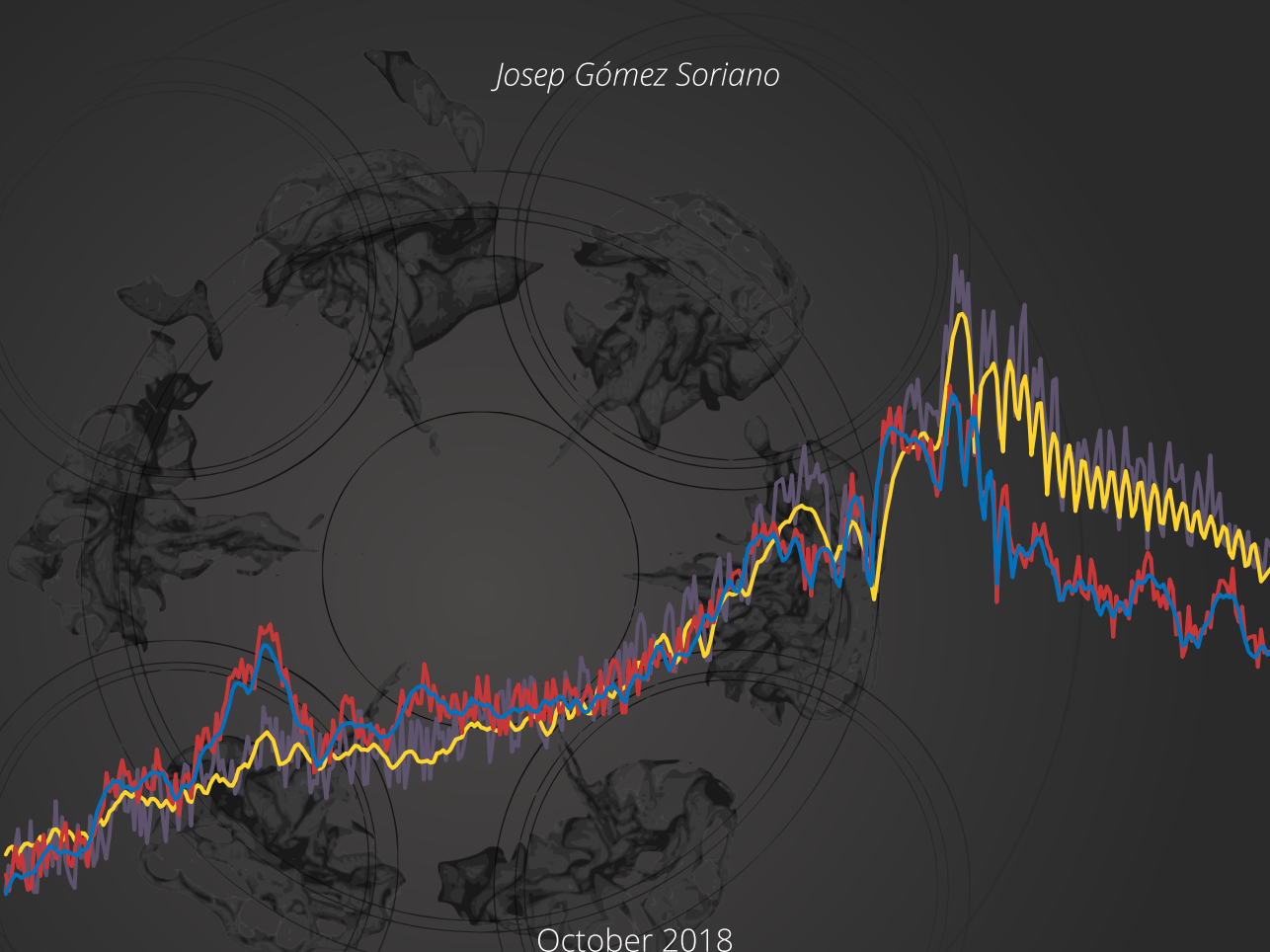
UNIVERSITAT POLITÈCNICA DE VALÈNCIA

COMPUTATIONAL ASSESSMENT OF COMBUSTION NOISE OF AUTOMOTIVE COMPRESSION-IGNITED ENGINES

Josep Gómez Soriano